LOW-THRUST TRAJECTORY DESIGN AND OPTIMIZATION OF LUNAR SOUTH POLE COVERAGE MISSIONS

A Dissertation
Submitted to the Faculty
of
Purdue University
by
Martin T. Ozimek

In Partial Fulfillment of the
Requirements for the Degree
of
Doctor of Philosophy

May 2010
Purdue University
West Lafayette, Indiana

"As far as we can discern, the sole purpose of human existence is to kindle a light of meaning in the darkness of mere being."

Carl Jung, *Memories, Dreams and Reflections* (1963)

ACKNOWLEDGMENTS

The pursuit of my goal to obtain a doctoral degree studying astrodynamics has been a deeply personal challenge. It has also ended up being a journey down a road with many unexpected twists and turns. It amazes me that even in pursing what seems like the most individualistic of goals, I have been far from alone along the way. While I have spent the past six years at a physical distance from my family, they have always been there to push me forward in the worst of times, to keep me grounded when I've (unjustifiably) thought too highly of myself, and to convince me to stop taking life so seriously and just relax. Such guidance is only possible from the ones that are closest to me. Professor Kathleen Howell, my advisor, has continued to provide the same mentorship that she has given me from day one. I truly believe that I owe many aspects of my professional development to her, in addition to the academic nurturing that so many have benefited from. I must also thank Professor James Longuski, who was the first person to call me at my home shortly after my acceptance to Purdue University, and one whom I credit in heavily influencing my decision to attend. In reaching the end of my time here at Purdue, I know that I will always be thankful that he did so. I am extremely indebted to my friend and co-researcher, Dan Grebow. Little did I know that when Dan offered his assistance on a bit of solar sail research that I was working on, it would become a long-term collaboration, turn into several research papers worth of work, and eventually culminate in a dissertation. We have had an interesting work dynamic, and I doubt that many of my ideas would have come to any fruition without our engaging, entertaining, frustrating, and ultimately rewarding discussions that were sometimes decided over a bet for a steak dinner (that I lost). The idea to study mission applications for lunar south pole coverage was made possible through the amazing opportunity to collaborate with the NASA Goddard Spaceflight Center, and through the NASA Graduate Student

Research Program Fellowship under NASA Grant number NNX07A017H. Additional support from NASA under contract numbers NNG05GM76G and NNX06AC22G is also greatly appreciated. While at NASA, Mr. Dave Folta was always able to help me with any question, and many of the mission applications investigated herein are his original concepts. I am grateful for his help. I would also like to thank the members of my research group, including my roommates Tom Pavlak and Todd Brown, as well as Lindsay Millard, Wayne Schlei, Masaki Kakoi, Diane Craig-Davis, Zubin Olikara, Chris Patterson, Raoul Rousch, and many others. I am especially indebted to Wayne and Todd for some of the visuals that appear throughout this work, which were created in the Eliason Visualization Laboratory. Lastly, I will miss the Friday lunches at Harry's, the 632 Barbecues, and my most recent roommate, Drew Brees.

TABLE OF CONTENTS

LIST OF TABLES

Table Page

LIST OF FIGURES

Figure Page

Appendix Figure

SYMBOLS

(x, y, z)	position of spacecraft in the rotating frame
$\boldsymbol{r}$	position vector of spacecraft in the rotating frame
(v_x, v_y, v_z)	velocity of spacecraft in the rotating frame
$\boldsymbol{v}$	velocity of spacecraft in the rotating frame
$\hat{x}$-$\hat{y}$-$\hat{z}$	unit vectors defining the rotating frame
m	spacecraft mass
P_1	larger primary body in the restricted three-body problem
P_2	smaller primary body in the restricted three-body problem
P_3	spacecraft in the restricted three-body problem
θ	angle between rotating and inertial frame
Ω	angular rate between rotating and inertial frame
l^*	characteristic length
t^*	characteristic time
m_B^*	characteristic mass for restricted three-body problem
m_B^*	characteristic mass for thrust acceleration model
γ	mass ratio of the smaller primary to the total system mass
G	gravitational constant
U	pseudo-potential function in the restricted three-body problem
C_j	Jacobi's Constant
(X, Y, Z)	velocity of spacecraft in the Earth mean-of-equator of J2000 frame
$\boldsymbol{R}$	velocity vector of spacecraft in the Earth mean-of-equator of J2000 frame
(V_X, V_Y, V_Z)	velocity of spacecraft in the Earth mean-of-equator of J2000 frame
$\boldsymbol{V}$	velocity vector of spacecraft in the Earth mean-of-equator of J2000 frame

$\hat{X}$-$\hat{Y}$-$\hat{Z}$	unit vectors defining the Earth mean-of-equator of J2000 frame
$\hat{X}_L$-$\hat{Y}_L$-$\hat{Z}_L$	unit vectors defining the International Astronomical Union frame
$m_{\leftmoon}$	mean radius of the moon
$m_{\oplus}$	mean radius of the Earth
$m_{\odot}$	mean radius of the sun
$r_{\leftmoon}$	mean radius of the moon
$r_{\oplus}$	mean radius of the Earth
$\boldsymbol{f}_G$	acceleration vector due to gravitational ephemerides
$\boldsymbol{f}_O$	acceleration vector due to Earth oblateness
$\boldsymbol{f}_S$	acceleration vector due to solar radiation pressure
$k_{\odot}$	material parameter dependent on absorptivity of the spacecraft surface
A	projected cross-sectional area of the spacecraft
$S_{\odot_0}$	solar light flux at one astronomical unit
c	speed of light
$\boldsymbol{f}_T$	thrust acceleration vector
$\boldsymbol{u}$	steering control vector
$\hat{\boldsymbol{u}}$	steering control unit vector
$\boldsymbol{u}_c$	control vector
κ	solar sail characteristic acceleration
$\boldsymbol{l}$	sun-to-spacecraft vector
$\hat{\boldsymbol{l}}$	sun-to-spacecraft unit vector
ω_s	lunar synodic angular rate
α	solar sail pitch angle
δ	solar sail clock angle
α_k	k^{th} Fourier coefficient for solar sail pitch angle
δ_k	k^{th} Fourier coefficient for solar sail clock angle
T	thrust magnitude
I_{sp}	specific impulse

g_0	Earth gravitational acceleration constant at sea level
P	engine power
θ_1, θ_2	direction cosine angles for shadowing conditions
$\boldsymbol{R}_g$	position vector of lunar ground station relative to the moon's center
θ_g	latitude that orients the lunar ground station in moon body-fixed coordinates
δ_g	latitude that orients the lunar ground station in moon body-fixed coordinates
$\mathbf{C}$	direction cosine matrix
α_L	right ascension angle between the International Astronomical Union frame and the moon-centered inertial, EMEJ2000 frame
δ_L	declination angle between the International Astronomical Union frame and the moon-centered inertial, Earth mean of equator, J2000 inertial frame
$(\phi_L, \vartheta_L, \psi_L)$	Euler 3-1-3 angle set orienting the International Astronomical Union frame and the moon-centered inertial, Earth mean of equator, J2000 inertial frame
$(\phi_{\leftmoon}, \vartheta_{\leftmoon}, \psi_{\leftmoon})$	Euler 3-1-3 angle set orienting the moon body-fixed and moon-centered inertial, Earth mean of equator, J2000 inertial frame
$\boldsymbol{X}$	variable vector
$n_{\boldsymbol{X}}$	length of variable vector
$\boldsymbol{F}$	constraint vector
$m_{\boldsymbol{X}}$	length of constraint vector
$\boldsymbol{S}$	search direction vector
α_d	step length for search direction
J	cost function
J'	augmented cost function
$\boldsymbol{\lambda}_{m_{\boldsymbol{X}}}$	Lagrange multiplier vector for minimum-norm problem

$\boldsymbol{f}$	dynamical system model vector
$\boldsymbol{\mu}$	parameter vector
n_{μ}	length of parameter vector
$\mathbf{A}$	Jacobian matrix for a linearized system of differential equations
$\boldsymbol{\Phi}$	state transition matrix
h_d	step size for finite difference derivatives
$\mathbb{P}$	orbital period
K	constant parameter for power-limited, finite-burning engine trajectory optimization problem
$\boldsymbol{g}$	general gravity field vector
$\boldsymbol{\psi}_0$	initial kinematic boundary condition vector
$\boldsymbol{\psi}_f$	final kinematic boundary condition vector
τ_1	time-like parameter for departure orbit
τ_2	time-like parameter for arrival orbit
$\boldsymbol{\nu}_1$	Lagrange multiplier vector associated with initial kinematic boundary conditions
$\boldsymbol{\nu}_2$	Lagrange multiplier vector associated with final kinematic boundary conditions
σ	engine power slack variable
H	Hamiltonian
$\boldsymbol{\lambda_r}$	position costate vector
$\boldsymbol{\lambda_v}$	velocity costate vector
$\boldsymbol{\lambda}_m$	mass costate
$\boldsymbol{\lambda}$	full costate vector
η_1, η_2	Lagrange multipliers for bounded controls
S	switching function
F_0	direct optimization cost function
Π	set of discrete mesh points
n	number of nodes

τ	normalized segment time
$\mathbf{M}$	7$^{\text{th}}$-degree piecewise polynomial coefficient matrix
$\mathbf{B}$	7$^{\text{th}}$-degree piecewise polynomial constant matrix
$\boldsymbol{\Delta}_{i,1}, \boldsymbol{\Delta}_{i,c}, \boldsymbol{\Delta}_{i,4}$	defect constraint vectors for higher-order collocation
$\boldsymbol{g}_i, \boldsymbol{g}_{i,2}, \boldsymbol{g}_{i,3}$	discretized path constraint vectors for higher-order collocation
$\boldsymbol{\eta}_i, \boldsymbol{\eta}_{i,2}, \boldsymbol{\eta}_{i,3}$	slack variable vectors for higher-order collocation
m	length of discretized path constraint vectors
ψ_i	control constraint for i^{th} node
h_r	specific nodal constraint function
T_i	burn time along the j^{th} thrust arc
δ_i	time ratio for i^{th} node
k	number of thrust arcs
$n_{b,j}$	number of nodes for the j^{th} thrust arc
$n_{c,j}$	number of nodes for the j^{th} coast arc
$T_{b,j}$	burn time along the j^{th} thrust arc
$T_{c,j}$	coast time along the j^{th} coast arc
$c_{b,j}$	positive time constraint for the j^{th} thrust arc
$c_{c,j}$	positive time constraint for the j^{th} coast arc
$\nu_{b,j}$	slack variable for the j^{th} thrust arc
$\nu_{c,j}$	slack variable for the j^{th} coast arc
$\psi_{b,j}$	continuous mass constraint for the j^{th} thrust arc
$\boldsymbol{Y}_{b,j}$	variable vector for the j^{th} thrust arc
$\boldsymbol{Y}_{b,j}$	variable vector for the j^{th} coast arc
$\boldsymbol{G}_{b,j}$	constraint vector for the j^{th} thrust arc
$\boldsymbol{G}_{b,j}$	constraint vector for the j^{th} coast arc
K	number of phases
e_i	integration error for the i^{th} trajectory segment
$\bar{e}$	mean integration error
θ_{Π}	piecewise constant function

I	integral function
ϵ	user-defined tolerance
$e_{\leftmoon}$	lunar two-body eccentricity
$i_{\leftmoon}$	lunar two-body inclination
$a_{\leftmoon}$	lunar two-body semi-major axis
$\omega_{\leftmoon}$	lunar two-body argument of periapse
$E_{\oplus}$	Earth two-body energy
$H_{\oplus}$	Earth two-body angular momentum
$\boldsymbol{\mathcal{H}}$	instantaneous angular momentum vector,
$\gamma_{\oplus}$	Earth two-body flight path angle
ϕ	elevation angle from the lunar south pole
ϕ_{lb}	prescribed minimum elevation angle boundary of spacecraft from the lunar south pole
ϕ_{min}	minimum elevation angle of spacecraft from the lunar south pole
ϕ_{avg}	mean elevation angle of spacecraft from the lunar south pole
ϕ_{max}	maximum elevation angle of spacecraft from the lunar south pole
a_{ub}	prescribed maximum altitude boundary of spacecraft from the lunar south pole
a_{min}	minimum altitude of spacecraft from the lunar south pole
a_{max}	maximum elevation of spacecraft from the lunar south pole
$\hat{\boldsymbol{h}}$	unit vector parallel to the angular momentum associated with the Earth's orbit relative to the sun
$\alpha_{\boldsymbol{u}}, \beta_{\boldsymbol{u}}$	adjoint control transformation angles

ABBREVIATIONS

ACT	adjoint control transformation
AU	astronomical unit
CSI	constant specific impulse
ECI	Earth-centered inertial
ECR	Earth-centered rotating
EMEJ2000	Earth mean of equator, J2000 inertial coordinate system
GTO	geosynchronous transfer orbit
IAU	International Astronomical Union
ISS	International Space Station
MCI	moon-centered inertial
MCR	moon-centered rotating
NLP	nonlinear programming
ODE	ordinary differential equation
RTBP	restricted three-body problem
SRP	solar radiation pressure
TOF	time-of-flight
TPBVP	two-point boundary-value problem
UTC	Coordinated Universal Time
VASIMR	Variable Specific Impulse Magnetoplasma Rocket
VSI	variable specific impulse

ABSTRACT

Ozimek, Martin T. Ph.D., Purdue University, May 2010. Low-Thrust Trajectory Design and Optimization of Lunar South Pole Coverage Missions. Major Professor: Kathleen C. Howell.

A framework for designing and optimizing low-thrust trajectories for lunar south pole coverage missions is developed. Such missions may involve three, two, or even one satellite to maintain continuous communications between a lunar ground station and the Earth. Special emphasis is dedicated to single satellite communication links, which involve the design and discovery of novel pole-sitter orbits. Pole-sitters are possible, given the availability of an efficient low-thrust force in the model. Low-thrust acceleration can be delivered in various forms; solar sails and electric propulsion engines are obvious examples. Low-thrust propulsion may also be employed to construct transfer trajectories to the coverage orbits of interest as well as end-of-life transfers. Additionally, a low-thrust thruster allows a spacecraft to shift between lunar coverage orbits. In this scenario, an optimal control-based approach is applicable for rapidly computing trajectories, however, in general, the many complexities involved in generating the trajectories are best solved with a direct transcription approach using collocation and mesh refinement. This general process is robust and allows for the inclusion of an unknown control history, path constraints, and the simultaneous optimization of multiple phases while exploiting matrix sparsity for maximum computational efficiency. Even incorporating higher-fidelity dynamical effects, the pole-sitter solutions can be sustained as a long-duration option, using a solar sail, or as a temporary option in excess of one year on a small 500 kg spacecraft, using a solar electric propulsion engine comparable to existing technology.

1. INTRODUCTION

As humans explore the possibilities of building a sustainable outpost on the moon for long-term exploration, the near-term space technology development efforts will require careful planning and the infrastructure to undertake such an ambitious plan. Currently, missions such as NASA's Lunar Reconnaissance Orbiter [1] (LRO) and Lunar Crater Observation and Sensing Satellite (LCROSS), [1] the Indian Space Research Organisation's Chandrayaan-1, [2] and JAXA's Selenological and Engineering Explorer [3] all involve a detailed analysis of the lunar geological composition and potential lunar ground site locations, with emphasis on the south pole region due to the existence of frozen water ice and continual sunlight. Should the lunar south pole be utilized for a future human outpost, relay satellites are a necessary component to maintain continuous communications with the Earth since a direct line-of-sight is unavailable from any Earth ground stations.

The use of efficient, high specific impulse, low-thrust propulsion yields potential fuel-saving benefits in the effort to establish and maintain reliable relay satellites. With the successful, long-duration technology demonstration of the Deep Space 1 and the SMART-1 probes, this technology now has a proven heritage, and continues to be proposed for missions where fuel savings are desirable at the expense of additional time-of-flight. New trajectory design options that are available to support a lunar south pole facility include long-duration, low-thrust transfers, the flexibility to shift between different mission orbits, and single-spacecraft “pole-sitter” orbits. The current state of low-thrust propulsion technology suggests that it is now possible to realize these capabilities. As the state of different types of low-thrust technology advances, the possibility of nearly propellant-free trajectories with solar sails may even soon be viable. Many trajectory options also exploit the dynamical structure available in the circular restricted three-body model. This environment exposes additional dynamical pathways that emerge as a result of the existence of five libration points. The three-body model and these corresponding equilibrium points open new possible regions for natural coverage orbits as well as controlled, path constrained orbits. The resulting three-body solutions are then accessible with fuel-efficient transfer trajectories that exploit the orbital stability properties.

The realization of low-thrust, lunar relay mission architectures involves the successful management of several design complexities. For example, a continuously changing steering direction is required to meet the prescribed problem constraints. This control history for the thruster must be determined for each specific mission application. An initial guess for the shape of a transfer trajectory as well as a pole-sitter orbit is necessary. It is also likely that the fuel consumption or time-of-flight are optimization objectives in a given phase of a mission, subject to conditions that must be met during all of the other phases. Additionally, robust and accurate numerical algorithms must be developed that retain their integrity under the effects of chaotic dynamical behavior. Designs must be verified with accurate higher-fidelity models as well. Finally, the overall performance of the trajectories as part of a larger mission framework must be defined and then assessed. These major design complexities and the associated challenges are considered within this work.

1.1 Problem Definition

The ultimate goal is the development of a framework for the design and optimization of low-thrust trajectories for lunar south pole coverage relays and the application to potential mission scenarios, given the state of current and future technology. All trajectories evaluated here are assumed to rely exclusively on low-thrust propulsion, that is, the advantages of a potential fuel expenditure savings compared to traditional high-thrust chemical options is considered a necessity. Applications for transfers, coverage orbits, and end-of-life scenarios are explored. The culmination of the design process involves the computation of all phases of the trajectory simultaneously in one multi-phase optimization process. The investigation of transfers includes the departure from an Earth orbit, deployment into a coverage orbit, and even transfers between orbits of interest. The investigation of coverage orbits includes a discussion and survey of naturally occurring options that incorporate two or more spacecraft for continuous coverage; and, a detailed investigation of the novel pole-sitter option is a primary design focus. Finally, end-of-life trajectories are incorporated as a mission planning necessity when a spacecraft may potentially exceed available fuel or power. Trajectory optimization is discussed for individual phases, but the methodology is also extended to optimize the fuel or the time associated with a specified phase, given the coupling between the variables in other phases. By linking the phases together in a single, larger-dimensioned process, improvements in the final optimization objective are possible. Finally, a detailed analysis and discussion of the optimized mission scenarios is included.

1.2 Previous Work

1.2.1 Brief History of Low-Thrust Propulsion

Three low-thrust propulsion technologies are the focus in this analysis. These technologies include solar electric propulsion (assumed to be constant specific impulse), variable specific impulse propulsion, and solar sailing. The first two forms of propulsion require fuel mass and kilowatt-class power sources, while solar sailing relies on the propellant-free effect of controlling solar radiation pressure through the use of reflecting material with a large surface area.

Modern electric thrusters operate at a specific impulse of about eight times that of chemical thrusters; this type of propulsion is commonly used on communications satellites for north–south stationkeeping and orbit raising. According to Sovey et al., [4] the higher specific impulse operation saves enough propellant mass, compared to a traditional chemical system, to nearly double the transponder hardware on a communications satellite. Experiments in ion propulsion began as early as 1916, when

Robert H. Goddard experimented with ionized thrust for near-vacuum conditions at high altitudes. [5] In 1923, Hermann Oberth, in the book "Wege zur Raumschiffahrt" (Ways to Spaceflight), [6] documented the possibilities of fuel mass savings from electric propulsion, and advocated the use of electrostatic propulsion from charged gases. A working ion thruster was built by Harold R. Kaufman in 1959 at the NASA Glenn facility. Substantial early testing of the innovative technology ensued in the 1960's and 1970's with the Space Electric Rocket Test (SERT) flights. Suborbital testing first commenced in 1964 with SERT I, which successfully operated for 31 minutes. The SERT II program followed with additional flight tests in the 1970's and included ground tests with sustained operation for 6,742 hours and 5,169 hours, respectively. The SERT II flight is considered the major in-space demonstration of the technology, with a six month orbital test of a thruster with a 0.85 kW maximum power level, providing operation at a 28 mN thrust level and 4,200 seconds specific impulse. At this time, the Air Force also established similar testing, through Program 661A in the 1960's. In the late 1960's, the Solar Electric Propulsion System Technology (SEPST) program [7] was established at the Jet Propulsion Laboratory (JPL) in an effort to use solar electric power for interplanetary spacecraft applications. Detailed ground tests were conducted on a 2.5 kW thruster capable of 88 mN of power and 3,600 seconds of specific impulse. In anticipation of the technology development, several astrodynamicists began examining methods to produce the corresponding trajectories. [8–10] By the late 1990's, ion propulsion systems finally emerged for operational use. In 1997, the Hughes Space and Communications Company launched 10 operational communications satellites with four 0.44 kW xenon ion thrusters, and on October 24, 1998 the Deep Space 1 spacecraft [11] was launched with the NSTAR solar electric thruster, capable of 0.5–2.3 kW of power, 19–92 mN of thrust, and 1,900–3,100 seconds of specific impulse. (See Figure 1.1.) By February 17, 2001, the NSTAR successfully operated for 9,241 continuous hours. [12] Significant missions involving solar electric spacecraft, examples since Deep Space 1, include the European Space Agency's SMART-1 [13] that involved a controlled collision into the moon, and NASA's 2007

Dawn mission that will explore the asteroid Vesta and the dwarf planet Ceres using three Deep Space 1 heritage thrusters. [14] Currently, almost 200 solar-powered satellites in Earth orbit utilize electric propulsion [15] and over the next few decades, many advanced ion propulsion missions are being suggested for further interplanetary flight, such as new comet missions, a Mars sample return, and proposed Europa landers.

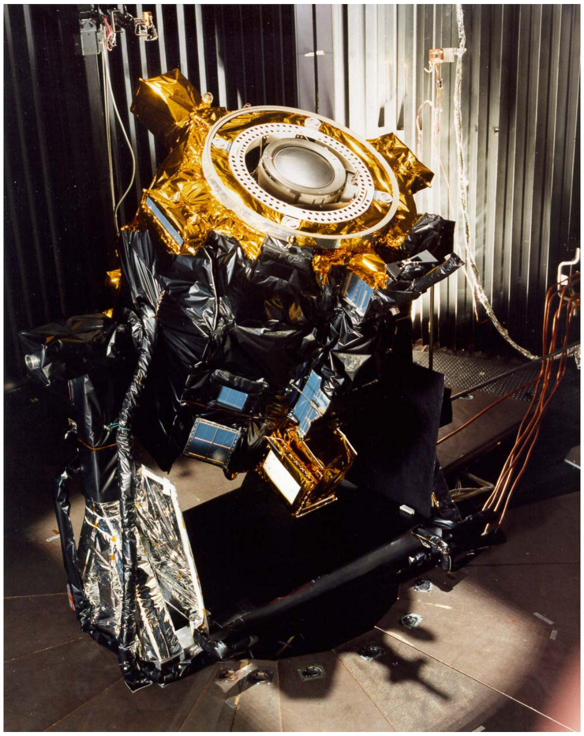

Figure 1.1. Ground Testing of the Deep Space 1 Spacecraft. [16]

A distinguishing characteristic of an electric thruster is the engine and its operation at a constant or a variable specific impulse. The commonly-employed electrostatic ion engines, such as the NSTAR engine, normally operate at constant specific impulse via the Coulomb force, but variable specific impulse thrusters, such as Hall effect thrusters, as flown aboard SMART-1 and the Variable Specific Impulse Magnetoplasma Rocket (VASIMR), incorporate the capability to vary the thrust magnitude. In particular, the VASIMR engine is a higher-power alternative that has been under development at NASA Johnson Space Center's Advanced Propulsion Laboratory since 1994. The existing prototype technology is expected to produce engines that can operate anywhere between 10–200 kW. Successful ground testing of the 200 kW power prototype has already occurred, and a flight test on the International Space Station is planned for 2013. [17] With the use of nuclear power in the megawatt range, the technology could be used to transport heavy lunar cargo and other large unmanned or even manned vehicles in the near future. [18] (See Figure 1.2.)

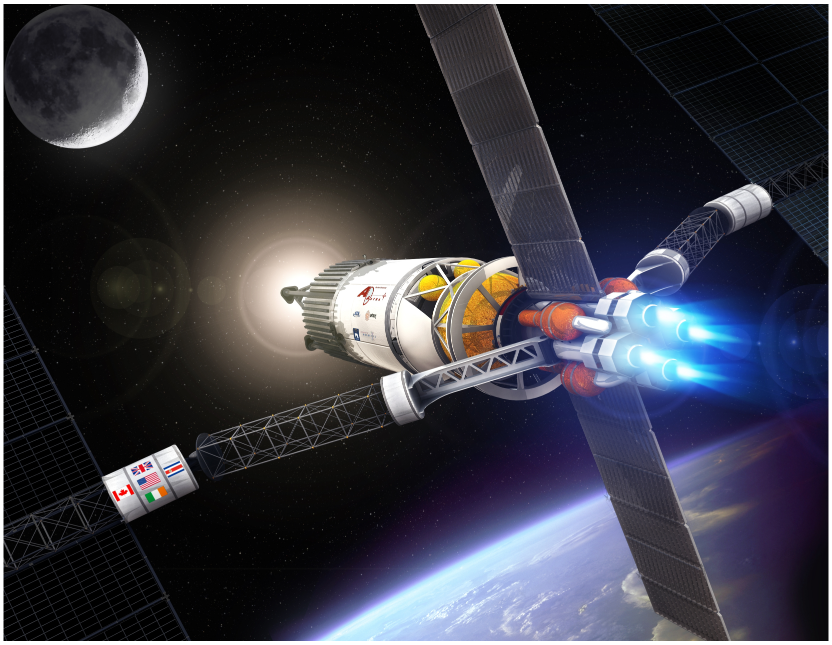

Figure 1.2. Conceptual Application of the VASIMR Engine. [19]

Finally, a propellant-free form of low-thrust propulsion is also available from a solar sail. (See Figure 1.3.) The concept of practical solar sailing was introduced as early as the 1920's, according to the writings of the Soviet pioneer Tsiolkovsky and his colleague Tsander. [20] Following a proposal by Richard Garwin of the IBM Watson Laboratory at Columbia University in 1958, who coined the term "solar sailing", more detailed studies ensued in the later 1950's, and the 1960's. Aided in part by mission applications envisioned by prominent science-fiction authors, [21] serious investigations continued to be pursued. In 1967, Vonbun proposed an interesting and relevant mission concept using low-thrust propulsion, not for transporting a spacecraft, but to maintain a stationary position at the Earth-moon L_2 point. [22] From 1976-1978, NASA initiated the first major mission design study incorporating a solar sail to rendezvous with Halley's Comet. In 1991, Robert L. Forward, proposed "statites" that would employ solar radiation pressure to levitate in non-Keplerian trajectories. [23] Forward also proposed "polestats", i.e., statites that hover above the polar regions of the Earth. These applications resemble Vonbun's hummingbird concept, but rely specifically on a solar sail for propulsion. In 2006, solar sails were also identified as one of five technological capabilities under consideration in NASA's Millennium Space Technology 9 (ST-9) mission. Proposals for ST-9 have included solar sails that produce thrust on the order of 0.58 mm/s^2 to values as high as 1.70 mm/s^2. [24] A recent study by West also considers these magnitudes of characteristic acceleration in designing lunar pole-sitters. [25]. Ongoing efforts continue to focus on an in-flight demonstration of a solar sail.

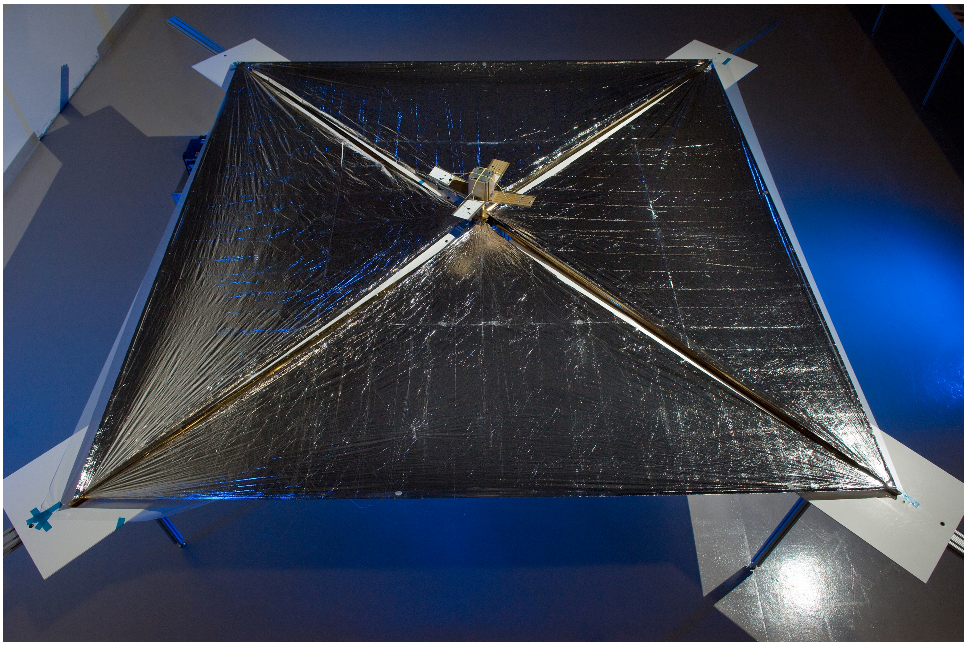

Figure 1.3. Nanosail-D: An Example of a Solar Sail. [26]

1.2.2 Low-Thrust Trajectory Design and Optimization

Systematic design of a low-thrust, deep-space or interplanetary spacecraft trajectory is not a straightforward procedure. Despite the potential fuel-savings offered by the technology, actually *computing* low-thrust trajectories and optimizing the result has remained an ongoing area of active research in astrodynamics since the 1960's. The key difficulty lies in the selection of a thrust magnitude and direction at each instant along the continuous path, while subject to a set of nonlinear differential equations that are unsolvable in closed form. Therefore, solutions are not known a priori. Since solutions are not unique under the existence of a control input, a trajectory optimization problem is formulated to minimize or maximize a performance index, such as burn time or fuel mass. Additional challenges in the implementation of this process include the fact that the dynamical model may elicit chaotic behavior, the trajectory may also require path constraints (e.g., thrusting within a specified region only), the thrust magnitude may vary, and the direction may be constrained (as in solar sails). In total, this complexity often implies a lack of intuition for potential solutions and additional computational difficulties. Over the last 50 years, three distinct low-thrust trajectory design and optimization strategies have emerged: (i,ii) locally optimizing methods, which are gradient-based, and can be subdivided into indirect and direct approaches, and (iii) globally optimizing methods (which are inherently direct methods, but are not necessarily gradient-based).

The original approach for solving a low-thrust trajectory optimization problem is the *indirect* method that locally minimizes a performance index using optimal control theory, resulting in a two-point boundary-value problem (TPBVP). [8–10] Indirect methods are advantageous because they yield a relatively low-dimensioned problem with an algebraic control law and a set of constraint equations, that, when satisfied, guarantee local optimality. Solving indirect problems requires *at most* an iterative root-solving procedure, such as Newton's method; accurate initial guesses often produce rapid convergence. Usually, an explicit numerical integration scheme in conjunction with a shooting method [27] produces a highly accurate result. However, in general, the radius of convergence for problems solved with indirect methods is small, usually requiring a very accurate initial guess. Numerical methods, such as multiple shooting [27, 28] can be used to decompose a trajectory into a series of segments and partition the sensitivities over many “nodes”, but sensitivities may still remain. Producing an initial guess for the associated *costate* boundary conditions, which are not typically physically intuitive, can be very complicated (although transformation relationships are sometimes available). [29] Furthermore, the optimality conditions are often increasingly cumbersome to derive if the boundary conditions become more complex. Changing the objective function or adding phases to the design often necessitates a nontrivial re-derivation of the entire problem. Finally, path constraints are difficult to enforce. Despite these disadvantages, however, indirect methods are still used extensively, [30–33] generally because many solutions can be quickly investigated and the converged solutions are very accurate.

As computational speeds have dramatically increased since the 1990’s, the larger dimensioned direct methods have risen in prominence, and have been developed almost primarily due to the perceived difficulty of solving the indirect problems. The most well-known direct approaches are *direct* transcription via collocation (or direct collocation) and the pseudospectral method. Both methods use collocation [34] and discretize the entire continuous path into node points that lie on a polynomial approximation to the actual path. In direct transcription via collocation, a local collocation approach is used with a number of fixed internal points. Many trajectory segments between the nodes parameterize the path via piecewise polynomials. [35, 36] With a pseudospectral method, the collocation is typically handled globally with a low number of trajectory segments and node points, but with a high number of collocation points that parameterize the path using only a few piecewise polynomials. [37, 38] While discretization only yields an approximation to the path and the exact optimality conditions, in the limit the Karush-Kuhn-Tucker (KKT) conditions are equivalent to the necessary conditions stipulated by the indirect method. [39] (In this work, the direct transcription approach with local collocation is employed.) With collocation and direct transcription, path constraints along the entire trajectory, e.g., restriction of the spacecraft position history to a region below the lunar south pole, are easily enforced. Once the necessary constraint and gradient information is obtained, a variety of numerical methods are available for computing feasible [27] and/or optimal [40] trajectories. For trade studies, direct collocation methods are also easily adapted for changes in the objective function or adding phases of flight to the overall trajectory design problem. A larger basin of convergence is observed with collocation. In many cases, arbitrary initial conditions still yield solutions, thus, the technique is extremely useful when there is little intuition about the problem. One possible disadvantage of solving problems with collocation and direct transcription is their large dimensionality. However, with the increasing speed of computers and the efficiency of modern (linear algebra) computer algorithms, these approaches are now more tractable. Collocation strategies are also implemented in some capacity in software packages such as COLSYS, [41] AUTO, [42] OTIS, [35] and SOCS. [43]

The preceding indirect and direct approaches characterize a variety of *local* optimization techniques. Often, many local extrema exist for the performance index in a given problem. In such cases, *global* optimization procedures may be employed to further improve a solution generated from a local method. While the software to compute a local optimum is typically a gradient-based procedure, many globally optimizing algorithms, such as genetic algorithms, are stochastic. In trajectory design, genetic algorithms have been applied with notable success to gravitational flyby arcs, which involve an extraordinarily large number of feasible and locally optimal possibilities. [44, 45] Global methods often involve significant computational expense, and require feasible or locally optimal solutions that can be rapidly generated. Currently, the trajectories explored in this work are only locally optimizing because the computational expense for a global investigation, given current computational capabilities, would require a very large cluster of processors.

1.2.3 Lunar South Pole Coverage

Shortly after the Vision for Space Exploration was announced in 2004, [46] strategies for lunar south pole constellation architectures were studied by considering the operation of three satellites in low-altitude, elliptically inclined lunar orbits, with two of the three vehicles always in view of the south pole. [47–50] These studies consider a perturbed two-body analysis without full consideration to the possible advantages of the multi-body regime. Later, in 2006, Grebow et al. [51] demonstrated that constant communications can alternatively be accomplished with two spacecraft in many different combinations of Earth-moon libration point orbits, however, the higher altitudes in these orbits may have implications on the required communications instrumentation. (See Hamera et al. [52] for a mission feasibility comparison of these two different orbit configuration concepts.) Designing the trajectories in the chaotic system of the restricted three-body problem also suggests that constant surveillance might be achieved with just one spacecraft in the presence of a small control input. This possibility was confirmed by Ozimek et al., [53] who explored the capabilities of solar sails comparable to those proposed for NASA's Millennium Space Technology (ST-9) mission and applied to continuous south pole surveillance. Lunar pole-sitters were also investigated by West. [25] As previously noted however, the solar sail technology to support these trajectories is still under ongoing development. Alternatively, temporary long-duration coverage may be accomplished with one spacecraft and electric propulsion. This option remains virtually unexplored by researchers. In fact, after extensive literature review, only two previous investigations were discovered, with both focusing on the capabilities of low-thrust engines operating as Earth-based and not moon-based pole-sitters. [54, 55]

1.3 Scope of the Present Work

In light of the challenges of low-thrust trajectory design, and the potential mission applications, the goal of this research effort is the utilization of systematic methodologies and algorithms for designing and optimizing low-thrust trajectories applied to the lunar coverage problem. The recurring applications of interest include transfers between libration point orbits, as well as the end-to-end design of a low-thrust pole-sitter mission using either a solar sail or a solar electric thruster. Emphasis is then placed on the implementation of a process to systematically model and design all of the significant trajectory phases in such missions, including transfer trajectories, coverage orbits, and even end-of-life options. These mission phases are first discussed independently, but then the systematic multi-phase transcription method is demonstrated as a means to complete this process with one large-dimensioned algorithm. Within this framework, any trajectory phase of interest can be optimized, while simultaneously considering the consequences of the functional dependency on the other phases. The remainder of this work is organized as follows:

- Chapter 2: A detailed derivation of all dynamical models is presented. The basic dynamical model that is employed for lower-fidelity analysis and preliminary design is the restricted three-body problem with the addition of low-thrust forces from electric propulsion or solar sails. A higher-fidelity model is also detailed, where the effects of planetary ephemerides, solar radiation pressure, and Earth-oblateness are incorporated. Other higher-fidelity effects of interest such as shadowing and lunar librations are also developed. Finally, coordinate transformations are derived between the reference frames of interest.

- Chapter 3: The trajectory design and optimization methods are derived in detail. The general approach for constructing, implementing, and applying the shooting method is initially developed. The focus then transitions to the optimization of an objective function, and employment of the calculus of variations to derive the two-point boundary-value problem that is applied to transfer trajectories using power-limited, variable specific impulse engines. The remainder of Chapter 3 is devoted to a description of the direct transcription process using higher-order collocation. The methodology is adaptable for multiple phases and includes a procedure to refine the discrete mesh points until a desired integration accuracy is achieved.

- Chapter 4: The initial focus of a multi-phase lunar relay architecture is the coverage orbit. Several mission options and potential applications are computed for these orbits. The possibilities include lunar frozen orbits, libration point orbits, and pole-sitter orbits. Although frozen orbits are not considered in this work as coverage orbits, they may be exploited in end-of-life scenarios in a multiple phase mission. The libration point orbits have also been studied elsewhere, but are especially useful for transfer trajectories. Finally, the pole-sitter solutions are covered in detail, as well as the general process for configuring the collocation and transcription method to generate preliminary orbits.

- Chapter 5: The process of trajectory design is discussed in terms of (i) a transfer trajectory to a coverage orbit, (ii) transfers between coverage orbits, or (iii) transfers into an end-of-life scenario. An illustrative example of the optimal control approach is presented for the design of a transfer between libration point coverage orbits using a variable specific impulse engine. The capability to rapidly explore the associated design space is demonstrated. Methodologies to develop an initial guess for the collocation and transcription method with basic control laws are outlined. Refinement of an initial guess with collocation is addressed for the solar sail pole-sitter scenario, leading to a discussion for the completed mission design. The initial guesses for the transfer trajectories involving a solar electric propulsion pole-sitter are stored as part of a large multi-phase direct transcription problem, and discussed in further depth in Chapter 6.

- Chapter 6: Preliminary orbit designs from Chapter 4 are combined with transfer trajectories and end-of-life arcs from Chapter 5 for the direct transcription solution of the multi-phase pole-sitter mission using a solar electric thruster. This mission application demonstrates the full implementation of the direct transcription methodology discussed in Chapter 3. A simpler, proof-of-concept implementation is first achieved with the lower-fidelity models and no mesh refinement, and then the designs are validated by returning to the same problem and again generating a solution, but with a model that incorporates higher-fidelity effects and a transcription scheme that includes mesh refinement. The complete results for both the lower-fidelity and higher-fidelity solutions are discussed and compared.

- Chapter 7: Concluding remarks are presented and potential future research directions are offered.

2. SYSTEM MODELS

The fundamental dynamical model to reflect the influence of gravity, used throughout this investigation, is the set of differential equations in the Circular Restricted Three-Body Problem (RTBP.) Then, spacecraft thrust acceleration is added to completely represent the most significant forces on the spacecraft. In the absence of thrusting, an important solution in the RTBP is the set of five equilibrium points that are the basis for the computation of special periodic and quasi-periodic orbits. The equations of motion in the RTBP are derived in detail; in addition, the constant of the motion is derived as well as the locations for the corresponding equilibrium points. When spacecraft thrusting is considered, three different low-thrust models are presented. Ultimately, transition to a higher-fidelity force model is desired. A representative higher-fidelity model is derived, one that includes the effects of planetary ephemerides, solar radiation pressure, and Earth oblateness. Other important factors such as shadowing and lunar librations are also discussed. Finally, all relevant coordinate transformations that are employed throughout the entire investigation are detailed.

2.1 Restricted Three-Body Problem with Low-Thrust

Designing trajectories for lunar south pole coverage requires a simplified dynamical model before higher levels of fidelity are incorporated. For this investigation, this simplified model is the Earth-moon Circular Restricted Three-Body Problem (RTBP) with the addition of low-thrust acceleration. Even though the RTBP is unsolvable in closed form, it is selected as a preliminary design model for several important reasons. First, the system still possesses useful dynamical properties that assist in the design of a preliminary trajectory, such as an energy-like integral of the motion, equilibrium points, time invariance, and symmetries. Another important property is the existence of families of periodic and quasi-periodic orbits. The growth of high-speed computing in recent decades has yielded the capability to rapidly compute these orbits through the use of numerical integration. Furthermore, many RTBP orbit solutions of particular interest in the problem of lunar south pole coverage do not exist in more basic dynamical models such as the two-body problem. These solutions of interest include non-Keplerian orbital motions, such as "figure-eight" orbits, "halo" orbits, and an infinite variety of other orbits. Through the use of a thruster, pole-sitters and other unique, path-constrained trajectories are also possible.

The RTBP describes the motion of an infinitesimally small point mass, P_3 (of mass m_3), moving with respect to two particles of finite mass, or primaries, P_1 (of mass m_1) and P_2 (of mass m_2). (Unless otherwise specified, in this analysis P_1 always represents the Earth and P_2 always refers to the moon. (See Figure 2.1.) Given an arbitrary inertial reference point, dynamical analysis indicates that 18 first-order differential equations of motion are required to mathematically model the system comprised of the three bodies. This number, however, is reduced by considering the relative motion. The masses are thus defined such that $m_1 > m_2 \gg m_3$, restricting the problem in the sense that all gravitational influence exerted by m_3 is neglected. With this assumption, the motion of P_1 and P_2 is entirely Keplerian, and reduced to the solution of the two-body problem. Additionally, this two-body motion is constrained by assuming that the primaries move in a circular orbit about their common center of mass, or barycenter, B. As a result, the problem only requires 6 first-order differential equations.

2.1.1 Geometry of the Restricted Three-Body Problem with Low-Thrust

An inertial reference frame, I, described in terms of unit vectors $\hat{X}_B$-$\hat{Y}_B$-$\hat{Z}_B$, is centered at the barycenter, B, such that the $\hat{X}_B$-$\hat{Y}_B$ plane is defined to be coincident with the orbital plane for the primary orbits, such that $\hat{z} = \hat{Z}_B$. (Note that unit vectors belonging to a right-handed, orthonormal coordinate system are denoted in non-bold font with a “ˆ” overbar.) The primaries maintain a circular orbit in the $\hat{X}_B$-$\hat{Y}_B$ plane, but the third body can move in any of the three spatial dimensions. A rotating frame, R, with coordinate axes $\hat{x}$-$\hat{y}$-$\hat{z}$ is initially aligned with I, then rotates through the angle θ, such that the $\hat{x}$-axis is always directed from P_1 toward P_2. Both the $\hat{z}$-direction and $\hat{Z}_B$-direction are parallel to the orbital angular velocity vector of the primaries, and thus, the $\hat{y}$ and $\hat{Y}_B$ axes complete the respective right-handed systems. Due to the circular primary motion, the angular rate, $\dot{\theta} = \Omega$, is constant and equal to the Keplerian mean motion, n_{12}. The position vector of each primary, P_i, with respect to the barycenter is defined by $\boldsymbol{r}_i$, and the relative position vector of P_3 with respect to P_1 and P_2 is defined by $\boldsymbol{r}_{13}$ and $\boldsymbol{r}_{23}$, respectively. Note that a bold, italic font indicates a vector quantity. Shifting the base-point to the moon-centered, rotating (MCR) reference frame $\hat{x}_M$-$\hat{y}_M$-$\hat{z}_M$ or the Earth-centered, rotating (ECR) reference frame $\hat{x}_E$-$\hat{y}_E$-$\hat{z}_E$ is often useful for visualization purposes. (Note that for simplicity, the subscripts indicating the central body are typically dropped unless the distinction is necessary.)

2.1.2 Lower-Fidelity Equations of Motion

The derivation of the differential equations that govern the behavior in the RTBP exploits the classical nondimensionalized form. It is useful to note that dimensional and nondimensional quantities will be used hereafter, with the latter more commonly employed throughout for numerical scaling purposes. Thus, if it is necessary to distinguish dimensional quantities, a “ ˜ ” overbar is introduced. In figures, the dimensions are always included in the axis labels to avoid any ambiguities. Given these notational considerations, the derivation proceeds.

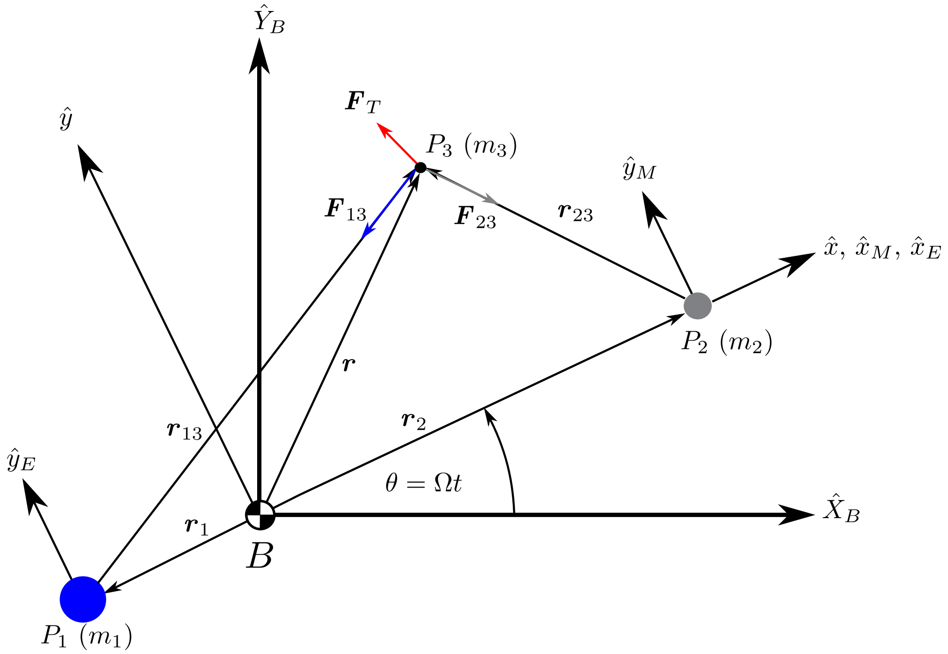

Figure 2.1. Geometry of the Earth-Moon System Model.

From Newton's 2nd Law, the vector differential equation describing the motion of P_3 is written

$$\begin{aligned}\tilde{\boldsymbol{F}}_3 &= \tilde{m}_3 \frac{{}^I d^2 \tilde{\boldsymbol{r}}}{d\tilde{t}^2} \\ &= \tilde{\boldsymbol{F}}_{13} + \tilde{\boldsymbol{F}}_{23} + \tilde{\boldsymbol{F}}_T \\ &= -\frac{\tilde{G}\tilde{m}_1\tilde{m}_3}{\left\|\tilde{\boldsymbol{r}}_{13}\right\|^3}\tilde{\boldsymbol{r}}_{13} - \frac{\tilde{G}\tilde{m}_2\tilde{m}_3}{\left\|\tilde{\boldsymbol{r}}_{23}\right\|^3}\tilde{\boldsymbol{r}}_{23} + \tilde{\boldsymbol{F}}_T\end{aligned} \tag{2.1}$$

where $\tilde{\boldsymbol{F}}_3$ is the total force acting on the spacecraft, $\tilde{t}$ is the time, $\tilde{G}$ is the universal gravitational constant, and the superscript I represents differentiation as viewed from an inertial perspective. The total force $\tilde{\boldsymbol{F}}_3$ is composed of the gravity force $\tilde{\boldsymbol{F}}_{13}$ due to the larger primary and along the direction of the relative position vector $\tilde{\boldsymbol{r}}_{13}$, the gravity force $\tilde{\boldsymbol{F}}_{23}$ due to the smaller primary parallel to the direction of position vector $\tilde{\boldsymbol{r}}_{23}$, and the thrust force $\tilde{\boldsymbol{F}}_T$. A traditional nondimensionalization process is employed to characterize mass, length, and time for interpreting the trajectories, and for preventing unwanted roundoff error during simulations. Since the mass of the third body is negligible, let the characteristic mass parameter for the bodies, m_b^*, be defined as the sum of the two primary masses

$$m_b^* \equiv \tilde{m}_1 + \tilde{m}_2 \tag{2.2}$$

To prevent significant round-off error during numerical simulations, if the thruster force model of interest, $\tilde{\boldsymbol{F}}_T$, includes a spacecraft mass term m, i.e., the mass of P_3, an alternative mass parameter is incorporated. The thruster is instead scaled by the initial spacecraft mass (typically the total wet mass in orbit), m_0, rather than m_b^*

$$m^* \equiv m_0 \tag{2.3}$$

This second mass scale is acceptable without any loss in generality, since the equations of motion ultimately reduce to dimensions of [length] / [time]^2. The characteristic length l^* is specified as the distance between the primaries

$$l^* \equiv \|\tilde{\boldsymbol{r}}_1\| + \|\tilde{\boldsymbol{r}}_2\| \tag{2.4}$$

and finally, the characteristic time is selected as the reciprocal of the mean motion of the system, thus scaling the nondimensional gravitational constant, G, to unity, i.e., $G = 1$.

$$t^* \equiv \sqrt{\frac{{l^*}^3}{\tilde{G} m_b^*}} \tag{2.5}$$

These newly-defined natural units lead to the following nondimensional quantities,

$$\boldsymbol{r} = \frac{\tilde{\boldsymbol{r}}}{l^*}, \quad \gamma = \frac{\tilde{m}_2}{m_b^*}, \quad t = \frac{\tilde{t}}{t^*} \tag{2.6}$$

where γ is the mass ratio of the smaller primary (moon) to the total system mass. Eliminating $\tilde{m}_3$ and nondimensionalizing equation (2.1) by the appropriate quantities from equations (2.2)-(2.5) yields

$$\frac{{}^I d^2 \boldsymbol{r}}{dt^2} = -\frac{1-\gamma}{\|\boldsymbol{r}_{13}\|^3}\boldsymbol{r}_{13} - \frac{\gamma}{\|\boldsymbol{r}_{23}\|^3}\boldsymbol{r}_{23} + \boldsymbol{f}_T \tag{2.7}$$

where the lowercase vector $\boldsymbol{f}_T$ now implies that the corresponding force $\boldsymbol{F}_T$ is scaled by the spacecraft mass, i.e., $\boldsymbol{f}_T = \boldsymbol{F}_T / m_3$. To complete the derivation of the equations of motion, the forces specified in equation (2.7) must be equated to kinematical relationships that incorporates the coordinates from a rotating frame. The following well-known operator relationships are employed

$$^{I}\dot{\boldsymbol{r}} = \frac{^{I}d\boldsymbol{r}}{dt} = \frac{^{R}d\boldsymbol{r}}{dt} + \boldsymbol{\Omega} \times \boldsymbol{r} \tag{2.8}$$

$$^{I}\ddot{\boldsymbol{r}} = \frac{^{I}d^2\boldsymbol{r}}{dt^2} = \frac{^{R}d^2\boldsymbol{r}}{dt^2} + 2\boldsymbol{\Omega} \times \frac{^{R}d\boldsymbol{r}}{dt} + \boldsymbol{\Omega} \times \boldsymbol{\Omega} \times \boldsymbol{r} \tag{2.9}$$

where $^{I}\boldsymbol{\omega}^{R} = \boldsymbol{\Omega} = \Omega\hat{z}$ is the constant angular velocity of the rotating frame, R, with respect to the inertial frame, I, consistent with the given assumptions from the RTBP. In component-form, the following nondimensional, Cartesian, rotating vectors can be expanded

$$\boldsymbol{r} = x\hat{x} + y\hat{y} + z\hat{z} \tag{2.10}$$

$$\frac{^{R}d\boldsymbol{r}}{dt} = \dot{x}\hat{x} + \dot{y}\hat{y} + \dot{z}\hat{z} \tag{2.11}$$

$$\frac{^{R}d}{dt}\left(\frac{d\boldsymbol{r}}{dt}\right) = \ddot{x}\hat{x} + \ddot{y}\hat{y} + \ddot{z}\hat{z} \tag{2.12}$$

$$\boldsymbol{f}_T = f_{T_x}\hat{x} + f_{T_y}\hat{y} + f_{T_z}\hat{z} \tag{2.13}$$

where dots indicate derivatives with respect to nondimensional time. Note that $\boldsymbol{\Omega} = n_{12}\hat{z} = \hat{z}$ since the nondimensional mean motion is equal to one. Substitution of the appropriate components from equations (2.10)-(2.12) into equation (2.9) yields

$$^{I}\ddot{\boldsymbol{r}} = (\ddot{x} - 2\dot{y} - x)\hat{x} + (\ddot{y} + 2\dot{x} - y)\hat{y} + \ddot{z}\hat{z} \tag{2.14}$$

The relative position vectors between the primaries are also expanded in rotating coordinates

$$\boldsymbol{r}_{13} = (x - \gamma)\hat{x} + y\hat{y} + z\hat{z} \tag{2.15}$$

$$\boldsymbol{r}_{23} = (x - (1 - \gamma))\,\hat{x} + y\hat{y} + z\hat{z} \tag{2.16}$$

where

$$\|\boldsymbol{r}_{13}\| = \sqrt{(x - \gamma)^2 + y^2 + z^2} \tag{2.17}$$

$$\|\boldsymbol{r}_{23}\| = \sqrt{(x - (1 - \gamma))^2 + y^2 + z^2} \tag{2.18}$$

Finally, the equations of motion in the rotating frame are completed by combining the kinematics (equations (2.14)-(2.16)) with the nondimensional force model (equation (2.7)). Solving for the second derivatives of the rotating components yields

$$\ddot{x} = 2\dot{y} + x - \frac{(1-\gamma)(x-\gamma)}{\|\boldsymbol{r}_{13}|\|^3} - \frac{\gamma(x+1-\gamma)}{\|\boldsymbol{r}_{23}\|^3} + f_{T_x} \tag{2.19}$$

$$\ddot{y} = -2\dot{x} + y - \frac{(1-\gamma)y}{\|\boldsymbol{r}_{13}|\|^3} - \frac{\gamma y}{\|\boldsymbol{r}_{23}\|^3} + f_{T_y} \tag{2.20}$$

$$\ddot{z} = -\frac{(1-\gamma)z}{\|\boldsymbol{r}_{13}|\|^3} - \frac{\gamma z}{\|\boldsymbol{r}_{23}\|^3} + f_{T_z} \tag{2.21}$$

The position terms in equations (2.19)-(2.21) are derivable from the pseudo-potential function U

$$U(\boldsymbol{r}) = \frac{(1-\gamma)}{\|\boldsymbol{r}_{13}\|} + \frac{\gamma}{\|\boldsymbol{r}_{23}\|} + \frac{1}{2}(x^2+y^2) \tag{2.22}$$

where

$$\boldsymbol{\nabla} U\left(\boldsymbol{r}\right) = \left(\frac{\partial U}{\partial x}, \frac{\partial U}{\partial y}, \frac{\partial U}{\partial z}\right) \tag{2.23}$$

such that equations (2.19)-(2.21) are also written

$$\ddot{x} = 2\dot{y} + \frac{\partial U}{\partial x} + f_{T_x} \tag{2.24}$$

$$\ddot{y} = -2\dot{x} + \frac{\partial U}{\partial y} + f_{T_y} \tag{2.25}$$

$$\ddot{z} = \frac{\partial U}{\partial z} + f_{T_z} \tag{2.26}$$

The availability of the pseudo-potential in equation (2.22) is especially useful when designing certain categories of lunar south pole coverage orbits.

When the equations are uncontrolled ($\boldsymbol{f}_T = \boldsymbol{0}$), an integral of the motion is available by first dotting equations (2.24), 2.25, (2.26) by $\dot{x}$, $\dot{y}$, and $\dot{z}$ respectively, and adding all three to yield

$$\dot{x}\ddot{x} + \dot{y}\ddot{y} + \dot{x}\ddot{z} = \frac{\partial U}{\partial x}\dot{x} + \frac{\partial U}{\partial y}\dot{y} + \frac{\partial U}{\partial x}\dot{x} = \frac{dU}{dt} \tag{2.27}$$

Integration of equation (2.27) yields

$$\dot{x}^2 + \dot{y}^2 + \dot{z}^2 = 2U + 2H \tag{2.28}$$

where H is the Hamiltonian of the RTBP. It is common to replace H with Jacobi's constant C_j, where $C_j = -2H$. Jacobi's constant is an energy-like constant with many useful properties, but for the purposes of this investigation it is primarily employed for numerical integration accuracy checks of the uncontrolled equations of motion. In Chapter 3, it is demonstrated that the Hamiltonian of the controlled system can also be used for similar checks.

2.1.3 Derivation of the Thruster Models

In this work, three different models are considered for the low-thrust acceleration term $\boldsymbol{f}_T$. The first model considers the acceleration force due to a solar sail. The magnitude of the solar radiation pressure force provided by the sail is defined as the characteristic acceleration κ, and it is directed along the vector $\boldsymbol{u}$, the control parameter normal to the surface and fixed on one side of the sail. Either side of the sail may be used to provide thrust. Although the force changes when modeling the effects of a real sail, the idealized, perfectly reflective model is assumed since this investigation is primarily concerned with a feasibility analysis. The proper thrust direction of the two-sided sail is realized when its acceleration is modeled as

$$\boldsymbol{f}_T = \kappa \hat{\boldsymbol{u}} \left(\hat{\boldsymbol{l}} \cdot \hat{\boldsymbol{u}} \right)^2 \operatorname{sgn} \left(\hat{\boldsymbol{l}} \cdot \hat{\boldsymbol{u}} \right) \tag{2.29}$$

where $\hat{\boldsymbol{l}}$ is the unit-vector directed from the sun to the spacecraft, and

$$\hat{\boldsymbol{u}} = \frac{\boldsymbol{u}}{\|\boldsymbol{u}\|} \tag{2.30}$$

In the model associated with the RTBP, $\hat{\boldsymbol{l}}$ is simplified to rotate in a circular orbit within the Earth-moon plane once per synodic lunar month, or with angular rate ω_s, i.e.

$$\hat{\boldsymbol{l}} = \left\{ \cos\left(\omega_s t\right), -\sin\left(\omega_s t\right), 0 \right\}^T \tag{2.31}$$

To further parameterize the thrust direction for the sail, it is often useful to introduce two steering angles. Let the clock angle δ be the angle between the projection of the sail normal unit vector $\hat{\boldsymbol{u}}$ in the Earth-moon plane and the vector $\hat{\boldsymbol{l}}$. Next, the pitch angle α is the out-of-plane angle measured from the Earth-moon plane to $\hat{\boldsymbol{u}}$. (See Figure 2.2.) Then the components of $\hat{\boldsymbol{u}}$ in the rotating frame can be computed from the angles δ and α, i.e.

$$\hat{\boldsymbol{u}} = \begin{Bmatrix} \cos\alpha\cos\left(\delta - \omega_s t\right) \\ \cos\alpha\sin\left(\delta - \omega_s t\right) \\ \sin\alpha \end{Bmatrix} \tag{2.32}$$

In addition to the solar sail, two different types of electric propulsion models are employed. The first model is that of a thrust-limited, constant specific impulse (CSI) engine. An example of such an engine is a solar electric thruster such as the NSTAR engine. Here, the thrust acceleration is modeled

$$\boldsymbol{f}_T = \frac{T}{m_0 - t \cdot T/(g_0 I_{sp})}\hat{\boldsymbol{u}} \tag{2.33}$$

where T is the constant thrust magnitude, g_0 is the Earth gravitational acceleration constant at sea level, and I_{sp} is the specific impulse. (Recall that the spacecraft mass and thrust magnitude are scaled by m^* instead of m_b^*.) This model assumes that sufficient power is always available for the engine to operate at a constant thrust level, even in the presence of solar array degradation. Because these engines operate at a relatively constant I_{sp}, the thrust is either always “on” at the constant maximum value, or completely “off” for coasting arcs, i.e., $T = 0$ and therefore $\boldsymbol{f}_T = \boldsymbol{0}$. As a result, the decrease in fuel mass is monotonic when the thruster is active, resulting in an increasing thrust acceleration magnitude. (When the thruster is off, then no fuel mass is lost.) The second electric propulsion model is a power-limited, variable specific impulse (VSI) engine, with the thrust acceleration vector modeled as

$$\boldsymbol{f}_T = \frac{T}{m}\hat{\boldsymbol{u}} \tag{2.34}$$

where

$$\dot{m} = -\frac{T^2}{2P} \tag{2.35}$$

and P denotes the engine power. An example of such an engine is the VASIMR engine being developed at NASA. [17] In the case of VASIMR, the variable I_{sp} (and, hence, variable thrust) is produced by varying the amount of energy dedicated to electron heating and the amount of propellant delivered for plasma generation. Such an engine might be used to bridge the gap between high-thrust, low-specific impulse propulsion systems and low-thrust, high-specific impulse systems. Due to the variable I_{sp}, the thrust magnitude T is controllable and not modeled as a constant value for the VSI engine. Hence, equation (2.35) cannot be solved in closed form, and the spacecraft mass, m, is considered an additional state variable when employing the VSI engine model.

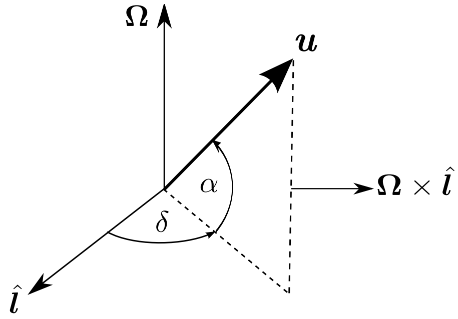

Figure 2.2. Relation of Control Angles to the Normal Vector $\boldsymbol{u}$ for a Solar Sail.

2.2 First-Order, Lower-Fidelity Equations of Motion

For later ease of reference, the lower-fidelity equations of motion are cast in first-order form in three different formats, depending on the thrust model. Setting $\boldsymbol{v} = {}^{R}d\boldsymbol{r}/dt$, and substituting equation (2.29) into equations (2.24)-(2.26), the restricted three-body differential equations that include a solar sail are

$$\begin{aligned} \dot{\boldsymbol{x}} = \boldsymbol{f}\left(t, \boldsymbol{x}, \boldsymbol{u}, \boldsymbol{\mu}\right) &= \begin{pmatrix} \dot{\boldsymbol{r}} \\ \dot{\boldsymbol{v}} \end{pmatrix} \\ &= \left\{ \begin{matrix} \boldsymbol{v} \\ \kappa \hat{\boldsymbol{u}} \left(\hat{\boldsymbol{l}} \cdot \hat{\boldsymbol{u}}\right)^2 \operatorname{sgn}\left(\hat{\boldsymbol{l}} \cdot \hat{\boldsymbol{u}}\right) - 2\boldsymbol{\Omega} \times \boldsymbol{v} + \boldsymbol{\nabla}^T U\left(\boldsymbol{r}\right) \end{matrix} \right\} \end{aligned} \tag{2.36}$$

where $\boldsymbol{\nabla}^T$ represents the gradient-transpose, and $\boldsymbol{\mu}$ is a problem parameter vector to be discussed further when the implementation of numerical corrections procedures are introduced. Similarly, the equations that incorporate a CSI engine are formed by substituting equation (2.33) into equations (2.24)-(2.26)

$$\begin{aligned} \dot{\boldsymbol{x}} &= \boldsymbol{f}\left(t, \boldsymbol{x}, \boldsymbol{u}, \boldsymbol{\mu}\right) = \begin{pmatrix} \dot{\boldsymbol{r}} \\ \dot{\boldsymbol{v}} \end{pmatrix} \\ &= \left\{ \begin{matrix} \boldsymbol{v} \\ \dfrac{T}{m_0 - t \cdot T/(g_0 I_{sp})} \hat{\boldsymbol{u}} - 2\boldsymbol{\Omega} \times \boldsymbol{v} + \boldsymbol{\nabla}^T U\left(\boldsymbol{r}\right) \end{matrix} \right\} \end{aligned} \tag{2.37}$$

And finally, with a VSI engine, the lower-fidelity equations are derived by substitution of equation (2.34) into equations (2.24)-(2.26)

$$\dot{\boldsymbol{x}} = \boldsymbol{f}\left(t, \boldsymbol{x}, \boldsymbol{u_c}, \boldsymbol{\mu}\right) = \begin{pmatrix} \dot{\boldsymbol{r}} \\ \dot{\boldsymbol{v}} \\ \dot{m} \end{pmatrix} = \left\{ \begin{matrix} \boldsymbol{v} \\ \dfrac{T}{m} \hat{\boldsymbol{u}} - 2\boldsymbol{\Omega} \times \boldsymbol{v} + \boldsymbol{\nabla}^T U\left(\boldsymbol{r}\right) \\ -T^2/2P \end{matrix} \right\} \tag{2.38}$$

where the control vector for the VSI engine $\boldsymbol{u_c}$ includes the steering direction $\hat{\boldsymbol{u}}$, in addition to the thrust magnitude T and power P, i.e.

$$\boldsymbol{u}_c = \begin{pmatrix} \hat{\boldsymbol{u}} \\ T \\ P \end{pmatrix} \tag{2.39}$$

Equations (2.36)-(2.38) are all in forms that are readily implemented into a numerical integration scheme, assuming that a value for the control history, $\boldsymbol{u}$, is available. Obtaining continuous values for the control, as a function of time, is explored further in Chapter 3.

2.3 The Libration Points

Since the natural equations of motion in the restricted problem (i.e., when $\boldsymbol{f}_T$ is set equal to zero) are time invariant when formulated within the context of a rotating frame, the possibility exists for equilibrium locations as constant solutions to the differential equations. Thus, such solutions are characterized by stationary position and velocity in the rotating frame R. These particular solutions are determined by nulling the velocity and acceleration terms in equations (2.19)-(2.21), resulting in the scalar equations,

$$-x_{eq} = -\frac{(1-\gamma)(x_{eq}-\gamma)}{\left\|\boldsymbol{r}_{13_{eq}}\right\|^3} - \frac{\gamma(x_{eq}+1-\gamma)}{\left\|\boldsymbol{r}_{23_{eq}}\right\|^3} \tag{2.40}$$

$$-y_{eq} = -\frac{(1-\gamma)y_{eq}}{\left\|\boldsymbol{r}_{13_{eq}}\right\|^3} - \frac{\gamma y_{eq}}{\left\|\boldsymbol{r}_{23_{eq}}\right\|^3} \tag{2.41}$$

$$0 = -\frac{(1-\gamma)z_{eq}}{\left\|\boldsymbol{r}_{13_{eq}}\right\|^3} - \frac{\gamma x_{eq}}{\left\|\boldsymbol{r}_{23_{eq}}\right\|^3} \tag{2.42}$$

Equation (2.42) is immediately solvable, yielding $z_{eq} = 0$. Substitution of this result into equations (2.40)-(2.41) produces a coupled system of two equations and two unknowns, x_{eq} and y_{eq}. As discovered by Lagrange, if $\|\boldsymbol{r}_{13}\| = \|\boldsymbol{r}_{23}\| = 1$, then equations (2.40)-(2.41) reduce to identity, implying that two of the equilibrium points, denoted L_4 and L_5, are located at vertices of two unique equilateral triangles. Thus, in Cartesian coordinates, the primaries comprise two of the common vertices of both triangles, with the remaining vertex defined by $x_{eq} = \frac{1}{2} - \gamma$ and $y_{eq} = \pm\frac{\sqrt{3}}{2}$. Three other equilibrium points also exist along the x-axis. Discovered first by Euler, they are denoted the collinear points and can be computed by forcing $y_{eq} = z_{eq} = 0$. Substitution into equation (2.40) yields

$$x_{eq} - \frac{(1-\gamma)(x_{eq}-\gamma)}{|x_{eq}-\gamma|^3} - \frac{\gamma(x_{eq}+1=\gamma)}{|x_{eq}+1-\gamma|^3} = 0 \tag{2.43}$$

Equation (2.43) is a quintic equation in x_{eq}. These solutions require numerical root solving methods that ultimately yield three real solutions, labeled L_1, L_2, and L_3. The L_1 and L_2 points are defined such that L_1 is between the primaries, L_2 is on the far side of the smaller mass, and L_3 is nearly a unit distance from the larger primary. The geometry of all five libration points appears in Figure 2.3.

2.4 Linear Instability of the Collinear Libration Points

This investigation is primarily concerned with orbits at or near the Earth-moon L_1 and L_2 collinear libration points, due to their potential use in lunar relay orbit

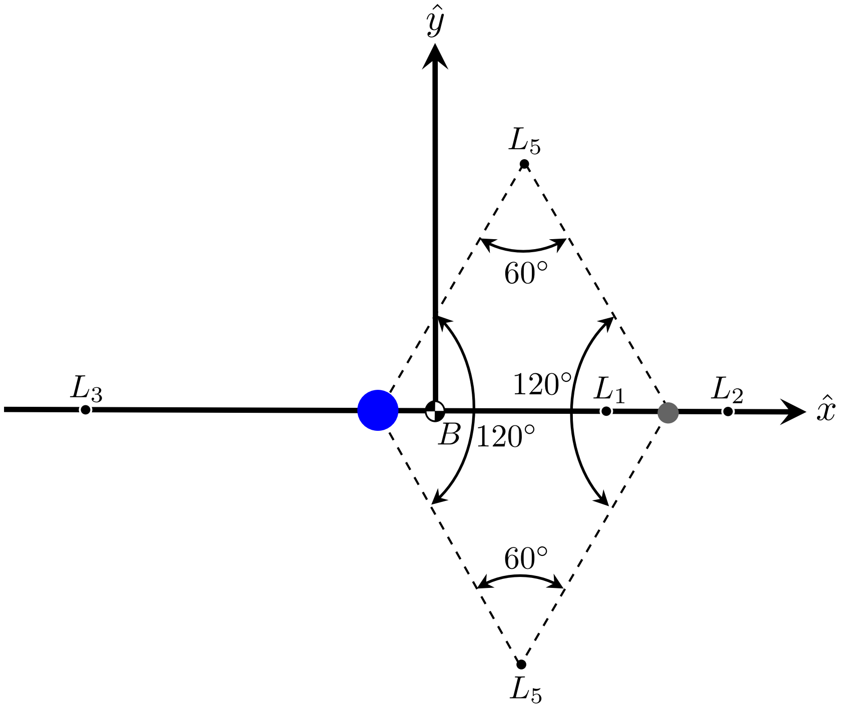

Figure 2.3. Equilibrium Point Locations in the Restricted Three-Body Problem.

design. Since the collinear points are linearly unstable, the dynamical structure in this region might be exploited for efficient transfer trajectories. To investigate the nonlinear dynamical behavior near these points, consider the natural, uncontrolled dynamics ($\boldsymbol{f}_T = 0$) that arise from equations (2.19)-(2.21) in the vicinity of L_i. Given that $\boldsymbol{x}_{eq}^T = (\boldsymbol{r}_{eq}^T, \boldsymbol{v}_{eq}^T) = (x_{eq}, y_{eq}, z_{eq}, 0, 0, 0)$ is an equilibrium state of the system, then without loss of generality, using any of the uncontrolled forms of equations (2.36)-(2.38)

$$\boldsymbol{f}\left(\boldsymbol{x}_{eq}\right) = \mathbf{0} \tag{2.44}$$

Suppose that $\boldsymbol{f}$ is differentiable at $\boldsymbol{x}_{eq}$ with derivatives $D\boldsymbol{f}(\boldsymbol{x}_{eq})$. When $\boldsymbol{x}$ is “close” to $\boldsymbol{x}_{eq}$, it follows from a first-order Taylor series expansion about $\boldsymbol{x}_{eq}$, as well as the definition of the first derivative, that

$$\boldsymbol{f}(\boldsymbol{x}) \approx \boldsymbol{f}(\boldsymbol{x}_{eq}) + D\boldsymbol{f}(\boldsymbol{x}_{eq})(\boldsymbol{x} - \boldsymbol{x}_{eq}) = D\boldsymbol{f}(\boldsymbol{x}_{eq})(\boldsymbol{x} - \boldsymbol{x}_{eq}) \tag{2.45}$$

Define a perturbed state as the variation $\delta\boldsymbol{x}$, i.e.

$$\delta\boldsymbol{x} = \boldsymbol{x} - \boldsymbol{x}_{eq} \tag{2.46}$$

then

$$\delta\dot{\boldsymbol{x}} = \boldsymbol{f}(\boldsymbol{x}) \approx D\boldsymbol{f}(\boldsymbol{x}_{eq})\delta\boldsymbol{x} = \mathbf{A}\delta\boldsymbol{x} \tag{2.47}$$

For the RTBP, this Jacobian matrix of derivatives becomes

$$\mathbf{A} = \begin{pmatrix} 0 & 0 & 0 & 1 & 0 & 0 \\ 0 & 0 & 0 & 0 & 1 & 0 \\ 0 & 0 & 0 & 0 & 0 & 1 \\ \dfrac{\partial^2 U(\boldsymbol{x}_{eq})}{\partial x \partial x} & \dfrac{\partial^2 U(\boldsymbol{x}_{eq})}{\partial x \partial y} & \dfrac{\partial^2 U(\boldsymbol{x}_{eq})}{\partial x \partial z} & 0 & 2 & 0 \\ \dfrac{\partial^2 U(\boldsymbol{x}_{eq})}{\partial y \partial x} & \dfrac{\partial^2 U(\boldsymbol{x}_{eq})}{\partial y \partial y} & \dfrac{\partial^2 U(\boldsymbol{x}_{eq})}{\partial y \partial z} & -2 & 0 & 0 \\ \dfrac{\partial^2 U(\boldsymbol{x}_{eq})}{\partial z \partial x} & \dfrac{\partial^2 U(\boldsymbol{x}_{eq})}{\partial z \partial y} & \dfrac{\partial^2 U(\boldsymbol{x}_{eq})}{\partial z \partial z} & 0 & 0 & 0 \end{pmatrix} \tag{2.48}$$

where the second partials are evaluated at the equilibrium point; the $\mathbf{A}$ matrix is constant. Applying a linear stability analysis, the determinant of $\mathbf{A}$ always yields one eigenvalue that is greater than zero corresponding to the collinear points L_1 and L_2. Then, the local unstable behavior associated with the nonlinear system, relative to $\boldsymbol{x}_{eq}$, is qualitatively the same as the corresponding linearized system. The remaining eigenvalues of the system, however, suggest that periodic solutions exist with the proper selection of initial conditions. Thus, periodic orbits in the vicinity of the collinear libration points exhibit linear instability that requires a stationkeeping capability, but this very behavior can also be exploited for fuel-efficient insertion into and departure from the orbits. This concept is of key importance in the successful application of invariant manifold theory. For general detail, see [56], and for further depth concerning low-thrust astrodynamics applications, the reader is referred to [57–60].

2.5 Gravity Contours for Stationary Trajectories

Although an infinite number of periodic orbits can be computed in the RTBP, only the five libration points exist as constant equilibrium solutions. Thus, if a particle (spacecraft) remains completely stationary, i.e., with zero velocity at any point other than the libration points, then the gravity forces must be completely offset by the thrust force $\boldsymbol{f}_T$. In this unique situation, the gravity force is dependent only on position, as is evident upon inspection of equations (2.24)-(2.26). The magnitude of this gravity force is simply $\|\boldsymbol{\nabla} U\|$. For developing single spacecraft "pole-sitter" trajectories, the value of $\|\boldsymbol{\nabla} U\|$ supplies a simple method of predicting the required thrust magnitude $\|\boldsymbol{f}_T\|$ to achieve a stationary trajectory at a given spatial location. From a design perspective, the instantaneous, two-dimensional, x-z contours of $\|\boldsymbol{\nabla} U\|$, as indicated in Figure 2.4, provide a simple visual tool to pre-determine these required thrust acceleration values for a given point in space.

As a sample application using Figure 2.4, consider the preliminary design of a stationary trajectory below the moon using the prescribed thrust range $0.5 \text{ mm/s}^2 \leq \|\boldsymbol{f}_T\| \leq 1.7 \text{ mm/s}^2$. Near the lower boundary of $\|\boldsymbol{f}_T\|$, inspection of the contours of constant $\|\boldsymbol{\nabla} U\|$ in Figure 2.4 indicate that a pole-sitting spacecraft is, at the lower thrust acceleration bound, restricted to the red regions that surround the collinear libration points L_1 and L_2. At the higher boundary, the spacecraft can potentially enter the yellow and green locations that wrap below the lunar south pole. For a solar sail, $\|\boldsymbol{f}_T\|$ is fixed and depends on the physical dimensions of the sail, but for the operation of a CSI or VSI engine, the value slowly increases across the given range due to fuel expenditure, allowing new regions to be accessed as time progresses. The utilization of this concept as an initial guess tool is revisited in Chapter 4.

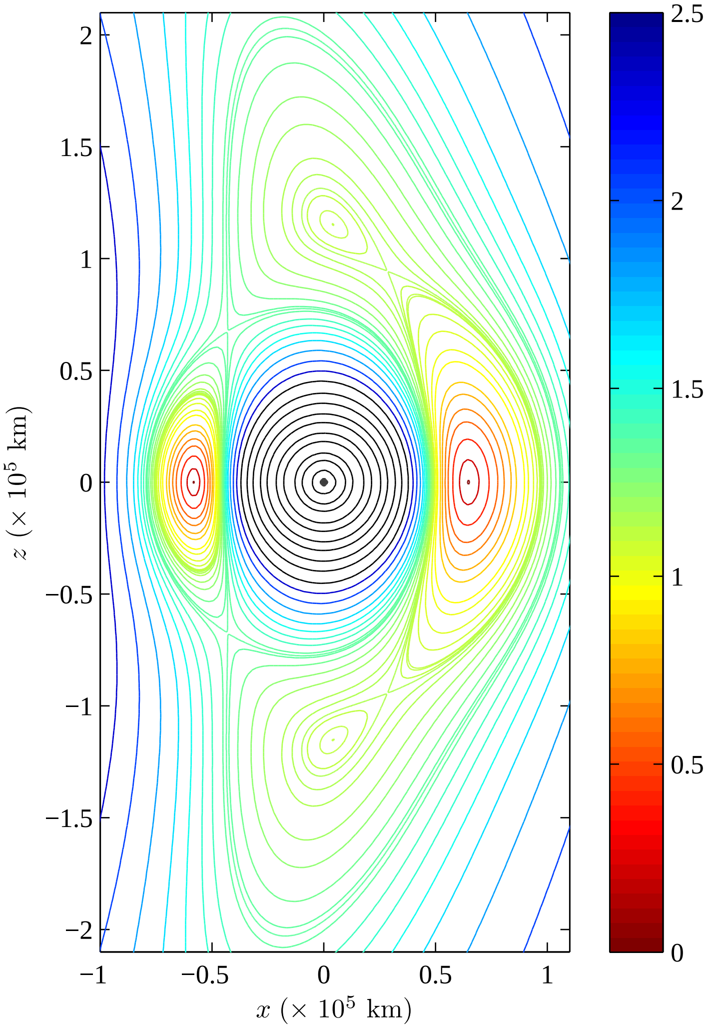

Figure 2.4. Contours of $\|\boldsymbol{\nabla} U\|$ in mm/s^2, MCR Frame.

2.6 The Body-Centered, Relative Equations of Motion

In transitioning the investigation to consider the higher-fidelity dynamical effects, beyond assumptions of the RTBP model, the formulation of a new set of ordinary differential equations governing the spacecraft motion is necessary.

2.6.1 Geometry

When deriving higher-fidelity differential equations, an arbitrary number of gravitational bodies can be considered, and the assumption that these bodies are constrained to circular orbits is eliminated. The numerical simulation is then accomplished in the standard Earth mean-of-equator of J2000 frame (EMEJ2000). Depending upon the focus in a particular simulation, it is either most convenient to consider the Earth-centered inertial (ECI) frame in EMEJ2000 coordinates, using the $\hat{X}_E$-$\hat{Y}_E$-$\hat{Z}_E$ vector basis, or, the moon-centered inertial (MCI) frame in EMEJ2000 coordinates, using the $\hat{X}_M$-$\hat{Y}_M$-$\hat{Z}_M$ coordinates as described in Figure 2.1. For simplicity, and consistent with standard nomenclature in this discipline, the subscripts are often dropped, and the $\hat{X}$-$\hat{Y}$-$\hat{Z}$ frame designation corresponds to the central body associated with the numerical integration process. Using the ECI and MCI frames, position vectors corresponding to the gravitating bodies are easily accessible using an ephemeris file without any additional transformations. For purposes of visualization and interpretation, it often convenient to view the evolution of the trajectory during a higher-fidelity simulation from the perspective of the rotating frame. Since the primaries no longer rotate in a circular orbit, the ECR and MCR reference frames introduced in Section 2.1.1 are rotating and pulsating. In addition to the EMEJ2000 and rotating frames, sometimes a more appropriate reference frame for visualizing a lunar orbit is the moon-centered, inertial, International Astronomical Union frame $\hat{X}_L$-$\hat{Y}_L$-$\hat{Z}_L$, to be discussed later in Section 2.8.2.

2.6.2 Derivation of a Higher-Fidelity Model

The most efficient and straightforward approach to simulate higher-fidelity, point mass, gravitational effects is to propagate in a body-centered inertial frame due to the availability of the locations of the sun, planets, and moons from highly accurate ephemeris files. This analysis employs the NASA Jet Propulsion Laboratory (JPL) DE405 ephemeris file that is available in binary format and capable of being read with an openly-available, pre-existing FORTRAN 77 subroutine. [61] More recently, comparable MATLAB® functions [62] have become available, but the use of a scripting interface involves a significant computational time penalty compared to the FORTRAN version.

Returning to Newton's Newton's 2nd Law, the vector differential equation of motion of a spacecraft subject to the gravitational forces of n_b bodies is

$$\tilde{\boldsymbol{F}}_i = \tilde{m}_i \frac{{}^I d^2 \tilde{\boldsymbol{R}}_i}{d\tilde{t}^2} = \tilde{G} \sum_{\substack{j=1 \\ j \neq i}}^{n_b} \frac{\tilde{m}_i \tilde{m}_j}{\left\| \tilde{\boldsymbol{R}}_{ij} \right\|^3} \tilde{\boldsymbol{R}}_{ij} \tag{2.49}$$

where the subscript i corresponds to the spacecraft, the subscript j is the summing index for the gravitational bodies, and the capitalized vector $\tilde{\boldsymbol{R}}$ now distinguishes an *inertial* vector. The vector $\tilde{\boldsymbol{R}}_{ij}$ is defined such that

$$\tilde{\boldsymbol{R}}_{ij} = \tilde{\boldsymbol{R}}_j - \tilde{\boldsymbol{R}}_i \tag{2.50}$$

As required by Newton's 2nd Law, the base point for the vectors $\boldsymbol{R}_i$ and $\boldsymbol{R}_j$ must be inertially fixed, and this point is again selected as the barycenter, B, illustrated in Figure 2.5. Use of a barycentric coordinate frame is impractical, however, and the state of the spacecraft relative to a gravitational body is preferred. In this analysis, this *central* body, q, is either the Earth or the moon as indicated in Figure 2.1. Rewriting the equations first requires the observation that $\tilde{\boldsymbol{R}}_i$ can be decomposed such that

$$\frac{{}^I d^2 \tilde{\boldsymbol{R}}_i}{d\tilde{t}^2} = \frac{{}^I d^2 \tilde{\boldsymbol{R}}_q}{d\tilde{t}^2} + \frac{{}^I d^2 \tilde{\boldsymbol{R}}_{qi}}{d\tilde{t}^2} \tag{2.51}$$

Equation (2.51) includes the vector $\tilde{\boldsymbol{R}}_{qi}$, the relative spacecraft position that is the significant dependent variable, and $\tilde{\boldsymbol{R}}_q$, the central body position vector relative to the barycenter, that is also subject to Newton's Newton's 2nd Law

$$\frac{{}^I d^2 \tilde{\boldsymbol{R}}_q}{d\tilde{t}^2} = \tilde{G} \sum_{\substack{j=1 \\ j \neq i}}^{n_b} \frac{\tilde{m}_j \tilde{\boldsymbol{R}}_{qj}}{\left\| \tilde{\boldsymbol{R}}_{qj} \right\|^3} \tag{2.52}$$

Substituting equation (2.52) into equation (2.51), and the result into equation (2.49) yields

$$\frac{{}^{I}d^{2}\tilde{\boldsymbol{R}}_{qi}}{d\tilde{t}^{2}} + \tilde{G}\sum_{\substack{j=1\\ j\neq i}}^{n_b} \frac{\tilde{m}_j \tilde{\boldsymbol{R}}_{qj}}{\left\|\tilde{\boldsymbol{R}}_{qj}\right\|^{3}} = \tilde{G}\sum_{\substack{j=1\\ j\neq i}}^{n_b} \frac{\tilde{m}_j}{\left\|\tilde{\boldsymbol{R}}_{ij}\right\|^{3}}\tilde{\boldsymbol{R}}_{ij} \tag{2.53}$$

Finally, by retaining the prior assumption that the spacecraft mass is negligible, isolating the spacecraft position vector relative to the central body, and applying the same characteristic quantities consistent with those in the RTBP model, equation (2.53) can be written as

$$\frac{{}^{I}d^{2}\boldsymbol{R}_{qi}}{dt^{2}} = -Gm_q \frac{\boldsymbol{R}_{qi}}{\|\boldsymbol{R}_{qi}\|^{3}} + \sum_{\substack{j=1\\ j\neq i}}^{n_b} Gm_j \left(\frac{\boldsymbol{R}_{ij}}{\|\boldsymbol{R}_{ij}\|^{3}} - \frac{\boldsymbol{R}_{qj}}{\|\boldsymbol{R}_{qj}\|^{3}} \right) \tag{2.54}$$

To reduce equation (2.54) to three scalar equations of motion for an arbitrary central body, let

$$\boldsymbol{R} \equiv \boldsymbol{R}_{qi} = X\hat{X} + Y\hat{Y} + Z\hat{Z} \tag{2.55}$$

$$\boldsymbol{R}_{qj} = X_j\hat{X} + Y_j\hat{Y} + Z_j\hat{Z} \tag{2.56}$$

where the $\hat{X}$-$\hat{Y}$-$\hat{Z}$ frame is an EMEJ2000 coordinate frame with a base point at the central body q. The components in equation (2.56) are the locations of the j perturbing gravitational bodies relative to the central body q that are readily available from the ephemeris file. Due to availability of these ephemeris positions, it is convenient to write $\boldsymbol{R}_{ij}$, the position vector from the spacecraft to perturbing body j, as

$$\boldsymbol{R}_{ij} = \boldsymbol{R}_{qj} - \boldsymbol{R}_{qi} = \boldsymbol{R}_{qj} - \boldsymbol{R} \tag{2.57}$$

$$\boldsymbol{R}_{ij} = (X_j - X)\hat{X} + (Y_j - Y)\hat{Y} + (Z_j - Z)\hat{Z} \tag{2.58}$$

The vector $\boldsymbol{R}_{ij}$ as expressed in equation (2.58), contains the position variables of interest (X, Y, Z) that will ultimately be numerically integrated as state variables, and the readily-available ephemeris positions (X_j, Y_j, Z_j). Finally, the three scalar, nondimensional, relative equations of motion are written by substituting equations (2.55)-(2.58) into equation (2.54) and equating the components

$$\ddot{X} = -\frac{Gm_q X}{\|\boldsymbol{R}_{qj}\|^3} - \sum_{\substack{j=1 \\ j \neq i,q}}^{n_b} Gm_j \left(\frac{X - X_j}{\|\boldsymbol{R}_{qj} - \boldsymbol{R}\|^3} + \frac{X_j}{\|\boldsymbol{R}_{qj}\|^3} \right) \tag{2.59}$$

$$\ddot{Y} = -\frac{Gm_q Y}{\|\boldsymbol{R}_{qj}\|^3} - \sum_{\substack{j=1 \\ j \neq i,q}}^{n_b} Gm_j \left(\frac{Y - Y_j}{\|\boldsymbol{R}_{qj} - \boldsymbol{R}\|^3} + \frac{Y_j}{\|\boldsymbol{R}_{qj}\|^3} \right) \tag{2.60}$$

$$\ddot{Z} = -\frac{Gm_q Z}{\|\boldsymbol{R}_{qj}\|^3} - \sum_{\substack{j=1 \\ j \neq i,q}}^{n_b} Gm_j \left(\frac{Z - Z_j}{\|\boldsymbol{R}_{qj} - \boldsymbol{R}\|^3} + \frac{Z_j}{\|\boldsymbol{R}_{qj}\|^3} \right) \tag{2.61}$$

Equations (2.59)-(2.61) represent a higher-fidelity point-mass gravitational model as compared to the differential equations in the RTBP, since an arbitrary number of gravitating bodies can be included, along with the ephemeris file that supplies accurate positions of the planets.

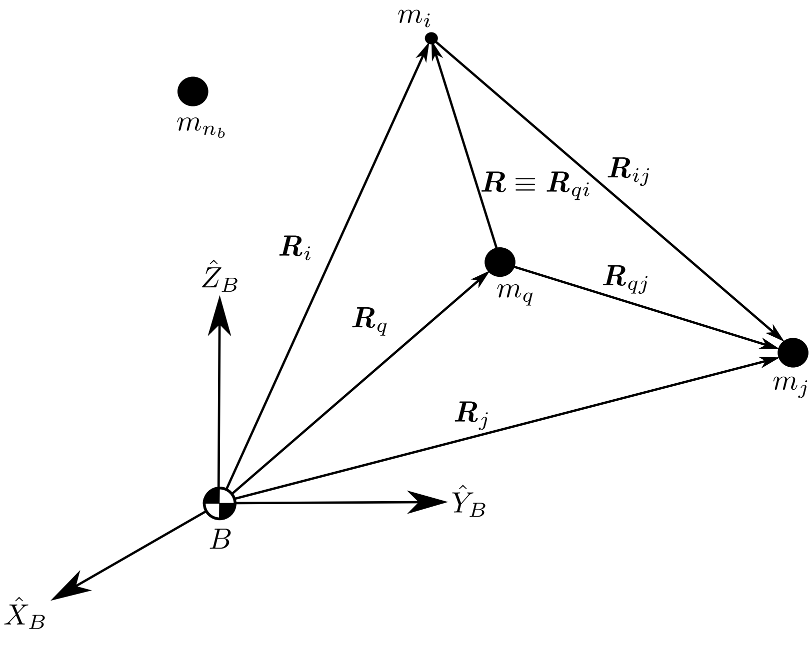

Figure 2.5. The General Problem of n_b Bodies.

2.7 First-Order, Higher-Fidelity, Equations of Motion

For the higher-fidelity model, the equations of motion in the body-centered, Earth mean equatorial of J2000 (EMEJ2000) frame are written in a compact form as

$$\begin{aligned} \dot{\boldsymbol{x}} = \boldsymbol{f}(t, \boldsymbol{x}, \boldsymbol{u}, \boldsymbol{\mu}) &= \begin{pmatrix} \dot{\boldsymbol{R}} \\ \dot{\boldsymbol{V}} \end{pmatrix} \\ &= \begin{Bmatrix} \boldsymbol{V} \\ \boldsymbol{f}_G + \boldsymbol{f}_O + \boldsymbol{f}_S + \boldsymbol{f}_T \end{Bmatrix} \end{aligned} \tag{2.62}$$

where the vector $\boldsymbol{R}$ is the body-centered (either Earth or moon) EMEJ2000 position vector with components X, Y, and Z as defined in equation (2.55). As in equations (2.36)-(2.38), the control is $\boldsymbol{u}$, and $\boldsymbol{\mu}$ is a problem parameter vector to be discussed in Chapter 3. For all computations, equation (2.62) is scaled with the same characteristic quantities as those defined in the Earth-moon RTBP, that is, m_B^*, m^*, l^*, and t^*, as described in equations (2.36)-(2.38). The right-hand side of equation (2.62) sums the acceleration vector $\boldsymbol{f}_G$ from gravitational point-mass accelerations due to the moon, the Earth, and the sun, $\boldsymbol{f}_O$ from Earth oblateness due to J_2, $\boldsymbol{f}_S$ from solar radiation pressure (not including the solar sail, if present), and the low-thrust acceleration $\boldsymbol{f}_T$. Equation (2.62) is in a form that may be numerically integrated once expressions for $\boldsymbol{f}_G$, $\boldsymbol{f}_O$, $\boldsymbol{f}_S$, and $\boldsymbol{f}_T$ are available in terms of the state variables. For simplicity, and because only the moon and Earth are employed as central bodies in this analysis, the models are detailed for both of the possible central bodies. Furthermore, the following notation is used: Body ☾ = moon, body $\oplus$ = Earth, and body $\odot$ = sun. (All other bodies are neglected.)

2.7.1 Moon-Centered Acceleration Model

The moon is employed as the central gravitating body for the majority of the higher-fidelity simulations, including transfers near the moon, coverage orbits, and end-of-life trajectories. When this model is employed, all positions and velocities, including the spacecraft states $\boldsymbol{R}$ and $\boldsymbol{V}$ are measured in terms of MCI, EMEJ2000 coordinates. The accelerations $\boldsymbol{f}_G$ due to the point-mass gravity of the moon, Earth, and sun are extracted from equations (2.59)-(2.61), that is

$$\begin{aligned}\boldsymbol{f}_G = & -Gm_{☾}\frac{\boldsymbol{R}}{\|\boldsymbol{R}\|^3} \\ & -Gm_{\oplus}\left(\frac{\boldsymbol{R}-\boldsymbol{R}_{☾\oplus}}{\|\boldsymbol{R}-\boldsymbol{R}_{☾\oplus}\|^3}+\frac{\boldsymbol{R}_{☾\oplus}}{\|\boldsymbol{R}_{☾\oplus}\|^3}\right) \\ & -Gm_{\odot}\left(\frac{\boldsymbol{R}-\boldsymbol{R}_{☾\odot}}{\|\boldsymbol{R}-\boldsymbol{R}_{☾\odot}\|^3}+\frac{\boldsymbol{R}_{☾\odot}}{\|\boldsymbol{R}_{☾\odot}\|^3}\right)\end{aligned} \tag{2.63}$$

where $\boldsymbol{R}_{☾\oplus}$ is the ephemeris position vector of the Earth relative to the moon, and $\boldsymbol{R}_{☾\odot}$ is the ephemeris position vector of the sun relative to the moon. The first term in equation (2.63) reflects the inverse square field due to moon, and the remaining terms represent the Earth and sun gravity perturbations. The perturbing acceleration $\boldsymbol{f}_O$ due to Earth oblateness from the J_2 term [63], [64] is modeled as

$$\boldsymbol{f}_O = -\frac{3}{2}\frac{Gm_{\oplus}J_2 r_{\oplus}^2}{\|\boldsymbol{R}-\boldsymbol{R}_{☾\oplus}\|^5}\left\{\begin{array}{l}(X-X_{☾\oplus})\left(1-5\dfrac{(Z-Z_{☾\oplus})^2}{\|\boldsymbol{R}-\boldsymbol{R}_{☾\oplus}\|^2}\right) \\ (Y-Y_{☾\oplus})\left(1-5\dfrac{(Z-Z_{☾\oplus})^2}{\|\boldsymbol{R}-\boldsymbol{R}_{☾\oplus}\|^2}\right) \\ (Z-Z_{☾\oplus})\left(3-5\dfrac{(Z-Z_{☾\oplus})^2}{\|\boldsymbol{R}-\boldsymbol{R}_{☾\oplus}\|^2}\right)\end{array}\right\} \tag{2.64}$$

where $r_{\oplus}$ is the mean radius of the Earth. The oblateness model assumes that the Earth's axis of rotation is fixed in inertial space along the positive $\hat{Z}$-axis of the EMEJ2000 frame. The solar radiation pressure perturbation $\boldsymbol{f}_S$ is modeled to be consistent with the authors in references [65] and [66]

$$\boldsymbol{f}_S = \frac{k_{\odot}AS_{\odot_0}\|\boldsymbol{R}_{\oplus\odot_0}\|^2}{cm}\frac{\boldsymbol{R}-\boldsymbol{R}_{☾\odot}}{\|\boldsymbol{R}-\boldsymbol{R}_{☾\odot}\|^3} \tag{2.65}$$

where $k_{\odot}$ is a material parameter dependent on absorptivity of the spacecraft surface, A is the projected cross-sectional area (a spherical body, and therefore a circular cross-section is assumed), c is the speed of light, $S_{\odot_0}$ is the solar light flux associated with the nominal distance $\|\boldsymbol{R}_{\oplus\odot_0}\| = 1$ AU, and m is the spacecraft mass. Finally, the accelerations due to the thruster are modeled with equations (2.29)-(2.33). When the higher-fidelity equations are employed, the directions for the thrust acceleration are written in terms of inertial components

$$\boldsymbol{f}_T = f_{T_X}\hat{X} + f_{T_Y}\hat{Y} + f_{T_Z}\hat{Z} \tag{2.66}$$

No higher-fidelity efforts in this investigation include the VSI engine model.

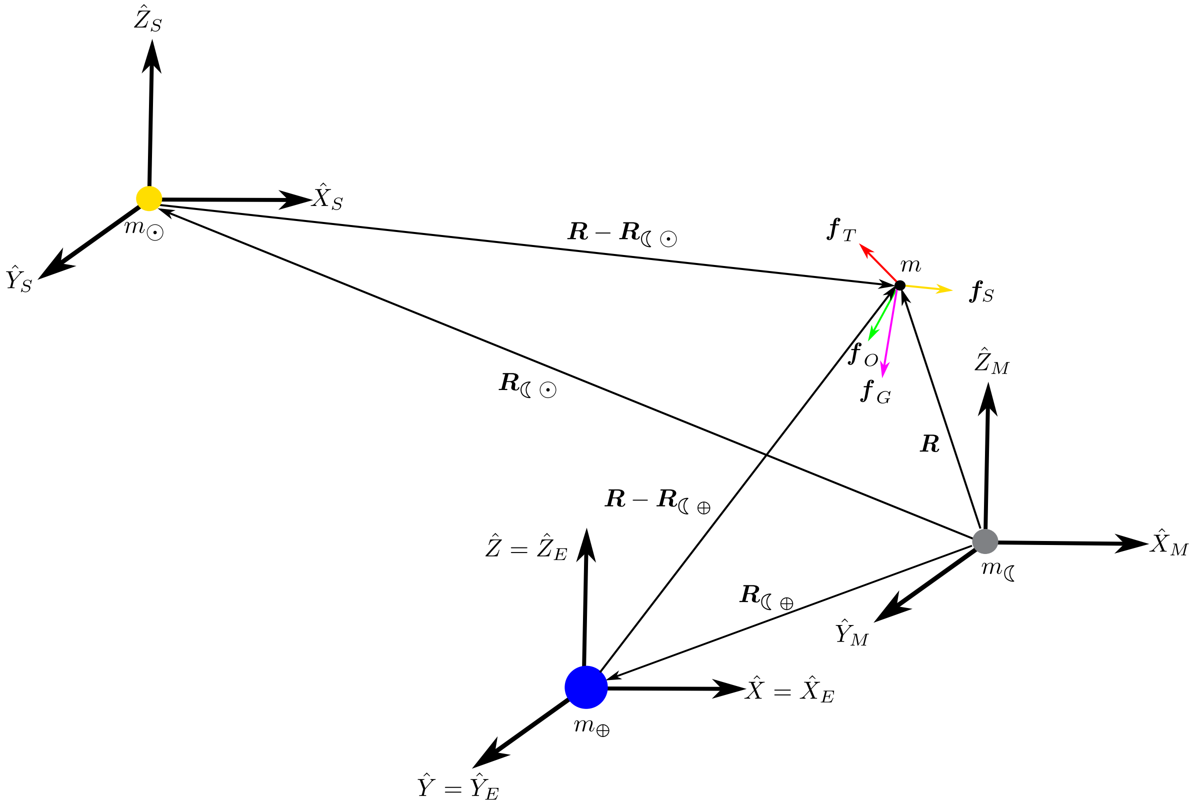

Figure 2.6. Geometry of the Moon-Centered, Higher-Fidelity System Model.

2.7.2 Earth-Centered Acceleration Model

The Earth is selected as the central gravitating body primarily for low-thrust transfer trajectories from low-Earth orbit that include many spirals. When this model is employed, all positions and velocities, including the spacecraft states $\boldsymbol{R}$ and $\boldsymbol{V}$ are measured in terms of ECI, EMEJ2000 coordinates. The corresponding accelerations become

$$\begin{aligned} \boldsymbol{f}_G = & -Gm_{\oplus}\frac{\boldsymbol{R}}{\|\boldsymbol{R}\|^3} \\ & -Gm_{\leftmoon}\left(\frac{\boldsymbol{R}-\boldsymbol{R}_{\oplus\leftmoon}}{\|\boldsymbol{R}-\boldsymbol{R}_{\oplus\leftmoon}\|^3}+\frac{\boldsymbol{R}_{\oplus\leftmoon}}{\|\boldsymbol{R}_{\leftmoon\oplus}\|^3}\right) \\ & -Gm_{\odot}\left(\frac{\boldsymbol{R}-\boldsymbol{R}_{\oplus\odot}}{\|\boldsymbol{R}-\boldsymbol{R}_{\oplus\odot}\|^3}+\frac{\boldsymbol{R}_{\oplus\odot}}{\|\boldsymbol{R}_{\oplus\odot}\|^3}\right) \end{aligned} \tag{2.67}$$

$$\boldsymbol{f}_O = -\frac{3}{2}\frac{Gm_{\oplus}J_2r_{\oplus}^2}{\|\boldsymbol{R}\|^5}\left\{\begin{matrix} X\left(1-5\dfrac{Z^2}{\|\boldsymbol{R}\|^2}\right) \\ Y\left(1-5\dfrac{Z^2}{\|\boldsymbol{R}\|^2}\right) \\ Z\left(3-5\dfrac{Z^2}{\|\boldsymbol{R}\|^2}\right) \end{matrix}\right\} \tag{2.68}$$

$$\boldsymbol{f}_S = \frac{k_{\odot}AS_{\odot_0}\|\boldsymbol{R}_{\oplus\odot_0}\|^2}{cm}\frac{\boldsymbol{R}-\boldsymbol{R}_{\oplus\odot}}{\|\boldsymbol{R}-\boldsymbol{R}_{\oplus\odot}\|^3} \tag{2.69}$$

where $\boldsymbol{R}_{\oplus\leftmoon}$ is the ephemeris position vector of the moon relative to the Earth, and $\boldsymbol{R}_{\oplus\odot}$ is the ephemeris position vector of the sun relative to the Earth. Similar to the moon-centered formulations, the accelerations due to the thruster are modeled consistent with with equations (2.29)-(2.33).

2.7.3 Shadowing

When the spacecraft is in the Earth's shadow, a crude approximation of the penumbra region is modeled with the sun as a point mass, as seen in Figure 2.8. Let a vector originate at the sun and terminate at the edge of the penumbra. Then, θ_1 is defined as the angle between this vector and the sun-to-Earth vector $\boldsymbol{R}_{\odot\oplus}$ available from the ephemeris file. This angle lies in the plane formed by $\boldsymbol{R}_{\odot\oplus}$ and the sun-to-spacecraft vector $\boldsymbol{l} = \boldsymbol{R}_{\odot\oplus} + \boldsymbol{R}$, where $\boldsymbol{R}$ is the ECI spacecraft position vector. As is apparent in Figure 2.8, these vectors sweep out the angle θ_2. Both angles,

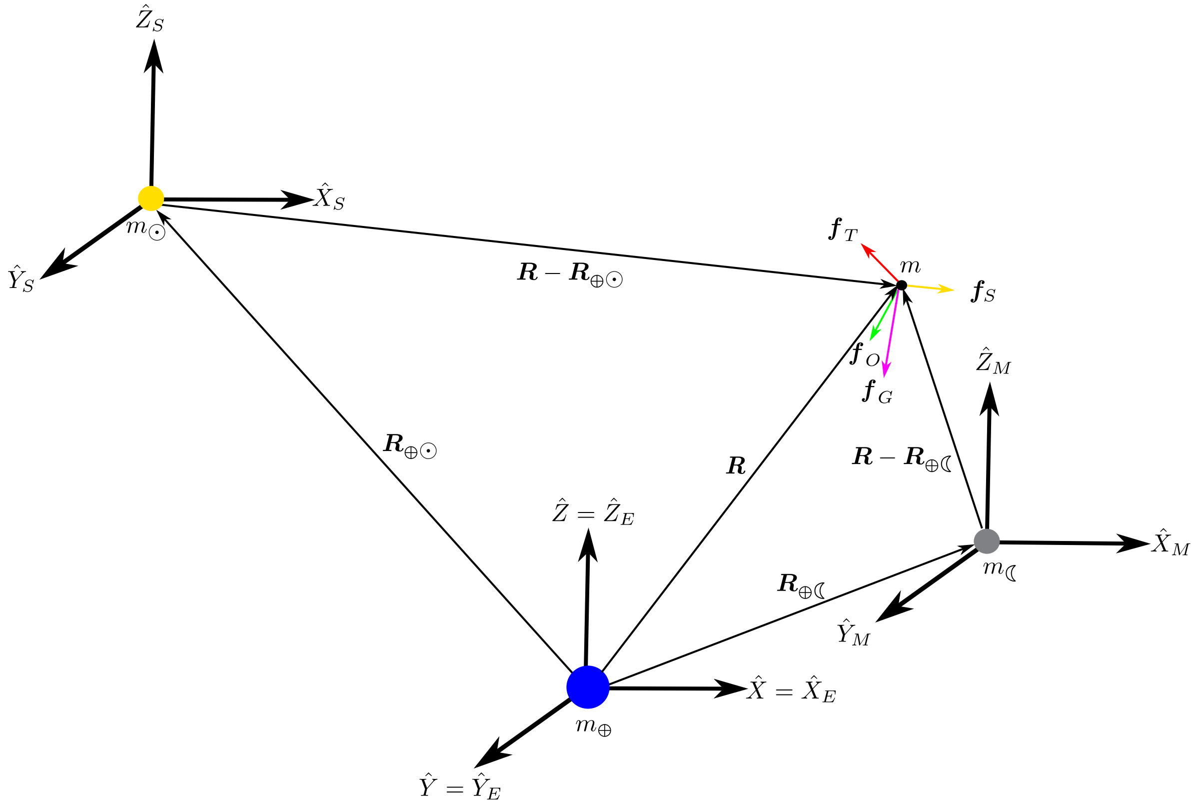

Figure 2.7. Geometry of the Earth-Centered, Higher-Fidelity System Model.

θ_1 and θ_2, are measured off of $\boldsymbol{R}_{\odot\oplus}$. Furthermore, it is assumed that θ_1 may be mathematically constructed as the angle between $\boldsymbol{R}_{\odot\oplus}$ and $\boldsymbol{R}_{\odot\oplus} + \boldsymbol{r}_\oplus$, where

$$\boldsymbol{r}_\oplus = r_\oplus \frac{(\boldsymbol{R}_{\odot\oplus} \times \boldsymbol{l}) \times \boldsymbol{R}_{\odot\oplus}}{\left\|(\boldsymbol{R}_{\odot\oplus} \times \boldsymbol{l}) \times \boldsymbol{R}_{\odot\oplus}\right\|} \tag{2.70}$$

Then, the angles θ_1 and θ_2 are computed as direction cosines in the same plane, and measured from $\boldsymbol{R}_{\odot\oplus}$

$$\theta_1 = \cos^{-1} \frac{(\boldsymbol{R}_{\odot\oplus} + \boldsymbol{r}_\oplus) \cdot \boldsymbol{R}_{\odot\oplus}}{\left\|(\boldsymbol{R}_{\odot\oplus} + \boldsymbol{r}_\oplus) \cdot \boldsymbol{R}_{\odot\oplus}\right\|} \tag{2.71}$$

$$\theta_2 = \cos^{-1} \frac{\boldsymbol{l} \cdot \boldsymbol{R}_{\odot\oplus}}{\left\|\boldsymbol{l} \cdot \boldsymbol{R}_{\odot\oplus}\right\|} \tag{2.72}$$

Note that θ_1 and θ_2 are both assumed positive to remove any quadrant ambiguity. Finally, the following sufficient conditions for spacecraft shadowing apply to $\boldsymbol{f}_T$ and $\boldsymbol{f}_S$

$$\begin{pmatrix} \boldsymbol{f}_T \\ \boldsymbol{f}_S \end{pmatrix} = \mathbf{0} \quad \text{if} \quad \begin{cases} \theta_2 < \theta_1 \\ \text{and} \\ \|\boldsymbol{l}\| > \left\|\boldsymbol{R}_{\odot\oplus}\right\| \end{cases}$$

Even though there is some visible light within the penumbra region, this basic criteria serves as a model for the worst-case scenario to represent $\boldsymbol{f}_T$ and $\boldsymbol{f}_S$, assuming that there is negligible SRP for a thrust force or perturbing acceleration and that insufficient power is available from the solar arrays to activate a CSI engine. The presence of the Earth's shadow poses considerable design complexity for a solar electric propulsion (CSI) engine or solar sail mission during the spiral-out phase from low-Earth orbit. As a result, the time-of-flight for a transfer sequence will increase, and is therefore frequently included in higher-fidelity low-thrust simulations. [67, 68] In particular, Flandro analytically demonstrates that a 27% time-of-flight penalty is incurred during his solar electric propulsion orbit-raising sequence when incorporating shadow entry and exit. [69] Currently, this shadow model is only implemented in the Earth-centered higher-fidelity model, and applied during a low-thrust spiral-out phase, where its effects have been demonstrated to be significant.

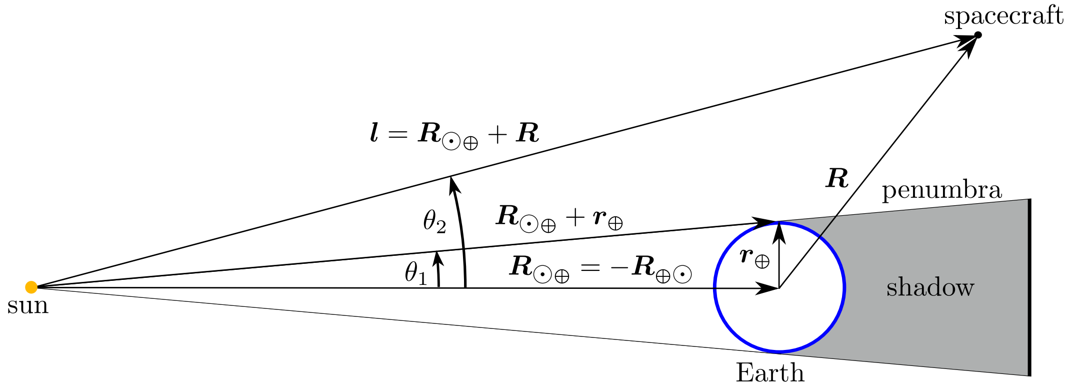

Figure 2.8. Eclipsing Conditions Schematic.

2.7.4 Lunar Librations

When implementing the moon-centered, higher-fidelity model and considering the design of orbits to support line-of-sight for a potential lunar ground station, incorporating the precise position of the ground station in a higher-fidelity model is crucial. Even though the moon is tidally locked with the Earth, a variety of factors, such as the eccentricity and inclination of the moon's orbit, as well as the rotation of the Earth, cause a perturbation that is manifested in lunar libration relative to its nominal orientation. Let $\boldsymbol{R}_g$ be defined as the position vector, relative to the lunar center, that locates the surface site on the moon. In moon-fixed coordinates, this position vector can be specified in terms of two angles: the latitude θ_g and longitude δ_g associated with the ground site

$$\boldsymbol{R}_g = r_{☾} \begin{Bmatrix} \cos\theta_g \cos\delta_g \\ \cos\theta_g \sin\delta_g \\ \sin\theta_g \end{Bmatrix} \tag{2.73}$$

where $r_{☾}$ is the mean radius of the moon. The angles θ_g and δ_g are available from the ephemeris file, and fully incorporate the effect of the lunar librations. Further discussion on the methods of modeling the lunar librations is available in [70]. Since the state variables are integrated in MCI, EMEJ2000 coordinates, $\boldsymbol{R}_g$ requires a coordinate transformation that is discussed in the next section.

2.8 Common Coordinate Transformations

2.8.1 EMEJ2000 Inertial Frame to P_1-P_2 Rotating Frame

In the problem analysis, it is often necessary to shift between inertial coordinates and coordinates defined in terms of the rotating frame. The following discussion summarizes the rotation matrix derivations by Anderson. [71] The system geometry, along with the ephemeris file (if required) is employed to formulate the rotation matrix

${}^{I}\mathbf{C}^{R}$ that transforms the vector coordinates from the rotating frame R to the inertial frame I such that

$$\begin{pmatrix} \hat{X} \\ \hat{Y} \\ \hat{Z} \end{pmatrix} = {}^{I}\mathbf{C}^{R} \begin{pmatrix} \hat{x} \\ \hat{y} \\ \hat{z} \end{pmatrix} \tag{2.74}$$

where

$${}^{I}\mathbf{C}^{R} = \begin{bmatrix} C_{11} & C_{12} & C_{13} \\ C_{21} & C_{22} & C_{23} \\ C_{31} & C_{32} & C_{33} \end{bmatrix} \tag{2.75}$$

As a direction cosine matrix, ${}^{I}\mathbf{C}^{R}$ is orthogonal, i.e., ${}^{R}\mathbf{C}^{I} = {}^{I}\mathbf{C}^{R^{-1}} = {}^{I}\mathbf{C}^{R^{T}}$ and ${}^{I}\mathbf{C}^{R^{T}}\,{}^{I}\mathbf{C}^{R} = \mathbf{I}$, where $\mathbf{I}$ is the identity matrix. When the higher-fidelity equations of motion are employed, the equations are non-autonomous, thus any direction cosine matrix is a function of time, i.e., $\mathbf{C} = \mathbf{C}(t)$. To transfer from inertial coordinates $\hat{X}$-$\hat{Y}$-$\hat{Z}$ to P_1-P_2 rotating coordinates $\hat{x}$-$\hat{y}$-$\hat{z}$, the ephemeris file is accessed to obtain

$${}^{I}\mathbf{C}^{R} = \left[\begin{matrix} \dfrac{\boldsymbol{R}_{\oplus\leftmoon}}{\|\boldsymbol{R}_{\oplus\leftmoon}\|} & \dfrac{\boldsymbol{R}_{\oplus\leftmoon} \times (\boldsymbol{R}_{\oplus\leftmoon} \times \boldsymbol{V}_{\oplus\leftmoon})}{\|\boldsymbol{R}_{\oplus\leftmoon} \times (\boldsymbol{R}_{\oplus\leftmoon} \times \boldsymbol{V}_{\oplus\leftmoon})\|} & \dfrac{\boldsymbol{R}_{\oplus\leftmoon} \times \boldsymbol{V}_{\oplus\leftmoon}}{\|\boldsymbol{R}_{\oplus\leftmoon} \times \boldsymbol{V}_{\oplus\leftmoon}\|} \end{matrix} \right] \tag{2.76}$$

Recall that the angular velocity of the rotating frame is defined as ${}^{I}\boldsymbol{\omega}^{R} = \dot{\theta}\hat{z}$, where θ is now time-varying in general. The well-known operator relationships from equations (2.8)-(2.9) are re-applied with equations (2.74)-(2.75) to yield

$$\begin{pmatrix} X \\ Y \\ Z \\ \dot{X} \\ \dot{Y} \\ \dot{Z} \\ \ddot{X} \\ \ddot{Y} \\ \ddot{Z} \end{pmatrix} = \begin{bmatrix} {}^{I}\mathbf{C}^{R} & \mathbf{0} & \mathbf{0} \\ {}^{I}\dot{\mathbf{C}}^{R} & {}^{I}\mathbf{C}^{R} & \mathbf{0} \\ {}^{I}\ddot{\mathbf{C}}^{R} & {}^{I}\dot{\mathbf{C}}^{R} & {}^{I}\mathbf{C}^{R} \end{bmatrix} \begin{pmatrix} x \\ y \\ z \\ \dot{x} \\ \dot{y} \\ \dot{z} \\ \ddot{x} \\ \ddot{y} \\ \ddot{z} \end{pmatrix} \tag{2.77}$$

where each entry in the matrix in equation (2.77) is a 3×3 sub-matrix. The associated matrix derivatives of ${}^{I}\mathbf{C}^{R}$ are expanded to

$$
{}^{I}\dot{\mathbf{C}}^{R} = \begin{bmatrix} \dot{\theta}C_{12} & -\dot{\theta}C_{11} & 0 \\ \dot{\theta}C_{22} & -\dot{\theta}C_{21} & 0 \\ \dot{\theta}C_{32} & -\dot{\theta}C_{31} & 0 \end{bmatrix} \tag{2.78}
$$

$$
{}^{I}\ddot{\mathbf{C}}^{R} = \begin{bmatrix} -\dot{\theta}^2 C_{11} + \ddot{\theta}C_{12} & -\ddot{\theta}C_{11} - \dot{\theta}^2 C_{12} & 0 \\ -\dot{\theta}^2 C_{21} + \ddot{\theta}C_{22} & -\ddot{\theta}C_{21} - \dot{\theta}^2 C_{22} & 0 \\ -\dot{\theta}^2 C_{31} + \ddot{\theta}C_{12} & -\ddot{\theta}C_{31} - \dot{\theta}^2 C_{32} & 0 \end{bmatrix} \tag{2.79}
$$

Finally, inertial coordinates are converted to rotating coordinates by inverting equation (2.77), where the matrix inverse is simply composed of the transpose of each of the nine, orthogonal sub-matrices

$$
\begin{pmatrix} X \\ Y \\ Z \\ \dot{X} \\ \dot{Y} \\ \dot{Z} \\ \ddot{X} \\ \ddot{Y} \\ \ddot{Z} \end{pmatrix} = \begin{bmatrix} {}^{R}\mathbf{C}^{I} & \mathbf{0} & \mathbf{0} \\ {}^{R}\dot{\mathbf{C}}^{I} & {}^{R}\mathbf{C}^{I} & \mathbf{0} \\ {}^{R}\ddot{\mathbf{C}}^{I} & {}^{R}\dot{\mathbf{C}}^{I} & {}^{R}\mathbf{C}^{I} \end{bmatrix} \begin{pmatrix} x \\ y \\ z \\ \dot{z} \\ \dot{y} \\ \dot{z} \\ \ddot{x} \\ \ddot{y} \\ \ddot{z} \end{pmatrix} \tag{2.80}
$$

Equation (2.77) and equation (2.80) are used to transform from inertial to rotating coordinates and vice versa, as required. Typical applications for the transformations include (i) shifting inertial position data into the rotating, pulsating ECR frame or (ii) into the MCR frame, both for visualization purposes, or (iii) translating an initial guess for a numerical scheme from the barycentric, rotating frame of the RTBP into ECI or MCI coordinates to use as an initial guess for the higher-fidelity models. If a base point shift is necessary during the transformation sequence, for example from ECI to MCR coordinates, then additional vector addition is required to complete the transformation to the new position vector.

2.8.2 EMEJ2000 Inertial Frame to International Astronomical Union Frame

The International Astronomical Union (IAU) frame, $\hat{X}_L$-$\hat{Y}_L$-$\hat{Z}_L$, is a moon-centered inertial frame that is useful for visualizing lunar coverage orbits. The fundamental plane of this inertial system is the lunar mean equator, frozen at 2000 January 1, 12:00:00 Coordinated Universal Time (UTC), or a Julian date of 2451545. To establish the frame, first define the $\hat{X}_L$ axis as the IAU node of J2000, as visualized by Figure 2.9. Next, define α_L and δ_L as right ascension and declination angles relative to the MCI, EMEJ2000 frame that orient the moon's mean north pole on the given Julian date. From [72], these angles are determined (in units of degrees), as

$$\begin{aligned}\alpha_L =&269.9949 - 3.8787\sin E_1 - 0.1204\sin E_2\\ &+ 0.0700\sin E_3 - 0.0172\sin E_4 + 0.0072\sin E_6\\ &- 0.0052\sin E_{10} + 0.0043\sin E_{13}\end{aligned} \tag{2.81}$$

$$\begin{aligned}\beta_L =&66.5392 + 1.5419\cos E_1 + 0.0239\cos E_2\\ &- 0.0278\cos E_3 + 0.0068\cos E_4 - 0.0029\cos E_6\\ &+ 0.0009\cos E_7 + 0.0008\cos E_{10} - 0.0009\cos E_{13}\end{aligned} \tag{2.82}$$

where trigonometric arguments in equations (2.81)-(2.82) are

$$\begin{aligned}E_1 &= 125.045\\ E_2 &= 250.089\\ E_3 &= 260.008\\ E_4 &= 176.625\\ E_6 &= 311.589\\ E_7 &= 134.963\\ E_{10} &= 15.134\\ E_{13} &= 25.053\end{aligned} \tag{2.83}$$

In degrees, the Euler 3-1-3 angle set (ϕ_L,ϑ_L,ψ_L) are defined using the right ascension and declination angles

$$\varphi_L = -90^\circ - \alpha_L \tag{2.84}$$

$$\vartheta_L = -90^\circ + \delta_L \tag{2.85}$$

$$\psi_L = 0^\circ \tag{2.86}$$

These angles are used to transform from MCI, EMEJ2000 (I frame) coordinates to IAU (L frame) coordinates

$$^{L}\mathbf{C}^{I} = \begin{pmatrix} \mathrm{c}\phi_L\mathrm{c}\psi_L - \mathrm{s}\phi_L\mathrm{c}\vartheta_L\mathrm{s}\psi_L & \mathrm{s}\phi_L\mathrm{c}\psi_L + \mathrm{c}\phi_L\mathrm{c}\vartheta_L\mathrm{s}\psi_L & \mathrm{s}\vartheta_L\mathrm{s}\psi_L \\ -\mathrm{c}\phi_L\mathrm{s}\psi_L - \mathrm{s}\phi_L\mathrm{c}\vartheta_L\mathrm{c}\psi_L & -\mathrm{s}\phi_L\mathrm{s}\psi_L + \mathrm{c}\phi_L\mathrm{c}\vartheta_L\mathrm{c}\psi_L & \mathrm{s}\vartheta_L\mathrm{c}\psi_L \\ \mathrm{s}\psi_L\mathrm{s}\vartheta_L & -\mathrm{c}\phi_L\mathrm{s}\vartheta_L & \mathrm{c}\vartheta_L \end{pmatrix} \tag{2.87}$$

where

$$\begin{pmatrix} \hat{X}_L \\ \hat{Y}_L \\ \hat{Z}_L \end{pmatrix} = {}^{L}\mathbf{C}^{I} \begin{pmatrix} \hat{X}_M \\ \hat{X}_M \\ \hat{Z}_M \end{pmatrix} \tag{2.88}$$

The "c" and "s" symbols that appear in equation (2.87) are shorthand for the cosine and sine functions, respectively. The matrix $^{L}\mathbf{C}^{I}$ is a constant matrix that only requires computation once, since both the IAU and the MCI, EMEJ2000 frame are inertial frames. Due to the alignment of the $\hat{Z}_L$ axis with the mean lunar north pole, the IAU frame is distinguished in the literature as a natural choice for lunar south pole trajectory design. [47]

2.8.3 Moon Body-Fixed Frame to EMEJ2000 Inertial Frame

The position of the lunar ground facility in the moon body-fixed frame, F, with components $\hat{x}_F$-$\hat{y}_F$-$\hat{z}_F$ often requires a transformation into the working MCI frame of interest or vice versa. To complete this transformation, it is first necessary to specify the orientation of the moon body-fixed frame relative to the MCI frame: Let $\hat{x}_F$ locate the intersection between the lunar equator and the prime meridian of the moon. The

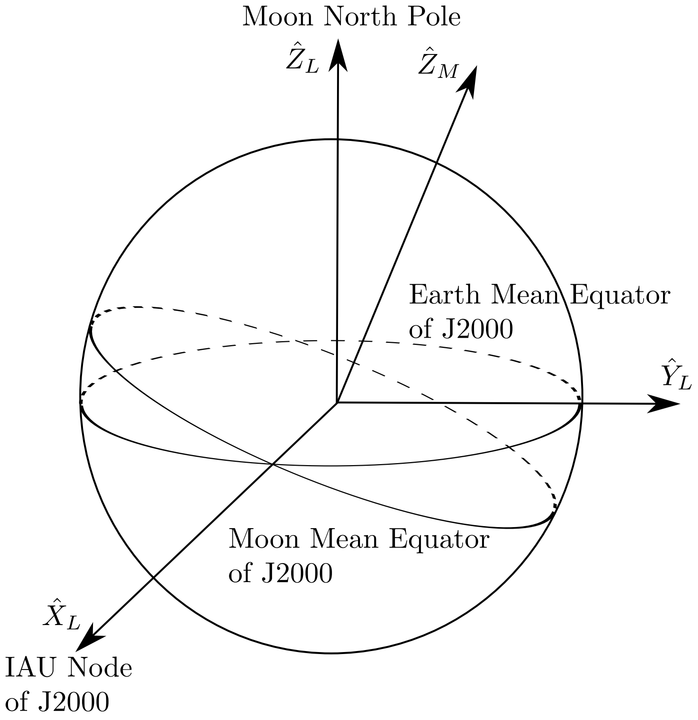

Figure 2.9. Geometry of the IAU frame with respect to the MCI, EMEJ2000 Frame. [72]

third vector in F, $\hat{z}_F$, is parallel to the spin axis of the moon. Finally, $\hat{y}_F = \hat{x}_F \times \hat{z}_F$ completes the right-handed set. The angle set ($\phi_{\leftmoon}$,$\vartheta_{\leftmoon}$,$\psi_{\leftmoon}$), corresponding to 3-1-3 Euler angles, is available from the JPL DE405 ephemeris file and serves to define the orientation rotation sequence, such that

$$\begin{pmatrix} \hat{x}_F \\ \hat{y}_F \\ \hat{z}_F \end{pmatrix} = {}^F\mathbf{C}^I \begin{pmatrix} \hat{X}_M \\ \hat{X}_M \\ \hat{Z}_M \end{pmatrix} \tag{2.89}$$

where

$${}^F\mathbf{C}^I = \begin{pmatrix} \mathrm{c}\phi_{\leftmoon}\,\mathrm{c}\psi_{\leftmoon} - \mathrm{s}\phi_{\leftmoon}\,\mathrm{c}\vartheta_{\leftmoon}\,\mathrm{s}\psi_{\leftmoon} & \mathrm{s}\phi_{\leftmoon}\,\mathrm{c}\psi_{\leftmoon} + \mathrm{c}\phi_{\leftmoon}\,\mathrm{c}\vartheta_{\leftmoon}\,\mathrm{s}\psi_{\leftmoon} & \mathrm{s}\vartheta_{\leftmoon}\,\mathrm{s}\psi_{\leftmoon} \\ -\mathrm{c}\phi_{\leftmoon}\,\mathrm{s}\psi_{\leftmoon} - \mathrm{s}\phi_{\leftmoon}\,\mathrm{c}\vartheta_{\leftmoon}\,\mathrm{c}\psi_{\leftmoon} & -\mathrm{s}\phi_{\leftmoon}\,\mathrm{s}\psi_{\leftmoon} + \mathrm{c}\phi_{\leftmoon}\,\mathrm{c}\vartheta_{\leftmoon}\,\mathrm{c}\psi_{\leftmoon} & \mathrm{s}\vartheta_{\leftmoon}\,\mathrm{c}\psi_{\leftmoon} \\ \mathrm{s}\psi_{\leftmoon}\,\mathrm{s}\vartheta_{\leftmoon} & -\mathrm{c}\phi_{\leftmoon}\,\mathrm{s}\vartheta_{\leftmoon} & \mathrm{c}\vartheta_{\leftmoon} \end{pmatrix} \tag{2.90}$$

With ${}^F\mathbf{C}^I$ available, the body-fixed coordinates may also be transformed to rotating coordinates by using ${}^I\mathbf{C}^R$ from the previous section to construct ${}^F\mathbf{C}^R = {}^F\mathbf{C}^{I\,I}\mathbf{C}^R$.

Similar combinations can also be accommodated with the IAU to MCI, EMEJ2000 transformation, ${}^{L}\mathbf{C}^{I}$. All required transformations can, thus, be accomplished.

2.9 Constant Parameters

During the course of this work, several constant parameters are used across many problems, and are listed in Table 2.1. When the spacecraft model is generated with either a CSI or a VSI engine, then the total spacecraft mass is included in the system model. In these cases, the initial mass is always equal to $m_0 = 500$ kg, and the minimum *allowable* mass, i.e., the dry mass, is $m_f = 50$ kg. For many transfers, the value of m_f is not constrained to reach the dry mass value, except for low-thrust pole-sitter missions, where the final mass is specified. Unless otherwise noted, for mission applications using higher-fidelity models, the location of the lunar ground station is assumed at the Shackleton Crater using the θ_g and δ_g coordinates specified in the Table 2.1.

Table 2.1 List of Constants.

Parameter	Value	Units
l^*	$384,431.4584485$	km
t^*	$375,236.314564115$	s
$Gm_{☾}$	$4,902.799140594719$	$\mathrm{km}^3/\mathrm{s}^2$
$Gm_{\oplus}$	$398,600.4480734463$	$\mathrm{km}^3/\mathrm{s}^2$
$Gm_{\odot}$	$132,712,439,935.4841$	$\mathrm{km}^3/\mathrm{s}^2$
$r_{☾}$	$1,738$	km
$r_{\oplus}$	$6,378.14$	km
J_2	0.0010827	
κ	0.58 or 1.70	$\mathrm{mm/s}^2$
m_0	500	kg
m_f	50	kg
g_0	9.80665	$\mathrm{m/s}^2$
T (CSI Engine)	150	mN
I_{sp} (CSI Engine)	$1,650$	s
$P_{\max}$ (VSI Engine)	2	kW
$k_{\odot}$	1.4	
$S_{\odot_0}$	$1,358.098$	$\mathrm{W/m}^2$
A	3.14159265358979	m^2
c	$299,792.458$	km/s
$\left\Vert \boldsymbol{R}_{\oplus\odot_0} \right\Vert$	$149,597,927$	km
θ_g	-89.9	$^\circ$
δ_g	0	$^\circ$

3. TRAJECTORY COMPUTATION AND OPTIMIZATION

There exist several iterative methodologies to design and optimize trajectories subject to differential equations that are not solvable in closed form. Choosing the best approach often depends on the trajectory design problem at hand, and the adequacy of the initial guess for the solution. When designing an uncontrolled, natural solution such as a periodic orbit in the restricted three-body problem, typically a shooting method based on Newton's method will yield a result that meets the desired endpoint and periodicity constraints. With the inclusion of low-thrust propulsion, there are associated controls, such as the thrust magnitude and steering direction that appear in the dynamical model, yielding an infinite number of candidate trajectories to satisfy the constraints in a given problem. To begin isolating a unique solution, then, a framework must be established to obtain a parameterization for such parameters.

In general, the selection of a control history to obtain a unique trajectory of interest is approached through the formulation of an optimal control problem. With the availability of control parameters, a natural choice for a unique solution is the *optimal* result. The criteria for the "best" trajectory is established by defining a performance index or cost function, but several approaches exist to actually compute the trajectory that solves the associated optimal control problem. The calculus-of-variations-based optimal control theory establishes a two-point boundary value problem that can be solved with the aforementioned shooting methods. The high sensitivity of the dynamics and the associated costates sometimes limits the ability to generate a solution, especially in designing long-duration, low-thrust trajectories involving many spirals around a primary. Relatively robust and rapid convergence is, however, observed in computing shorter time-of-flight transfers between orbits using power-limited variable specific impulse engines.

For purposes of robustness and systematic implementation, the primary method in this analysis to design and optimize a controlled trajectory is a direct transcription scheme via collocation. The collocation approach involves a complete discretization of the trajectory with a higher-order Gauss-Lobatto approach. Collocation is well-suited for generating feasible solutions with a minimum-norm approach and for transcription of the discretetized optimal control problem into the latest nonlinear programing software parameter optimization routines. If the initial guess is suitable, a feasible minimum-norm solution based on Newton's method is often an immediate option to rapidly explore trajectory designs. The minimum-norm approach may even be utilized to generate near-optimal solutions if, in fact, an optimal trajectory is known to lie near the boundary of a given set of path constraints. Given the sensitivities involved in trajectories for lunar south pole coverage, generation of a feasible solution is also a first step toward generating an optimal solution with the transcription method. Despite the fact that collocation involves a large-scale problem of many variables and nonlinear constraints, efficient methods exist to handle the corresponding sparse matrix algebra involved in generating a solution. Finally, the transcription methodology is easily modified to add different mission phases. When multiple phases are considered, functional dependencies between seemingly independent portions of a trajectory can be connected in an even larger optimization process to achieve an improved locally optimal result.

3.1 Multi-Variable Newton's Method

A recurring theme throughout this investigation is the iterative computation of a trajectory that satisfies all of the mission design constraints. Regardless of the design approach, the selection of feasible trajectories directly relies on the process of a multi-variable Newton-Raphson method, including root-solving software packages that are primarily quasi-Newton methods. To begin, consider the general problem of iteratively adjusting the $n_{\boldsymbol{X}}$-vector $\boldsymbol{X} = (X_1, X_2, ..., X_{n_{\boldsymbol{X}}})$ until the vector $\boldsymbol{F}(\boldsymbol{X})$ of $m_{\boldsymbol{X}}$ nonlinear equations

$$\boldsymbol{F}(\boldsymbol{X}) = \begin{pmatrix} F_1(\boldsymbol{X}) \\ \vdots \\ F_{m_{\boldsymbol{X}}}(\boldsymbol{X}) \end{pmatrix} = \boldsymbol{0} \tag{3.1}$$

is satisfied. For at least one solution, it is necessary that $n_{\boldsymbol{X}} \geq m_{\boldsymbol{X}}$. The iterative method for updating a given point $\boldsymbol{X} = (X_1, X_2, ..., X_{n_{\boldsymbol{X}}})^T$ is of the form

$$\boldsymbol{X}^{j+1} = \boldsymbol{X}^j + \alpha_d \boldsymbol{S} \tag{3.2}$$

where $\boldsymbol{X}^{j+1}$ is the updated estimate on $\boldsymbol{X}$ to solve equation (3.1), α_d is the scalar step length along the direction $\boldsymbol{S}$. Since the system $\boldsymbol{F}(\boldsymbol{X})$ is not readily solvable with algebraic manipulation, consider re-writing the entire system as an approximation using the first two terms of a Taylor series expansion about the current point $\boldsymbol{X}^j$

$$\boldsymbol{F}(\boldsymbol{X}) \approx \boldsymbol{F}(\boldsymbol{X}^j) + D\boldsymbol{F}(\boldsymbol{X}^j)(\boldsymbol{X} - \boldsymbol{X}^j) \tag{3.3}$$

where

$$D\boldsymbol{F} = \begin{bmatrix} \dfrac{\partial F_1}{\partial X_1} & \dfrac{\partial F_1}{\partial X_2} & \cdots & \dfrac{\partial F_1}{\partial X_{n_{\boldsymbol{X}}}} \\ \dfrac{\partial F_2}{\partial X_1} & \dfrac{\partial F_2}{\partial X_2} & \cdots & \dfrac{\partial F_2}{\partial X_{n_{\boldsymbol{X}}}} \\ \vdots & \vdots & \ddots & \vdots \\ \dfrac{\partial F_{m_{\boldsymbol{X}}}}{\partial X_1} & \dfrac{\partial F_{m_{\boldsymbol{X}}}}{\partial X_2} & \cdots & \dfrac{\partial F_{m_{\boldsymbol{X}}}}{\partial X_{n_{\boldsymbol{X}}}} \end{bmatrix} \tag{3.4}$$

When $n_{\boldsymbol{X}} = m_{\boldsymbol{X}}$, equation (3.3) is immediately solvable for an updated value of $\boldsymbol{X} = \boldsymbol{X}^{j+1}$, i.e.

$$\boldsymbol{X}^{j+1} = \boldsymbol{X}^{\boldsymbol{j}} - D\boldsymbol{F}^{-1}(\boldsymbol{X}^j)\boldsymbol{X}^{\boldsymbol{j}} \tag{3.5}$$

where equation (3.5) is in the form of equation (3.2) with $\alpha_d = 1$ and

$$\boldsymbol{S} = -D\boldsymbol{F}^{-1}(\boldsymbol{X}^j)\boldsymbol{X}^{\boldsymbol{j}} \tag{3.6}$$

When $n_{\boldsymbol{X}} > m_{\boldsymbol{X}}$, the number of free variables is greater than the number of nonlinear constraints, and infinitely many potential solutions exist. Often, it is desirable to locate the solution with a Euclidian norm that is nearby the initial guess. For this solution, let $\alpha_d = 1$ and the goal is then to solve the following optimization problem for the under-determined system of linearized constraints

$$\begin{gathered}\text{Min } J(\boldsymbol{S}) = \boldsymbol{S}^T\boldsymbol{S} = \left(\boldsymbol{X} - \boldsymbol{X}^j\right)^T \left(\boldsymbol{X} - \boldsymbol{X}^j\right) \\ \text{Subject to } \ \boldsymbol{F}(\boldsymbol{X}^j) + D\boldsymbol{F}(\boldsymbol{X}^j)(\boldsymbol{S}) = \boldsymbol{0}\end{gathered}$$

If the cost function is augmented to produce an unconstrained problem using the $m_{\boldsymbol{X}}$-vector, $\boldsymbol{\lambda}_{m_{\boldsymbol{X}}}$ of Lagrange multipliers, such that

$$J'(\boldsymbol{S}, \boldsymbol{\lambda}_{m_{\boldsymbol{X}}}) = J(\boldsymbol{S}) + {\boldsymbol{\lambda}_{m_{\boldsymbol{X}}}}^T(\boldsymbol{F}(\boldsymbol{X}^j) + D\boldsymbol{F}(\boldsymbol{X}^j)\boldsymbol{S}) \tag{3.7}$$

$$= \boldsymbol{S}^T\boldsymbol{S} + {\boldsymbol{\lambda}_{m_{\boldsymbol{X}}}}^T(\boldsymbol{F}(\boldsymbol{X}^j) + D\boldsymbol{F}(\boldsymbol{X}^j)\boldsymbol{S}) \tag{3.8}$$

then the necessary conditions for a stationary value of J are

$$\frac{dJ'}{d\boldsymbol{S}}^T = 2\boldsymbol{S} + D\boldsymbol{F}(\boldsymbol{X}^j)^T\boldsymbol{\lambda}_{m_{\boldsymbol{X}}} = \boldsymbol{0} \tag{3.9}$$

$$\frac{dJ'}{d\boldsymbol{\lambda}_{m_{\boldsymbol{X}}}}^T = \boldsymbol{F}(\boldsymbol{X}^j) + D\boldsymbol{F}(\boldsymbol{X}^j)\boldsymbol{S} = \boldsymbol{0} \tag{3.10}$$

Solving equations (3.9)-(3.10) for $\boldsymbol{S}$ yields the minimum-norm search direction, that is

$$\boldsymbol{S} = -D\boldsymbol{F}\left(\boldsymbol{X}^j\right)^T \left[D\boldsymbol{F}\left(\boldsymbol{X}^j\right) \cdot D\boldsymbol{F}\left(\boldsymbol{X}^j\right)^T\right]^{-1} \boldsymbol{F}\left(\boldsymbol{X}^j\right) \tag{3.11}$$

A simple second-derivative test on equation (3.7) yields

$$\frac{d^2J}{d\boldsymbol{S}^2} = 2 > 0 \tag{3.12}$$

to confirm that the solution for $\boldsymbol{S}$ is minimizing. Both the Newton and the minimum-norm search direction will satisfy equation (3.1) with a quadratic rate of convergence, as long as the initial guess for $\boldsymbol{X}$ is within the convergence radius. Unfortunately, the convergence radius for a given problem is not known a priori, and the sensitivity to the initial guess will vary from problem to problem. To combat this issue, many nonlinear equation solving software packages have been designed to iterate with a variable step length α_d such that a more robust convergence capability results at the expense of quadratic convergence. Some of these packages include, but are not limited to, MATLAB®'s "fsolve" routine, the feasible solver in SNOPT, [73] and the FORTRAN package NS11AD from the archive of the Harwell Subroutine Library. [74]

3.2 Explicit Integration

The first class of trajectory design and optimization methods employ explicit numerical integration or propagation through the use of ordinary differential equation (ODE) solving subroutines such as MATLAB®'s ODE45 or ODE113. To obtain state information over the time interval $t_a \leq t \leq t_b$, these solvers require the equations of motion in terms of $n_{\boldsymbol{x}}$ first-order ODE's. Consider, for example, the arbitrary system

$$\dot{\boldsymbol{x}} = \begin{pmatrix} \dot{x}_1 \\ \dot{x}_2 \\ \vdots \\ \dot{x}_{n_{\boldsymbol{x}}} \end{pmatrix} = \boldsymbol{f}(t, \boldsymbol{x}, \boldsymbol{\mu}) = \begin{pmatrix} f_1(t, x_1(t), \ldots, x_{n_{\boldsymbol{x}}}(t), \mu_1, \ldots, \mu_{n_{\boldsymbol{\mu}}}) \\ f_2(t, x_1(t), \ldots, x_{n_{\boldsymbol{x}}}(t), \mu_1, \ldots, \mu_{n_{\boldsymbol{\mu}}}) \\ \vdots \\ f_{n_{\boldsymbol{x}}}(t, x_1(t), \ldots, x_{n_{\boldsymbol{x}}}(t), \mu_1, \ldots, \mu_{n_{\boldsymbol{\mu}}}) \end{pmatrix} \tag{3.13}$$

where it is assumed here that the control, if present, is expressed as a function of the $n_{\boldsymbol{\mu}}$-vector of parameters $\boldsymbol{\mu}$ and time t. Using an ODE solver, the system is converted into an initial value problem by supplying t_a, $\boldsymbol{x}(t_a)$, and $\boldsymbol{\mu}$ to obtain $\boldsymbol{x}(t_b)$. This process consumes most of the function evaluations within the shooting method for feasible and optimal solutions.

3.3 The Shooting Method

The preceding root-finding methods are adaptable to solving boundary value problems in trajectory design. The only difference is that a shooting method is intended to satisfy equation (3.1) when it is functionally dependent on the integration of a system of ODE's. Consider the arbitrary first-order system in equation (3.13). Using the shooting method, the goal is to guess a propagation time, initial state, and parameters for $\boldsymbol{X} = (t_f, \boldsymbol{x}(t_0)^T, \boldsymbol{\mu}^T)^T$ such that

$$\boldsymbol{F}(\boldsymbol{X}) = \boldsymbol{F}(t_f, \boldsymbol{x}(t_f), \boldsymbol{\mu}) = \boldsymbol{0} \tag{3.14}$$

Even though the constraints in equation (3.14) depend on the final state, they are functionally dependent on numerical integration originating with the initial states. The general approach representing the shooting method can be summarized as follows:

1. Guess the initial conditions, $\boldsymbol{X}^0 = (t_f, \boldsymbol{x}(t_0)^T, \boldsymbol{\mu}^T)^T$.

2. Propagate the differential equations from t_0 to t_f.

3. Evaluate the error in the boundary conditions $\boldsymbol{F}(\boldsymbol{X}) = \boldsymbol{F}(t_f, \boldsymbol{x}(t_f), \boldsymbol{\mu})$. If $\boldsymbol{F}(\boldsymbol{X}) < \epsilon$, then stop.

4. Use Newton's method, or a nonlinear equation solver package to adjust $\boldsymbol{X}$ to satisfy $\boldsymbol{F}(\boldsymbol{X})$. Repeat steps 2-4.

where ϵ is a user-defined tolerance. While the above procedure is illustrative of a *single* shooting procedure, shooting methods can easily be expanded to include constraints at several intermediate steps over the course of a trajectory. When such a condition occurs, intermediate calls to numerical integration subroutines are required to complete the process, but the adaptation into a so-called "multiple" or "parallel" shooting formulation is straightforward. A detailed explanation of this process is available in [75].

3.3.1 The State Transition Matrix

Analytical derivative information for a shooting method requires, among other types of derivatives, partial derivatives that relate, or map, variations in an initial state to variations in a final state. While a closed-form solution (if it exists) to a given set of differential equations provides an exact mapping, an approximation in the form of a *linear* mapping is available for these derivatives through the use of a state transition matrix approach. In addition to linearizing relative to the libration points as detailed in Section 2.3, the equations of motion, when expressed in first-order form, may also be linearized at each instant in time in the neighborhood of the trajectory of interest. Consider the contemporaneous variation $\delta\boldsymbol{x}$ for the arbitrary system described in equation (3.13)

$$\delta\boldsymbol{x} = \boldsymbol{x} - \boldsymbol{x}^* \tag{3.15}$$

where the "$*$" superscript indicates a condition along a reference trajectory. When $\boldsymbol{x}$ is in the neighborhood of the reference trajectory, then the first-order Taylor expansion relative to the reference approximates the system model such that

$$\boldsymbol{f}(t, \boldsymbol{x}, \boldsymbol{\mu}) \approx \boldsymbol{f}(t, \boldsymbol{x}^*, \boldsymbol{\mu}) + D\boldsymbol{f}(t, \boldsymbol{x}^*, \boldsymbol{\mu})(\boldsymbol{x} - \boldsymbol{x}^*) \tag{3.16}$$

Then, from equations (3.15)-(3.16)

$$\begin{aligned} \delta\dot{\boldsymbol{x}} = \dot{\boldsymbol{x}} - \dot{\boldsymbol{x}^*} &= \boldsymbol{f}(t, \boldsymbol{x}, \boldsymbol{\mu}) - \boldsymbol{f}(t, \boldsymbol{x}^*, \boldsymbol{\mu}) \\ &= D\boldsymbol{f}(t, \boldsymbol{x}^*, \boldsymbol{\mu})\delta\boldsymbol{x} \\ &= \mathbf{A}(t)\delta\boldsymbol{x} \end{aligned} \tag{3.17}$$

The solution of equation (3.17) is available by solving

$$\dot{\boldsymbol{\Phi}}(t, t_0) = \mathbf{A}(t)\dot{\boldsymbol{\Phi}}(t, t_0) \tag{3.18}$$

where $\boldsymbol{\Phi}(t, t_0)$ is defined as the state transition matrix (STM) and the initial conditions are defined as

$$\boldsymbol{\Phi}(t_0, t_0) = \mathbf{I} \tag{3.19}$$

Here, the matrix $\mathbf{I}$ is the $n_{\boldsymbol{x}} \times n_{\boldsymbol{x}}$ identity matrix. Given the applications that follow, let $\boldsymbol{x} = (x, y, z, v_x, v_y, v_z)^T$. (For a higher-fidelity model in inertial coordinates, this vector is replaced with $\boldsymbol{x} = (X, Y, Z, V_X, V_Y, V_Z)^T$.) The components of the STM are then interpreted as the partial derivatives that relate the initial states to the final states of interest.

$$\mathbf{\Phi}(t, t_0) = \begin{pmatrix} \dfrac{\partial x}{\partial x_0} & \dfrac{\partial x}{\partial y_0} & \dfrac{\partial x}{\partial z_0} & \dfrac{\partial x}{\partial v_{x0}} & \dfrac{\partial x}{\partial v_{y_0}} & \dfrac{\partial x}{\partial v_{z0}} \\ \dfrac{\partial y}{\partial x_0} & \dfrac{\partial y}{\partial y_0} & \dfrac{\partial y}{\partial z_0} & \dfrac{\partial y}{\partial v_{x0}} & \dfrac{\partial y}{\partial v_{y_0}} & \dfrac{\partial y}{\partial v_{z0}} \\ \dfrac{\partial z}{\partial x_0} & \dfrac{\partial z}{\partial y_0} & \dfrac{\partial z}{\partial z_0} & \dfrac{\partial z}{\partial v_{x0}} & \dfrac{\partial z}{\partial v_{y_0}} & \dfrac{\partial z}{\partial v_{z0}} \\ \dfrac{\partial v_x}{\partial x_0} & \dfrac{\partial v_x}{\partial y_0} & \dfrac{\partial v_x}{\partial z_0} & \dfrac{\partial v_x}{\partial v_{x0}} & \dfrac{\partial v_x}{\partial v_{y_0}} & \dfrac{\partial v_x}{\partial v_{z0}} \\ \dfrac{\partial v_y}{\partial x_0} & \dfrac{\partial v_y}{\partial y_0} & \dfrac{\partial v_y}{\partial z_0} & \dfrac{\partial v_y}{\partial v_{y_0}} & \dfrac{\partial v_y}{\partial v_{y_0}} & \dfrac{\partial v_y}{\partial v_{z0}} \\ \dfrac{\partial v_z}{\partial x_0} & \dfrac{\partial v_z}{\partial y_0} & \dfrac{\partial v_z}{\partial z_0} & \dfrac{\partial v_z}{\partial v_{z0}} & \dfrac{\partial v_z}{\partial v_{y_0}} & \dfrac{\partial v_z}{\partial v_{z0}} \end{pmatrix} \tag{3.20}$$

Assuming that analytical expressions for these partial derivatives are constructed, the vector equation (3.18) implies that an additional $n_{\boldsymbol{x}}^2$ differential equations, in addition to the equations of motion, must be numerically integrated simultaneously to properly evaluate the state and the STM at every instant in time. The $n_{\boldsymbol{x}}^2$ elements of $\mathbf{A}(t)$ must be computed a priori for the given system model. Despite this additional analytical effort and computational expense, the derivatives $\mathbf{\Phi}$ representing the linear mapping are usually as accurate as the integrated state variables. (An exception might possibly occur if the elements of $\mathbf{A}(t)$ are very complicated or formulated in some manner that allows significant round-off error.) The computational expense is also typically far less than an alternative lower-accuracy central differencing method. Once the STM is available, many of the necessary analytical partial derivatives are available to obtain a search direction and produce an update as part of the shooting scheme. When implementing this partial derivative information into a shooting algorithm, this information is used to complete step #4 in Section 3.1.

3.3.2 Finite Difference Derivatives

Sometimes, a derivative element in the Jacobian matrix, $\boldsymbol{DF}$, is cumbersome or difficult to evaluate analytically. At the cost of numerical accuracy and some additional computations, these elements may alternatively be evaluated by numerical finite-difference derivatives. A standard approach is to implement the central differencing formula. For the j^{th} scalar constraint element F_j, the derivative with respect to the i^{th} scalar variable X_i in $D\boldsymbol{F}$ becomes

$$\frac{\partial F_j}{\partial X_i} \approx \frac{F_j(X_i + h_d) - F_j(X_i - h_d)}{2h_d} \tag{3.21}$$

where h_d is a "small" step size. The approximate derivative in equation (3.21) is of order $O(h_d^2)$. The selection of an appropriate step size h_d is important to minimize the truncation error without overly inducing round-off error due to subtractive cancellation, however methods to deal with this choice are available in [76]. Note that each derivative that is constructed from equation (3.21) requires two evaluations of F_j, each potentially involving costly numerical integrations. For a large $D\boldsymbol{F}$ matrix, this finite-differencing procedure clearly leads to increased numerical expense. If F_j is analytic, and the computing platform supports the evaluation of F_j in terms of complex numbers, then the complex-step finite-differencing method can be employed. [77] Consider the third-order, complex Taylor series approximation of F_j

$$F_j(X_j + \hat{i}h_d) = F_j(X_j) + \hat{i}h_d\frac{\partial F_j}{\partial X_i} - h_d^2\frac{\partial^2 F_j}{\partial X_i^2} - \hat{i}h_d^3\frac{\partial^3 F_j}{\partial X_i^3} + ... \tag{3.22}$$

where $\hat{i}$ is an imaginary step direction. Isolating the imaginary components and solving for $\partial F_j/\partial X_i$ yields

$$\frac{\partial F_j}{\partial X_i} = \frac{\Im\left[F_j(X_i + \hat{i}h_d)\right]}{h_d} + h_d^2\frac{\partial^3 F_j}{\partial X_i^3} + ... \tag{3.23}$$

$$\approx \frac{\Im\left[F_j(X_i + \hat{i}h_d)\right]}{h_d} \tag{3.24}$$

where the notation "$\Im$" denotes only the imaginary component of the function. Here, $\partial F_j/\partial X_i$ is approximated to order $O(h_d^2)$, yet the subtractive cancellation round-off error issue observed in the central differencing formula of equation (3.21) does not appear. Hence, a very small step size is selected to achieve derivatives to machine precision and, thus, equivalent to the accuracy of analytical derivatives. Ongoing research in the complex-step method indicates that derivatives that are functionally dependent on a numerically integrated initial condition, such as finite-differenced STM elements, are also possible. [78]

3.3.3 Periodic Orbits in the Restricted Three-Body Problem

The application of a shooting method is easily illustrated through the computation of natural periodic orbits in the RTBP. First, consider the use of the uncontrolled equations of motion ($\boldsymbol{f}_T = \mathbf{0}$) in equation (2.36) or equation (2.37) without any parameters $\boldsymbol{\mu}$. For L_1 and L_2 halo and vertical orbits, as well as L_2 butterfly orbits, a perpendicular crossing with the $\hat{x}$-$\hat{z}$ plane is always observed such that the velocity components in the x- and z-directions is zero. If the time-of-flight for the orbit is specified as a period $\mathbb{P}$, and the initial state is selected at one perpendicular crossing, then the following three constraints must be satisfied

$$\boldsymbol{F}(\boldsymbol{X}) = \begin{pmatrix} y(\mathbb{P}/2) \\ v_x(\mathbb{P}/2) \\ v_z(\mathbb{P}/2) \end{pmatrix} = \mathbf{0} \tag{3.25}$$

where the vector of free variables $\boldsymbol{X} = (x_0, z_0, v_{y_0})^T$ is defined as a subset of the states at $t = 0$. The values of $\boldsymbol{X}$ are then used to update the initial state vector $\boldsymbol{x}_0 = (x_0, 0, z_0, 0, v_{y_0}, 0)^T$. The necessary derivative information is obtained by evaluating

$$D\boldsymbol{F} = \begin{pmatrix} \dfrac{\partial y(\mathbb{P}/2)}{\partial x_0} & \dfrac{\partial y(\mathbb{P}/2)}{\partial z_0} & \dfrac{\partial y(\mathbb{P}/2)}{\partial v_{y_0}} \\ \dfrac{\partial v_x(\mathbb{P}/2)}{\partial x_0} & \dfrac{\partial v_x(\mathbb{P}/2)}{\partial z_0} & \dfrac{\partial v_x(\mathbb{P}/2)}{\partial v_{y_0}} \\ \dfrac{\partial v_z(\mathbb{P}/2)}{\partial x_0} & \dfrac{\partial v_z(\mathbb{P}/2)}{\partial z_0} & \dfrac{\partial v_z(\mathbb{P}/2)}{\partial v_{y_0}} \end{pmatrix} \tag{3.26}$$

All of the required information is then in place to implement the shooting procedure. For step #1, an initial guess is supplied to $\boldsymbol{X} = (x_0, z_0, v_{y_0})^T$ with the initial time set to $t_0 = 0$ and the final time fixed at $t_f = \mathbb{P}/2$. For step #2, the initial guess is employed to integrate the initial state and the STM via equation (2.36) with $\boldsymbol{f}_T = \mathbf{0}$

and equations (3.18)-(3.19). Given the sensitivity in the RTBP, the guess will likely not satisfy the constraints within the prescribed tolerances for step #3, so an update is computed for $\boldsymbol{X}$ via equation (3.2) and equation (3.6) since $n_{\boldsymbol{X}} = m_{\boldsymbol{X}}$. If initial conditions are not available for $\boldsymbol{X}^0$, then a guess from the linearization about the libration points (as explored in Section 2.4) is one possible source. The shooting process is easily modified for other orbit symmetries, or, to obtain the same periodic orbits with a different approach. For example, the position and velocity corresponding to a periodic orbit at a fixed initial x location in the $\hat{x} - \hat{z}$ plane is preferred, then the variable vector becomes

$$\boldsymbol{X} = \begin{pmatrix} z_0 \\ v_{y_0} \end{pmatrix} \tag{3.27}$$

where a degree of freedom for t_f (a quantity that must still implicitly vary) is automatically removed given that a termination condition is supplied to the integrator to force an $\hat{x}$-$\hat{z}$ plane crossing, i.e., $y_f = 0$. The constraints are then modified, i.e.

$$\boldsymbol{F}(\boldsymbol{X}) = \begin{pmatrix} v_x(t_f) \\ v_z(t_f) \end{pmatrix} = \boldsymbol{0} \tag{3.28}$$

and the constraint matrix, including the functional dependency on the unspecified half-period final time, becomes

$$D\boldsymbol{F} = \begin{pmatrix} \dfrac{\partial v_x(t_f)}{\partial z_0} & \dfrac{\partial v_x(t_f)}{\partial v_{y_0}} & \dfrac{\partial v_x(t_f)}{\partial t_f} \\ \dfrac{\partial v_z(t_f)}{\partial z_0} & \dfrac{\partial v_z(t_f)}{\partial v_{y_0}} & \dfrac{\partial v_z(t_f)}{\partial t_f} \end{pmatrix} \tag{3.29}$$

Given an initial guess for $\boldsymbol{X}$, the steps corresponding to the shooting method are re-visited for this alternative problem formulation to determine a nearby solution. In this case, $n_{\boldsymbol{X}} > m_{\boldsymbol{X}}$, so equation (3.11) serves as the basis to compute the search direction in equation (3.2) and to complete in step #4 in the shooting scheme.

3.4 Indirect Trajectory Optimization via Optimal Control Theory

For some problems, the application of a calculus of variations formulation to optimize a trajectory is a simple and relatively robust approach. An advantage of this approach is that the solution, once fully formulated through application of the Euler-Lagrange equations, merely involves the solution of a system of nonlinear constraints from a two-point boundary value problem. Compared to alternative approaches, this type of solution process involves a relatively low-dimensioned problem where an optimal trajectory is rapidly produced. To solve this system of nonlinear equations, the shooting method is again employed with either numerical, or preferably, analytical partial derivatives. Because of this structuring of the entire optimization problem through constraint equations, the method is termed an *indirect* method. The disadvantage of the indirect approach is that the nonlinear equations are composed not only of kinematic boundary conditions, but also optimality or *natural* boundary conditions. The sensitivity of an initial guess to the satisfaction of both the kinematic *and* the natural boundary constraints is well-documented. Betts, [79] in particular notes the following passage from page 215 of the landmark textbook by Bryson and Ho [80]

> “The main difficulty with these methods is *getting started*; i.e., finding a first estimate of the unspecified conditions at one end that produces a solution reasonably close to the specified conditions at the other end. The reason for this peculiar difficulty is the extremal solutions are often *very sensitive* to small changes in the unspecified boundary conditions...Since the system equations and the Euler-Lagrange equations are coupled together, it is not unusual for the numerical integration, with poorly guessed initial conditions to produce “wild trajectories” in the state space.”

These problems are especially present in trajectories that involve many spirals, such as a long-duration, low-thrust transfer from LEO to the moon. (In such a case, a systematic procedure is required to produce a convergent initial guess for the shooting method.) Nevertheless, relatively robust convergence in the indirect approach is observed in the computation of shorter-duration transfers trajectories that employ low-thrust. The general theoretical framework for optimal control applied to spacecraft trajectory optimization is completely presented in the work by Lawden, [8] but the derivation of the complete two-point boundary value problem is still *highly* dependent on the details of the optimization problem under consideration. The specifics of the formulation of a low-thrust trajectory optimization problem are presented such that the methodology is still generalizable to a wide array of orbital transfer applications.

3.4.1 Application to Power-Limited, Finite-Burn Engine Transfers

Designing a fuel-optimal, low-thrust transfer between libration point orbits is well-suited for an indirect method. The analysis here is applied to VSI engines, but for comparable derivations using a CSI engine, see [33]. Key points from optimal control theory, for this application are summarized. First, the fixed-time optimization problem is posed

$$\text{Min } J = -\kappa \cdot m_f \tag{3.30}$$

where m_f is the spacecraft mass at the final time, and κ is a constant parameter. To avoid the well-documented infinite-time solutions associated with the VSI engine, [58] the time-of-flight is fixed by specifying the initial and final times t_0 and t_f. The cost function in equation (3.30) is subject to the dynamical constraints

$$\dot{\boldsymbol{x}} = \boldsymbol{f}(t, \boldsymbol{x}, \boldsymbol{u}_c) = \begin{pmatrix} \dot{\boldsymbol{r}} \\ \dot{\boldsymbol{v}} \\ \dot{m} \end{pmatrix} = \begin{Bmatrix} \boldsymbol{v} \\ \dfrac{T}{m}\hat{\boldsymbol{u}} + \boldsymbol{g}(\boldsymbol{r}, \boldsymbol{v}) \\ -T^2/(2P) \end{Bmatrix} \tag{3.31}$$

where equation (3.31) reduces to equation (2.38) for the RTBP with $\boldsymbol{g}(\boldsymbol{r}, \boldsymbol{v})$ equal to the gravity field forces as written in terms of rotating coordinates. The generalization, however, implies that higher- or lower-fidelity gravity models can easily be represented by the function $\boldsymbol{g}(\boldsymbol{r}, \boldsymbol{v})$. Recall that the full vector of controls $\boldsymbol{u}_c$ for the VSI engine includes the steering direction and engine controls in equation (2.39). Optimization of the cost is also subject to the kinematic boundary conditions

$$\boldsymbol{\psi}_0 = \begin{pmatrix} \boldsymbol{r}_0 - \boldsymbol{r}(\tau_1) \\ \boldsymbol{v}_0 - \boldsymbol{v}(\tau_1) \end{pmatrix} \tag{3.32}$$

$$\boldsymbol{\psi}_f = \begin{pmatrix} \boldsymbol{r}_f - \boldsymbol{r}(\tau_2) \\ \boldsymbol{v}_f - \boldsymbol{v}(\tau_2) \end{pmatrix} \tag{3.33}$$

and constraints on the control

$$\begin{pmatrix} \hat{\boldsymbol{u}}^T \hat{\boldsymbol{u}} = 1 \\ P = P_{\max} \sin^2 \sigma \end{pmatrix} \tag{3.34}$$

The first constraint forces $\hat{\boldsymbol{u}}$ to be a vector of unit magnitude, and the second constraint employs the slack variable σ to enforce the switching conditions on the power P with a maximum value of $P_{\max}$. The variables τ_1 and τ_2 denote time-like parameters that locate a state on the initial and final orbit, respectively. To begin deriving the necessary conditions for optimality, define the Hamiltonian function for the Mayer problem, that is

$$\begin{aligned} H &= \boldsymbol{\lambda}^T \boldsymbol{f} && (3.35) \\ &= \boldsymbol{\lambda}_{\boldsymbol{r}}^T \boldsymbol{v} + \boldsymbol{\lambda}_{\boldsymbol{v}}^T \left((T/m)\hat{\boldsymbol{u}} + \boldsymbol{g}\right) - \lambda_m T^2/(2P) && (3.36) \end{aligned}$$

where $\boldsymbol{\lambda} = (\boldsymbol{\lambda}_{\boldsymbol{r}}^T, \boldsymbol{\lambda}_{\boldsymbol{r}}^T, \lambda_m)^T$ are defined as the costate variables. Next, the cost function J is augmented into an unconstrained optimization function J' by adjoining the Lagrange multipliers $\boldsymbol{\nu}_1 = (\boldsymbol{\nu}_{\boldsymbol{r}_1}^T, \boldsymbol{\nu}_{\boldsymbol{v}_1}^T)^T$ and $\boldsymbol{\nu}_2 = (\boldsymbol{\nu}_{\boldsymbol{r}_2}^T, \boldsymbol{\nu}_{\boldsymbol{v}_2}^T)^T$ to the boundary conditions as well as the time-varying costates $\boldsymbol{\lambda}$ and Lagrange multipliers η_1, and η_2 to the dynamic constraints and controls, respectively, i.e.

$$J' = \Theta + \int_{t_0}^{t_f} \left[\mathrm{I} - \boldsymbol{\lambda}^T \dot{\boldsymbol{x}}\right] dt \tag{3.37}$$

where

$$
\begin{aligned}
\Theta &= -\kappa \cdot m_f + \boldsymbol{\nu}_{\mathbf{1}}^T \boldsymbol{\psi}_0 + \boldsymbol{\nu}_{\mathbf{2}}^T \boldsymbol{\psi}_f && (3.38) \\
\mathrm{I} &= H + \eta_1(\hat{\boldsymbol{u}}^T \hat{\boldsymbol{u}} - 1) + \eta_2(P - P_{\max} \sin^2 \sigma) && (3.39) \\
&= \boldsymbol{\lambda}_{\boldsymbol{r}}^T \boldsymbol{v} + \boldsymbol{\lambda}_{\boldsymbol{v}}^T \left((T/m)\hat{\boldsymbol{u}} + \boldsymbol{g}\right) - \lambda_m T^2/(2P) \\
&\quad + \eta_1(\hat{\boldsymbol{u}}^T \hat{\boldsymbol{u}} - 1) + \eta_2(P - P_{\max} \sin^2 \sigma) && (3.40)
\end{aligned}
$$

Since the initial and final times are fixed, a local maximum or minimum is available by nulling the total variation in J'

$$
\begin{aligned}
dJ' = \delta J' = &\frac{\partial \Theta}{\partial \tau_1}\delta\tau_1 + \frac{\partial \Theta}{\partial \tau_2}\delta\tau_2 + \left(\frac{\partial \Theta}{\partial \boldsymbol{x}_f} - \boldsymbol{\lambda}_f^T\right)\delta \boldsymbol{x}_f + \frac{\partial \Theta}{\partial \boldsymbol{\nu}_1}\delta\boldsymbol{\nu}_1 + \frac{\partial \Theta}{\partial \boldsymbol{\nu}_2}\delta\boldsymbol{\nu}_2 \\
+ \int_{t_0}^{t_f} &\left[\left(\frac{\partial \mathrm{I}}{\partial \boldsymbol{x}} + \dot{\boldsymbol{\lambda}}^T\right)\delta\boldsymbol{x} + \frac{\partial \mathrm{I}}{\partial \boldsymbol{u}_c}\delta\boldsymbol{u}_c + \frac{\partial \mathrm{I}}{\partial \eta_1}\delta\eta_1 + \frac{\partial \mathrm{I}}{\partial \eta_2}\delta\eta_2 + \frac{\partial \mathrm{I}}{\partial \sigma}\delta\sigma\right] dt = 0 \qquad (3.41)
\end{aligned}
$$

Equation (3.41) contains the required information to extract the Euler-Lagrange equations, the transversality conditions, and the requirements for the optimal controls. A term-by-term analysis is now undertaken to guarantee that the free variable selection ensures the satisfaction of equation (3.41). For arbitrary variations along the path, $\delta\boldsymbol{x} \neq \mathbf{0}$ in general; then to satisfy equation (3.41), it is required that

$$
\begin{aligned}
\dot{\boldsymbol{\lambda}} &= -\frac{\partial \mathrm{I}}{\partial \boldsymbol{x}}^T \\
&= -\frac{\partial H}{\partial \boldsymbol{x}}^T && (3.42)
\end{aligned}
$$

where

$$
\begin{aligned}
\dot{\boldsymbol{\lambda}}_{\boldsymbol{r}} &= -\frac{\partial \boldsymbol{g}}{\partial \boldsymbol{r}}^T \boldsymbol{\lambda}_{\boldsymbol{v}} && (3.43) \\
\dot{\boldsymbol{\lambda}}_{\boldsymbol{v}} &= -\boldsymbol{\lambda}_{\boldsymbol{r}} - \frac{\partial \boldsymbol{g}}{\partial \boldsymbol{v}}^T \boldsymbol{\lambda}_{\boldsymbol{v}} && (3.44) \\
\dot{\lambda}_m &= -\left\|\boldsymbol{\lambda}_{\boldsymbol{v}}\right\| \frac{T}{m^2} && (3.45)
\end{aligned}
$$

For variations in the controls, slack variables, and the Lagrange multipliers within the integral expression in equation (3.41), examination of equation (3.40) leads to the following

$$\frac{\partial \mathrm{I}}{\partial \hat{\boldsymbol{u}}}^T = \boldsymbol{\lambda_v}/m + 2\eta_1 \hat{\boldsymbol{u}} = \boldsymbol{0} \tag{3.46}$$

$$\frac{\partial \mathrm{I}}{\partial T} = \boldsymbol{\lambda_v}^T \hat{\boldsymbol{u}}/m - \lambda_m T/P = 0 \tag{3.47}$$

$$\frac{\partial \mathrm{I}}{\partial P} = \lambda_m T^2/(2P^2) + \eta_2 = 0 \tag{3.48}$$

$$\frac{\partial \mathrm{I}}{\partial \sigma} = -2\eta_2 P_{\max} \sin\sigma \cos\sigma = 0 \tag{3.49}$$

$$\frac{\partial \mathrm{I}}{\partial \eta_1} = \hat{\boldsymbol{u}}^T \hat{\boldsymbol{u}} - 1 = 0 \tag{3.50}$$

$$\frac{\partial \mathrm{I}}{\partial \eta_2} = P - P_{\max} \sin^2\sigma = 0 \tag{3.51}$$

Equations (3.50)-(3.51) recover the constraints on the controls. If equation (3.50) is satisfied, then $\hat{\boldsymbol{u}}$ must, in general, be directed such that the direction nulls the other term in equation (3.46). Therefore $\hat{\boldsymbol{u}} = \pm\boldsymbol{\lambda_v}/\left\|\boldsymbol{\lambda_v}\right\|$. To evaluate which of the two possible sign options yields a *minimizing* control, via Pontryagin's Minimum Principle, the Hamiltonian in equation (3.36) is minimized such that

$$\hat{\boldsymbol{u}} = -\frac{\boldsymbol{\lambda_v}}{\|\boldsymbol{\lambda_v}\|} \tag{3.52}$$

where $\boldsymbol{\lambda_v}$ is Lawden's well-known primer vector. [8] Equation (3.47) is now solved by substituting from equation (3.52) to produce

$$T = -\frac{\|\boldsymbol{\lambda_v}\| P}{\lambda_m m} \tag{3.53}$$

Eliminating $\hat{\boldsymbol{u}}$ from H yields

$$H = \boldsymbol{\lambda_r}^T \boldsymbol{v} + \boldsymbol{\lambda_v}^T \boldsymbol{g} - T \cdot S \tag{3.54}$$

where S is Lawden's switching function defined as

$$S \equiv \frac{\|\boldsymbol{\lambda_v}\|}{m} + \frac{T}{2P}\lambda_m \tag{3.55}$$

Applying the Minimum Principle a second time for P reveals: if λ_m is always negative in S (which is later demonstrated to be true), then selecting $P = P_{\max}$ always minimizes H. Other switching options need not be considered, and the optimal controls for power as well as thrust, from equation (3.53) are

$$P = P_{\max}, \qquad T = -\frac{\|\boldsymbol{\lambda}_{\boldsymbol{v}}\| \, P_{\max}}{\lambda_m m} \tag{3.56}$$

These controls are logically consistent with equations (3.48)-(3.49), where either η_2, $\cos\sigma$, or $\sin\sigma$ equal zero. Inspection of equation (3.51) suggests three possibilities: (i) if $\cos\sigma = 0$, then $P = P_{\max}$; (ii) if $\sin\sigma = 0$, then $P = 0$; and, (iii) if $\eta_2 = 0$, then $0 \leq P \leq P_{\max}$. Clearly, then, the preceding analysis is consistent with case (i). The boundary constraints that emerge from the remaining terms in equation (3.41) are denoted the natural boundary conditions or the transversality conditions

$$\frac{\partial \Theta}{\partial \tau_1} = \boldsymbol{\lambda}_{\boldsymbol{r}_0}^T \boldsymbol{v}_0 + \boldsymbol{\lambda}_{\boldsymbol{v}_0}^T \boldsymbol{g}_0 = 0 \tag{3.57}$$

$$\frac{\partial \Theta}{\partial \tau_2} = \boldsymbol{\lambda}_{\boldsymbol{r}_f}^T \boldsymbol{v}_f + \boldsymbol{\lambda}_{\boldsymbol{v}_f}^T \boldsymbol{g}_f = 0 \tag{3.58}$$

$$\frac{\partial \Theta}{\partial \boldsymbol{x}_f}^T - \boldsymbol{\lambda}_f = \left(\boldsymbol{\nu}_{\boldsymbol{r}_2}^T - \boldsymbol{\lambda}_{\boldsymbol{r}_f}^T, \boldsymbol{\nu}_{\boldsymbol{v}_2}^T - \boldsymbol{\lambda}_{\boldsymbol{v}_f}^T, -\kappa - \lambda_{m_f} \right)^T = \boldsymbol{0} \tag{3.59}$$

$$\frac{\partial \Theta}{\partial \boldsymbol{\nu}_1}^T = \boldsymbol{\psi}_0 = \boldsymbol{0} \tag{3.60}$$

$$\frac{\partial \Theta}{\partial \boldsymbol{\nu}_2}^T = \boldsymbol{\psi}_f = \boldsymbol{0} \tag{3.61}$$

Equations (3.57)-(3.58) require an iterative solution along with the kinematic boundary conditions. Equation (3.59) is trivial except for the term that equates $\lambda_{m_f} = -\kappa$. Since κ is a positive constant, selecting $\lambda_{m_0} = -1$ removes a degree of freedom from the problem and satisfies the condition on λ_{m_f} because λ_m monotonically decreases consistent with equation (3.45). Finally, note that there is no explicit time dependency in equation (3.36), i.e. $H \neq H(t)$, and thus by equations (3.35) and (3.42)

$$\begin{aligned}\frac{dH}{dt} &= \frac{\partial H}{\partial \boldsymbol{x}}\frac{d\boldsymbol{x}}{dt} + \frac{\partial H}{\partial \boldsymbol{\lambda}}\frac{d\boldsymbol{\lambda}}{dt} + \frac{\partial H}{\partial t} \\ &= \frac{\partial H}{\partial \boldsymbol{x}}\frac{d\boldsymbol{x}}{dt} + \frac{\partial H}{\partial \boldsymbol{\lambda}}\frac{d\boldsymbol{\lambda}}{dt} \\ &= -\dot{\boldsymbol{\lambda}}^T\dot{\boldsymbol{x}} + \boldsymbol{f}^T\dot{\boldsymbol{\lambda}} \qquad (3.62) \\ &= 0 \qquad (3.63)\end{aligned}$$

Thus,

$$H = \text{constant} \qquad (3.64)$$

The Hamiltonian of the problem is therefore an integral of the motion, and is especially useful for numerical integration accuracy checks.

3.4.2 Solution via Indirect Shooting

The derivation of the optimal control problem to fuel-optimally transfer between two orbits using a VSI engine appears in the previous section. However, the problem still requires an iterative solution and must be formally posed as a two-point boundary value problem. The unknown terms that may vary are collected into the vector $\boldsymbol{X}$ of free variables

$$\boldsymbol{X} = \begin{pmatrix} \boldsymbol{\lambda}_{\boldsymbol{r}_0} \\ \boldsymbol{\lambda}_{\boldsymbol{v}_0} \\ \tau_1 \\ \tau_2 \end{pmatrix} \qquad (3.65)$$

The values corresponding to the states at τ_1 and τ_2 are $(\boldsymbol{r}(\tau_1)^T, \boldsymbol{v}(\tau_1)^T)^T$ and $(\boldsymbol{r}(\tau_2)^T, \boldsymbol{v}(\tau_2)^T)^T$, respectively. These values are generated using a spline parameterization over τ_1 and τ_2 that is computed a priori, or simply from separate time indices that are integrated from periodic orbits at fixed states and epochs. The constraints are the kinematic boundary conditions (equations (3.32)-(3.33)) and the non-trivial natural boundary conditions (equations (3.57)-(3.58))

$$\boldsymbol{F}(\boldsymbol{X}) = \begin{pmatrix} \boldsymbol{r}_f - \boldsymbol{r}(\tau_2) \\ \boldsymbol{v}_f - \boldsymbol{v}(\tau_2) \\ \boldsymbol{\lambda}_{\boldsymbol{r}_0}^T \boldsymbol{v}_0 + \boldsymbol{\lambda}_{\boldsymbol{v}_0}^T \boldsymbol{g}_0 \\ \boldsymbol{\lambda}_{\boldsymbol{r}_f}^T \boldsymbol{v}_f + \boldsymbol{\lambda}_{\boldsymbol{v}_f}^T \boldsymbol{g}_f \end{pmatrix} \tag{3.66}$$

Thus, the well-formed, two-point boundary value problem with 8 free variables and 8 constraints is completed. The required derivative information to implement the shooting method becomes

$$D\boldsymbol{F} = \begin{pmatrix} \frac{\partial \boldsymbol{r}_f}{\partial \boldsymbol{\lambda}_{\boldsymbol{r}_0}} & \frac{\partial \boldsymbol{r}_f}{\partial \boldsymbol{\lambda}_{\boldsymbol{v}_0}} & \frac{\partial \boldsymbol{r}_f}{\partial \tau_1} & -\frac{\partial \boldsymbol{r}(\tau_2)}{\partial \tau_2} \\ \frac{\partial \boldsymbol{v}_f}{\partial \boldsymbol{\lambda}_{\boldsymbol{r}_0}} & \frac{\partial \boldsymbol{v}_f}{\partial \boldsymbol{\lambda}_{\boldsymbol{v}_0}} & \frac{\partial \boldsymbol{v}_f}{\partial \tau_1} & -\frac{\partial \boldsymbol{v}(\tau_2)}{\partial \tau_2} \\ \boldsymbol{v}_0^T & \boldsymbol{g}_0^T & \boldsymbol{\lambda}_{\boldsymbol{r}_0}^T \frac{\partial \boldsymbol{v}_0}{\partial \tau_1} + \boldsymbol{\lambda}_{\boldsymbol{v}_0}^T \left(\frac{\partial \boldsymbol{g}_0}{\partial \boldsymbol{r}_0} \frac{\partial \boldsymbol{r}_0}{\partial \tau_1} + \frac{\partial \boldsymbol{g}_0}{\partial \boldsymbol{v}_0} \frac{\partial \boldsymbol{v}_0}{\partial \tau_1} \right) & 0 \\ \frac{\partial F_8}{\partial \boldsymbol{\lambda}_{\boldsymbol{r}_0}} & \frac{\partial F_8}{\partial \boldsymbol{\lambda}_{\boldsymbol{v}_0}} & \frac{\partial F_8}{\partial \tau_1} & 0 \end{pmatrix} \tag{3.67}$$

where

$$\frac{\partial F_8}{\partial \boldsymbol{\lambda}_{\boldsymbol{r}_0}} = \boldsymbol{v}_f^T \frac{\partial \boldsymbol{\lambda}_{\boldsymbol{r}_f}}{\partial \boldsymbol{\lambda}_{\boldsymbol{r}_0}} + \boldsymbol{\lambda}_{\boldsymbol{r}_f}^T \frac{\partial \boldsymbol{v}_f}{\partial \boldsymbol{\lambda}_{\boldsymbol{r}_0}} + \boldsymbol{g}_f^T \frac{\partial \boldsymbol{\lambda}_{\boldsymbol{v}_f}}{\partial \boldsymbol{\lambda}_{\boldsymbol{r}_0}} + \boldsymbol{\lambda}_{\boldsymbol{v}_f}^T \left(\frac{\partial \boldsymbol{g}_f}{\partial \boldsymbol{r}_f} \frac{\partial \boldsymbol{r}_f}{\partial \boldsymbol{\lambda}_{\boldsymbol{r}_0}} + \frac{\partial \boldsymbol{g}_f}{\partial \boldsymbol{v}_f} \frac{\partial \boldsymbol{v}_f}{\partial \boldsymbol{\lambda}_{\boldsymbol{r}_0}} \right) \tag{3.68}$$

$$\frac{\partial F_8}{\partial \boldsymbol{\lambda}_{\boldsymbol{v}_0}} = \boldsymbol{v}_f^T \frac{\partial \boldsymbol{\lambda}_{\boldsymbol{r}_f}}{\partial \boldsymbol{\lambda}_{\boldsymbol{v}_0}} + \boldsymbol{\lambda}_{\boldsymbol{r}_f}^T \frac{\partial \boldsymbol{v}_f}{\partial \boldsymbol{\lambda}_{\boldsymbol{v}_0}} + \boldsymbol{g}_f^T \frac{\partial \boldsymbol{\lambda}_{\boldsymbol{v}_f}}{\partial \boldsymbol{\lambda}_{\boldsymbol{v}_0}} + \boldsymbol{\lambda}_{\boldsymbol{v}_f}^T \left(\frac{\partial \boldsymbol{g}_f}{\partial \boldsymbol{r}_f} \frac{\partial \boldsymbol{r}_f}{\partial \boldsymbol{\lambda}_{\boldsymbol{v}_0}} + \frac{\partial \boldsymbol{g}_f}{\partial \boldsymbol{v}_f} \frac{\partial \boldsymbol{v}_f}{\partial \boldsymbol{\lambda}_{\boldsymbol{v}_0}} \right) \tag{3.69}$$

$$\frac{\partial F_8}{\partial \tau_1} = \boldsymbol{v}_f^T \frac{\partial \boldsymbol{\lambda}_{\boldsymbol{r}_f}}{\partial \tau_1} + \boldsymbol{\lambda}_{\boldsymbol{r}_f}^T \frac{\partial \boldsymbol{v}_f}{\partial \tau_1} + \boldsymbol{g}_f^T \frac{\partial \boldsymbol{\lambda}_{\boldsymbol{v}_f}}{\partial \tau_1} + \boldsymbol{\lambda}_{\boldsymbol{v}_f}^T \left(\frac{\partial \boldsymbol{g}_f}{\partial \boldsymbol{r}_f} \frac{\partial \boldsymbol{r}_f}{\partial \tau_1} + \frac{\partial \boldsymbol{g}_f}{\partial \boldsymbol{v}_f} \frac{\partial \boldsymbol{v}_f}{\partial \tau_1} \right) \tag{3.70}$$

Satisfying the constraints $\boldsymbol{F}(\boldsymbol{X})$ with this formulation of the problem is an indirect shooting approach because it simply involves solving a system of nonlinear constraints that minimize the value of J without any actual manipulation or evaluation of equation (3.30). The process is implemented as follows:

1. If necessary, generate a spline approximation for $(\boldsymbol{r}(\tau_1)^T, \boldsymbol{v}(\tau_1)^T)^T$ and $(\boldsymbol{r}(\tau_2)^T, \boldsymbol{v}(\tau_2)^T)^T$ using pre-generated data representing a periodic orbit.
2. Guess the initial conditions, $\boldsymbol{X}^0$.

3. Propagate the state and costate system, equation (3.31) and equations (3.43)-(3.45) from t_0 to t_f using the optimal controls derived in equation (3.52) and equation (3.56), and let $\lambda_{m_0} = -1$. If analytical partial derivatives are desired, then simultaneously propagate equation (3.18). (Additional analytical differentiation is required to compute $\mathbf{A}(t)$ a priori for the full state and costate system model.)
4. Evaluate the error in the boundary conditions $\boldsymbol{F}(\boldsymbol{X})$. If $\boldsymbol{F}(\boldsymbol{X}) < \epsilon$, then stop.
5. Use equation (3.6), or a nonlinear equation solver package to adjust $\boldsymbol{X}$ to satisfy $\boldsymbol{F}(\boldsymbol{X})$. Repeat steps 3-5.

Recall the comment from Bryson and Ho (Section 3.4) concerning the indirect methods and the difficulties in "getting started". Delivering a *first guess* for step #2 is considerably aided by using the adjoint control transformation (ACT) [29] to obtain $\boldsymbol{\lambda}_{\boldsymbol{r}_0}$ and $\boldsymbol{\lambda}_{\boldsymbol{v}_0}$. For details about this application of the ACT process, see Appendix A.

3.4.3 Solution via Direct Shooting

Another viable option to solve the optimal control problem for fuel-optimal, low-thrust transfers between orbits with a VSI engine is to employ a direct shooting method. In contrast to indirect shooting, the direct shooting approach involves elimination of the highly sensitive natural boundary conditions, i.e., equations (3.57)-(3.58). Then, a cost function for the under-constrained problem is directly minimized with nonlinear programming software. In the literature, this strategy that employs the calculus of variations derivation for the control laws, but minimizes with an NLP algorithm has also been labeled a hybrid method. [59], [81], [82] For some problems, the direct minimization via NLP widens the convergence radius, although some accuracy in the local minimum is possibly sacrificed. The NLP cost function F_0 is posed as follows

$$\text{Min } F_0(\boldsymbol{X}) = -m_f \qquad (3.71)$$

where the constant κ in equation (3.30) is now removed without loss of generality. The unknown parameters in $\boldsymbol{X}$ remain the same as in equation (3.65). The constraints, however, are now only equations (3.32)-(3.33)

$$\boldsymbol{F}(\boldsymbol{X}) = \begin{pmatrix} \boldsymbol{r}_f - \boldsymbol{r}(\tau_2) \\ \boldsymbol{v}_f - \boldsymbol{v}(\tau_2) \end{pmatrix} \tag{3.72}$$

Thus, the required constraint derivative information to implement the shooting method becomes

$$D\boldsymbol{F} = \begin{pmatrix} \frac{\partial \boldsymbol{r}_f}{\partial \boldsymbol{\lambda}_{\boldsymbol{r}0}} & \frac{\partial \boldsymbol{r}_f}{\partial \boldsymbol{\lambda}_{\boldsymbol{v}0}} & \frac{\partial \boldsymbol{r}_f}{\partial \tau_1} & -\frac{\partial \boldsymbol{r}(\tau_2)}{\partial \tau_2} \\ \frac{\partial \boldsymbol{v}_f}{\partial \boldsymbol{\lambda}_{\boldsymbol{r}0}} & \frac{\partial \boldsymbol{v}_f}{\partial \boldsymbol{\lambda}_{\boldsymbol{v}0}} & \frac{\partial \boldsymbol{v}_f}{\partial \tau_1} & -\frac{\partial \boldsymbol{v}(\tau_2)}{\partial \tau_2} \end{pmatrix} \tag{3.73}$$

Gradient-based NLP software also requires derivatives of the cost with respect to $\boldsymbol{X}$, i.e.

$$DF_0 = \left(-\frac{\partial m_f}{\partial \boldsymbol{\lambda}_{\boldsymbol{r}_0}}^T, -\frac{\partial m_f}{\partial \boldsymbol{\lambda}_{\boldsymbol{v}_0}}^T, 0, 0 \right) \tag{3.74}$$

The process is now executed as follows:

1. If necessary, generate a spline approximation for $(\boldsymbol{r}(\tau_1)^T, \boldsymbol{v}(\tau_1)^T)^T$ and $(\boldsymbol{r}(\tau_2)^T, \boldsymbol{v}(\tau_2)^T)^T$ using pre-generated data representing a periodic orbit.

2. Guess initial conditions, $\boldsymbol{X}$.

3. Propagate the state and costate system, equation (3.31) and equations (3.43)-(3.45) from t_0 to t_f using the optimal controls derived in equation (3.52) and equation (3.56), and let $\lambda_{m_0} = -1$. If analytical partial derivatives are desired, then simultaneously propagate equation (3.18). (Additional analytical differentiation is required to compute $\mathbf{A}(t)$ a priori for the full state and costate system model.)

4. Evaluate the error in the boundary conditions $\boldsymbol{F}(\boldsymbol{X})$ and the optimality of F_0. If $\boldsymbol{F}(\boldsymbol{X}) < \epsilon$ and F_0 is minimal, then stop.

5. Adjust $\boldsymbol{X}$ to satisfy $\boldsymbol{F}(\boldsymbol{X})$ and minimize F_0. Repeat steps 3-5.

Here, steps #3-#5 are typically completed via the NLP software, once the necessary cost, constraint, and derivative information is available for the iteration procedure. The ACT is optionally used for an initial guess, consistent with Appendix A.

3.5 Direct Trajectory Optimization via the Transcription Approach

Among the options for solving a general trajectory design and optimization problem, often the best choice is a direct transcription scheme via collocation, also known as direct collocation. In contrast to the previously discussed approaches, direct collocation fundamentally relies on completely discretizing a solution to the equations of motion with an *implicit integration* scheme. Feasible solutions are first computed by allowing the states and controls at points along the entire trajectory to enter the problem as unknown variables. Such a process is especially useful when there is very little intuition about the solution space. Knowledge of a control law is not required; the thrust vector is oriented exactly as needed at every instant to satisfy objective constraints. Unlike explicit integration subroutines, where the problem sensitivity depends only on the initial state, a larger convergence radius is expected for implicit schemes that partition the sensitivities over the many discrete points. This feature is especially important for design in chaotic systems, where a slight change in the initial state could induce large variations and unpredictable behavior downstream. In recent decades, computational speed increases and improved techniques for exploiting sparse matrices have resulted in faster implicit schemes, in addition to the robustness, allowing for rapid exploration of the design space. They are also readily adapted for direct optimization. According to Betts, [79] the direct transcription method is decomposed into three fundamental steps:

1. Convert the dynamic system into a problem with a finite set of variables. This process involves discretization with a collocation approach.
2. Solve the finite-dimensional problem using a parameter optimization method. (Feasible solutions may also be alternatively considered.)

3. Assess the accuracy of the finite-dimensional approximation and if necessary repeat the transcription and optimization steps. This is known as the process of *mesh refinement*.

The formulation and implementation of the direct transcription method using collocation follows.

3.5.1 Collocation

The core of the transcription approach is to convert the continuous time problem into a discrete domain that can be reduced to a system of many nonlinear equations and solved iteratively with Newton's method, a nonlinear equation solving package, or NLP software for optimization. This concept contrasts with indirect and direct shooting methods for continuous systems that are tied to a requirement for explicit integration, and thus, enforcement of constraints only at the boundaries of the integrated path. To begin the discretization process, let n nodes partition the solution into $n-1$ segments consistent with the fixed mesh

$$\Pi : t_1 < t_2 < \cdots < t_{n-1} < t_n \tag{3.75}$$

The time interval along a given segment can be converted from $[t_i, t_{i+1}]$ to $\tau \in [0, 1]$ using

$$\tau = \frac{t - t_i}{\Delta t_i} \tag{3.76}$$

where $\Delta t_i = t_{i+1} - t_i$. Given this discrete domain, a high-accuracy solution is still desired, and therefore a 7^{th}-degree piecewise polynomial approach using Gauss-Lobatto points is employed.

Seventh-Degree Gauss-Lobatto Approach

One approach to solve the problem is to employ highly-accurate 7th-degree piecewise continuous polynomials and the method of collocation, resulting in a 12th-order accurate solution. The polynomials representing the segment are defined

$$\boldsymbol{x}(\tau) = \mathbf{M} \times \{1 \quad \tau \quad \tau^2 \quad \tau^3 \quad \tau^4 \quad \tau^5 \quad \tau^6 \quad \tau^7\}^T \tag{3.77}$$

where $\mathbf{M}$ is the matrix of coefficients. Let $\boldsymbol{x}_j = \boldsymbol{x}(\tau_j)$, $\boldsymbol{u}_j = \boldsymbol{u}(\tau_j)$, and $\boldsymbol{x}'_j = \boldsymbol{x}'(\tau_j)$, where the subscript "$j$" is prescribed in Figure 3.1. Prime indicates a derivative with respect to normalized time τ, i.e., $\boldsymbol{x}'_j = \Delta t_i \boldsymbol{f}(t_j, \boldsymbol{x}_j, \boldsymbol{u}_j, \boldsymbol{\mu})$. Only the four points $\boldsymbol{x}_i$, $\boldsymbol{x}_{i,2}$, $\boldsymbol{x}_{i,3}$, $\boldsymbol{x}_{i+1}$ are necessary to uniquely determine the polynomials represented by equation (3.77). Additionally there are three defect points and, therefore, seven points total are required to construct the Gauss-Lobatto integration constraints. The points are distributed on the normalized time interval consistent with the set $\{0,\ \tau_{i,1},\ \tau_{i,2},\ \tau_{i,c},\ \tau_{i,3},\ \tau_{i,4},\ 1\}$. The normalized time values $\tau_{i,1}$, $\tau_{i,2}$, $\tau_{i,c}$, $\tau_{i,3}$, $\tau_{i,4}$ are the same for every segment and selected to minimize the local truncation error. (See Table 3.1.) Recall that the known points along the segment are $\boldsymbol{x}_i$, $\boldsymbol{x}_{i,2}$, $\boldsymbol{x}_{i,3}$, $\boldsymbol{x}_{i+1}$. From equation (3.77), the points must satisfy

$$\{\boldsymbol{x}_i \quad \boldsymbol{x}'_i \quad \boldsymbol{x}_{i,2} \quad \boldsymbol{x}'_{i,2} \quad \boldsymbol{x}_{i,3} \quad \boldsymbol{x}'_{i,3} \quad \boldsymbol{x}_{i+1} \quad \boldsymbol{x}'_{i+1}\} = \mathbf{MB} \tag{3.78}$$

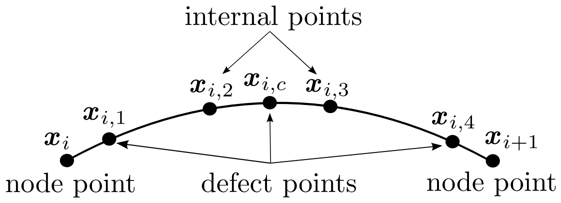

Figure 3.1. The Seventh-Degree Gauss-Lobatto Node Segment

where

$$\mathbf{B} = \begin{bmatrix} 1 & 0 & 1 & 0 & 1 & 0 & 1 & 0 \\ 0 & 1 & \tau_{i,2} & 1 & \tau_{i,4} & 1 & 1 & 1 \\ 0 & 0 & \tau_{i,2}^2 & 2\tau_{i,2} & \tau_{i,3}^2 & 2\tau_{i,3} & 1 & 2 \\ 0 & 0 & \tau_{i,2}^3 & 3\tau_{i,2}^2 & \tau_{i,3}^3 & 3\tau_{i,3}^2 & 1 & 3 \\ 0 & 0 & \tau_{i,2}^4 & 4\tau_{i,2}^3 & \tau_{i,3}^4 & 4\tau_{i,3}^3 & 1 & 4 \\ 0 & 0 & \tau_{i,2}^5 & 5\tau_{i,2}^4 & \tau_{i,3}^5 & 5\tau_{i,3}^4 & 1 & 5 \\ 0 & 0 & \tau_{i,2}^6 & 6\tau_{i,2}^5 & \tau_{i,3}^6 & 6\tau_{i,3}^5 & 1 & 6 \\ 0 & 0 & \tau_{i,2}^7 & 7\tau_{i,2}^6 & \tau_{i,3}^7 & 7\tau_{i,3}^6 & 1 & 7 \end{bmatrix} \tag{3.79}$$

Since the left side of equation (3.78) is given and $\mathbf{B}$ is a known (constant) matrix, the coefficients $\mathbf{M}$ are computed from equation (3.78). Then, to satisfy the system equations, the time derivatives of the polynomials must also satisfy the system ODEs at the defect points $\boldsymbol{x}_{i,1}$, $\boldsymbol{x}_{i,c}$, and $\boldsymbol{x}_{i,4}$. (See Figure 3.2 for a geometric representation of the defect constraints.) Using equation (3.77), the interpolated expressions for these quantities are

$$\begin{aligned} \boldsymbol{x}_{i,1} = a_i^1\boldsymbol{x}_i + a_{i,2}^1\boldsymbol{x}_{i,2} + a_{i,3}^1\boldsymbol{x}_{i,3} + a_{i+1}^1\boldsymbol{x}_{i+1} \\ +\Delta t_i \left(v_i^1\boldsymbol{f}_i + v_{i,2}^1\boldsymbol{f}_{i,2} + v_{i,3}^1\boldsymbol{f}_{i,3} + v_{i+1}^1\boldsymbol{f}_{i+1}\right) \end{aligned} \tag{3.80}$$

$$\begin{aligned} \boldsymbol{x}_{i,c} = a_i^c\boldsymbol{x}_i + a_{i,2}^c\boldsymbol{x}_{i,2} + a_{i,3}^c\boldsymbol{x}_{i,3} + a_{i+1}^c\boldsymbol{x}_{i+1} \\ +\Delta t_i \left(v_i^c\boldsymbol{f}_i + v_{i,2}^c\boldsymbol{f}_{i,2} + v_{i,3}^c\boldsymbol{f}_{i,3} + v_{i+1}^c\boldsymbol{f}_{i+1}\right) \end{aligned} \tag{3.81}$$

$$\begin{aligned} \boldsymbol{x}_{i,4} = a_i^4\boldsymbol{x}_i + a_{i,2}^4\boldsymbol{x}_{i,2} + a_{i,3}^4\boldsymbol{x}_{i,3} + a_{i+1}^4\boldsymbol{x}_{i+1} \\ +\Delta t_i \left(v_i^4\boldsymbol{f}_i + v_{i,2}^4\boldsymbol{f}_{i,2} + v_{i,3}^4\boldsymbol{f}_{i,3} + v_{i+1}^4\boldsymbol{f}_{i+1}\right) \end{aligned} \tag{3.82}$$

where $\boldsymbol{f}_j = \boldsymbol{f}(t_j, \boldsymbol{x}_j, \boldsymbol{u}_j, \boldsymbol{\mu})$, and unless otherwise specified, the control is based upon a piecewise linear parameterization between the nodes, i.e.

$$\boldsymbol{u}(t) = \left(\frac{\boldsymbol{u}_{i+1} - \boldsymbol{u}_i}{t_{i+1} - t_i}\right) t + \boldsymbol{u}_i, \quad t_i \le t \le t_{i+1} \tag{3.83}$$

The resulting defect constraint equations are

$$\begin{aligned} \boldsymbol{\Delta}_{i,1}(\boldsymbol{x}_i, \boldsymbol{u}_i, \boldsymbol{x}_{i,2}, \boldsymbol{x}_{i,4}, \boldsymbol{x}_{i+1}, \boldsymbol{u}_{i+1}, \boldsymbol{\mu}) = b_i^1\boldsymbol{x}_i + b_{i,2}^1\boldsymbol{x}_{i,2} + b_{i,3}^1\boldsymbol{x}_{i,3} + b_{i+1}^1\boldsymbol{x}_{i+1} \\ +\Delta t_i \left(w_i^1\boldsymbol{f}_i + w_{i,1}^1\boldsymbol{f}_{i,1} + w_{i,2}^1\boldsymbol{f}_{i,2} + w_{i,3}^1\boldsymbol{f}_{i,3} + w_{i+1}^1\boldsymbol{f}_{i+1}\right) = \mathbf{0} \end{aligned} \tag{3.84}$$

$$\begin{aligned}\boldsymbol{\Delta}_{i,c}(\boldsymbol{x}_i, \boldsymbol{u}_i, \boldsymbol{x}_{i,2}, \boldsymbol{x}_{i,4}, \boldsymbol{x}_{i+1}, \boldsymbol{u}_{i+1}, \boldsymbol{\mu}) &= b_i^c \boldsymbol{x}_i + b_{i,2}^c \boldsymbol{x}_{i,2} + b_{i,3}^c \boldsymbol{x}_{i,3} + b_{i+1}^c \boldsymbol{x}_{i+1} \\ &+ \Delta t_i \left(w_i^c \boldsymbol{f}_i + w_{i,2}^c \boldsymbol{f}_{i,2} + w_{i,c}^c \boldsymbol{f}_{i,c} + w_{i,3}^c \boldsymbol{f}_{i,3} + w_{i+1}^c \boldsymbol{f}_{i+1} \right) = \boldsymbol{0}\end{aligned} \tag{3.85}$$

$$\begin{aligned}\boldsymbol{\Delta}_{i,4}(\boldsymbol{x}_i, \boldsymbol{u}_i, \boldsymbol{x}_{i,2}, \boldsymbol{x}_{i,4}, \boldsymbol{x}_{i+1}, \boldsymbol{u}_{i+1}, \boldsymbol{\mu}) &= b_i^4 \boldsymbol{x}_i + b_{i,2}^4 \boldsymbol{x}_{i,2} + b_{i,3}^4 \boldsymbol{x}_{i,3} + b_{i+1}^4 \boldsymbol{x}_{i+1} \\ &+ \Delta t_i \left(w_i^4 \boldsymbol{f}_i + w_{i,2}^4 \boldsymbol{f}_{i,2} + w_{i,3}^4 \boldsymbol{f}_{i,3} + w_{i,4}^4 \boldsymbol{f}_{i,4} + w_{i+1}^4 \boldsymbol{f}_{i+1} \right) = \boldsymbol{0}\end{aligned} \tag{3.86}$$

The coefficients a, v, b, and w that appear in equations (3.80)-(3.86) are the same for every segment, and are listed in Table 3.1.

3.5.2 Establishing the Free Variables and Constraints

To compute a continuous solution, the defects $\boldsymbol{\Delta}_{i,1}$, $\boldsymbol{\Delta}_{i,c}$, and $\boldsymbol{\Delta}_{i,4}$, for every segment must be reduced to zero. This step is accomplished by allowing $\boldsymbol{x}_i$ and $\boldsymbol{u}_i$ to vary at every node point, and the internal collocation points $\boldsymbol{x}_{i,2}$ and $\boldsymbol{x}_{i,3}$ to vary as well. Therefore, there are a total of $18n - 12$ defect constraint equations and $21n - 12$ free variables for the n nodes (with an additional p free variables that represent parameters, if they are present in the problem). It is also often necessary to apply control constraints ψ_i over the entire path. Typically, this control constraint

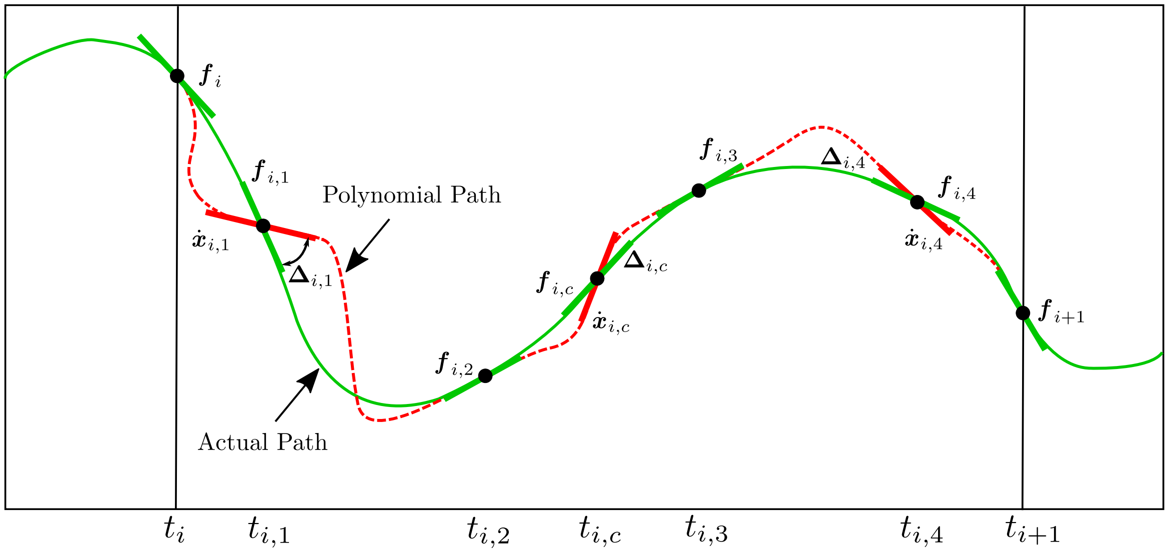

Figure 3.2. Defect Constraint Illustration

Table 3.1 List of Constants for Numerical Integration

$\tau_{i,1}$ = +8.48880518607166d-2

$\tau_{i,2}$ = +2.65575603264643d-1

$\tau_{i,c}$ = +5d-1

$\tau_{i,3}$ = +7.34424396735357d-1

$\tau_{i,4}$ = +9.15111948139283d-1

a_i^1	=	+6.18612232711785d-1	b_i^1	=	+8.84260109348311d-1
$a_{i,2}^1$	=	+3.34253095933642d-1	$b_{i,2}^1$	=	−8.23622559094327d-1
$a_{i,3}^1$	=	+1.52679626438851d-2	$b_{i,3}^1$	=	−2.35465327970606d-2
a_{i+1}^1	=	+3.18667087106879d-2	b_{i+1}^1	=	−3.70910174569208d-2
v_i^1	=	+2.57387738427162d-2	w_i^1	=	+1.62213410652341d-2
			$w_{i,1}^1$	=	+1.38413023680783d-1
$v_{i,2}^1$	=	−5.50098654524528d-2	$w_{i,2}^1$	=	+9.71662045547156d-2
$v_{i,3}^1$	=	−1.53026046503702d-2	$w_{i,3}^1$	=	+1.85682012187242d-2
v_{i+1}^1	=	−2.38759243962924d-3	w_{i+1}^1	=	+2.74945307600086d-3
a_i^c	=	+1.41445282326366d-1	b_i^c	=	+7.86488731947674d-2
$a_{i,2}^c$	=	+3.58554717673634d-1	$b_{i,2}^c$	=	+8.00076026297266d-1
$a_{i,3}^c$	=	+3.58554717673634d-1	$b_{i,3}^c$	=	−8.00076026297266d-1
a_{i+1}^c	=	+1.41445282326366d-1	b_{i+1}^c	=	−7.86488731947674d-2
v_i^c	=	+9.92317607754556d-3	w_i^c	=	+4.83872966828888d-3
$v_{i,2}^c$	=	+9.62835932121973d-2	$w_{i,2}^c$	=	+1.00138284831491d-1
			$w_{i,c}^c$	=	+2.43809523809524d-1
$v_{i,3}^c$	=	−9.62835932121973d-2	$w_{i,3}^c$	=	+1.00138284831491d-1
v_{i+1}^c	=	−9.92317607754556d-3	w_{i+1}^c	=	+4.83872966828888d-3
a_i^4	=	+3.18667087106879d-2	b_i^4	=	+3.70910174569208d-2
$a_{i,2}^4$	=	+1.52679626438851d-2	$b_{i,2}^4$	=	+2.35465327970606d-2
$a_{i,3}^4$	=	+3.34253095933642d-1	$b_{i,3}^4$	=	+8.23622559094327d-1
a_{i+1}^4	=	+6.18612232711785d-1	b_{i+1}^4	=	−8.84260109348311d-1
v_i^4	=	+2.38759243962924d-3	w_i^4	=	+2.74945307600086d-3
$v_{i,2}^4$	=	+1.53026046503702d-2	$w_{i,2}^4$	=	+1.85682012187242d-2
$v_{i,3}^4$	=	+5.50098654524528d-2	$w_{i,3}^4$	=	+9.71662045547156d-2
			$w_{i,4}^4$	=	+1.38413023680783d-1
v_{i+1}^4	=	−2.57387738427162d-2	w_{i+1}^4	=	+1.62213410652341d-2

is implemented to force the control direction, $\boldsymbol{u}_i = \hat{\boldsymbol{u}}_i$, as indicated in equation (2.30) to possess unit magnitude. This requirement is enforced by adding n additional constraints

$$\psi_i(\boldsymbol{u}_i) = \|\boldsymbol{u}_i\|^2 - 1 = 0 \quad \text{for } i = 1, 2, .., n \tag{3.87}$$

Alternatively, equation (3.87) can be removed, leaving $\boldsymbol{u}_i$ unconstrained, and then impose equation (2.30) directly in the equations of motion. This choice reduces the number of constraints, but there is a chance that unbounding $\boldsymbol{u}_i$ leads to numerical ill-conditioning. Additional inequality *path constraints* are also easily included in the collocation scheme. These constraints are useful in bounding the entire solution to a particular region of the phase space. The path constraints are of the form $\bar{\boldsymbol{g}}(\boldsymbol{x}, \boldsymbol{u}) < 0$, where $\bar{\boldsymbol{g}}$ is an m-element column vector. The continuous constraints are discretized, and converted to $m(3n-2)$ equality constraints by introducing $m(3n-2)$ slack variables, i.e.

$$\begin{array}{rcrcrcll}
\boldsymbol{g}_i(\boldsymbol{x}_i, \boldsymbol{u}_i, \boldsymbol{\eta}_i) & = & \bar{\boldsymbol{g}}_i(\boldsymbol{x}_i, \boldsymbol{u}_i) & + & \boldsymbol{\eta}_i^2 & = & \boldsymbol{0} & \text{for } i = 1, 2, .., n \\
\boldsymbol{g}_{i,2}(\boldsymbol{x}_{i,2}, \boldsymbol{\eta}_{i,2}) & = & \bar{\boldsymbol{g}}_{i,2}(\boldsymbol{x}_{i2}) & + & \boldsymbol{\eta}_{i,2}^2 & = & \boldsymbol{0} & \text{for } i = 1, 2, .., n-1 \\
\boldsymbol{g}_{i,3}(\boldsymbol{x}_{i,3}, \boldsymbol{\eta}_{i,3}) & = & \bar{\boldsymbol{g}}_{i,3}(\boldsymbol{x}_{i3}) & + & \boldsymbol{\eta}_{i,3}^2 & = & \boldsymbol{0} & \text{for } i = 1, 2, .., n-1
\end{array} \tag{3.88}$$

where the $\boldsymbol{\eta}^2$ terms are vectors, i.e., the element-wise square of the m-element slack variable $\boldsymbol{\eta}$, and of the same dimension. Finally, it is sometimes useful to constrain specific node states and/or control. The general form for these constraints is

$$h_r = 0 \quad \text{for } r = 1, 2, .., l \tag{3.89}$$

In contrast to the constraints in equation (3.88), the constraints in equation (3.87) and equation (3.89) are scalar-valued.

In summary, there are a total of $21n + m(3n-2) - 12 + p$ free parameters in general: $6n$ associated with the node states, $3n$ associated with the node controls, $12n - 12$ associated with the states at the internal points, $m(3n-2)$ for all the slack variables, and p associated with the parameter vector $\boldsymbol{\mu}$. Therefore, the vector $\boldsymbol{X}$ is defined as

$$\begin{aligned}\boldsymbol{X}^T = \big(&\boldsymbol{x}_1^T, \boldsymbol{u}_1^T, \boldsymbol{x}_{1,2}^T, \boldsymbol{x}_{1,3}^T, \boldsymbol{x}_2^T, \boldsymbol{u}_2^T, \boldsymbol{x}_{2,2}^T, \boldsymbol{x}_{2,3}^T, ..., \boldsymbol{x}_n^T, \boldsymbol{u}_n^T, \\ &\boldsymbol{\eta}_1^T, \boldsymbol{\eta}_{1,2}^T, \boldsymbol{\eta}_{1,3}^T, \boldsymbol{\eta}_2^T, \boldsymbol{\eta}_{2,2}^T, \boldsymbol{\eta}_{2,3}^T, ..., \boldsymbol{\eta}_n^T, \boldsymbol{\mu}^T\big)\end{aligned} \tag{3.90}$$

There are also a total of $19n+m\,(3n-2)+l-18$ constraints: $18n-18$ for the defects, n for the node controls, $m\,(3n-2)$ for the path constraints, and l for additional node constraints. The full constraint vector is

$$\begin{aligned}\boldsymbol{F}\,(\boldsymbol{X})^T = \big(&\boldsymbol{\Delta}_{1,1}^T, \boldsymbol{\Delta}_{1,c}^T, \boldsymbol{\Delta}_{1,4}^T, \boldsymbol{\Delta}_{2,1}^T, \boldsymbol{\Delta}_{2,c}^T, \boldsymbol{\Delta}_{2,4}^T, ..., \boldsymbol{\Delta}_{n-1,1}^T, \boldsymbol{\Delta}_{n-1,c}^T, \boldsymbol{\Delta}_{n-1,4}^T, \\ &\psi_1, \psi_2, ..., \psi_n, \boldsymbol{g}_1^T, \boldsymbol{g}_{1,2}^T, \boldsymbol{g}_{1,3}^T, \boldsymbol{g}_2^T, \boldsymbol{g}_{2,2}^T, \boldsymbol{g}_{2,3}^T, ..., \boldsymbol{g}_n^T, h_1, h_2, ..., h_l\big)\end{aligned} \tag{3.91}$$

Then, the goal is to either determine a nearby feasible solution $\boldsymbol{X}^{**}$ that satisfies the constraint $\boldsymbol{F}\,(\boldsymbol{X}^{**}) = \boldsymbol{0}$, or to solve the transcription problem of determining $\boldsymbol{X}^{**}$ that satisfies $\boldsymbol{F}\,(\boldsymbol{X}^{**}) = \boldsymbol{0}$ and optimizes $F_0(\boldsymbol{X}^{**})$ using nonlinear programming.

Modification for Thrusting and Coasting Arcs

When a CSI engine such as a solar electric thruster is employed, extra development of the constraints and free variables is required to accommodate an arbitrary number of thrusting and coasting arcs. It is assumed that CSI engines operate on the principle of "bang-bang" control and, thus, either $T = 0$ or $T = T_{\max}$ for an arbitrary arc that is composed of many Gauss-Lobatto node segments. Furthermore, since no fuel is being expended, the spacecraft mass must remain unchanged when the spacecraft is coasting. The basic thrust-coast structure is depicted in Figure 3.3, where coast arcs are blue and thrust arcs are red. A similar problem structure appears in Enright, [39] however, the algorithm in the reference accommodates only two thrust arcs. In this analysis the number of thrust arcs, k, is predetermined and a coast arc is always inserted between two thrust arcs. For example, for $k = 2$ there are two thrust arcs separated by one coast arc: the structure is simply *thrust-coast-thrust*. The collocation strategy then shifts the arcs in configuration space as necessary to satisfy the problem constraints, including the optimality conditions for direct transcription.

A relationship between time and initial mass is available from the denominator of equation (2.33). Therefore, the initial mass $m_{0,j}$ for each thrust arc is adjusted accordingly, so that the time is zero at the beginning of the arc. (For coasting when an RTBP model is used, no adjustment is necessary due to time invariance in the model.) The total times along the j^{th} arc, that is, $T_{b,j}$ and $T_{c,j}$, are specified as problem variables, and so the strategy is capable of removing unnecessary arcs by reducing $T_{b,j}$ or $T_{c,j}$ to zero. Inequality constraints ensure that $T_{b,j}$ and $T_{c,j}$ remain nonnegative. The black dots along the trajectory in Figure 3.3 represent nodes, with $n_{b,j}$ indicating the number of nodes for the j^{th} thrust arc and similarly for $n_{c,j}$. Each value of $n_{b,j}$ and $n_{b,c}$ is predetermined, so that the number of nodes per arc is a user-defined input. The shared node that connects thrust and coast arcs is formulated as part of the thrust arc. Node times are specified as a fixed ratio of the total time for each arc. For example, for the j^{th} thrust arc, the times corresponding to each node are specified as $T_{b,j} \times \{0, \delta_2, \delta_3, ..., \delta_{n_{b,j}-2}, \delta_{n_{b,j}-1}, 1\}$, where the ratios δ_i are such that $0 < \delta_2 < \delta_3 < \cdots < \delta_{n_{b,j}-2} < \delta_{n_{b,j}-1} < 1$. For each arc, the time ratios δ_i are fixed, but may be different for different arcs. The number and spacing of the nodes is determined by the initial accuracy desired for the solution, although there may be a change during mesh refinement.

For thrust arcs, the problem dependent parameters are $\boldsymbol{\mu}_i = (T_{b,j}, m_{0,j})^T$. Thus, $T_{b,j}$ and $m_{0,j}$ are assumed to be *independent* variables for each node segment. For coast arcs, the problem dependent parameter is just $\boldsymbol{\mu}_i = T_{c,j}$. Consequently, constraint equations are applied to enforce the requirement that $\boldsymbol{\mu}_i$ be the same for each node segment along the arc. The constraint equations are imposed on adjacent node segments, or

$$\boldsymbol{h}_l = \boldsymbol{\mu}_l - \boldsymbol{\mu}_{l-1} = \boldsymbol{0} \tag{3.92}$$

Here, $l = 2, .., n_{b,j} - 1$ and $l = 2, .., n_{c,j} - 1$, for thrusting and coasting, respectively. Formulating the problem in this manner may appear nonintuitive, seeming to increase the size of the problem unnecessarily. However, the assumption of independent vectors $\boldsymbol{\mu}_i$ significantly increases the sparsity of $D\boldsymbol{F}$ and $D\boldsymbol{F} \cdot D\boldsymbol{F}^T$. Computing $D\boldsymbol{F}$ is

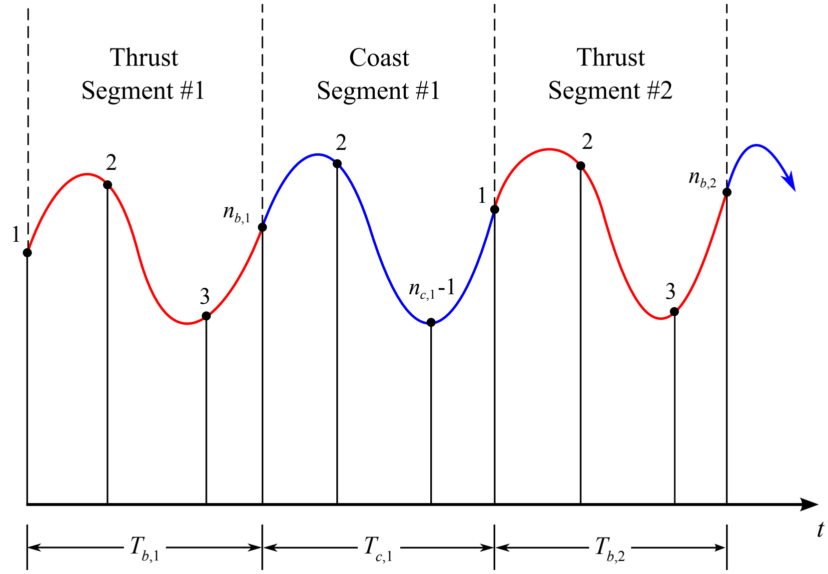

Figure 3.3. Thrust-Coast Problem Structure.

also more tractable, since now all the constraints do not depend on single variables representing $T_{b,j}$ and $m_{0,j}$, or $T_{c,j}$. Manipulating the dependencies in this way can impact the structure of $D\boldsymbol{F}$ considerably, and may mean the difference between an algorithm that requires a few seconds to complete versus one that terminates only after many hours.

Constraints are also imposed on each arc. To ensure that $T_{b,j}$ and $T_{c,j}$ remain nonnegative and that mass is continuous, enforce

$$\begin{aligned} c_{b,j} &= & -T_{b,j} + \nu_{b,j}^2 & \quad = 0, & \text{for } j = 1,..,k \\ c_{c,j} &= & -T_{c,j} + \nu_{c,j}^2 & \quad = 0, & \text{for } j = 1,..,k-1 \\ \psi_{b,j} &= & m_{0,j} - (m_{0,j-1} - T \cdot T_{b,j-1}/(g_0 I_{sp})) & \quad = 0, & \text{for } j = 2,..,k \end{aligned} \tag{3.93}$$

where $\nu_{b,j}$ and $\nu_{c,j}$ are new slack variables introduced into the problem. Equation (3.93) is only applied to the last node segment along each arc, i.e., the variables that appear in equation (3.93) correspond to $\boldsymbol{\mu}_{n_{b,j}-1}$ and $\boldsymbol{\mu}_{n_{c,j}-1}$.

For all the phases, the problem variables and constraints are composed of those from each thrust and coast arc. Therefore, the construction of $\boldsymbol{X}$ and $\boldsymbol{F}$ is the same for all three phases. That is,

$$\boldsymbol{X}^T = \left(\boldsymbol{Y}_{b,1}^T, \boldsymbol{Y}_{c,1}^T, \boldsymbol{Y}_{b,2}^T, \boldsymbol{Y}_{c,2}^T, ..., \boldsymbol{Y}_{b,k}^T, \nu_{b,1}, \nu_{c,1}, \nu_{b,2}, \nu_{c,2}, ..., \nu_{b,k}\right) \tag{3.94}$$

and

$$\begin{aligned} \boldsymbol{F}\left(\boldsymbol{X}\right)^T = \big(&\boldsymbol{G}_{b,1}^T, \boldsymbol{G}_{c,1}^T, \boldsymbol{G}_{b,2}^T, \boldsymbol{G}_{c,2}^T, ..., \boldsymbol{G}_{b,k}^T, c_{b,1}, c_{c,1}, c_{b,2}, c_{c,2}, ..., c_{b,k}, \\ &\psi_{b,2}, \psi_{b,3}, ..., \psi_{b,k}\big) \end{aligned} \tag{3.95}$$

where the vectors $\boldsymbol{Y}_{b,j}$ and $\boldsymbol{Y}_{c,j}$ are comprised of the variables for the thrust and coast arcs, respectively. Similarly, the constraint vectors for each arc are $\boldsymbol{G}_{b,j}$ and $\boldsymbol{G}_{c,j}$. That is,

$$\begin{aligned} \boldsymbol{Y}_{b,j}^T &= \Big(\boldsymbol{x}_1^T, \boldsymbol{u}_1^T, \boldsymbol{x}_{1,2}^T, \boldsymbol{x}_{1,3}^T, \boldsymbol{\mu}_1^T, \boldsymbol{x}_2^T, \boldsymbol{u}_2^T, \boldsymbol{x}_{2,2}^T, \boldsymbol{x}_{2,3}^T, \boldsymbol{\mu}_2^T, ..., \boldsymbol{x}_{n_{b,j}}^T, \boldsymbol{u}_{n_{b,j}}^T, \\ &\qquad \boldsymbol{\eta}_1^T, \boldsymbol{\eta}_{1,2}^T, \boldsymbol{\eta}_{1,3}^T, \boldsymbol{\eta}_2^T, \boldsymbol{\eta}_{2,2}^T, \boldsymbol{\eta}_{2,3}^T, ..., \boldsymbol{\eta}_{n_{b,j}}^T\Big) \\ \boldsymbol{Y}_{c,j}^T &= \Big(\boldsymbol{x}_{1,2}^T, \boldsymbol{x}_{1,3}^T, \boldsymbol{\mu}_1^T, \boldsymbol{x}_2^T, \boldsymbol{x}_{2,2}^T, \boldsymbol{x}_{2,3}^T, \boldsymbol{\mu}_2^T, \boldsymbol{x}_3^T, ..., \boldsymbol{x}_{n_{c,j}-1,2}^T, \boldsymbol{x}_{n_{c,j}-1,3}^T, \boldsymbol{\mu}_{n_{c,j}-1}^T, \\ &\qquad \boldsymbol{\eta}_{1,2}^T, \boldsymbol{\eta}_{1,3}^T, \boldsymbol{\eta}_2^T, \boldsymbol{\eta}_{2,2}^T, \boldsymbol{\eta}_{2,3}^T, \boldsymbol{\eta}_3^T, ..., \boldsymbol{\eta}_{n_{c,j}-1,2}^T, \boldsymbol{\eta}_{n_{c,j}-1,3}^T\Big) \\ \boldsymbol{G}_{b,j}^T &= \Big(\boldsymbol{\Delta}_{1,1}^T, \boldsymbol{\Delta}_{1,c}^T, \boldsymbol{\Delta}_{1,4}^T, ..., \boldsymbol{\Delta}_{n_{b,j}-1,1}^T, \boldsymbol{\Delta}_{n_{b,j}-1,c}^T, \boldsymbol{\Delta}_{n_{b,j}-1,4}^T, \boldsymbol{h}_1^T, \boldsymbol{h}_2^T, ..., \boldsymbol{h}_l^T, \\ &\qquad \boldsymbol{g}_1^T, \boldsymbol{g}_{1,2}^T, \boldsymbol{g}_{1,3}^T, \boldsymbol{g}_2^T, \boldsymbol{g}_{2,2}^T, \boldsymbol{g}_{2,3}^T, ..., \boldsymbol{g}_n^T\Big) \\ \boldsymbol{G}_{c,j}^T &= \Big(\boldsymbol{\Delta}_{1,1}^T, \boldsymbol{\Delta}_{1,c}^T, \boldsymbol{\Delta}_{1,4}^T, ..., \boldsymbol{\Delta}_{n_{c,j}-1,1}^T, \boldsymbol{\Delta}_{n_{c,j}-1,c}^T, \boldsymbol{\Delta}_{n_{c,j}-1,4}^T, \boldsymbol{h}_1^T, \boldsymbol{h}_2^T, ..., \boldsymbol{h}_l^T, \\ &\qquad \boldsymbol{g}_{1,2}^T, \boldsymbol{g}_{1,3}^T, \boldsymbol{g}_2^T, \boldsymbol{g}_{2,2}^T, \boldsymbol{g}_{2,3}^T, \boldsymbol{g}_3^T, ..., \boldsymbol{g}_{n_c-1,2}^T, \boldsymbol{g}_{n_c-1,3}^T\Big) \end{aligned} \tag{3.96}$$

The vectors $\boldsymbol{g}_i$, $\boldsymbol{g}_{i,2}$, and $\boldsymbol{g}_{i,3}$ represent possible path constraints imposed on the trajectory, and the associated slack variables are $\boldsymbol{\eta}_i$, $\boldsymbol{\eta}_{i,2}$, and $\boldsymbol{\eta}_{i,3}$. Notice that the variables in $\boldsymbol{Y}_{c,j}$ begin and end at *internal points* along the node segment since the shared endpoint nodes are already included in $\boldsymbol{Y}_{b,j}$. Note also that $\boldsymbol{G}_{b,j}$ depends exclusively on $\boldsymbol{Y}_{b,j}$, whereas $\boldsymbol{G}_{c,j}$ depends on $\boldsymbol{Y}_{c,j}$ and also the shared node states between adjacent thrust arcs.

3.5.3 Optimization via Nonlinear Programming

After a thorough exploration of the feasible design space, *extremal* solutions are often desired. Obtaining a general extremal trajectory implies the minimization of an objective function of the design variables. This problem can succinctly be posed as

$$\begin{aligned} &\text{Min } J = F_0(\boldsymbol{X}) \\ &\text{subject to } \boldsymbol{F}(\boldsymbol{X}) = \boldsymbol{0} \end{aligned} \tag{3.97}$$

The problem is still solved with equation (3.2). However, now α_d and $\boldsymbol{S}$ must direct $\boldsymbol{X}^{j+1}$ to detect the convex, stationary point associated with the cost function, in addition to satisfying the nonlinear constraints. This type of problem is a nonlinear programming problem (NLP), and there are many approaches that produce solutions. In general, however, this parameter optimization formulation does not explicitly involve the Euler-Lagrange constraints and, hence, the objective function is directly minimized without resorting to costate differential equations. It can be demonstrated, however, that the result of the direct method implicitly satisfies the Euler-Lagrange equations. [83]

One NLP technique is sequential quadratic programming (SQP). This process first uses minor iterations for constructing $\boldsymbol{S}$, and then major iterations with equation (3.2). The minor iterations involve solving a quadratic programming (QP) sub-problem. The constraints associated with this QP sub-problem involve linearization of the elements of $\boldsymbol{F}(\boldsymbol{X})$, and the objective function of the sub-problem is a quadratic approximation to the Lagrangian function. The sub-problem is posed as

$$\begin{aligned} &\text{Min } Q\left(\boldsymbol{S}^q\right) = F_0(\boldsymbol{X}^j) + DF_0\left(\boldsymbol{X}^j\right)\boldsymbol{S}^q + \tfrac{1}{2}\boldsymbol{S}^{q^T}\mathbf{G}\boldsymbol{S}^q \\ &\text{subject to } D\boldsymbol{F}\left(\boldsymbol{X}^j\right)\boldsymbol{S}^q + \beta_d\boldsymbol{F}\left(\boldsymbol{X}^j\right) = \boldsymbol{0} \end{aligned} \tag{3.98}$$

Here, q is the minor iteration number, $\mathbf{G}$ is a positive-definite matrix that approaches the Hessian of the Lagrangian during an iterative procedure, and the scalar β_d is a problem-dependent parameter, where typically $0 < \beta_d \leq 1$. Once $\boldsymbol{S}$ is obtained from the QP sub-problem, the major iterations determine α_d from a one-dimensional search on the first-order conditions. (For full details on an SQP algorithm, see Gill et al. [40])

Almost all of the necessary ingredients for the direct transcription process are available from the formulation of the preceding feasible solution. In fact, the only additional information required is the set of relationships for $F_0(\boldsymbol{X})$ and $DF_0(\boldsymbol{X})$. For most NLP algorithms to solve the direct transcription procedure, including SQP, this first-order information is sufficient. Hence, direct transcription is a natural design transition from the feasible solution method using collocation. As with the approach to produce the feasible solution, the efficient handling of the often large, sparse Jacobian matrix $D\boldsymbol{F}$ is crucial. The general-purpose NLP software package SNOPT is one useful tool to solve such problems, while also exploiting the sparse Jacobian matrix structure for economical computation. [40] The NLP problem is also continually re-solved during nodal refinement iterations to converge upon a desired integration error tolerance, while maintaining an optimal solution. [84]

3.5.4 Multi-Phase Optimization

The solution for a feasible or an optimal trajectory may also involve multiple phases as part of one large corrections process. For example, the design of a solar electric propulsion pole-sitter mission might involve several transfer phases in addition to the coverage orbit phase. Furthermore, there is no requirement that a given phase possess the same system model as another phase. By considering a combination of the problem into one large process, the functional dependencies of all phases can be considered in the optimization of a single phase while at the same time satisfying all of the constraints. Returning to the electric propulsion pole-sitter example, this implies that if a maximum time-of-flight for the coverage orbit is the optimization objective, then the transcription process is capable of saving fuel in the transfer phases and expending that fuel instead during the orbit for additional flight time. This example, which will be explored throughout this investigation, highlights how the multi-phase problem formulation is capable of further improving the value of an optimization objective. For numerical efficiency, the phases are initially assumed to be independent, and boundary conditions are required to ensure (i) that the states, parameters, and/or controls match user-specified values at the beginning and end of the complete trajectory, and (ii) that there exists state, parameter, and control continuity at the interface between each phase. Dependency between the phases is established by requirement (ii). These boundary conditions are straightforward to formulate, and comprise the constraint vector $\boldsymbol{F}_{\mathrm{BC}}$. Then, to solve the larger collocation problem for K phases, the variable vector becomes

$$\boldsymbol{X}^T = \left(\boldsymbol{X}_1^T, \boldsymbol{X}_2^T, ..., \boldsymbol{X}_K^T\right) \tag{3.99}$$

The respective constraints of the problem simply "stack" in similar fashion, and the entire constraint vector is

$$\boldsymbol{F}^T = \left(\boldsymbol{F}_1^T, \boldsymbol{F}_2^T, ..., \boldsymbol{F}_K^T, \boldsymbol{F}_{\mathrm{BC}}^T\right) \tag{3.100}$$

Since the phases are initially assumed to be independent, the Jacobian matrix is block diagonal, composed of the Jacobian sub-matrices for each phase and the highly sparse matrix $D\boldsymbol{F}_{\mathrm{BC}}(\boldsymbol{X})$. Thus, $D\boldsymbol{F}(\boldsymbol{X})$ is easily constructed by inserting the sub-matrices $D\boldsymbol{F}_1(\boldsymbol{X}_1), D\boldsymbol{F}_2(\boldsymbol{X}_2), ..., D\boldsymbol{F}_K(\boldsymbol{X}_K)$ into the appropriate locations, and computing $D\boldsymbol{F}_{\mathrm{BC}}(\boldsymbol{X})$. The resulting block diagonal $D\boldsymbol{F}(\boldsymbol{X})$ is extremely sparse, since each sub-matrix is also sparse.

A feasible solution is still calculated with equation (3.2) and equation (3.11) using equation (3.99) and equation (3.100), or with nonlinear equation solving packages. Depending on the problem sensitivity, quadratic convergence in the Newton and minimum-norm schemes can be sacrificed by reducing the step length α_d as necessary, however, α_d is typically reset to one to regain the quadratic rate when entering the basin of attraction. (The nonlinear equation solver packages will automate this procedure.) A feasible solution serves as an initial guess for the optimization procedure with NLP software, and a performance index composed of variables from any phase j may be minimized, i.e.

$$\text{Min } F_0(\boldsymbol{X}_j) \tag{3.101}$$

subject to the equality constraints in equation (3.100).

3.5.5 Mesh Refinement

An optimal mesh (1) equally distributes the error associated with each segment, and (2) reduces the equally distributed error below a user-specified tolerance. Therefore, mesh refinement is based on an error analysis between the actual and approximate polynomial solutions. The previously described Gauss-Lobatto scheme possesses an order of accuracy equal to 12. Since the order of the method is greater than eight (one more than the degree), the error for the i^{th} segment is

$$e_i = C\Delta t_i^8 \left\|\boldsymbol{x}^{(8)}\right\|_i + O(\Delta t_i^9) \tag{3.102}$$

where $\boldsymbol{x}^{(8)}$ is the eighth time derivative of $\boldsymbol{x}$. Using the analysis presented in the Appendix from Russell and Christiansen, [85] the constant C (dimensionless) for the 7^{th}-degree Gauss-Lobatto scheme is

$$C = 2.93579395141895\text{d-}9 \tag{3.103}$$

In general, $\boldsymbol{x}^{(8)}$ is unknown. In fact, using the 7^{th}-degree polynomial representation in equation (3.77), $\boldsymbol{x}^{(8)} = \boldsymbol{0}$. De Boor [86] circumnavigates this potential problem by approximating $||\boldsymbol{x}^{(8)}||$ with the piecewise constant function $\boldsymbol{x}^{(7)}(\tau)$ and a difference formula. From de Boor

$$||\boldsymbol{x}^{(8)}|| \approx \theta_\Pi(t) \triangleq \begin{cases} \max\left[2\dfrac{|\boldsymbol{y}_1 - \boldsymbol{y}_2|}{\Delta t_1 + \Delta t_2}\right] & , \text{ on } (t_1, t_2) \\ \max\left[\dfrac{|\boldsymbol{y}_{i-1} - \boldsymbol{y}_i|}{\Delta t_{i-1} + \Delta t_i} + \dfrac{|\boldsymbol{y}_{i+1} - \boldsymbol{y}_{i+2}|}{\Delta t_{i+1} + \Delta t_{i+2}}\right] & , \text{ on } (t_i, t_{i+1}),\ i = 2, ..., n-2 \\ \max\left[2\dfrac{|\boldsymbol{y}_{n-2} - \boldsymbol{y}_{n-1}|}{\Delta t_{n-2} + \Delta t_{n-1}}\right] & , \text{ on } (t_{n-1}, t_n) \end{cases} \tag{3.104}$$

where

$$\begin{aligned} \boldsymbol{y}_i &= \boldsymbol{x}^{(7)}(\tau)/\Delta t_i^7 \qquad \text{on } (t_i, t_{i+1}) \\ &= 7!\ \left\{\boldsymbol{x}_i \quad \boldsymbol{x}'_i \quad \boldsymbol{x}_{i,2} \quad \boldsymbol{x}'_{i,2} \quad \boldsymbol{x}_{i,3} \quad \boldsymbol{x}'_{i,3} \quad \boldsymbol{x}_{i+1} \quad \boldsymbol{x}'_{i+1}\right\} \times \boldsymbol{b}/\Delta t_i^7 \end{aligned} \tag{3.105}$$

The vector $\boldsymbol{b}$ in equation (3.105) is the last column of $\mathbf{B}^{-1}$.

Equidistribution

A potential solution that satisfies the problem constraints may have widely varying error Δe_i for the initial mesh Π. The function $\theta_\Pi(t)$ can be used to determine a new mesh that asymptotically equidistributes the error. The new mesh points are selected such that

$$t_{i+1} = I^{-1}\left[\frac{iI(t_n)}{n-1}\right],\ i = 1, ..., n-2 \tag{3.106}$$

where

$$I(t) = \int_{t_1}^{t} \theta_\Pi(s)^{1/8} ds \tag{3.107}$$

Since $\theta_\Pi(t)$ is a piecewise constant function, the integral $I(t)$ is a monotonically increasing piecewise linear function and can easily be determined using a rectangle rule. In equation (3.106), I^{-1} represents the inverse integral, and the process reduces to solving for t where $I(t)$ takes the value in the argument. Given the new mesh, the polynomial expressions are used to interpolate the state variables associated with the new times. Interpolating the new state variables minimizes the constraint violation introduced from the new mesh. The slack variables are selected such that the path constraints are initially satisfied. A new solution with a better equidistribution of error is then computed with Newton's method. The process repeats until the error is equally distributed and within a specified tolerance.

Meeting an Integration Tolerance

Given a specified number of nodes n, generally one equidistribution iteration sufficiently distributes the error. If the error has been sufficiently equidistributed, the number of nodes is updated with

$$n = \left(\frac{\bar{e}}{\epsilon/10} \right)^{1/8} \tag{3.108}$$

The variable $\bar{e}$ represents the mean error associated with the equidistributed mesh ($\bar{e} \approx \Delta e_i$). The user-defined tolerance is ϵ. Equation (3.108) determines the number of nodes required such that the error will reach an order of magnitude less than the specified tolerance. Given the new number of nodes n, a new mesh Π is then constructed with equation (3.106). Again, the state variables for the mesh are interpolated from the polynomial and slack variables are computed that initially satisfy the path constraints. The approximation is re-converged with a Newton's method, minimum norm, or nonlinear equation solving procedure for feasible solutions or NLP software for optimization. A series of equidistribution iterations brings the maximum error (and, therefore, also the maximum difference in error) below ϵ. In summary, the algorithm runs as follows:

1. Obtain an initial guess $\boldsymbol{X}$ and Π.
2. Update $\boldsymbol{X}$ until either:
    a. $\boldsymbol{F}(\boldsymbol{X}) = \boldsymbol{0}$ using Newton's method or a nonlinear equation solving package for a feasible solution, or
    b. $\boldsymbol{F}(\boldsymbol{X}) = \boldsymbol{0}$ and F_0 is minimized using NLP software for an optimal solution.
3. Update Π consistent with equation (3.106) and construct the new $\boldsymbol{X}$.
4. Repeat 2-3 until the error is approximately equidistributed (start with 2, end with 2).
5. Update n using equation (3.108).

6. Repeat 2-3 until the error is below ϵ (start with 3, end with 2).

The process usually requires only a few refinements to meet the desired tolerance.

4. DESIGN AND SELECTION OF COVERAGE ORBITS

The end-to-end trajectory design and optimization of low-thrust, lunar south pole coverage missions begins with the design and selection of a coverage orbit. The design process initially involves a thorough exploration of many different types of orbits that are capable of providing continuous communications to a lunar ground station. This rapid generation and exploration process is decoupled from an explicit optimization objective, and is especially useful because a large body of candidate solutions are investigated even in the presence of changing optimization goals. After extensive design and investigation of the coverage orbits, four possible orbit types have emerged: two-body lunar frozen orbits, Earth-moon L_1 and L_2 libration point orbits, and pole sitter orbits with either a solar sail or solar electric propulsion. The first two orbit classes have been largely explored elsewhere, but brief summaries are warranted for completeness. The novel pole-sitter orbits are explored in detail, and are achievable with an efficient means of propulsion. Given that only small thrust magnitudes are available for maintaining a long-duration pole-sitter, however, locating an accessible region for continuous coverage requires the exploitation of the RTBP "gravity wells" near the Earth-moon L_1 and L_2 points, as detailed in Section 2.5. With little intuition other than this accessible region for the pole-sitter, a crude initial guess is adjusted into an optimized coverage orbit with the collocation and direct transcription approach. The solar sail pole-sitters serve as a long-duration option for lunar coverage, and are immediately transitioned and validated within a higher-fidelity model. Near-optimal solutions in terms of minimum elevation angle performance are also generated. The solar electric propulsion option is a temporary solution due to fuel limitations, and therefore the trajectory development in this chapter is dedicated only to obtaining a preliminary orbit. In later chapters, the solar electric propulsion pole-sitter orbit is combined with the transfer phases as part of a larger optimization problem to maximize the time-of-flight for lunar surveillance. Each orbit option ultimately exhibits several advantages and disadvantages for a potential lunar south pole coverage mission, therefore a qualitative summary of the options is provided.

4.1 Lunar Frozen Orbits

The type of orbit originally conceived for a lunar south pole coverage mission is the lunar frozen orbit and has been thoroughly explored by Ely et al., [47,48] Folta et al., [49] as well as Elipe. [87] While these orbits are not explored in this work, they are briefly mentioned to allow context for the various orbit options that follow. According to Prado, [88] the conditions that produce a lunar frozen orbit require a selection of lunar orbital elements for the values of argument of periapse, $\omega_{\leftmoon}$, inclination, $i_{\leftmoon}$, and eccentricity, $e_{\leftmoon}$, such that

$$\frac{de_{\leftmoon}}{dt} = \frac{di_{\leftmoon}}{dt} = \frac{d\omega_{\leftmoon}}{dt} = 0 \tag{4.1}$$

in the traditional third-body perturbing problem. Here, $da_{\leftmoon}/dt = 0$ is already true, and a detailed analysis on a double-averaged form of Lagrange's planetary equations reveals that the following conditions

$$\sin 2\omega_{\leftmoon} = 0 \quad \text{and} \quad e_{\leftmoon}^2 + \frac{5}{3}\cos^2 i_{\leftmoon} = 1 \tag{4.2}$$

satisfy equation (4.1). Thus, the conditions of interest for lunar frozen orbits occur when $\omega_{\leftmoon} = 90°$, $e_{\leftmoon} = 0.6$, and $i_{\leftmoon} = 56.2°$. While these conditions are not precisely satisfied in higher-order models, they exhibit acceptable bounded behavior with no fuel expenditure in simulations for up to 10 years using a low-altitude orbit with $a_{\leftmoon} = 15,000$ km. [50] The low-altitudes, however, imply that line-of-site losses occur frequently enough to necessitate two or three spacecraft to ensure continuous coverage of the lunar south pole. The required inclinations also limit the maximum elevation angle performance of the spacecraft with respect to the lunar horizon. (The current simulations indicate that at least one spacecraft remains above 15° at all times.) This need for multiple spacecraft, the relatively low elevation angles, as well as the difficulties of departing these stable orbits has motivated the exploration of the additional orbit options. For further detail on this frozen orbit option for lunar coverage, see [47–50].

4.2 Libration Point Orbits

Additional lunar south pole coverage orbit options for continuous communications emerge from exploiting the properties of the lower-fidelity, RTBP model. Families of orbits are available with maximum lunar altitudes on the order of 60,000-100,000 km. In the RTBP, these orbits share the common symmetry of a perpendicular crossing with the $\hat{x}$-$\hat{z}$ plane, and therefore the shooting algorithm applied in Section 3.3.3 is immediately employed. The maximum altitude bound of 100,000 km from the ground site is assumed as a communications instrument constraint; a minimum bound of 50 km is selected arbitrarily to avoid a subsurface arc. Orbits that are within the acceptable altitude ranges from the L_1 and L_2 southern halo orbit families appear in the MCR frame in Figure 4.1. [51], [89] The halo orbits (a term first coined by Farquhar [90]), bifurcate from both the L_1 and L_2 Lyapunov family of planar orbits, and resemble a halo-like shape about the moon when viewed from the Earth in the rotating frame. The orbits are particularly effective in the lunar south pole coverage problem since the motion is almost always within line-of-of sight to the Earth due to the periodicity within the rotating frame, and the orbits maintain large maximum elevation angles with respect to the lunar horizon. (The best configurations result in at least one spacecraft remaining 65° above the horizon at all times, in contrast with only 15° for the lunar frozen orbits.) The family is composed of halo orbits, with a shape that resembles the traditional “halo”, as well as highly “elliptic”, near-rectilinear orbits with passage very close to the moon’s surface. For almost the entire period of motion, a spacecraft in any near-rectilinear halo orbit possesses a line-of-sight to the lunar south pole. The halo orbit families have been thoroughly investigated by Farquhar, [90], Breakwell and Brown, [91], Howell, [92], and Gómez et al. [93] imum elevation angles with respect to the lunar horizon. (The best configurations result in at least one spacecraft remaining 65° above the horizon at all times, in contrast with only 15° for the lunar frozen orbits.) The family is composed of halo orbits, with a shape that resembles the traditional "halo", as well as highly "elliptic", near-rectilinear orbits with passage very close to the moon's surface. For almost the entire period of motion, a spacecraft in any near-rectilinear halo orbit possesses a line-of-sight to the lunar south pole. The halo orbit families have been thoroughly investigated by Farquhar, [90], Breakwell and Brown, [91], Howell, [92], and Gómez et al. [93]

Members of the southern L_1 and L_2 vertical orbit family are depicted in Figure 4.2. The motion consists of a doubly symmetric, "figure-8" shaped pattern when viewed in the $\hat{y}$-$\hat{z}$ plane. These orbits occur near the libration points. The existence of the orbits was predicted by Moulton in 1920, [94] and they have also been studied recently by Dichmann et al. [95] Large amplitude L_1 vertical orbits terminate when they become exactly vertical, while large amplitude L_2 vertical orbits encompass both primaries (although these trajectories are not included due to the mission constraints). The orbits also possess the characteristic of bending toward both the north and south poles of the moon, a favorable trait for maintaining line-of-sight over a pole. An additional family also includes orbits that remain in view of the lunar south pole for significant intervals of time. Some of these orbits possess characteristics similar to the near-rectilinear halo orbits. The orbits bifurcate from a 6-day near-rectilinear L_2 halo orbit and might be described in terms of a "butterfly" shape. (See Figure 4.3). Comparable motions around the smaller primary have been documented by Robin and Markellos. [96] Similar to vertical orbits, the motion in a butterfly orbit resembles a"figure-8" shape, however, these orbits wrap around both the near- and far-side of the moon, such that a direct line-of-sight to the lunar south pole exists for nearly the entire orbital period.

The time to complete one full period is used as a design parameter for orbit selection to be applied in the coverage problem using libration point orbits. Let the maximum excursion distance along the rotating x-axis identify a particular orbit, i.e., the maximum $|x_m|$ value along an orbit. In Figure 4.4, orbital periods are plotted against maximum excursion distance during initial design selection. Commensurate orbits are sought to phase multiple spacecraft for complete line-of-sight coverage. One such region might consist of orbits in L_1 and L_2 halo families sharing periods between 7.9 and 12.2 days. An example that exhibits feasible south pole coverage is a 12-day L_1 and 12-day L_2 halo orbit combination, illustrated by the black dashed line in Figure 4.4. Another region with commensurate combinations consists of orbits with a ratio of periods equal to 2:1, that is, one period is exactly twice that of the other. Note that L_2 halo orbits with periods between 6.0 and 7.2 days exhibit this behavior with the entire L_2 butterfly orbit family. This is not actually surprising when the shapes of the orbits are viewed in Figure 4.1 and Figure 4.3. An example from this region consists of a 14-day L_2 butterfly orbit and a 7-day L_2 halo orbit combination, as noted by the two red dashed lines in Figure 4.4. The information in Figure 4.4 serves as a basis for the determination of many other commensurate orbit combinations that lead to complete south pole coverage. Stability criteria may also play a factor in the selection of the periodic orbits of interest. [51]

Once two libration point orbits of given periods are selected, they are phased accordingly to maximize the out-of-plane distance $|z_m|$ *below* the Earth-moon fundamental plane such that at least one spacecraft maintains line-of-sight, i.e., to maintain 100% line-of-sight and minimize the maximimum value of $z_m - r_{☾}$ over the coverage duration. This design parameter is chosen for avoidance of line-of-sight obstacles such as the lip of a crater, or other geographical terrain. As an example, consider two spacecraft in a single L_1 halo orbit. A typical two-spacecraft coverage scheme is achieved by displacing the motion of each spacecraft by a half-period. Thus, the two spacecraft are then phase-shifted in the L_1 halo orbit with the corresponding z_m displacement of each spacecraft as a function of time appearing in Figure 4.5. The dashed line highlights the z_m value at which the two spacecraft possess a common z_m component but are moving in opposite z_m directions along the orbit. The dashed line in Figure 4.5 demonstrates that the z_m crossing occurs significantly below the fundamental plane, ensuring that at least one spacecraft is always within direct line of sight to the south pole. Due to the symmetry of the RTBP, several points will lie on the dashed line, but the behavior is slightly perturbed when ephemerides and lunar librations are incorporated in higher-fidelity models. While further detailed analysis of these libration point orbit families for lunar coverage is not a central focus of this work, extensive further investigation appears in [51] and [89]. The lower-fidelity, RTBP solutions presented here are easily transitioned to a higher-fidelity model using a multiple shooting algorithm as described in [75]. All of the orbit solutions require stationkeeping propellant, but previous analysis indicates that, among the options investigated for lunar south pole coverage, the total $||\Delta\tilde{\boldsymbol{V}}||$ ranges between 4.82-171.82 m/s per year for each spacecraft. While the expenditure of any $||\Delta\tilde{\boldsymbol{V}}||$ is disadvantageous compared to the lunar frozen orbits, which require none, the instability of the libration point orbits is advantageous for the generation of fuel-efficient transit between orbits. This possibility is explored in the next chapter.

4.3 Solar Sail Pole-Sitter Orbits

With the use of an efficient long-term thrust device, the number of spacecraft for continuous coverage of the lunar south pole can be reduced to just one. These "pole-sitter" orbits require only a low-thrust component of force by exploiting the system properties of the lower-fidelity, RTBP system model. One possible thruster choice that supplies an additional force to produce a long-duration pole-sitter orbit is a solar sail. The current technology readiness level of a solar sail with the acceleration magnitudes required for such a mission is not adequate to exploit all possible orbits. However, sails are in ongoing development and the proposed ranges have been suggested in recent technology demonstration proposals. [24] Many complexities

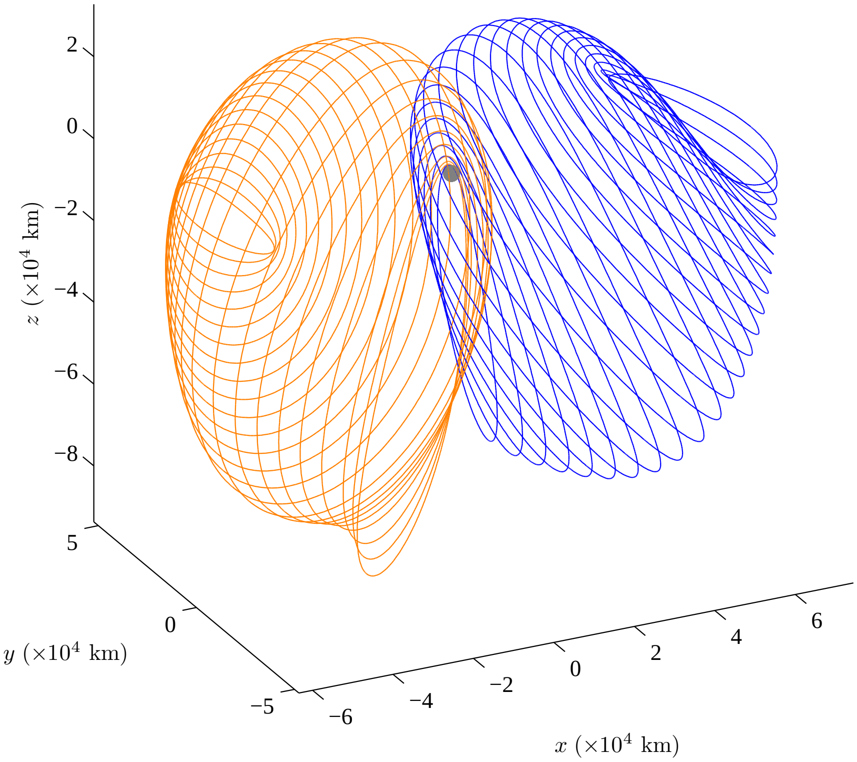

Figure 4.1. Southern Halo Orbit Families, MCR Frame: Earth-Moon L_1 (Orange) and L_2 (Blue).

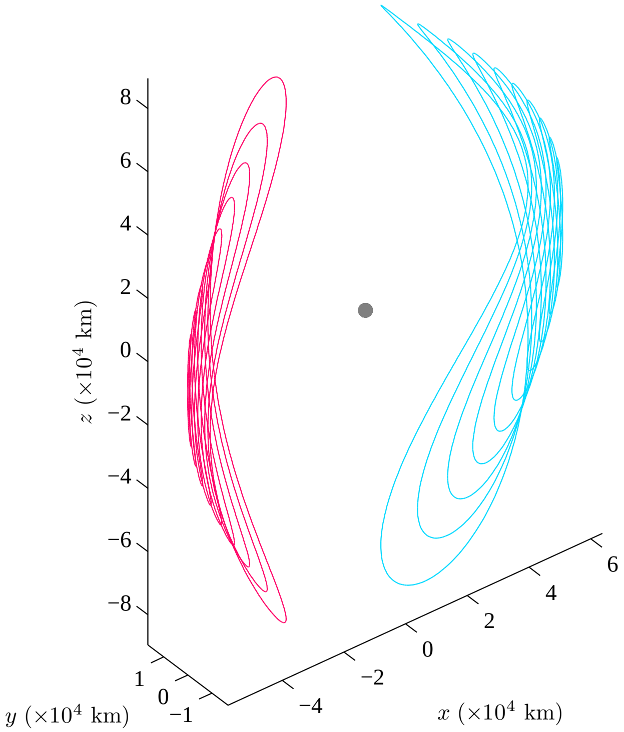

Figure 4.2. Southern Vertical Orbit Families, MCR Frame: Earth-Moon L_1 (Red) and L_2 (Cyan).

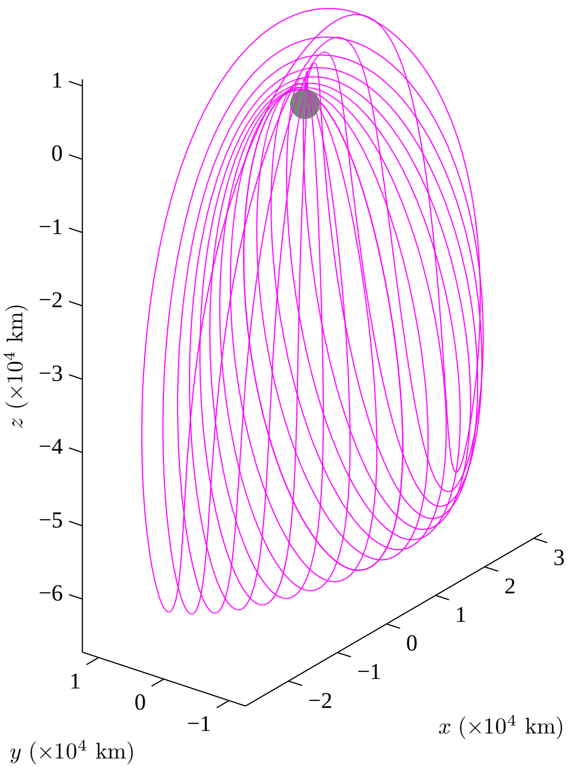

Figure 4.3. Southern L_2 Butterfly Orbit Family, MCR Frame.

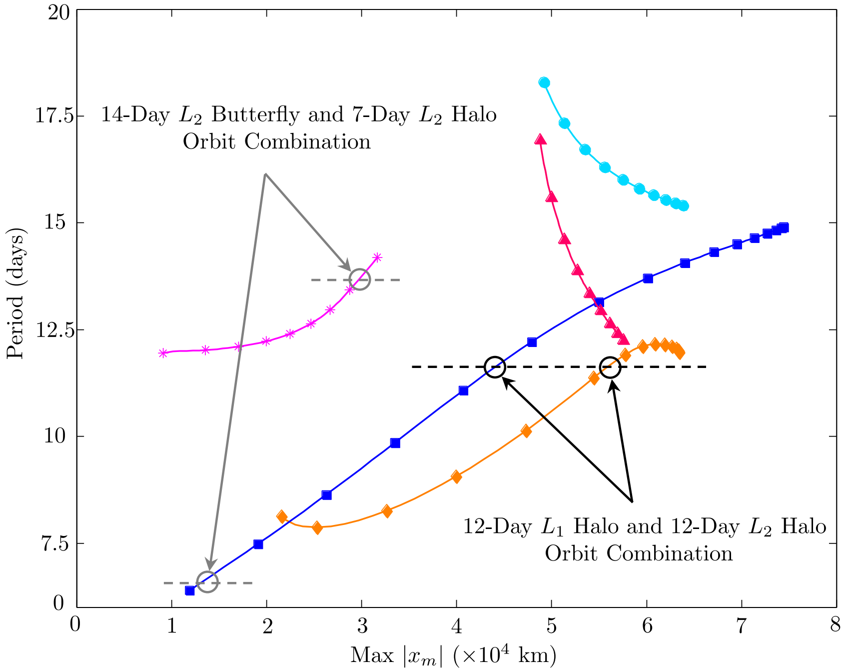

Figure 4.4. Period Versus Maximum x_m Distance from the Moon.

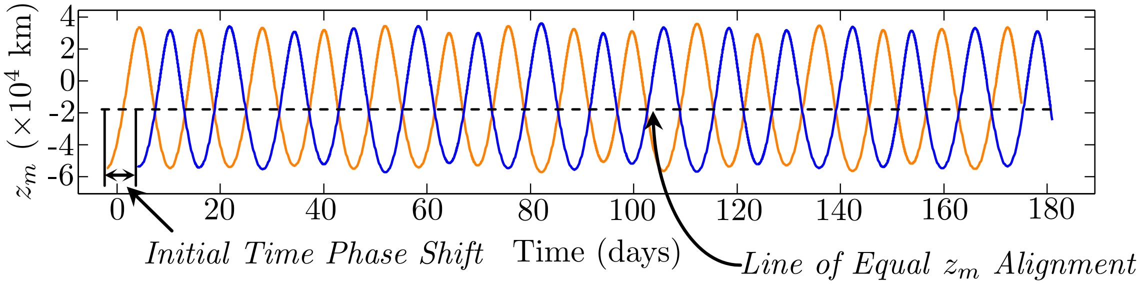

Figure 4.5. Out-of-Plane Displacement, z_m, in the Rotating Frame for Two Spacecraft in 12-day L_1 Halo Orbits.

are involved with actually computing pole-sitter orbits. Little intuition exists for the shape of the orbits or for the corresponding control history that is required to maintain them. Furthermore, the high sensitivity to variations in any initial guess demands robust convergence. There are also many potential methods of measuring performance, so a solution that is decoupled from the optimization of a cost function is initially desired. For these reasons, the collocation approach detailed in Sections 3.5.1-3.5.2 is employed, along with the mesh refinement strategy from Section 3.5.5 using the minimum-norm strategy outlined in Section 3.1. After the solution approach is implemented, optimization is then approached implicitly by adjusting the appropriate path constraint boundaries.

When initially computing the solar sail pole-sitter orbits, the complexity of the problem is reduced by searching for feasible solutions that are singly periodic in the lower-fidelity, RTBP model. Then, due to their ergodic behavior, the solutions are preserved for all time within the model in equation (2.36). These initial periodic orbits occur at periods commensurate with the lunar synodic month. In this analysis, only orbits with periods equal to one lunar synodic month are investigated, although this is not a necessary condition for the existence of periodic solar sail orbits in the Earth-moon RTBP. The periodic orbits are not embedded in families because solutions for the controlled sail are not unique. As a consequence, this study is primarily an investigation of suitable point solutions for several orbits that support lunar south pole coverage. The problem-specific periodicity constraints are introduced, and path constraints amenable for lunar south pole coverage are derived. The collocation method is very robust, converging on periodic solutions when almost no information about the orbit shape or control history is known. Finally, the process is employed to compute many point solutions, but only five near-optimal solutions for lunar south pole coverage are presented. These solutions are then validated in a higher-fidelity model that includes ephemerides, an accurate direction of the incoming sun-to-spacecraft line, and the effects of lunar librations.

4.3.1 Path and Periodicity Constraints for Continuous Coverage in the Lower-Fidelity Model

In addition to the defect constraints, preliminary design of perfectly repeating periodic orbits in the RTBP, with solar sail thrust, are determined with periods equal to one lunar synodic month, or period $\mathbb{P} = 2\pi/\omega_s = 29.64$ days. For the orbits in this investigation, the magnitude of the gravity gradient experienced by the spacecraft remains relatively constant. Therefore, during implementation of the collocation schemes for these orbits, a fixed value of Δt_i is adequate for a given number of nodes n. Then, let $\Delta t_i = \mathbb{P}/\left(n-1\right)$. For a periodic orbit, the initial state and control must equal the final state and control, or

$$\begin{aligned} h_1\left(x_1, x_n\right) &= x_n - x_1 = 0, & h_4\left(v_{x_1}, v_{x_n}\right) &= v_{x_n} - v_{x_1} = 0 \\ h_2\left(y_1, y_n\right) &= y_n - y_1 = 0, & h_5\left(v_{y_1}, v_{y_n}\right) &= v_{y_n} - v_{y_1} = 0 \\ h_3\left(z_1, z_n\right) &= z_n - z_1 = 0, & h_6\left(v_{z_1}, v_{z_n}\right) &= v_{z_n} - v_{z_1} = 0 \end{aligned} \tag{4.3}$$

$$\begin{aligned} h_7\left(u_1^{(1)}, u_n^{(1)}\right) &= u_n^{(1)} - u_1^{(1)} = 0 \\ h_8\left(u_1^{(2)}, u_n^{(2)}\right) &= u_n^{(2)} - u_1^{(2)} = 0 \\ h_9\left(u_1^{(3)}, u_n^{(3)}\right) &= u_n^{(3)} - u_1^{(3)} = 0 \end{aligned} \tag{4.4}$$

where $\boldsymbol{u}_i = \left(u_i^{(1)}, u_i^{(2)}, u_i^{(3)}\right)^T$. These constraints, in addition to the defect constraints and control constraints $\psi_i = 0$ in equation (3.87), are the only constraints necessary for computing periodic orbits with the collocation schemes. The problem dependent parameters $\boldsymbol{\mu}$ appearing in equation (3.90) are unnecessary for this orbit design formulation that employs piecewise linear control.

It is also necessary to apply path constraints that completely confine the spacecraft to a region of phase space. For continuous lunar south pole coverage with only one spacecraft, path constraints are required on the minimum elevation angle ϕ_{lb} and maximum altitude a_{ub} of the spacecraft from the lunar south pole, forming a "bounding cone" beneath the lunar south pole. Ignoring lunar librations, the constraints that accomplish this objective are

$$\begin{aligned}
\boldsymbol{g}_i\left(\boldsymbol{r}_i, \boldsymbol{\eta}_i\right) &= \left\{\begin{matrix} \sin\phi_{lb} + \dfrac{z_i + r_{\leftmoon}}{a_i} \\ a_i - a_{ub} \end{matrix}\right\} + \boldsymbol{\eta}_i^2 = \boldsymbol{0} \\
\boldsymbol{g}_{i,2}\left(\boldsymbol{r}_{i,2}, \boldsymbol{\eta}_{i,2}\right) &= \left\{\begin{matrix} \sin\phi_{lb} + \dfrac{z_{i,2} + r_{\leftmoon}}{a_{i,2}} \\ a_{i,2} - a_{ub} \end{matrix}\right\} + \boldsymbol{\eta}_{i,2}^2 = \boldsymbol{0} \\
\boldsymbol{g}_{i,3}\left(\boldsymbol{r}_{i,3}, \boldsymbol{\eta}_{i,3}\right) &= \left\{\begin{matrix} \sin\phi_{lb} + \dfrac{z_{i,3} + r_{\leftmoon}}{a_{i,3}} \\ a_{i,3} - a_{ub} \end{matrix}\right\} + \boldsymbol{\eta}_{i,3}^2 = \boldsymbol{0}
\end{aligned} \tag{4.5}$$

where $a = \sqrt{(x - 1 + \gamma)^2 + y^2 + \left(z + r_{\leftmoon}\right)^2}$ and recall that $r_{\leftmoon}$ is the non-dimensional mean radius of the moon. (The number of path constraints is, thus, $m = 2$.) The problem is now fully defined. The design variable vector $\boldsymbol{X}$ and constraint vector $\boldsymbol{F}$ can be constructed as indicated in equation (3.90) and equation (3.91).

4.3.2 Solving the System of Nonlinear Equations

A solution $\boldsymbol{X}^{j+1}$ such that $\|\boldsymbol{F}(\boldsymbol{X}^{j+1})\| < \|\boldsymbol{F}(\boldsymbol{X}^{j})\|$ until $\boldsymbol{F}(\boldsymbol{X}) = \boldsymbol{0}$ is required. There are exactly $2n - l + 6$ more free variables than controls, and therefore $D\boldsymbol{F}(\boldsymbol{X}^j)$ is a non-square matrix. As a consequence, there are generally an infinite number of solutions $\boldsymbol{X}^{j+1}$ that satisfy $\boldsymbol{F}$. Rather than satisfying an optimization objective, the minimum-norm update to $\boldsymbol{X}^{j+1}$ detailed in equation (3.11) is employed to locate a solution nearby the initial guess that satisfies the continuous path constraints.

In general, the Jacobian matrix $D\boldsymbol{F}$ is very large and sparse. The general form of $D\boldsymbol{F}$ for the higher-order Gauss-Lobatto method and $l = 0$ appears in Appendix B. Consider a problem with only 100 nodes and with only one path constraint applied to $\boldsymbol{g}_i$, $\boldsymbol{g}_{i,2}$, and $\boldsymbol{g}_{i,3}$ in equation (3.88), i.e., $m = 1$. The length of the design variable vector $\boldsymbol{X}$ is 2,386. If there are no other node constraints ($l = 0$), the length of the corresponding constraint vector $\boldsymbol{F}$ is 2,180. Then the size of $D\boldsymbol{F}$ is $2,180 \times 1,000$. Therefore, $D\boldsymbol{F}$ is a $2,180 \times 2,386$ matrix. Due to the large number of design variables, it is apparent that even these relatively smaller problems (where $n = 100$, $m = 1$, and $l = 0$) require efficient methods for the implementation of equation (3.11). The efficiency of the computation is increased by utilizing the sparseness of $\boldsymbol{DF}$. Recall from equations (3.84)-(3.86) that the $\boldsymbol{\Delta}$ constraints depend only on the adjacent node states and controls, and are independent of all the other node states and controls and also any other variables that appear in equation (3.90). As a result, $\boldsymbol{DF}$ is primarily a block diagonal matrix of non-zero sub-matrices $D\boldsymbol{\Delta}_{i,1}$, $D\boldsymbol{\Delta}_{i,c}$, and $D\boldsymbol{\Delta}_{i,4}$. The sparsity of $\boldsymbol{DF}$ is even more apparent when considering $D\psi_i$, $D\boldsymbol{g}_i$, and Dh_k, all of which only depend on specific node states and/or controls. In fact, there cannot be more than $n\,(60m + 30l + 543) - 24m - 12l - 540$ non-zero entries in $\boldsymbol{DF}$. This implies that for the case when $n = 100$, $m = 1$, and $l = 0$, there exist no more than 1.51% of the total number of entries in $\boldsymbol{DF}$, as demonstrated in Figure 4.6. There are a number of ways to exploit the sparsity to increase efficiency. First, when

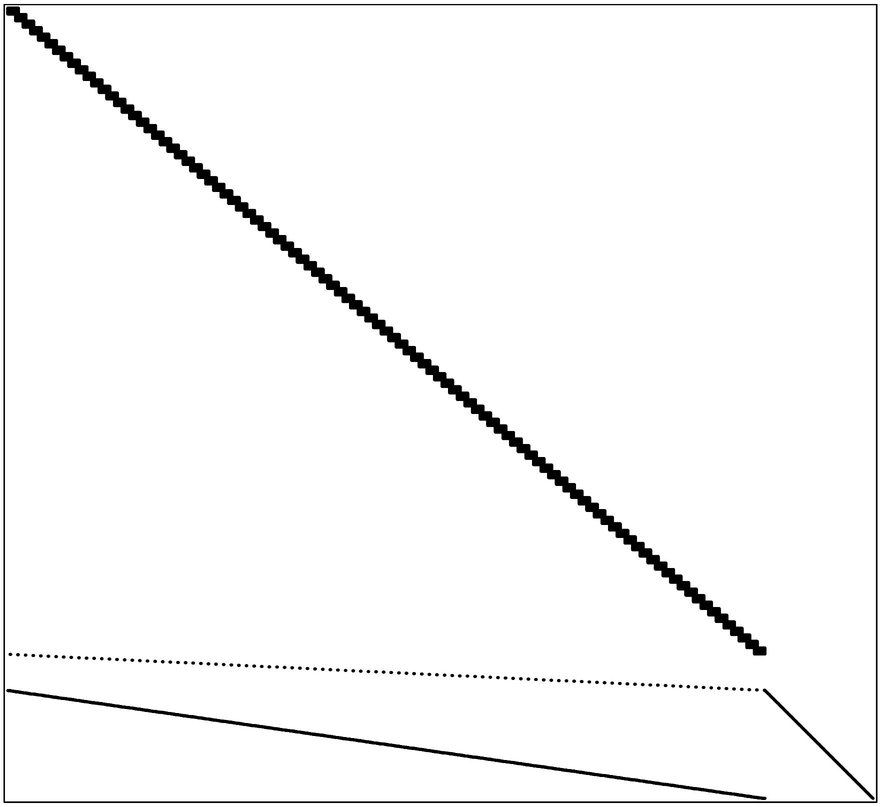

Figure 4.6. Sparse Structure of $\boldsymbol{DF}$ when $n = 100$, $m = 1$, and $l = 0$.

pre-allocating the size of $\boldsymbol{DF}$, memory is only allocated for the maximum number of non-zero entries, and not for all of the zero entries (which can be *very* large). Also, considering the sparsity of $\boldsymbol{DF}$, perhaps the most efficient means of computing $\left[D\boldsymbol{F} \cdot D\boldsymbol{F}^T\right]^{-1} \boldsymbol{F}$ is to use sparse Cholesky factorization. The standard package CHOLMOD is commonly used and appears in MATLAB®. [97] Finally, to avoid the cost of computing derivatives numerically, the non-zero elements in $D\boldsymbol{F}$ are computed analytically whenever tractable. For example, $D\psi_i$, $D\boldsymbol{g}_i$, $D\boldsymbol{g}_{i,2}$, $D\boldsymbol{g}_{i,3}$, and Dh_k are all computed analytically, and their expressions are, in general, straightforward. Unfortunately, the defect derivatives $D\boldsymbol{\Delta}_{i,1}$, $D\boldsymbol{\Delta}_{i,c}$, and $D\boldsymbol{\Delta}_{i,4}$ are already very involved, and cumbersome to compute analytically. In this case, a numerical scheme may be more tractable. For example, consider computing the 6×30 sub-matrix $D\boldsymbol{\Delta}_{i,c}$ with the complex-step method in equation (3.23). If $\boldsymbol{x}_i = \left(x_i^{(1)}, x_i^{(2)}, x_i^{(3)}, x_i^{(4)}, x_i^{(5)}, x_i^{(6)}\right)^T$ and $\boldsymbol{u}_i = \left(u_i^{(1)}, u_i^{(2)}, u_i^{(3)}\right)^T$, then

$$D\boldsymbol{\Delta}_{i,c} = \left(\frac{\partial \boldsymbol{\Delta}_{i,c}}{\partial \boldsymbol{x}_i}, \frac{\partial \boldsymbol{\Delta}_{i,c}}{\partial \boldsymbol{u}_i}, \frac{\partial \boldsymbol{\Delta}_{i,c}}{\partial \boldsymbol{x}_{i,2}}, \frac{\partial \boldsymbol{\Delta}_{i,c}}{\partial \boldsymbol{x}_{i,3}}, \frac{\partial \boldsymbol{\Delta}_{i,c}}{\partial \boldsymbol{x}_{i+1}}, \frac{\partial \boldsymbol{\Delta}_{i,c}}{\partial \boldsymbol{u}_{i+1}}\right) \tag{4.6}$$

where

$$\begin{aligned}
\frac{\partial \boldsymbol{\Delta}_{i,c}}{\partial x_i^{(j)}} &= \frac{\Im\left\{\boldsymbol{\Delta}_{i,c}\left(x_i^{(j)} + \hat{i}h_d\right)\right\}}{h_d}, & \frac{\partial \boldsymbol{\Delta}_{i,c}}{\partial u_i^{(j)}} &= \frac{\Im\left\{\boldsymbol{\Delta}_{i,c}\left(u_i^{(j)} + \hat{i}h_d\right)\right\}}{h_d} \\
\frac{\partial \boldsymbol{\Delta}_{i,c}}{\partial x_{i,2}^{(j)}} &= \frac{\Im\left\{\boldsymbol{\Delta}_{i,c}\left(x_{i,2}^{(j)} + \hat{i}h_d\right)\right\}}{h_d}, & \frac{\partial \boldsymbol{\Delta}_{i,c}}{\partial x_{i,3}^{(j)}} &= \frac{\Im\left\{\boldsymbol{\Delta}_{i,c}\left(x_{i,3}^{(j)} + \hat{i}h_d\right)\right\}}{h_d} \\
\frac{\partial \boldsymbol{\Delta}_{i,c}}{\partial x_{i+1}^{(j)}} &= \frac{\Im\left\{\boldsymbol{\Delta}_{i,c}\left(x_{i+1}^{(j)} + \hat{i}h_d\right)\right\}}{h_d}, & \frac{\partial \boldsymbol{\Delta}_{i,c}}{\partial u_{i+1}^{(j)}} &= \frac{\Im\left\{\boldsymbol{\Delta}_{i,c}\left(u_{i+1}^{(j)} + \hat{i}h_d\right)\right\}}{h_d}
\end{aligned} \tag{4.7}$$

and h_d is chosen as a very small step at, or below, machine precision. Therefore, all the columns of $D\boldsymbol{\Delta}_{i,c}$ in equation (4.6) can be computed using equations (4.7). Note that equations (4.7) are only numerical approximations of the actual partial derivatives $\frac{\partial \boldsymbol{\Delta}_{i,c}}{\partial x_i^{(j)}}$, $\frac{\partial \boldsymbol{\Delta}_{i,c}}{\partial u_i^{(j)}}, \frac{\partial \boldsymbol{\Delta}_{i,c}}{\partial x_{i,2}^{(j)}}, \frac{\partial \boldsymbol{\Delta}_{i,c}}{\partial x_{i,3}^{(j)}}, \frac{\partial \boldsymbol{\Delta}_{i,c}}{\partial x_{i+1}^{(j)}}$, and $\frac{\partial \boldsymbol{\Delta}_{i,c}}{\partial u_{i+1}^{(j)}}$. However, the expressions are written as equalities in equations (4.7) because, while they are only approximations, the full advantages of double-precision accuracy are exploited. Furthermore, recall that unlike the alternative central differencing scheme, it is not necessary to determine an optimal value for h_d.

4.3.3 Near-Optimal Orbits in the Restricted Problem

In computing solar sail pole-sitter orbits, the elevation and altitude constraints are a priority. For this sample scenario, no initial guess is available for $\boldsymbol{X}$, which includes all the node states and controls, slack variables, and additional states and slack variables for internal points. Once the problem formulation of the constraints, free variables, and Jacobian matrix derivatives is completed, the corrections with equation (3.11) (or a nonlinear equation solving package) are very robust with only a few pieces of information necessary to determine an initial guess that converges to a periodic solution. In general, the only information required to generate a converging initial guess is established as follows:

1. Examine Figure 2.4 and approximate a feasible region given a desired characteristic solar sail acceleration κ.
2. Specify desirable values of ϕ_{lb} and a_{ub} that encompass this region.
3. Within the bounds imposed by ϕ_{lb} and a_{ub}, select any set of feasible positions for all the position variables.

It should be noted that the first two steps in the process may be interchanged. For example, another option is to first specify a region of interest with ϕ_{lb} and a_{ub} and then determine the value of κ necessary to maintain the spacecraft within this region. For application in the lower-fidelity, RTBP model, the orbits are initially assumed to be stationary, therefore all the position variables are initially constant and all the velocity variables are always initially set to zero. The initial time is also zero, i.e., $t_1 = 0$. An initial guess for the slack variables is determined by solving for $\boldsymbol{\eta}_i$, $\boldsymbol{\eta}_{i,2}$, and $\boldsymbol{\eta}_{i,3}$ that satisfy equation (3.88).

Initially, for all node points, $\delta = 0°$, and $\alpha = -35.26°$ to maximize the out-of-plane component of sail thrust in the negative z-direction. [98] Then, for an initial guess, the components of $\hat{\boldsymbol{u}}_i$ in the rotating frame can be computed from the angles δ and α in equation (2.32). Except for selecting a realistic value of κ from Figure 2.4, very little information about the natural dynamics is necessary for computing the periodic orbits that satisfy the boundary constraints with this scheme. A control pattern is established for a solution that is close to the initial guess and meets the specified constraints. Given a feasible value of κ and an appropriate number of nodes n, the method generally determines a solution with a smooth control history in less than five iterations of equation (3.11). Difficulties are only encountered when the path constraints that are selected force the spacecraft to a region that is physically impossible to maintain for the given characteristic acceleration κ, implying that, for the bounds selected, a nearby solution does not exist. Using this strategy, many orbits favorable for lunar south pole coverage are easily computed. In fact, the entire process is adapted into a graphical user interface (GUI) tool in MATLAB®. (A screenshot of the tool appears in Figure 4.7.) Using this tool, a user may visually inspect Figure 2.4, specify the path constraints that form the bounding "cone", select a feasible region to place the nodes, and converge an initial guess using the transcription process for feasible solutions in real time. From all the orbits investigated in this process, five orbits of interest are selected from three different regions. (See Figure 4.8.) For comparison, in Figure 4.9 the elevation angle histories for the five orbits are plotted versus time. (Hereafter, the color schemes for the different orbits will remain as defined in Figure 4.8.) Inspection of Figure 2.4 reveals that for the realistic sail $\kappa = 0.58$ mm/s^2, any orbits favorable for lunar south pole coverage will be located just below L_1 and L_2. Positioning the initial guess just below the L_1 and L_2 points, ϕ_{lb} is selected to be as large as physically possible for the characteristic acceleration value $\kappa = 0.58$ mm/s^2. The limiting boundary for feasible trajectories that maintain constant south pole surveillance occurs at elevation angles $\phi_{lb} = 4.2°$ for L_1 and $\phi_{lb} = 6.8°$ for L_2. A sail can reach even greater elevation angles of constant surveillance when the characteristic acceleration κ is slightly increased. For example, when $\kappa = 1.70$ mm/s^2, the limiting boundaries are $\phi_{lb} = 15.8°$ and $\phi_{lb} = 18.8°$ for L_1 and L_2, respectively. In fact, an entirely new type of orbit that appears to "hover" under the lunar south pole, is available for $\kappa = 1.70$ mm/s^2 and this trajectory can be computed from an initial guess just under the lunar south pole. The boundary of feasible solutions for this orbit is $\phi_{lb} = 15.0°$. From these results, and several other orbits investigated, it appears that for constant surveillance of the lunar south pole with a solar sail, a spacecraft near L_2 may yield the highest minimum elevation angle for both $\kappa = 0.58$ mm/s^2 and $\kappa = 1.70$ mm/s^2. Such a conclusion is consistent with Figure 2.4, where the contours corresponding to these characteristic accelerations near L_2 extend further below the x-axis than the L_1 contours. A spacecraft in any one of these orbits also maintains constant line-of-sight with the Earth, since the solar sail orbits are displaced sufficiently far below the x-y plane. The L_2 orbits are in constant view of the far-side of the moon as well, a feature that may be useful for future lunar missions.

The control time histories for the L_2 orbit with $\kappa = 0.58$ mm/s^2 appear in Figure 4.10. For this study, fluctuations in the control are not constrained, but the method is general enough that they could be added. The possible off-nominal accelerations of the sail have not been modeled. Though the system allows the spacecraft to use both sides of the sail, all the orbits investigated only employ one side. For example, from Figure 4.10 it is clear that for the L_2 orbit with $\kappa = 0.58$ mm/s^2, $-90° < \delta < 90°$. Also, since the driving factor in the investigation is ϕ_{lb}, for all computations a_{ub} is set to some arbitrarily large value. For all simulations, the Gauss-Lobatto scheme is employed with the constraints described previously and $n = 100$. This corresponds to a time-step of about 0.3 days or roughly 0.07 nondimensional time units. With the constraints implemented, the sizes of $\boldsymbol{X}$ and $\boldsymbol{F}$ are $2,684$ and $2,487$, respectively. Thus, over 98.6% of the entries in the matrix $D\boldsymbol{F}$ are zero.

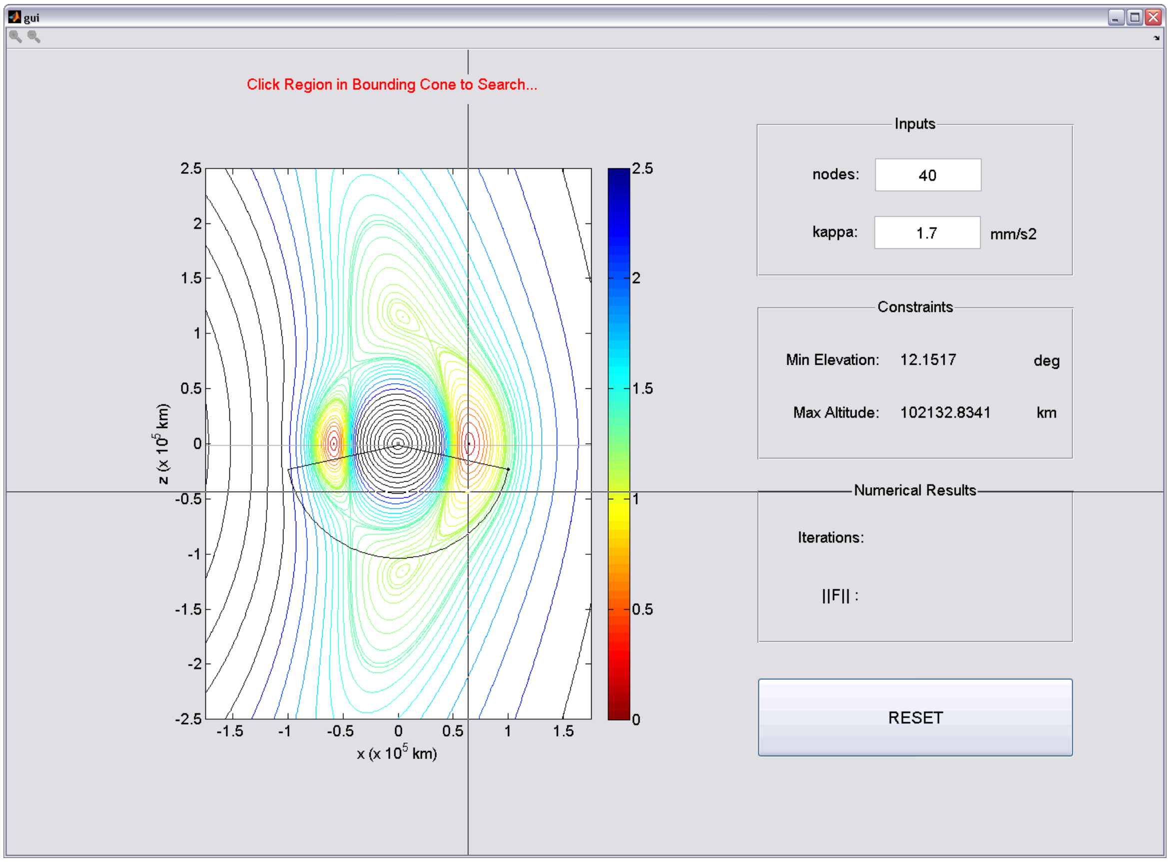

Click Region in Bounding Cone to Search...

Inputs

nodes: 40

kappa: 1.7 mm/s2

Constraints

Min Elevation: 12.1517 deg

Max Altitude: 102132.8341 km

Numerical Results

Iterations:

||F|| :

Figure 4.7. Screenshot of MATLAB® Solar Sail Pole-Sitter Orbit Design GUI.

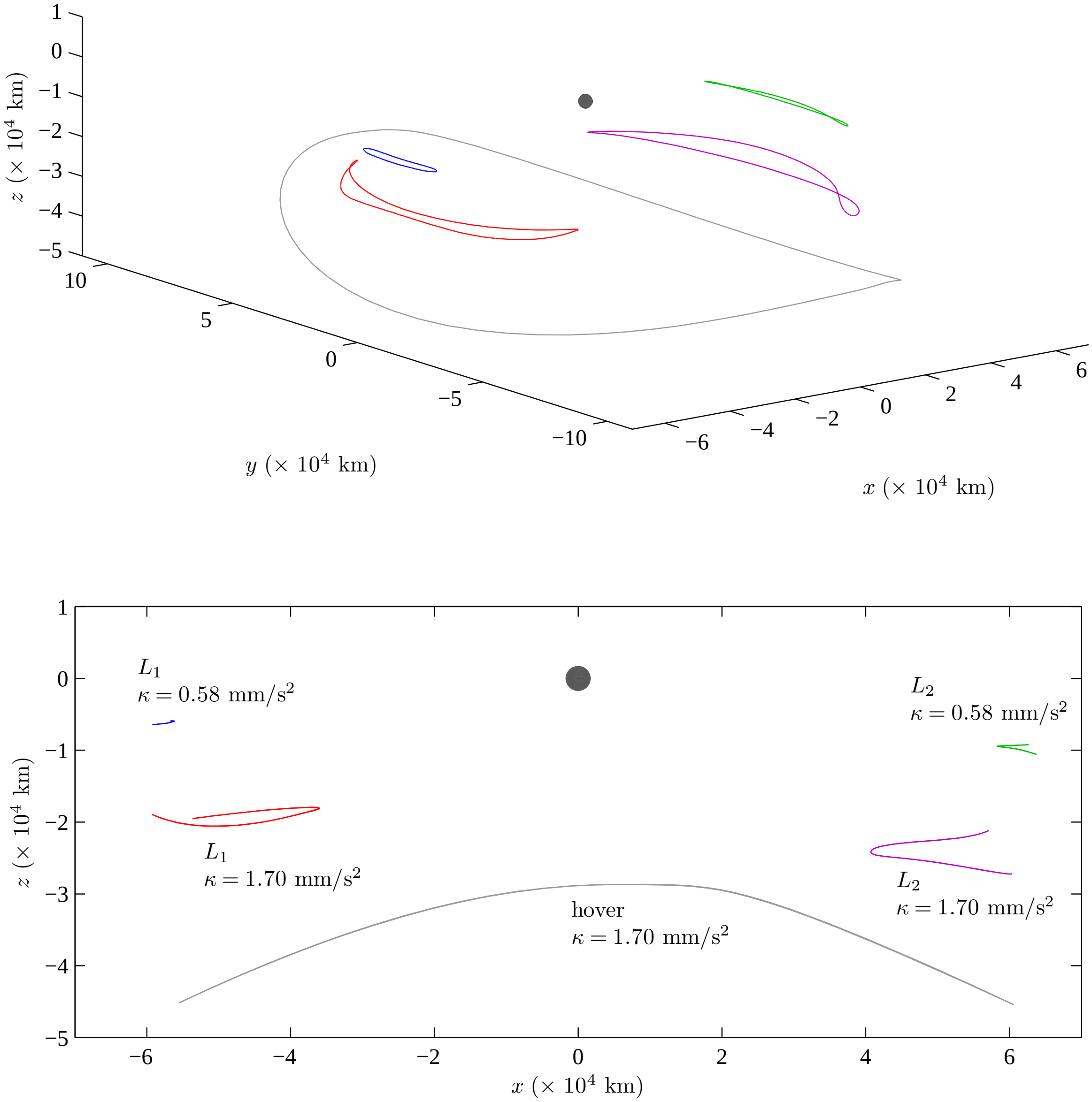

Figure 4.8. Periodic Solar Sail Pole-Sitter Orbits in the Lower-Fidelity Model, MCR Frame (Top) and x-z Projection (Bottom).

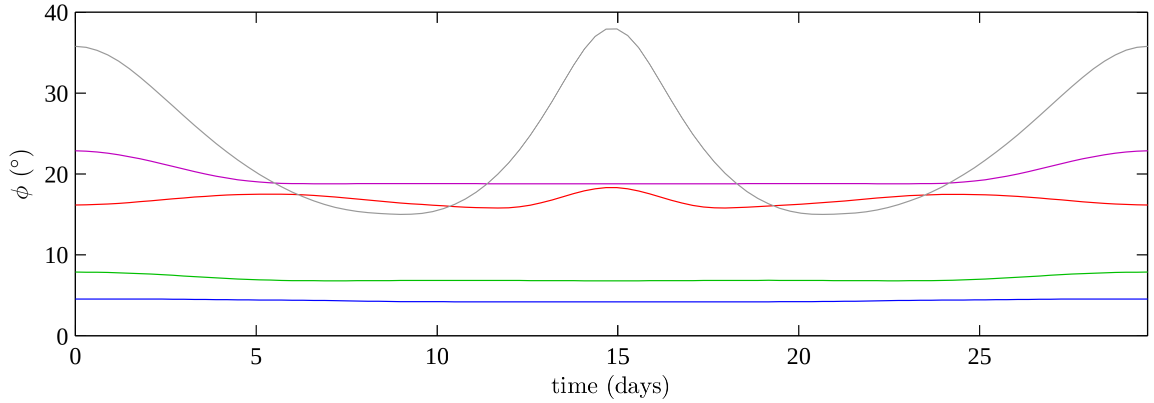

Figure 4.9. Elevation Angle ϕ for Periodic Orbits in the Lower-Fidelity Model.

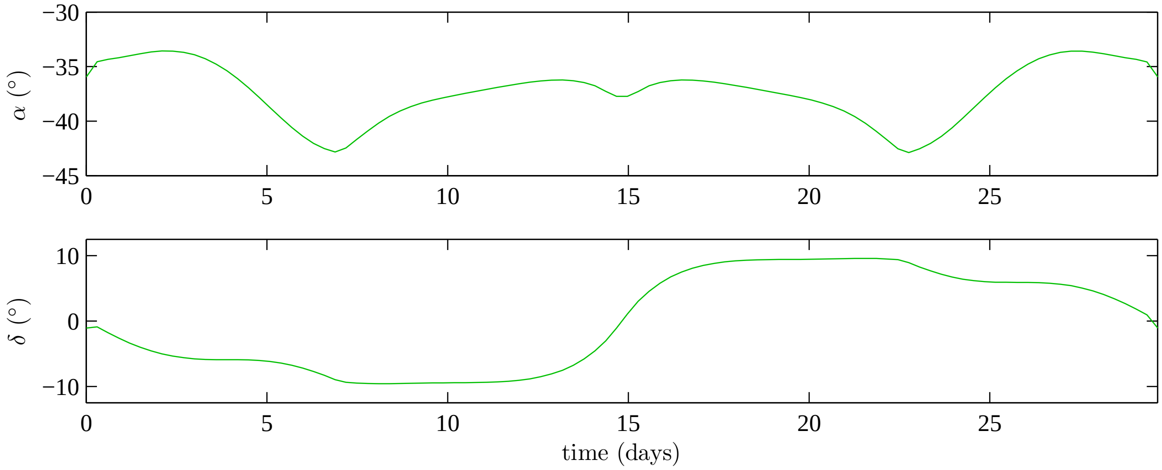

Figure 4.10. Control History for the L_2, $\kappa = 0.58$ mm/s^2 Periodic Orbit in the Lower-Fidelity Model.

An Alternative Control Parameterization

Recall that the components of the control vector $\hat{\boldsymbol{u}}$ in equation (2.36) can also be parameterized by the angles δ and α. By inspection of the previously converged control histories, for example the solution appearing in Figure 4.10, the behavior for the angle α resembles an even sinusoidal function, while the angle δ appears to closely follow an odd-valued sinusoid as a function of time. Given the problem symmetries and the physical interpretation of these angles, an alternative to the general piecewise linear parameterization for the cartesian components of $\boldsymbol{u}$ is to instead parameterize the angles α and δ using an even and odd Fourier series. Here, α and δ can be represented as

$$\begin{aligned} \alpha(t) &= \alpha_0 + \sum_{k=1}^{N} \alpha_k \cos(k\omega_s t) \\ \delta(t) &= \qquad \sum_{k=1}^{N} \delta_k \sin(k\omega_s t) \end{aligned} \tag{4.8}$$

By construction, the period of $\alpha(t)$ and $\delta(t)$ is $\mathbb{P} = 2\pi/\omega_s$. For implementation of the control in the collocation scheme, the Fourier coefficients are varied until the precise control law is uncovered for a given orbit. This result is achieved by storing the coefficients in the problem parameters vector $\boldsymbol{\mu}$ for corrections, i.e.

$$\boldsymbol{\mu}^T = (\alpha_0, \alpha_1, ..., \alpha_N, \delta_1, ..., \delta_N) \tag{4.9}$$

Since the control is periodic by definition, no constraint h is needed to force the control to repeat. When formulating $\boldsymbol{X}$ according to equation (3.90), there is also no longer a need to include the control $\boldsymbol{u}_j$ at any node j as an independent variable because the parameters $\boldsymbol{\mu}$ globally define the steering law over the entire trajectory. In other words, the sail acceleration vector $\boldsymbol{f}_T$ in equation (2.29) is completely defined with $\hat{\boldsymbol{u}}$ in equation (2.32), which is continuously defined by a selection of the coefficients $\boldsymbol{\mu}$ in equation (4.8). Once a solution is computed and the corresponding vector $\boldsymbol{\mu}$ is determined, an additional benefit of the Fourier series approach is that extraction of the control rates is straightforward. The control rates $\dot{\alpha}$ and $\dot{\delta}$, which represent changes in the angles relative to $\hat{\boldsymbol{l}}$, follow as

$$\begin{aligned} \dot{\alpha}(t) &= -\sum_{k=1}^{N} \alpha_k k\omega_s \sin(k\omega_s t) \\ \dot{\delta}(t) &= \sum_{k=1}^{N} \delta_k k\omega_s \cos(k\omega_s t) \end{aligned} \tag{4.10}$$

The Fourier series control law provided in equation (4.8) is sufficiently general for implementation using the shooting method with explicit integration. Note, however, that this possibility is only available given the a posteriori observation of the control history trends found from the converged solutions that employ the more general piecewise linear control approach, which allows the nodal controls $\boldsymbol{u}_j$ to enter the problem as free variables. The resulting orbits and control histories bear close resemblance to the trajectories by the piecewise linear control approach. The data summary in Table 4.1 indicates that with only a small number of Fourier coefficients, the minimum elevation angle $\phi_{\min}$ along any orbit deviates by at most 0.2° compared to the minimum elevation angle found with the piecewise linear control parameterization. No control rate boundaries are imposed on $\dot{\alpha}$ and $\dot{\delta}$, but all rates remain close to the 12.1°/day baseline rate that is already necessary for the sail to turn to continuously face the sun in the rotating frame. The mesh refinement algorithm is also successfully applied to the resulting orbits. Using an initial "coarse" grid of points, the transcription approach for feasible solutions is used to find solutions that are accurate to 1×10^{-12} nondimensional units in position and velocity.

4.3.4 Transition to the Ephemeris

From a number of simplifications in the lower-fidelity model, two critical assumptions must be further examined. First, in the RTBP the sun-to-spacecraft line is assumed to move in the Earth-moon plane. In reality, the moon's orbit plane is inclined with respect to that of the Earth by about 5.15°. This difference is significant, and it is therefore necessary to demonstrate that *any* solar sail trajectory

Table 4.1 Data Summary for Near-Optimal Solar Sail Orbits in the Lower-Fidelity Model.

	$\kappa = 0.58$ mm/s^2		$\kappa = 1.70$ mm/s^2		
Type	L_1	L_2	L_1	L_2	Hover
Color	Blue	Green	Red	Purple	Gray
x_0	+8.334577959416795d-1	+1.156211421789636d-0	+8.358382331873345d-1	+1.133709934961812d-0	+1.142606758444961d-0
z_0	−1.674447029156162d-2	−2.785681461021011d-2	−5.080489933754771d-2	−7.014221018336932d-2	−1.079440386848905d-1
$\dot{y}_0$	−2.970274544651623d-2	−7.264216970640185d-2	−1.035256763465011d-1	−1.321776217291153d-1	−2.309935244587937d-1
α_0	−6.343037134654265d-1	−6.532727216254634d-1	−6.550832921434782d-1	−8.076988446188386d-1	−7.176650914056956d-1
α_1	−1.639142648497209d-2	−3.496431271743909d-3	+1.109111936118494d-2	−3.760510052379947d-2	−9.455764413908209d-2
α_2	−1.005162216606042d-3	+2.525294068828327d-2	−7.204002256366904d-3	+9.198677776698262d-2	−1.657526877433217d-1
α_3	+4.186000055059244d-2	−6.282315518132125d-3	+7.724704156521697d-2	+4.178169912132836d-2	+4.081942483021073d-2
α_4	+1.276497472641706d-2	−2.827459153365777d-2	−9.084935129312299d-3	−5.380796885631299d-3	+9.546331387483088d-2
α_5	−7.108087578028680d-3	−1.076977595277608d-2	−3.141687535102539d-2	+1.457063836041965d-2	+1.510595399780250d-2
δ_1	+9.923829906300495d-2	−1.978177053068336d-1	+4.240662342949236d-1	−4.206338880883266d-1	−5.455275819483647d-1
δ_2	+1.024195843920122d-3	−4.157860433873927d-2	−7.898408737806689d-4	+6.788375238824441d-2	−6.872290868371695d-3
δ_3	+3.345688507820322d-3	−7.153711065518781d-2	−1.269064717140005d-1	−1.503551493545528d-1	+1.478868620356161d-1
δ_4	+8.333198429994938d-4	−3.504456801267981d-3	+1.277367799213988d-1	+3.061175727108182d-2	+2.429599424843301d-2
δ_5	+6.021023233999644d-3	−1.440196545516193d-2	+1.736235859640061d-2	−2.337621947580810d-2	−5.042661386056409d-2
$\phi_{\min}$ (°)*	4.2	6.8	15.8	18.8	15.0
$\phi_{\min}$ (°)	4.2	6.8	15.6	18.6	15.0
$\dot{\alpha}_{\max}$ (°/day)	2.28	2.27	4.60	3.48	9.61
$\dot{\delta}_{\max}$ (°/day)	1.76	7.06	12.78	15.14	10.78
Initial n	15	15	15	15	15
Initial Size $\boldsymbol{X}$	355	355	355	355	355
Mesh Refinements	2	2	2	2	2
Final n	51	50	79	68	83
Final Size $\boldsymbol{X}$	1,219	1,195	1,891	1,627	1,987

---

*Values from piecewise linear control parameterization

modeled in the lower-fidelity, RTBP model (irrespective of the mission design objective) is sufficiently accurate for transitioning into the higher-fidelity model. Second, the lower-fidelity model currently ignores lunar librations, assuming that the south pole of the moon is directly below the moon's center and stationary for all time. In the reality, the lunar equatorial plane is inclined to Earth's orbit plane by about 1.55°. Considering these two angles, that is, the angles between the Earth orbit plane and both the lunar orbit plane and the lunar equatorial plane, it appears likely that even if the orbits can be transferred to the higher-fidelity model, some of the orbits from the RTBP model, for example, the L_1 orbit for $\kappa = 0.58$ mm/s^2 with a minimum elevation angle of $\phi_{\min} = 4.2°$, will not maintain a positive elevation angle with respect to the actual lunar south pole. However, the collocation schemes can be adapted for computations in the higher-fidelity model. In fact, all the orbits can be transitioned to the higher-fidelity model while ensuring that most maintain a positive elevation angle $\phi_{\min}$.

Given multiple revolutions of any baseline orbits from the lower-fidelity model, the goal is computation of a nearby periodic solution in the higher-fidelity model. The only constraints necessary for computing the nearby solution are the usual defect constraints and the control constraints $\psi_i = 0$. It is still, however, useful to enforce the path constraints that are ideal for lunar south pole coverage. To ensure that the desired elevation angles and altitudes are satisfied with respect to the actual lunar south pole, equation (4.5) must be modified. At any given time t_i, the exact position of the ground station $\boldsymbol{R}_g$ at lunar south pole $(\theta_g, \delta_g) = (-90°, 0°)$ can be determined by manipulating the Euler 3-1-3 sequence for lunar librations available in the JPL DE405 ephemeris file, as discussed in Section 2.7.4. Then, the continuous path constraints for elevation angle and altitude in the higher-fidelity model are discretized as

$$
\begin{aligned}
\boldsymbol{g}_i(\boldsymbol{R}_i, \boldsymbol{\eta}_i) &= \left\{ \begin{matrix} \sin(\phi_{lb}) + \dfrac{\boldsymbol{R}_{g_i} \cdot (\boldsymbol{R}_{g_i} - \boldsymbol{R}_i)}{||\boldsymbol{R}_i - \boldsymbol{R}_{g_i}||||\boldsymbol{R}_{g_i}||} \\ ||\boldsymbol{R}_i - \boldsymbol{R}_{g_i}|| - a_{ub} \end{matrix} \right\} + \boldsymbol{\eta}_i^2 = \boldsymbol{0} \\
\boldsymbol{g}_{i,2}(\boldsymbol{R}_{i,2}, \boldsymbol{\eta}_{i,2}) &= \left\{ \begin{matrix} \sin(\phi_{lb}) + \dfrac{\boldsymbol{R}_{g_{i,2}} \cdot \left(\boldsymbol{R}_{g_{i,2}} - \boldsymbol{R}_{i,2}\right)}{||\boldsymbol{R}_{i,2} - \boldsymbol{R}_{g_{i,2}}||||\boldsymbol{R}_{g_{i,2}}||} \\ ||\boldsymbol{R}_{i,2} - \boldsymbol{R}_{g_{i,2}}|| - a_{ub} \end{matrix} \right\} + \boldsymbol{\eta}_{i,2}^2 = \boldsymbol{0} \\
\boldsymbol{g}_{i,3}(\boldsymbol{R}_{i,3}, \boldsymbol{\eta}_{i,3}) &= \left\{ \begin{matrix} \sin(\phi_{lb}) + \dfrac{\boldsymbol{R}_{g_{i,3}} \cdot \left(\boldsymbol{R}_{g_{i,3}} - \boldsymbol{R}_{i,3}\right)}{||\boldsymbol{R}_{i,3} - \boldsymbol{R}_{g_{i,3}}||||\boldsymbol{R}_{g_{i,3}}||} \\ ||\boldsymbol{R}_{i,3} - \boldsymbol{R}_{g_{i,3}}|| - a_{ub} \end{matrix} \right\} + \boldsymbol{\eta}_{i,3}^2 = \boldsymbol{0}
\end{aligned}
\tag{4.11}
$$

Recall that even though the vector bases are now associated with the MCI, EMEJ2000 frame, all quantities are still nondimensional based on the characteristic quantities in the RTBP given in Table 2.1.

Before the application of the transcription procedure, it is first necessary to transform all the states from the barycentric, rotating frame in the RTBP to the EMEJ2000 frame in the higher-fidelity model. Since the orbits are relatively close to the moon, the moon is set as the central body in equation (2.62) using $\boldsymbol{f}_T$ from equation (2.29) and $\boldsymbol{f}_G$ from equation (2.63). (The remaining higher-fidelity effects are neglected for this analysis.) Thus, all higher-fidelity simulations employ coordinates in the MCI frame. Recall that the additional perturbing bodies include the Earth and the sun, and the defects in equations (3.84)-(3.86) are now computed with respect to the function $\boldsymbol{f}$, available from equation (2.62). Since the orbits are only quasi-periodic in the higher-fidelity model, the more general piecewise linear control approach is again selected. Thus, the choice for the node controls $\boldsymbol{u}_i$ must also be adjusted to be defined relative to the real sun-to-spacecraft line. Therefore, given $\boldsymbol{u}_i = \left(u_i^{(1)}, u_i^{(2)}, u_i^{(3)}\right)^T$ from the lower-fidelity, RTBP model, first α_i and δ_i are computed, i.e.

$$\begin{aligned} \alpha_i &= \sin^{-1} u_i^{(3)} \\ \delta_i &= \tan^{-1}\left(\frac{u_i^{(1)} \sin\omega_s t_i + u_i^{(2)} \cos\omega_s t_i}{u_i^{(1)} \cos\omega_s t_i - u_i^{(2)} \sin\omega_s t_i}\right) \end{aligned} \tag{4.12}$$

where $-90° \leq \sin^{-1}(\cdot) \leq 90°$ and $-180° \leq \tan^{-1}(\cdot) \leq 180°$, and ω_s is as calculated in lower-fidelity model. Then, to determine $\boldsymbol{u}_i$ in the EMEJ2000 frame given α_i and δ_i, consider using

$$\boldsymbol{u}_i = \begin{bmatrix} \hat{\boldsymbol{l}}_i & \dfrac{\hat{\boldsymbol{h}}_i \times \hat{\boldsymbol{l}}_i}{\left\|\hat{\boldsymbol{h}}_i \times \hat{\boldsymbol{l}}_i\right\|} & \hat{\boldsymbol{l}}_i \times \dfrac{\hat{\boldsymbol{h}}_i \times \hat{\boldsymbol{l}}_i}{\left\|\hat{\boldsymbol{h}}_i \times \hat{\boldsymbol{l}}_i\right\|} \end{bmatrix} \begin{Bmatrix} \cos\alpha_i \cos\delta_i \\ \cos\alpha_i \sin\delta_i \\ \sin\alpha_i \end{Bmatrix} \tag{4.13}$$

where both $\hat{\boldsymbol{l}}_i$ and $\hat{\boldsymbol{h}}_i$ possess unit magnitudes. Here the instantaneous direction of the sun-to-spacecraft line $\hat{\boldsymbol{l}}_i$ is no longer computed with the simplified model given in equation (2.31). Instead, the direction is extracted from the ephemeris files. In MCI coordinates, this vector is simply

$$\hat{\boldsymbol{l}} = \frac{\boldsymbol{R} - \boldsymbol{R}_{☾\odot}}{\left\|\boldsymbol{R} - \boldsymbol{R}_{☾\odot}\right\|} \tag{4.14}$$

The vector $\hat{\boldsymbol{h}}_i$ is the unit vector parallel to the angular momentum associated with the Earth's orbit relative to the sun, i.e.

$$\hat{\boldsymbol{h}} = \frac{\boldsymbol{R}_{\oplus☾} \times \boldsymbol{V}_{\oplus☾}}{\left\|\boldsymbol{R}_{\oplus☾} \times \boldsymbol{V}_{\oplus☾}\right\|} \tag{4.15}$$

and is also easily determined from the files.

4.3.5 Quasi-Periodic Orbits in the Ephemeris Model

Since the orbits are periodic in the RTBP, multiple revolutions can be quickly obtained by "stacking" the node states and controls for a baseline 25-revolution, two-year mission. The number of nodes per revolution is adjusted to 35, for a total number of nodes $n = 851$. From equation (2.29) and equation (2.31), it is apparent that an epoch must be identified when the moon is at opposition to match the conditions at $t = 0$ for the lower-fidelity model. The total lunar eclipse of 2011 December 10, 14:31:46 UTC meets this requirement and is selected as the epoch for all of the orbits. Since the segment time Δt_i remains fixed, all the body locations in the system model, as well as the location of the lunar south pole, are computed prior to applying the collocation scheme and stored in memory for future access. Therefore, the ephemeris files are never called during implementation of the collocation schemes. As previously stated, the node states and controls (as well as the states corresponding to the internal points for the Gauss-Lobatto scheme) are transformed into the MCI, EMEJ2000 frame, and the values of ϕ_{lb} and a_{ub} are selected. The values for the bounds ϕ_{lb} and a_{ub} must be such that the initial guess is feasible or at least very close to feasible. If the initial guess is infeasible, then using equation (3.88) to compute initial values for the slack variables, the variables are defined in terms of the real components (and the imaginary components are discarded). Using the transformed guess from the barycentric, lower-fidelity model and the bounds described in equation (4.11), equation (3.11) is once again applied in an iterative manner. In just a few iterations, the scheme successfully computes quasi-periodic solutions for solar sail trajectories.

All five orbits designed in the lower-fidelity model are successfully transitioned to the higher-fidelity model using the higher-order Gauss-Lobatto transcription method for feasible trajectories. The results appear in Figure 4.11 where the orbits are plotted in the MCR frame. A corresponding data summary appears in Table 4.2. For comparison, elevation angle is plotted as a function of time for both L_2 orbits in Figure 4.12. After transition, the L_1 orbit with $\kappa = 0.58$ mm/s^2 possesses a minimum elevation angle $\phi_{\min} = -2.70°$, that is, "below" the horizon and out of sight of the south pole. Thus, lunar librations completely eliminate the possibility for continuous line-of-sight with the lunar south pole for the set of orbits near L_1 when $\kappa = 0.58$ mm/s^2. In contrast, for this same value of κ, the L_2 orbit is still barely feasible after transitioning to the higher-fidelity model, where $\phi_{\min} = 0.01°$. Therefore, it appears that for the more realistic sail with $\kappa = 0.58$ mm/s^2, only orbits near L_2 maintain constant surveillance of the lunar south pole in the higher-fidelity model. For the slightly larger characteristic acceleration $\kappa = 1.70$ mm/s^2, however, all the orbits maintain positive elevation angles in the higher-fidelity model. The minimum elevation angles for L_1 and L_2 are $\phi_{\min} = 9.10°$ and $\phi_{\min} = 11.91°$, respectively, and $\phi_{\min} = 8.20°$ for the hover orbit. Due to the lunar librations, it is not surprising that nearly all the orbits lose about 6.7° of elevation between the lower-fidelity and higher-fidelity models. As characteristic acceleration increases for the sails, a large increase in elevation angle is observed as a larger out-of-plane force is available. The unique "hover orbit" possesses the best maximum elevation angle, but suffers a smaller minimum elevation angle and a greater maximum altitude than the other orbits. All of the altitudes for the solar sail pole-sitter orbits are comparable to the maximum apolune altitudes in a previous libration point orbit architecture analysis by Grebow et al. [51] Ongoing analysis by other researches has indicated that these altitudes are feasible for use with existing communications hardware. [52]

A sample of the control time histories for the L_2 orbit for $\kappa = 0.58$ mm/s^2 appears in Figure 4.13. Note that upon transition to the higher-fidelity model, the control histories remain smooth, and are also relatively slow. (At most, only a few degrees of re-orientation are required per day.) Quasi-periodic orbits may be computed for up to 100 revolutions of the baseline orbit, and the results do not vary. Note that for 100 revolutions (approximately 8 years), $n = 3,401$, setting the size of $\boldsymbol{X}$ and $\boldsymbol{F}$ to 91,811 and 85,003, respectively. However, roughly 99.97% of the entries in the matrix $D\boldsymbol{F}$ are zero.

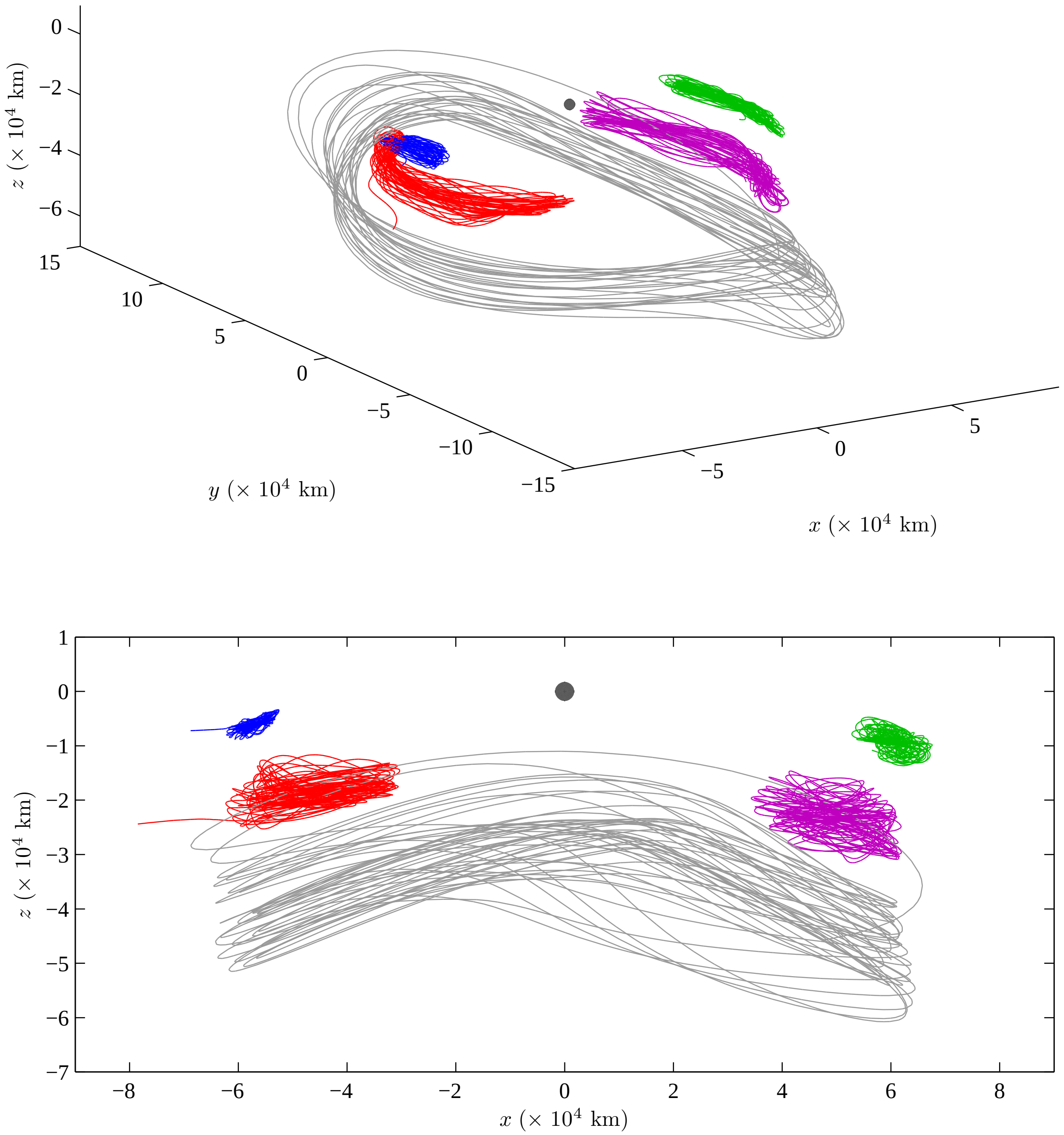

Figure 4.11. Quasi-Periodic Orbits in the Ephemeris Model, MCR Frame (Top) and *X*-*Z* Projection (Bottom).

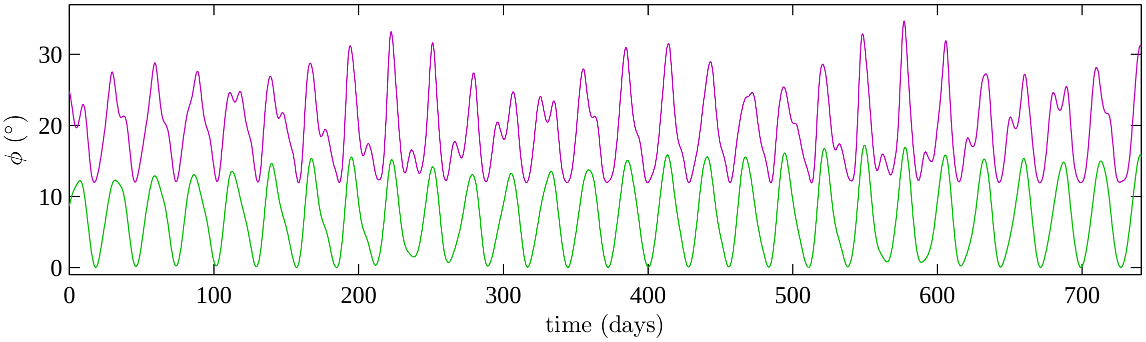

Figure 4.12. Elevation Angle ϕ for the L_2 Quasi-Periodic Orbits in the Higher-Fidelity Model.

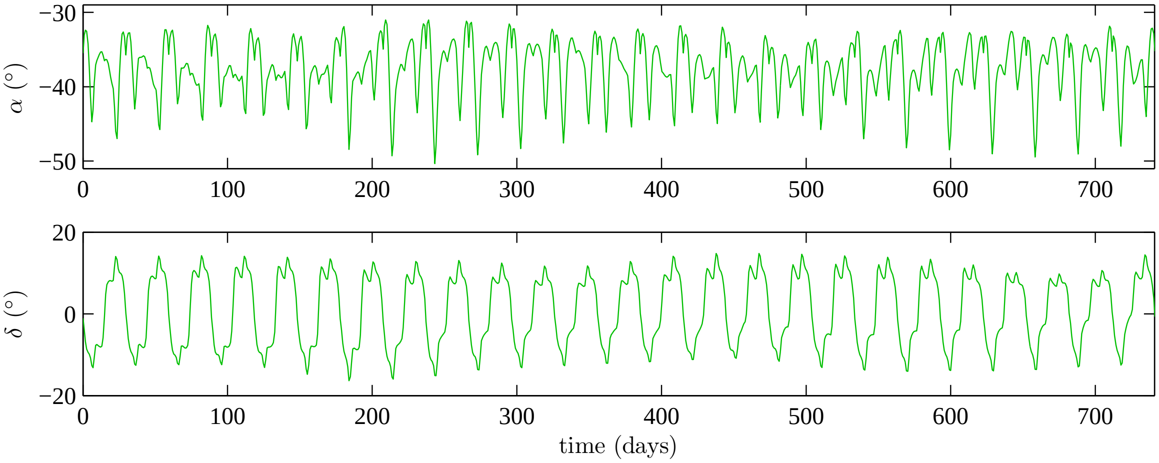

Figure 4.13. Control History for the L_2, $\kappa = 0.58$ mm/s^2 Quasi-Periodic Orbit in the Higher-Fidelity Model.

Table 4.2 Data Summary for Near-Optimal Solar Sail Orbits in the Higher-Fidelity Model.

	$\kappa = 0.58$ mm/s^2		$\kappa = 1.70$ mm/s^2		
Type	L_1	L_2	L_1	L_2	hover
ϕ_{min} (°)	-2.70	0.01	9.10	11.91	8.20
ϕ_{max} (°)	12.46	17.21	27.43	34.68	45.68
ϕ_{avg} (°)	4.18	7.13	16.14	19.37	22.37
a_{min} (km)	53,000	58,000	55,500	57,000	68,500
a_{max} (km)	70,000	70,500	84,500	76,000	138,000

4.4 Solar Electric Propulsion Pole-Sitter Orbits

Pole-sitter orbits can also be constructed with a more conventional low-thrust device such as solar electric propulsion, i.e., a CSI engine. However, because a CSI engine is limited by propellant, these long duration pole-sitter orbits are ultimately temporary in nature. For a near-term application that might be of interest for a planned lunar facility, consider the allocation of payload space for a small 500 kg spacecraft in a launch to the International Space Station (ISS). The coverage capabilities of this spacecraft (for example, dry mass 50 kg) might offer new options if equipped with a thruster similar to Deep Space 1's NSTAR (thrust magnitude 150 mN, specific impulse 1,650 s). Departing from the International Space Station (ISS) orbit, the entire low-thrust mission is characterized by three distinct phases:

1. Earth-centered, spiral out from the International Space Station to the Moon.

2. Pole-sitting position maintained for as long as possible.

3. Moon-centered, spiral down to an elliptically inclined stable orbit.

Note that after a transfer to the coverage orbit and the completion of a significant surveillance period, an added advantage of the mission is that the spacecraft uses its remaining fuel to spiral-down into a stable lunar orbit for continued surveillance; the spacecraft is then the first piece of the long duration, multiple-spacecraft constellation discussed in Section 4.1. Such a mission would be beneficial for temporarily maintaining constant surveillance with only one spacecraft, while waiting for the remaining spacecraft in the constellation, that is, those that are launched at a later time. Solving for the end-to-end mission trajectory design, one that optimizes phase #2 while considering the functional dependencies of phases #1 and #3, is ultimately part of a multi-phase direct transcription process. However, the phases are first considered independently, with a priority on selecting an appropriate coverage orbit that is continuous and satisfies the required path constraints. The following solar electric propulsion mission design and analysis, therefore, pertains only to the selection of a preliminary coverage orbit that can later be combined into a larger problem.

4.4.1 Preliminary Orbit Design in the Lower-Fidelity Model

As with the solar sailing pole-sitter, preliminary design for the temporary pole-sitter mission with a CSI engine begins with a priority on the coverage orbit, or phase #2. The initial mass upon arrival is usually close to 320 kg, yielding an initial thrust acceleration magnitude such that $\|\boldsymbol{f}_T\| = 0.47$ mm/s^2. As is apparent in equation (2.33), this value is the lowest thrust acceleration level over the duration of the coverage orbit, and, thus, a conservative estimate of worst-case coverage performance. To formulate the initial guess, the general concept introduced in Section 4.3.3 is repeated. The lower bound on elevation angle is fixed at $\phi_{lb} = 13.0°$ and the upper bound on altitude is $a_{ub} = 100,000$ km. As is demonstrated in Figure 2.4, the assumed initial thrust acceleration limits the spacecraft to regions near L_1 and L_2. However, since the spacecraft is continuously burning fuel, it cannot remain exactly stationary. In fact, the thrust acceleration increases with time. As indicated by Figure 2.4, increasing thrust acceleration allows the spacecraft to possibly enter the yellow and green locations that wrap below the lunar south pole. Thus, as phase #2 progresses, the coverage capabilities of the spacecraft increase.

Given the likelihood that the trajectory will shift as fuel is expended, the position variables for the entire trajectory are "stacked" near L_1 or L_2 such that the boundary constraints are satisfied. (Initially, there is no y-component for the trajectory position.) Using the stationary assumption, the variables corresponding to velocity are all set to zero. The thruster is initially aligned strictly in the negative z-direction. The user then specifies the number of thrust arcs k. Since the magnitude of the pseudo-potential gradient force experienced by the spacecraft remains relatively constant, the nodes are spaced evenly over the arc. The time duration along all the thrust arcs is initially assumed to be equal, and the total thrust time is determined by the user-specified final mass. Here, the final mass after completion of the coverage phase is assumed to be 65 kg. The variables corresponding to initial mass are determined by the thrust times. An initial estimate of the total coverage time minus the total thrust time then allows the total coast time to be divided evenly over the number of coast arcs. The problem formulation in Section 3.5.2 is applied to the design of a low-thrust, quasi-periodic coverage orbit using a CSI engine with the system model that is consistent with equation (2.37). Now $\boldsymbol{X}^0$ is assimilated in accordance with equation (3.94), where initial guesses for the slack variables are such that the corresponding constraint is initially satisfied. Alternative approaches to develop the initial guess for the coverage phase are available, however, the previous formulation is perhaps the simplest. The construction best utilizes the pole-sitting assumption, and nearby solutions determined via equations (3.2) and (3.11) are not biased by a more complicated non-stationary initial guess. Furthermore, any other initial guess strategy must assume a certain behavior across the entire solution, and such knowledge is, at this point, unknown. Since the designs are preliminary, the transcription method for feasible solutions is applied without any mesh refinements. This entire preliminary orbit design procedure is also enhanced with a GUI design tool analogous to the one introduced in Section 4.3.3 and Figure 4.7 for the solar sailing pole-sitter.

By investigating initial guesses near L_1 and L_2, low-thrust trajectories are quickly computed that satisfy a constraint such that the minimum elevation angle equals 13.0°. The collocation scheme automatically determines the thruster alignment, and positions the thrusting and coasting arcs as needed. It is observed that the spacecraft thrusts whenever approaching the specified boundary. Hence, thrusting generally occurs near the "top" of the trajectory and coasting near the bottom. A few candidate results appear in Figure 4.14, where thrust arcs are red and blue represents a coast arc. There are two characteristic types of solutions. For long duration trajectories, initial estimates of total coverage time are 475 days and 600 days for L_1 and L_2, respectively. These trajectories include a total of 76 thrust arcs and, primarily, the solutions involve an engine pulsing in the negative z-direction, remaining below the libration points. The trajectories appear in the left plots in Figure 4.14(a). The corrected coverage times are 289.44 days for the L_1 trajectory, and 445.03 days for L_2. Given the large number of thrust arcs, the pulsing solutions require many small thrusting segments, each about 3 days in duration. The solutions might be considered impractical from an operational standpoint, where thrusters most likely require longer, more sustained thrusting and coasting times. Non-pulsing solutions are computed by decreasing the number of total arcs while retaining a total coverage time that is high. For these solutions, the total number of thrust arcs is set to 36, and initial guesses for the coverage times are 425 days and 500 days for L_1 and L_2, respectively. The resulting solutions near L_1 and L_2 can be viewed in the right plots in Figure 4.14(b). The corrected time for the trajectory near L_1 is 320.22 days, and the L_2 trajectory sustains coverage for 398.56 days. The thrusting segments for these solutions are about 8 days in duration.

All the solutions shift toward the moon as coverage time increases, as predicted due to the increase in thrust acceleration as fuel is consumed. Each solution continuously maintains direct line-of-sight with both the lunar south pole and the Earth. The non-pulsing solutions are similar to the pulsing ones, which appear to expand in the y-direction to satisfy the increase in arc time. Therefore, whereas motion is primarily

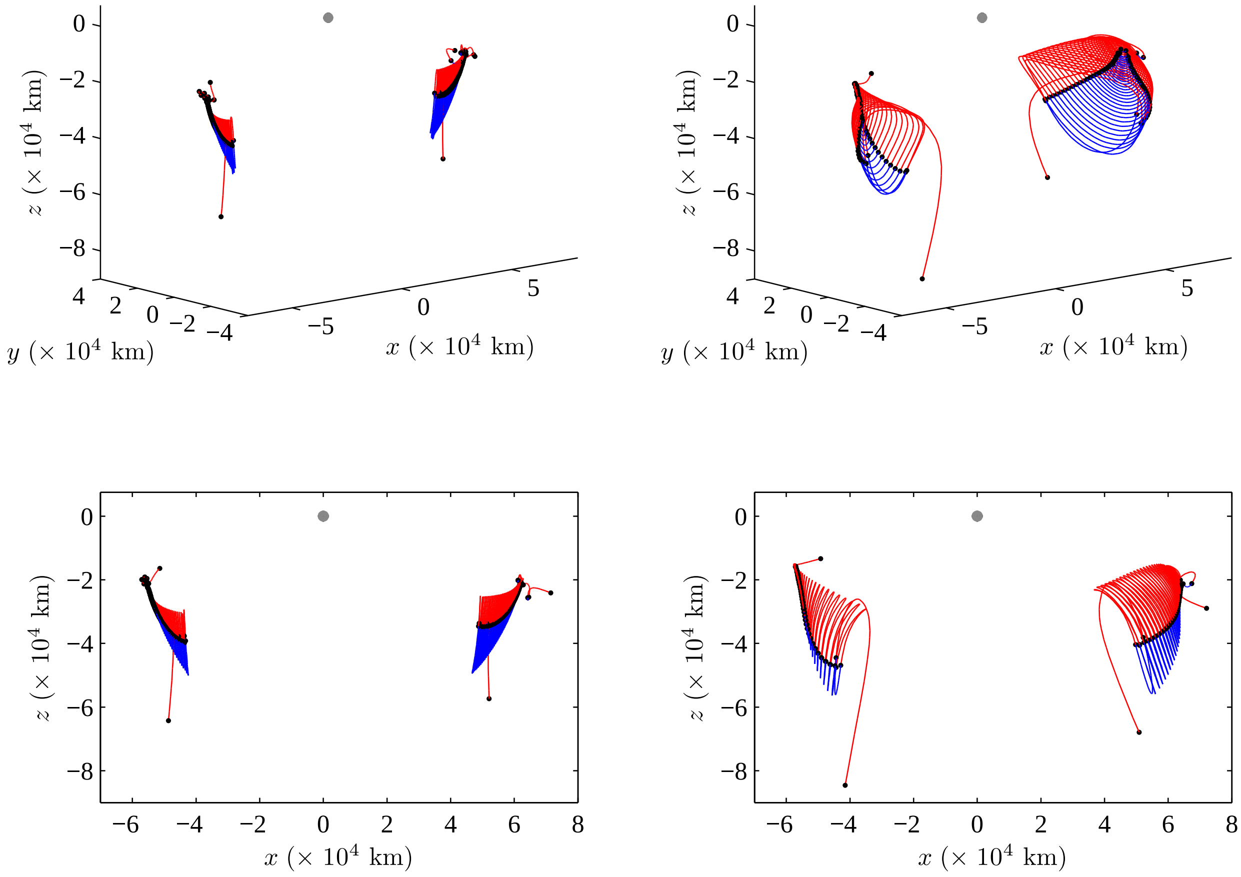

(a)

(b)

Figure 4.14. (a) Pulsing and (b) Non-Pulsing Trajectories for the Coverage Phase, MCR Frame.

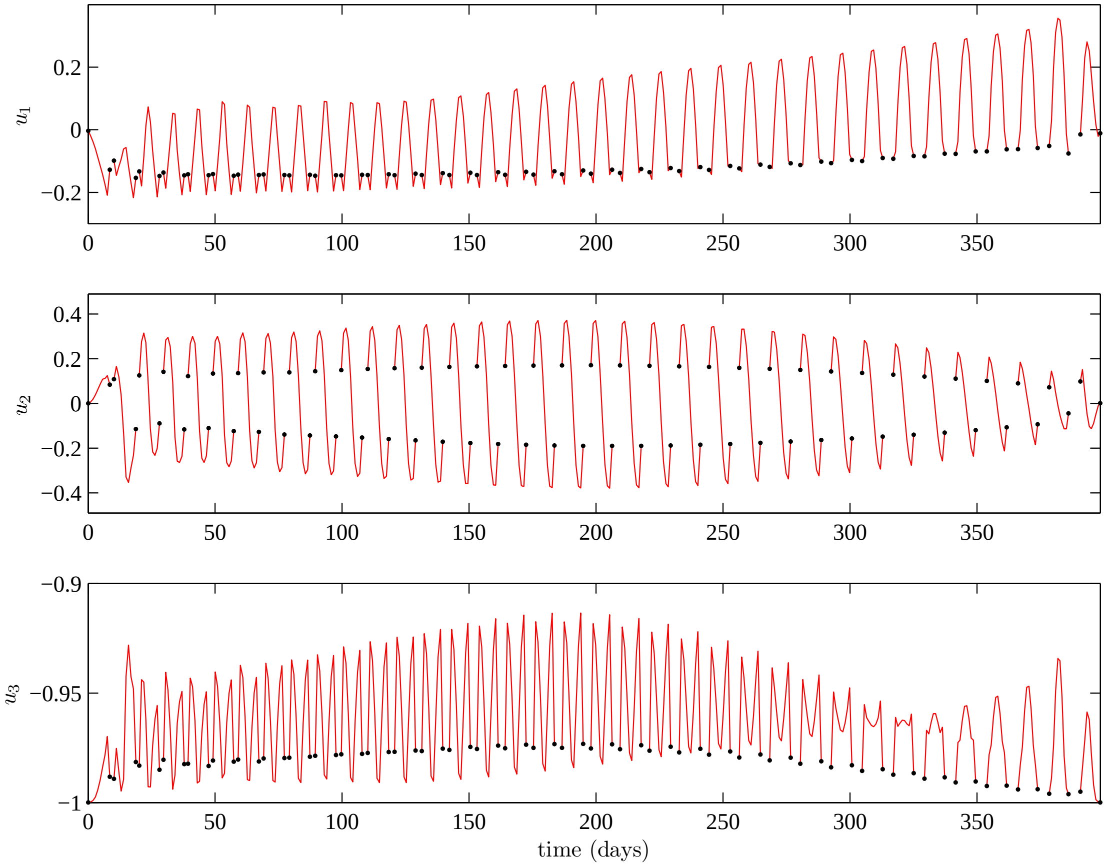

Figure 4.15. Control History for an L_2 Non-Pulsing Solution.

in the x-z plane for the pulsing solutions, the non-pulsing solutions appear to be more three-dimensional in nature. A striking feature about the non-pulsing solutions is that the motion seems to be confined to a three-dimensional surface very similar to the surfaces corresponding to the L_1 and L_2 southern halo orbit families in Figure 4.1. The solutions not only appear to move along the family as energy changes, but they also significantly alter the surface shape to allow satisfaction of the problem constraints. Given that the optimal solutions are driven toward the constraint boundary, the behavior of the feasible solution offers a mission design benefit: At the expense of time-of-flight for a given quantity of fuel, the spacecraft can obtain a gradual increase in elevation angle for improved line-of-sight as the mission progresses.

Since the L_2 non-pulsing solution is more practical for implementation, and yields long-duration coverage time, it is selected as the coverage orbit for the mission design sequence. However, if any of the other trajectories are desired, they can easily be incorporated into the three-phase design without significantly altering the process. The control history for the L_2 non-pulsing solution appears in Fig. 4.15 and the coverage results and thrust acceleration are plotted in Figure 4.16. The elevation angle results confirm that the spacecraft is always at least 13° above the south pole horizon. As expected, the thrust acceleration increases with time, thereby altering the energy and coverage capabilities of the spacecraft. In fact, the final thrust acceleration is near 1.75 $\mathrm{mm/s^2}$, allowing the spacecraft to enter the light blue regions in Figure 2.4, and so the trajectory shifts away from the boundary constraint and toward the moon.

4.4.2 Preliminary Orbit Design in the Higher-Fidelity Model

To generate a comparable, preliminary, design of the phase #2 coverage orbit, the preceding problem is solved again with the MCI higher-fidelity model from equation (2.62), detailed in Section 2.7.1, and retaining the problem formulation in Section 3.5.2. The effects of shadowing (Section 2.7.3) and lunar librations (Section 2.7.4) are also considered. To converge on the initial coverage orbit, the transcription

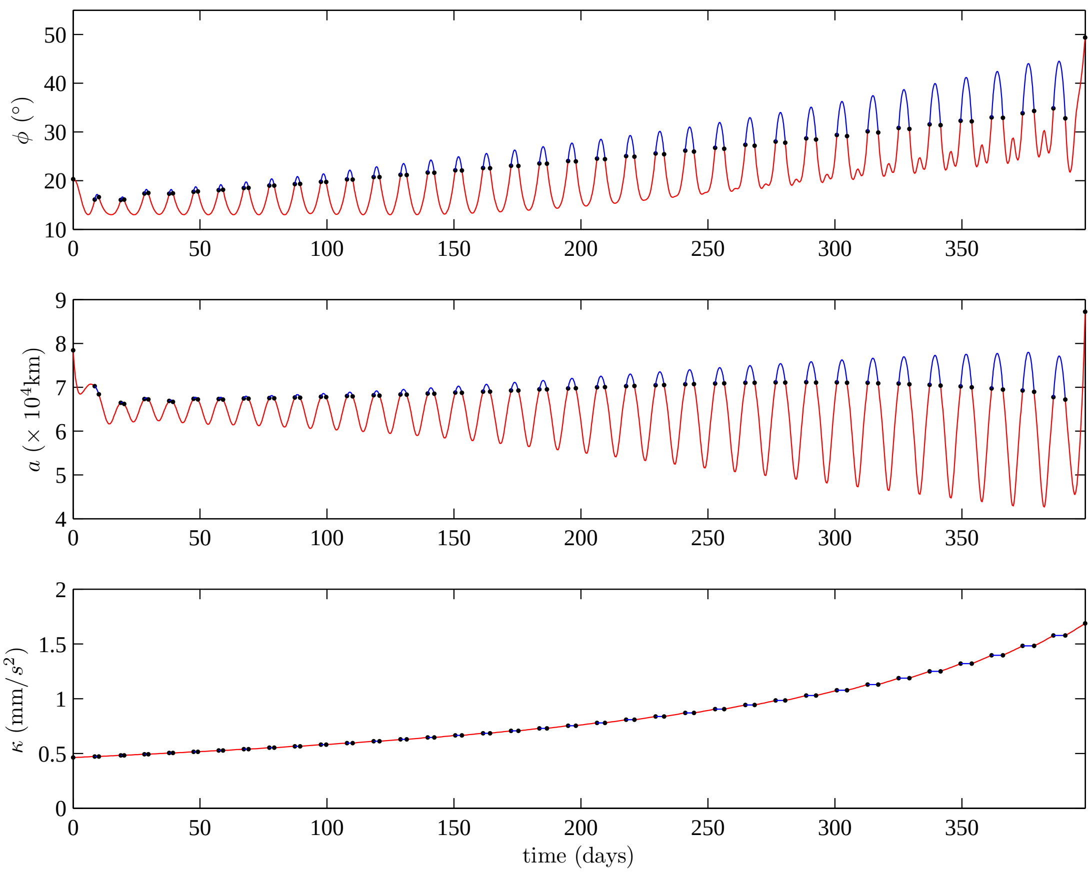

Figure 4.16. Elevation Angle, Altitude, and Thrust-Acceleration for the L_2 Solution.

method for feasible solutions is employed using the minimum-norm approach (equation (3.11)), and the mesh refinement algorithm of Section 3.5.5 with a fully converged initial guess from the lower-fidelity model. Recall that the x-y plane corresponds to the moon orbit plane. A sample lower-fidelity feasible solution near L_2 with 36 thrust arcs appears in Figure 4.17. Here, the orbit is positioned in a region approximately $38,400$ km below the L_2 point, and is within direct line-of-sight of the Shackleton Crater. The trajectory appearing in Figure 4.17 is precisely the initial guess trajectory that is input to the transcription approach with the higher-fidelity model. Like the lower-fidelity coverage orbit, approximations are still required for phases #1 and #3 in the higher-fidelity model, as discussed in the following chapter. Then, in Chapter 6, all three phases enter a larger collocation scheme that applies boundary conditions to ensure continuity between the phases.

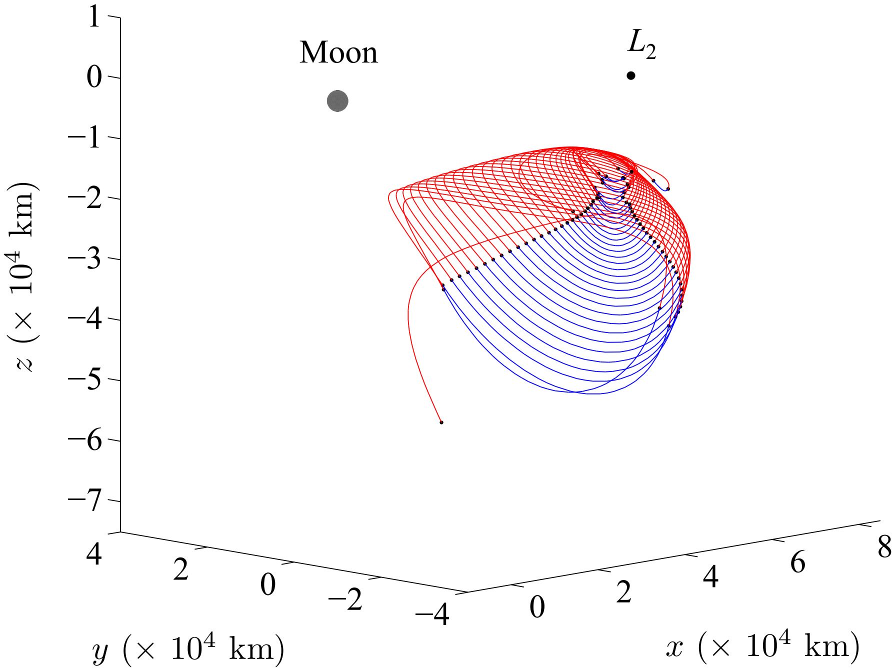

Figure 4.17. Feasible Solution for Phase #2 in the Lower-Fidelity Model, Thrust Arcs (Red) and Coast Arcs (Blue), MCR Frame.

4.5 Summary of Orbit Options

Four different orbit options for lunar south pole coverage have been introduced. Furthermore, the transcription method is demonstrated on sample pole-sitter orbit mission scenarios involving solar sails as well as solar electric propulsion. Each of the four orbit choices have distinct advantages and disadvantages that are qualitatively summarized in Table 4.3. Recall that the first two orbits can be considered natural options because they require only stationkeeping fuel at most. With these options, two to three spacecraft are always required given the orbit configurations that are possible with the natural dynamics of the system. At the expense of an additional spacecraft, the need for any stationkeeping can be completely avoided with the lunar frozen orbit option. The selection of libration point orbits requires stationkeeping propellant, but the inherent unstable behavior implies that the spacecraft are not permanently limited to a specific coverage orbit, due to the possibility of fuel-efficient transfers. Once a low-thrust device is available, then the computation of single spacecraft pole-sitter options is possible. As the technology development for solar sailing continues, a very long-duration pole-sitter orbit might one day be available to maintain continuous communications. Contemporary fuel-limited technology, comparable to the NSTAR solar electric thruster, may also utilize the pole-sitter concept for a temporary, continuous coverage mission that is part of the gradual establishment of a long-term, multi-spacecraft constellation of naturally occurring orbits.

Table 4.3 Attributes of Candidate Lunar Coverage Orbits.

Orbit Type	Advantages	Disadvantages
Lunar Frozen Orbit	• Low altitude • Stable • Well-known • Long-duration	• Gravity harmonics • Multiple spacecraft • Mission compatibility
Libration Point Orbits	• Many configurations • Large elevation angles available • Fuel-efficient transfers	• High altitude • Multiple spacecraft • Additional propellant • No end-of-life
Solar Sail Pole-Sitter	• One spacecraft • Continuous thrust	• Advanced technology required • Higher altitude • Mission specific
EP Pole-Sitter	• One spacecraft • Technology available • Mission capability • End-of-life	• Higher altitude • Limited by fuel

5. TRANSFERS

Once one or multiple coverage orbits are selected, the next stage of the design process is to compute a transfer trajectory to arrive, and if needed, depart from the orbit of interest. Transferring to the coverage orbit from an Earth parking orbit with low-thrust initially requires a large number of spirals to depart the vicinity of the Earth, leading to extremely high sensitivity in numerical corrections processes. In this case, even the robust collocation approach requires an accurate initial guess to compute a transfer arc. Typically, these initial guess schemes are based upon maximizing two-body kinetic energy by thrusting along the inertial velocity direction. This guess strategy can be implemented without restrictions for the lower-fidelity design of CSI and VSI transfers. However, additional constraints are necessary for the initial guess if the effects of shadowing in the higher-fidelity model are incorporated. When a solar sail is employed, additional geometry considerations must be included due to the fact that the sun's location restricts how often the sail can be steered in a desired direction. Once these preliminary thrusting laws produce a transfer arc that nearly converges with an explicit propagation, then, if desired, the trajectory may be immediately refined with collocation. In the case of the solar sail transfer, the collocation process immediately begins linking the transfer to the previously computed sail pole-sitter orbit within the higher-fidelity model. However, in the case of a solar electric propulsion mission, the initial guess for the spiral-out from Earth is stored and later inserted into a larger multi-phase direct transcription problem that includes other phases, such as the coverage orbit, and an end-of-life transfer trajectory. The approach to generating an initial guess for such end-of-life trajectories is similar to the guess strategies for Earth departures. Transfer trajectories may also be sought to transit between libration point orbits. For L_i-toL_i transfers, the relatively low times-of-flight allow the optimal control-based formulation to be employed for rapid trajectory optimization.

The computation of different types of transfer trajectories are approached as summarized below. The most successful strategy is dependent upon the coverage orbit option. Thus, the schemes are organized by coverage orbit:

I. Lunar Frozen Orbits
    i. Transfer from Earth parking orbit is not investigated here. However, many previous efforts have focused on transfers to two-body lunar orbits. [81]
    ii. Due to stability of the orbits, transfer between different frozen orbits is not deemed feasible for this analysis.
    iii. These orbits are suitable as a final insertion location for end-of-life transfers in a temporary solar electric propulsion pole-sitter mission.

II. Libration Point Orbits
    i. Transfer from Earth parking orbit is not investigated here, however, extensive analysis was previously completed. [82]
    ii. Many transfers between libration point orbits are rapidly computed by implementing an optimal control strategy. The optimal control formulation is tractable due to lower times-of-flight and numerical sensitivities.
    iii. End-of-life trajectories are currently not considered because only a small amount of stationkeeping propellant is required to remain in the libration point orbits.

III. Solar Sail Pole-Sitter Orbits
    i. An initial guess for a long-duration spiral trajectory from LEO is determined by explicitly integrating a velocity-tangent steering law in backward time while targeting the two-body eccentricity and angular momentum required to arrive at the orbit. The path is then decomposed into node points.

    ii. Assuming that the coverage orbit is not part of the corrections process, discontinuities in the boundary conditions are resolved by implementing the transcription method for feasible solutions. Since the solar sail pole-sitter orbits are already near-optimal in minimum elevation angle, the converged transfers complete the mission design process.
    iii. End-of-life trajectories are not considered because it is assumed that the orbits are maintained for long durations with the solar sail, and hence, without the use of significant fuel.

IV. Solar Electric Propulsion Pole-Sitter Orbits

    i. Transfer Spiral-Out to the Orbit:
        a. An initial guess for the transfer is generated by explicitly integrating in forward time, starting from a low-altitude Earth orbit. The explicit control law for the initial guess involves tangent steering along the ECI velocity vector.
        b. A thrust-coast-thrust structure is assumed.
        c. The states, controls, and problem parameters are stored as node points for a multi-phase direct transcription method.
    ii. End-of-life Spiral-Down to a Lunar Frozen Orbit:
        a. An initial guess for the transfer is generated by explicitly integrating in forward time, starting at the end of the coverage orbit. The explicit control law for the initial guess involves tangent steering along the MCI anti-velocity vector.
        b. A thrust-coast-thrust structure is assumed.
        c. The states, controls, and problem parameters are stored as node points for a multi-phase direct transcription method.

Mission design applications are described where these steps for low-thrust transfer trajectory computation are successfully implemented.

5.1 Transfers Between Libration Point Orbits

Several future mission concepts are possibly enabled with low-thrust, fuel-optimal transfers between libration point orbits using a VSI engine. Most collinear libration point orbits are linearly unstable, thus, they may be exploited for fuel-efficient transfers to support cargo transportation for relay satellites or for shifts along multiple coverage orbits during a single mission. The low-dimensioned indirect shooting approach from optimal control theory offers the capability to rapidly investigate many possible locally optimal transfers within the design space. Given the selection of a departure and arrival orbit, the availability of such solutions allows a trajectory of interest to emerge based on a desired time or a fuel performance requirement. Furthermore, the time history of the engine performance along a given solution may be cross-checked against the requirements for a given VSI thruster.

5.1.1 Example: Transfers Between Two L_1 Southern Halo Orbits

As a preliminary design scenario, consider the computation and investigation of transfers between two different L_1 southern halo orbits in the Earth-moon system, selected from the family displayed in Figure 4.1. The two selected orbits appear in Figure 5.1, with the departure orbit in orange and the arrival orbit in blue. The departure orbit possesses a period $\mathbb{P} = 12$ days and a z-amplitude of 13,000 km, with a nondimensional, rotating, barycentric initial state, $\boldsymbol{x}_0$, equal to

$$\begin{aligned} \boldsymbol{x}_0^T &= (\boldsymbol{r}_0^T, \boldsymbol{v}_0^T) \\ &= (0.8234713145012070, 0, -0.0343599127302230, 0, 0.1438549685353680, 0) \end{aligned} \tag{5.1}$$

The arrival orbit is a near-rectilinear halo orbit with a period $\mathbb{P} = 10$ days and a z-amplitude of 72,000 km. The corresponding rotating, barycentric state, $\boldsymbol{x}_f$, is

$$\begin{aligned} \boldsymbol{x}_f^T &= (\boldsymbol{r}_f^T, \boldsymbol{v}_f^T) \\ &= (0.8652779595914100, 0, -0.1870934422517150, 0, 0.2471872973128290, 0) \end{aligned} \tag{5.2}$$

The initial values of $\boldsymbol{x}_0$ and $\boldsymbol{x}_f$ simply locate reference states when time-like parameters $\tau_1 = 0$ and $\tau_2 = 0$, respectively. Then, recall that these parameters enter the optimization problem as free variables that locate an optimal departure and insertion location to maximize the final spacecraft mass, i.e., to minimize fuel. The VSI engine parameters from Table 2.1 are implemented, and the lower-fidelity system model in equation (2.38) is selected. The adjoint control transformation [29] (Appendix A) is applied once to generate initial costates such that the VSI thruster is initially oriented parallel to the velocity vector. Then, both the indirect shooting method from Section 3.4.2 and the direct shooting method described in Section 3.4.3 are employed with central differencing gradients to generate $D\boldsymbol{F}$. After the initial converged solution is obtained, each remaining trajectory is determined via continuation, with t_f as the continuation parameter. Thus, the process maintains the previously converged $\boldsymbol{X}^{**}$ as the new initial guess $\boldsymbol{X}^0$, except that the variable t_f is updated. Since the initial burn time is fixed at $t_0 = 0$, updating t_f for each new solution is equivalent to updating the time-of-flight. With this formulation, converged trajectories are quickly computed for an entire family of solutions. Several sample optimal transfer trajectories appear in Figure 5.2, each with a different time-of-flight (TOF). Note that red indicates the powered arc, with the arrows in the thrusting direction. The green paths along each orbit depict the variation in the time-like-parameters τ_1 and τ_2 from the reference states in equations (5.1)-(5.2).

The representative transfers in Figure 5.2 are only six example optimal solutions out of 5,000 that are rapidly computed from the indirect shooting approach. The large set of solutions can be viewed as a locally optimal Pareto front in the multi-objective trade space represented as propellant consumed vs. time-of-flight, as appears in Figure 5.3. (The “jump” in the data near the 6-day mark in Figure 5.3 indicates a location where the optimization terminates due to numerical difficulties. The process is then restarted with new initial conditions, and new locally optimal solutions are obtained along a new solution branch. This may well reflect a dynamical challenge and warrants further investigation.) This multi-objective trade space represents a simple,

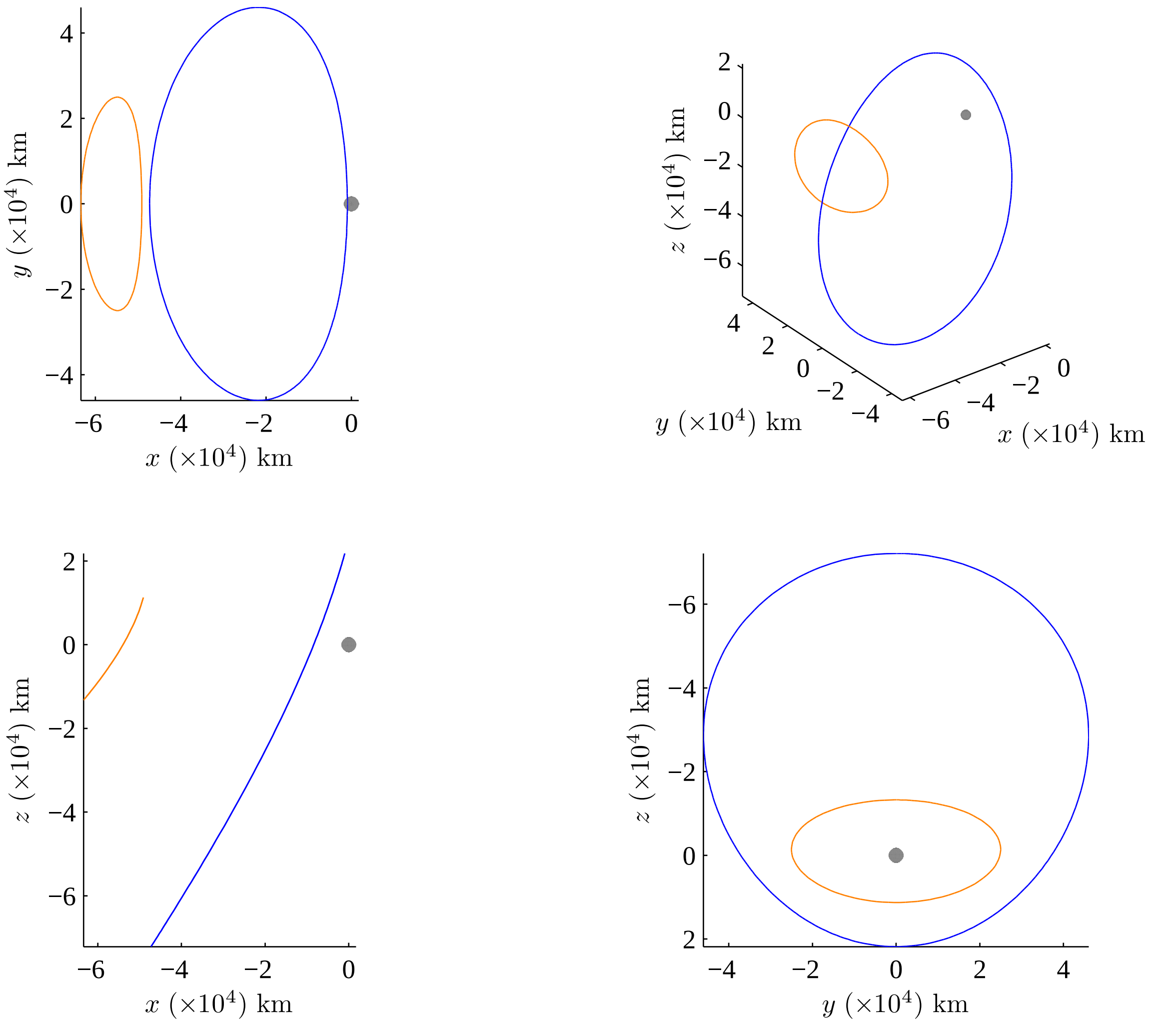

Figure 5.1. Projections of the Departure (Orange) and Arrival (Blue) L_1 Southern Halo Orbits, MCR Frame.

yet powerful selection tool for preliminary selection of a transfer based on the mission needs. Since neither the thrust magnitude nor specific impulse are constrained, the required engine performance for a given optimal transfer is available in Figures 5.4-5.5. Thus, for any transfer trajectory of interest, the physical limitations of the engine are quickly evaluated against the engine parameters required for implementation. As expected with the VSI engine, a longer time-of-flight allows the engine to increase I_{sp} and reduce the thrust, thus, increasing efficiency as the time-of-flight is increased.

The indirect and direct shooting methods exhibit similar convergence behavior. Initially, the indirect method is implemented using MATLAB®'s nonlinear equation solving package, "fsolve" with central difference gradients. However, a large time penalty is incurred due to the scripting language employed in a bounded, quasi-newton search with numerical gradients. The "real-time" speed is increased by a factor of 7,200 in the indirect shooting approach by switching to FORTRAN 90 (a compilable language), and incorporating SNOPT in its feasible mode. The direct shooting approach is also tested with similar success in FORTRAN 90, with slightly more robust behavior, but less rapidity in convergence. For further time comparison data on the specific machine used for the study, see Table 5.1.

Table 5.1 Time Comparison of Solution Methods Using Numerical Gradients.

Solution Method	Software Package	Coding	Number of Runs	Actual Time* (Minutes)
Indirect Shooting	fsolve	MATLAB	50	360
Indirect Shooting	SNOPT (Feasible Mode)	FORTRAN 90	5,000	5
Direct Shooting	SNOPT	FORTRAN 90	2,000	2

---

*Intel® Core™2 Quad 2.4 Ghz. CPU

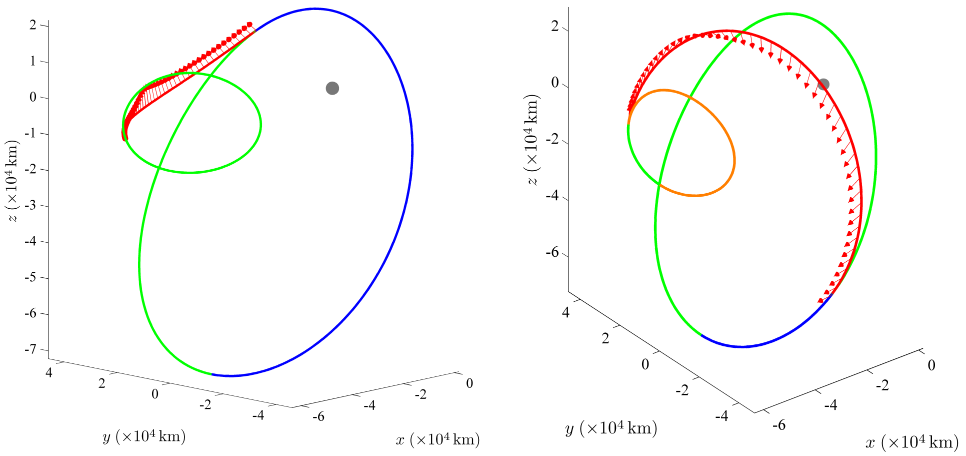

(a) TOF = 2.18 Days.

(b) TOF = 6.54 Days.

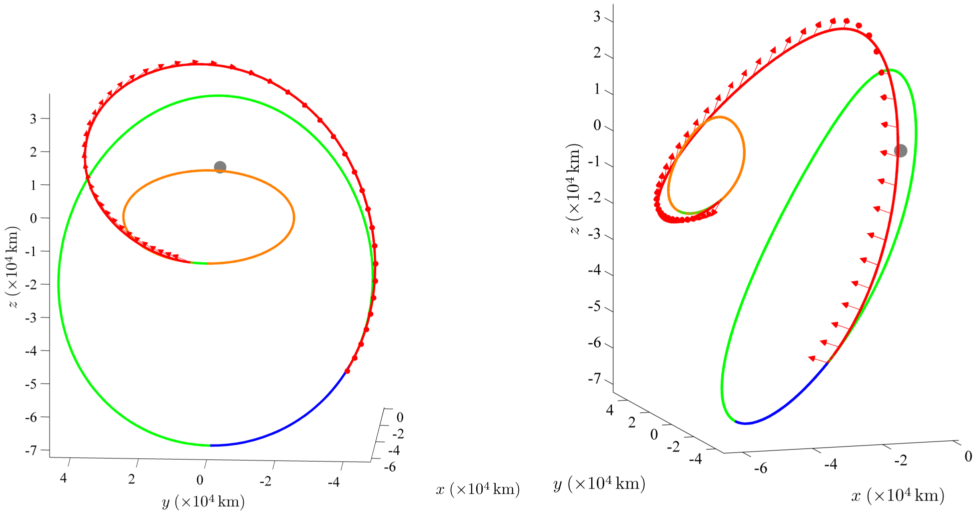

(c) TOF = 8.73 Days.

(d) TOF = 10.91 Days.

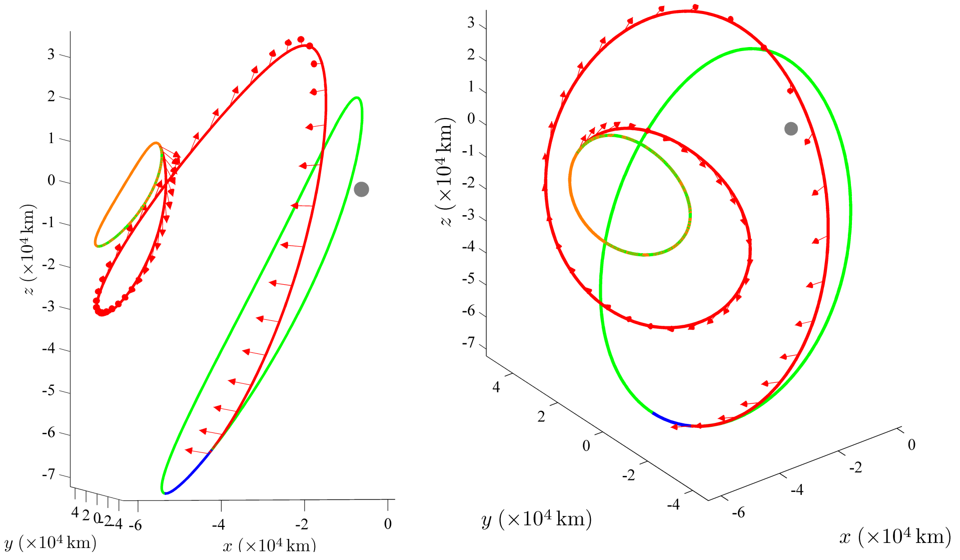

(e) TOF = 15.3 Days.

(f) TOF = 19.6 Days.

Figure 5.2. Optimal Transfers between 12-Day L_1 Halo Orbits Using a VSI Engine, MCR Frame.

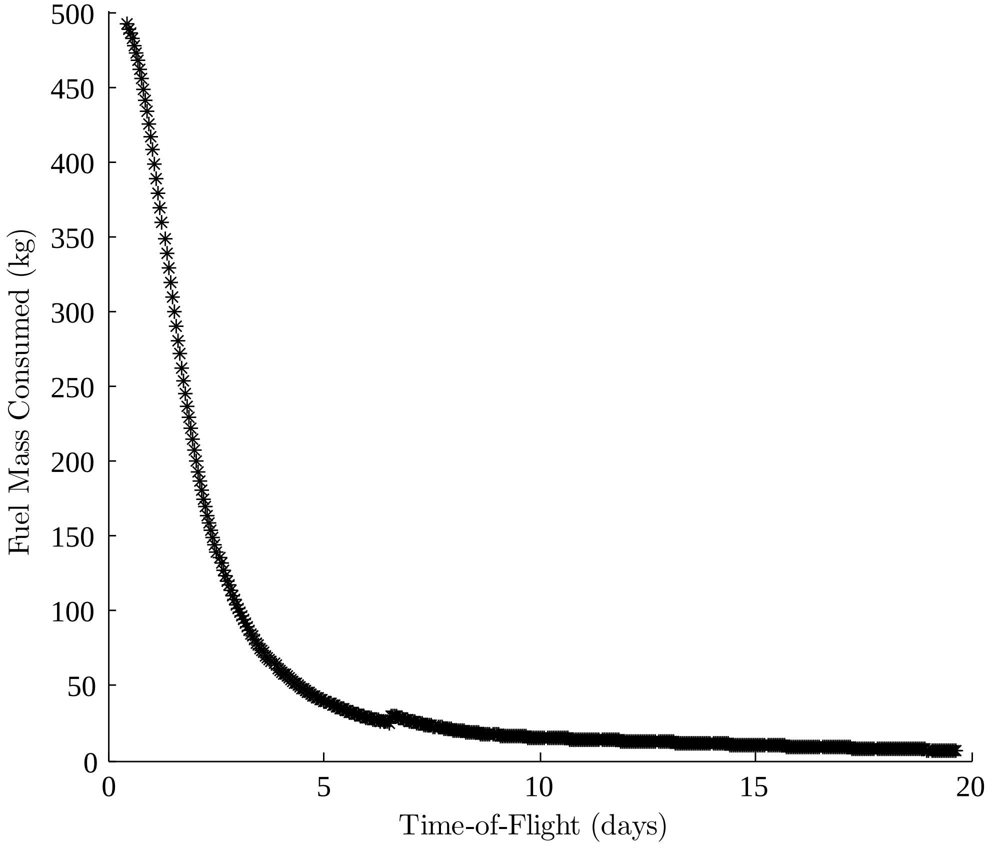

Figure 5.3. Fuel Mass Consumed vs. Time-of-Flight Locally Optimal Pareto Front.

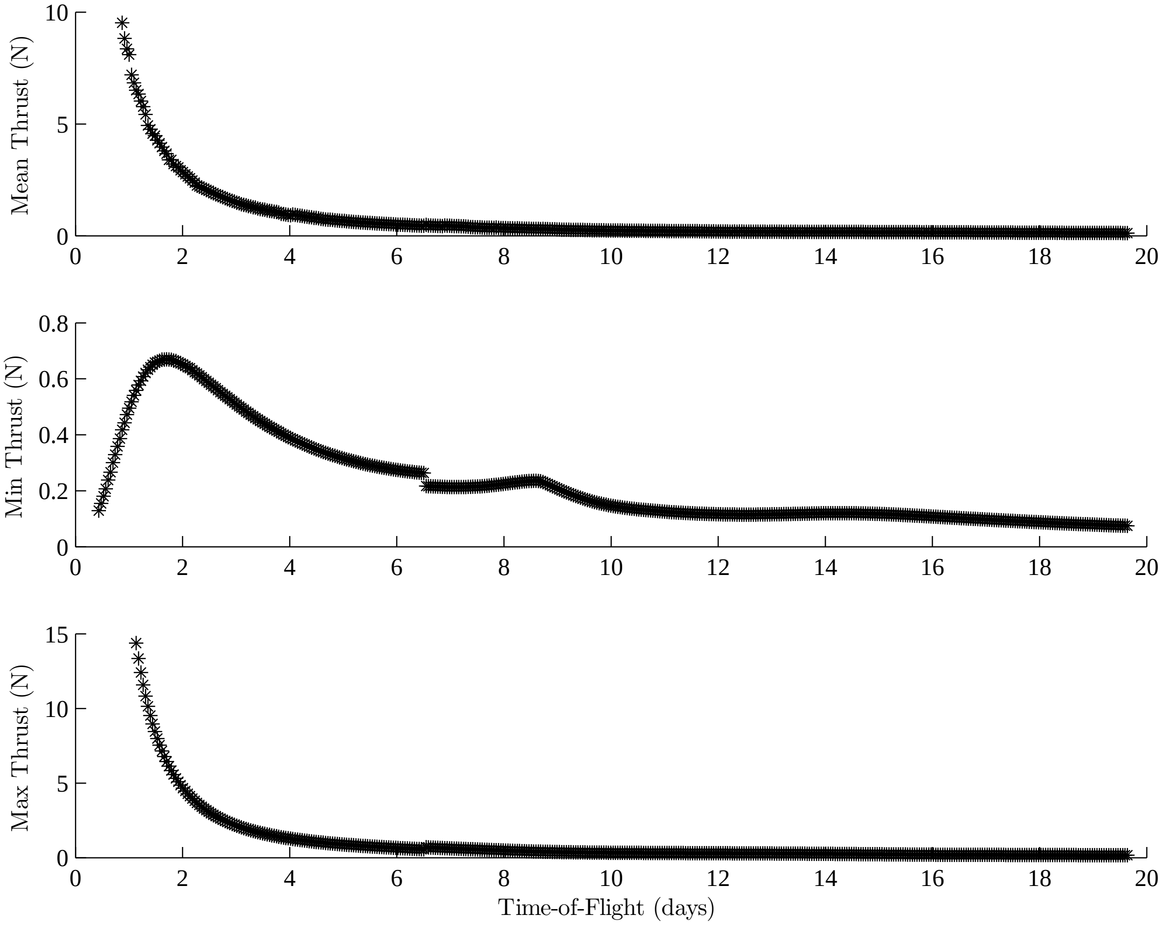

Figure 5.4. Thrust Values Corresponding to Optimal Solutions.

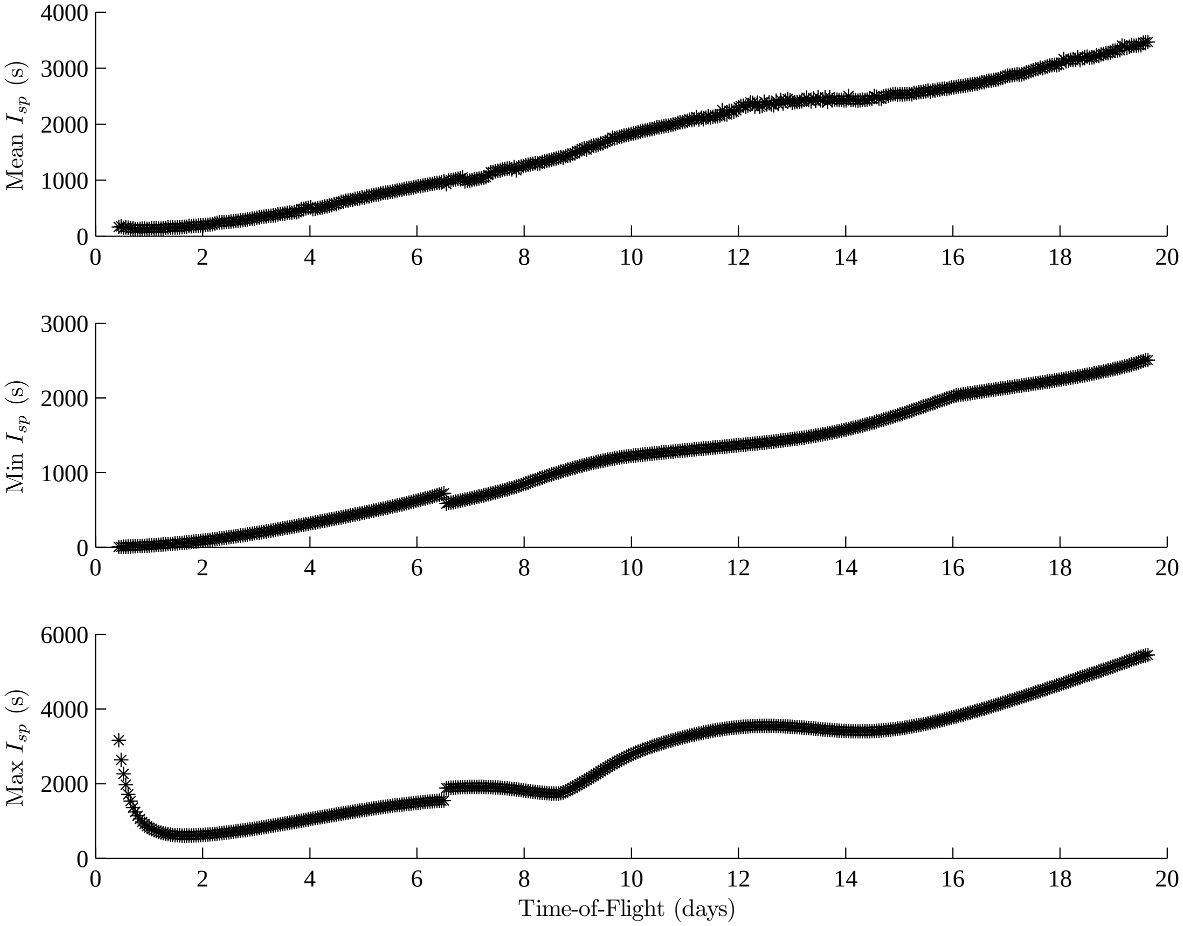

Figure 5.5. Specific Impulse Values Corresponding to Optimal Solutions.

5.2 Higher-Fidelity, Solar Sail Orbit Transfers

The exclusive use of a solar sail for lunar south pole coverage implies that the spacecraft ideally inserts into the pole-sitter orbit from a propellant-free transfer trajectory using only the sail. (Alternative schemes are also available, but the use of propellant for thrusting is required. [82]) Although a spiral-out from low-Earth orbit is impractical due to atmospheric drag, an initial "piggy-back" leg along a geosynchronous transfer orbit (GTO) has been proposed as a viable option by previous researchers. [20] To reduce the potential effects of drag, which are not modeled in this analysis, periapsis altitude for the GTO is defined as 1,000 km. To compute a solar sail transfer, an intuitive preliminary control law is employed to generate an accurate initial guess. All trajectory design occurs in the ECI higher-fidelity model, that is, equation (2.62), that includes the forces $\boldsymbol{f}_G$ described in equation (2.67) due to point mass gravity of additional bodies in the ephemeris model, and $\boldsymbol{f}_T$ as described in equation (2.29) using the actual sun-to-spacecraft line $\hat{\boldsymbol{l}}$. The oblateness term $\boldsymbol{f}_O$ in equation (2.68), the non-sail related SRP force $\boldsymbol{f}_S$ in equation (2.69) and shadowing criteria in Section 2.7.3 are neglected in this preliminary analysis. Since the transfer is essentially free of any propellant, fuel optimization is not required, and the solution only requires feasibility as determined from numerical corrections using the transcription method with the minimum norm search direction. Mesh refinement iterations are not implemented, however, the time spacing of the node points matches those input by the explicitly integrated initial guess. Once the guess that is supplied to the transcription method converges, the boundary conditions corresponding to the departure GTO and the previously identified near-optimal coverage orbits are satisfied. Thus, the end-to-end baseline mission design for a solar sail pole-sitter in support of lunar south pole communications is complete, and the concluding analysis for the transfers is discussed.

5.2.1 Preliminary Control Law

Due to very long flight times and sensitive, nonlinear dynamical behavior near the Earth, an accurate initial guess is required to refine a transfer trajectory with the collocation procedure. An intuitive, explicitly integrated initial guess scheme is developed by assuming a steering law for the solar sail. All integration occurs in the ECI, EMEJ2000 coordinate frame in the higher-fidelity model using the assumptions from the previous section, since the RTBP offers no major simplifying assumptions that can be exploited with this transfer scheme. Numerical integration also occurs in backward time, allowing the initial state to be fixed on the lunar south pole coverage orbit at the proper insertion date in the ephemeris model; as a consequence, the exact GTO remains unspecified. Then, the initial guess scheme requires only that the two-body energy $E_\oplus$ and the orbital angular momentum $H_\oplus$ with respect to the Earth, are matched as close as possible to the corresponding GTO values when the propagation terminates.

To reduce the energy during backward numerical integration, the velocity-tangent steering law, detailed in Figure 5.6, is employed. The sail acceleration, $\boldsymbol{f}_T$, is initially aligned along the inertial velocity vector $\boldsymbol{V}$, but when $\hat{\boldsymbol{l}} \cdot \boldsymbol{V}$ is negative, the sail is oriented such that $\boldsymbol{u} \perp \hat{\boldsymbol{l}}$ produces no thrust. For a two-sided sail, $\boldsymbol{u}$ flips 180° at the completion of every cycle, and as a consequence $\boldsymbol{u}$ is either parallel or anti-parallel to $\boldsymbol{V}$ during thrusting. When the sail requires re-orientation to an attitude that yields no acceleration, i.e., the sail is "off", $\delta = \pm 90^\circ$ and α is oriented such that $\boldsymbol{u}$ is as close as possible to $\boldsymbol{V}$ (or $-\boldsymbol{V}$ depending on the cycle) to ensure a smooth control transition the next time the sail is activated.

Using only this algorithm, $E_\oplus$ is reduced without any attention to the rate of decrease in $H_\oplus$. Problems arise during backward propagation because $H_\oplus$ decreases too quickly, resulting in a highly elliptical orbit that passes through the Earth. Other possible approaches, such as McInnes' locally optimal steering law, [20] reduce $H_\oplus$ even faster, since most thrusting occurs in the vicinity of apoapsis. For similar rates of decrease in $E_\oplus$ and $H_\oplus$, the velocity-tangent steering law is, therefore, modified to force maneuvers away from apoapsis during the transfer. This modification is accomplished by selecting the Earth-relative flight-path-angle $\gamma_\oplus$ as an additional switching condition. Thus, the sail is now always off unless $\hat{\boldsymbol{l}} \cdot \boldsymbol{V} = 0$ and $\gamma_\oplus$ lies within an acceptable region, at which point the sail switches on. This new "*E-H*" steering law corresponds to wait-times until the correct phasing of the transfer with the sun-to-spacecraft line occurs. Details for the full implementation of this method are available by examination of the function generator in Figure 5.7. For numerical considerations upon transition to the transcription method, initial guesses that pass through the Earth are avoided. The stopping condition for the integration, that is, $E_\oplus = 0$ and $H_\oplus > 0$, is sufficient to ensure this behavior. Backwards integration of the *E-H* steering law is also repeated at initial conditions corresponding to nodes around the baseline ephemeris coverage orbit (computed in Section 4.3.4) until an accurate initial guess is obtained. Since the coverage orbit is a converged ephemeris solution, a successful transfer obtained from the collocation scheme results in a continuous insertion without a maneuver.

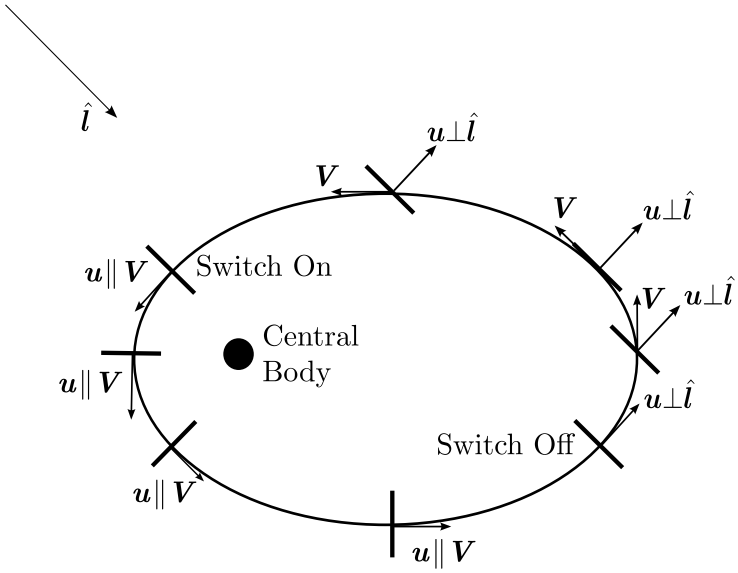

Figure 5.6. Velocity-Tangent Steering Law.

```
Input $\gamma_{min}$ & $E_{GTO}$, and set $s = 1$.
    DO WHILE $E_\oplus < E_{GTO}$
        DO WHILE $\gamma_\oplus < \gamma_{min}$
            Propagate equation. (2.62) with $\boldsymbol{f}_T = 0$ until
                $\hat{\boldsymbol{l}} \cdot \boldsymbol{V} = 0$ & $d(\hat{\boldsymbol{l}} \cdot \boldsymbol{V})/dt < 0$.
            Update $\gamma_\oplus$.
        END
        Propagate equation. (2.62) with $\boldsymbol{u} \parallel (s\boldsymbol{V})$ until
            $\hat{\boldsymbol{l}} \cdot \boldsymbol{V} = 0$ & $d(\hat{\boldsymbol{l}} \cdot \boldsymbol{V})/dt > 0$.
        Update $E$, and set $s = -s$.
    END
```

Figure 5.7. Function Generator for the *E*-*H* Steering Law.

5.2.2 Refinement with the Transcription Method

From an accurate initial guess generated with the *E*-*H* thrusting law, the trajectory must be refined with collocation to generate a feasible solution. The variable vector is again filled with the elements in equation (3.90), however, there is no need to specify any slack variables $\boldsymbol{\eta}_i$,$\boldsymbol{\eta}_{i,2}$, and $\boldsymbol{\eta}_{i,3}$ or problem parameters $\boldsymbol{\mu}$. In formulating the new constraint vector (equation (3.91)), the defect constraints $\boldsymbol{\Delta}_{i,1}$, $\boldsymbol{\Delta}_{i,c}$, and $\boldsymbol{\Delta}_{i,4}$ (equations (3.84)-(3.86)), and the control-magnitude constraints ψ_i (equation (3.87)) are enforced as usual, but no path constraints (equation (3.88)) are required, i.e. $m = 0$. The boundary conditions that bracket the transfer are enforced by adding general constraints (equation (3.89)) at the 1$^{\text{st}}$ node and the n^{th} node. These boundary conditions are defined as the insertion state on the lunar south pole coverage orbit and the energy and angular momentum associated with GTO, i.e.

$$
\begin{array}{lll}
h_1\left(X_n\right) = X_n - X^* & & \\
h_2\left(Y_n\right) = Y_n - Y^* & & \\
h_3\left(Z_n\right) = Z_n - Z^* & \qquad & h_1\left(\boldsymbol{x}_1\right) = \left\|\boldsymbol{V}_1\right\|^2/2 - \left(1 - Gm_{\oplus}\right)/\left\|\boldsymbol{R}_1\right\| - E_{\text{GTO}} \\
h_4\left(V_{X_n}\right) = V_{X_n} - V_X^* & \qquad & h_8\left(\boldsymbol{x}_1\right) = \left\|\boldsymbol{R}_1 \times \boldsymbol{V}_1\right\| - H_{\text{GTO}} \\
h_5\left(V_{Y_n}\right) = V_{Y_n} - V_Y^* & & \\
h_6\left(V_{Z_n}\right) = V_{Z_n} - V_Z^* & &
\end{array}
\tag{5.3}
$$

where the superscript "*" identifies a condition along the coverage orbit. Since the transfer involves a large number of spirals around the Earth, one strategy to compensate for the sensitive dynamical region is to implement the mesh refinement scheme. However, for simplicity, using pre-specified time ratios from the explicit integration of the E-H thrusting law is effective. These time ratios are already spaced in recognition of the sensitive dynamics, and since an accurate initial guess is input to the procedure, adaptive refinement is bypassed. Since the time on each trajectory segment is fixed, the locations of all celestial bodies within the DE405 ephemeris file are only initialized once. The Earth-centered formulation of equation (2.62) is useful for numerical accuracy due to the many spirals that pass near the Earth. For each transfer, 5,000 nodes are selected, resulting in 104,988 free variables, 94,990 total constraints, and a $\boldsymbol{DF}$ matrix including over 99.96% zero entries. The states and controls are adjusted until a control history is determined along a continuous trajectory that satisfies the constraints in equation (3.91).

A successfully converged, higher-fidelity sample transfer to the L_2 orbit, corresponding to a sail acceleration level $\kappa = 0.58$ mm/s^2, appears in Figure 5.8. The total transfer time from GTO is 401 days, with 106 days of on-time, and 397 on/off switches of the sail to arrive at the orbit (in green). These switches can be visualized in Figure 5.8 since the red arcs correspond to on-times and the blue phases correspond to off-times. Inspection of the control history in Figure 5.9 reveals these switch times as the instances when $\delta = \pm 90°$. Proper phasing of the sun, orbit, and sail is important, since the sail is only active 26% of the time. It is again emphasized that this resulting transfer requires no actual propellant, despite the fact that the transfer time appears long. Such long times are feasible for the mission concept of satellites designed for purposes of communications. The resulting transfer trajectories are preliminary and do not consider the possibility of thermal issues. Unlike the coverage orbits, the transfers also assume that the sail can change directions beyond the capacity of current sail technology. With additional constraints on the sail turning rates, however, this problem may still be avoided in future trajectory design iterations. All transfers are currently computed independent of the coverage orbits and therefore alternate sources of thrust can also be employed to support a pole-sitter mission.

5.2.3 Transfer Design Summary for the Solar Sail Pole-Sitter Mission

With the transfer trajectories computed, the full mission trajectory for the solar sail pole-sitter for lunar coverage is complete. Hundreds of orbit scenarios were generated during the course of the investigation, but recall that only the five near-optimal orbits from Section 4.3 are specifically selected as feasible and also possess the largest elevation angle lower bound ϕ_{lb}. Each scenario of interest is successfully transitioned to the higher-fidelity model. (See Table 5.2.) A higher percentage of sail on-time is observed in the orbits with a lower characteristic acceleration. When more thrust acceleration is available, the transfer time is not necessarily faster due to the unique phasing required in the system. This unique phasing increases the times-of-flight, a range over 248-446 days, due to the fact that the sail provides thrust only 8%-32% of that time. Despite the penalty on flight time, the tremendous advantage is that each transfer is potentially propellent-free.

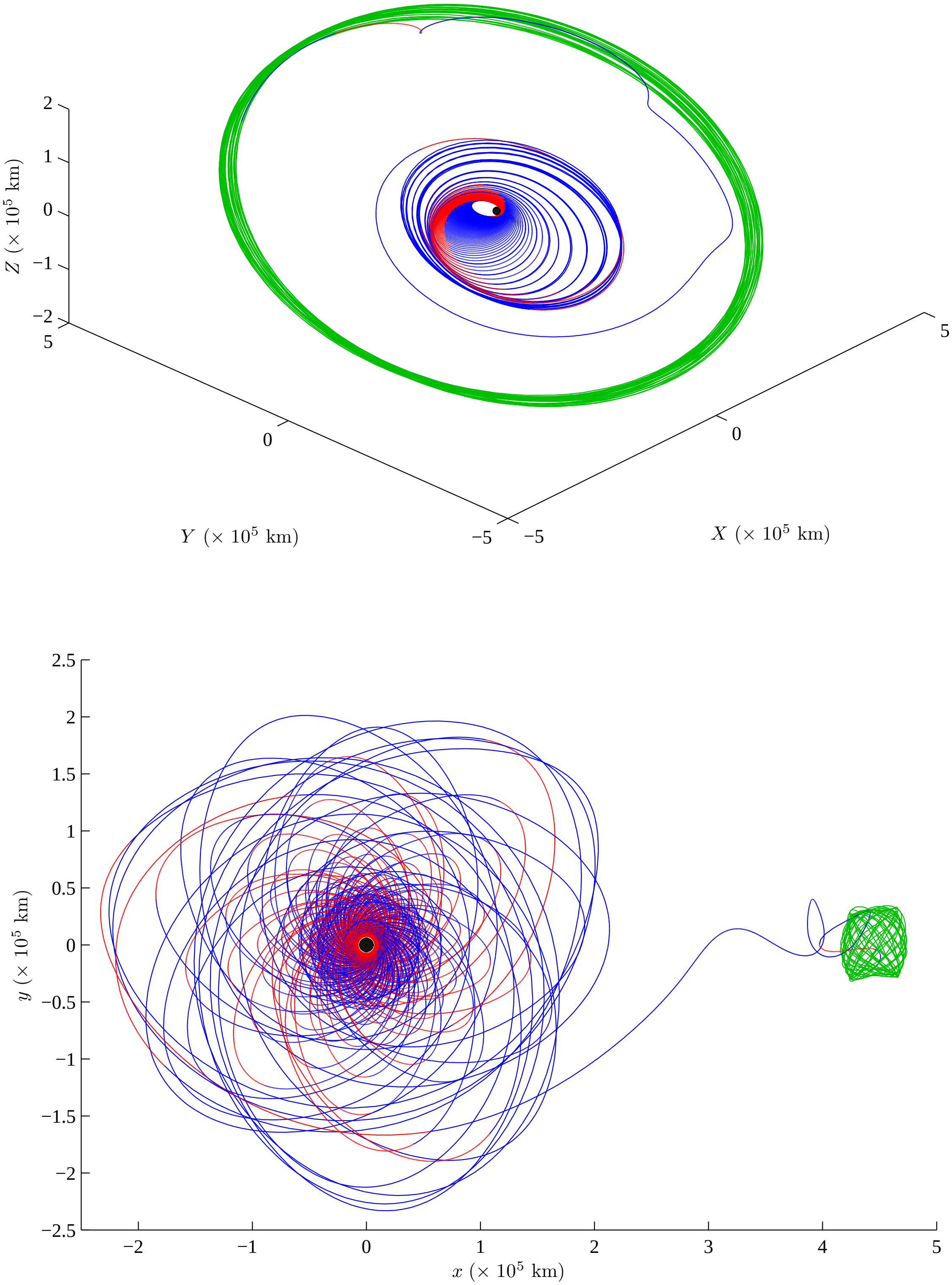

Figure 5.8. Transfer to the L_2, $\kappa = 0.58$ mm/s^2 Quasi-Periodic Pole-Sitter Orbit in the Higher-Fidelity Model, ECI Frame (Top) and x-y projection in the ECR Frame (Bottom).

Table 5.2 Transfer Data Summary for Solar Sail Example Scenarios in the Higher-Fidelity Model.

	$\kappa = 0.58$ mm/s^2		$\kappa = 1.70$ mm/s^2		
Type	L_1	L_2	L_1	L_2	hover
Epoch (UTC)	4 Feb 2011 16:48:00	8 Nov 2010 04:48:00	26 May 2011 02:24:00	17 Oct 2010 07:12:00	23 Apr 2011 16:48:00
Transfer Time (days)	309	401	199	446	248
On-Time (days)	99	106	35	34	35
% On-Time	32	26	17	8	14
No. Switches	429	397	113	113	119
Insertion Date (UTC)	10 Dec 2011 14:24:00	14 Dec 2011 02:24:00	10 Dec 2011 14:24:00	6 Jan 2012 14:24:00	27 Dec 2011 04:48:00

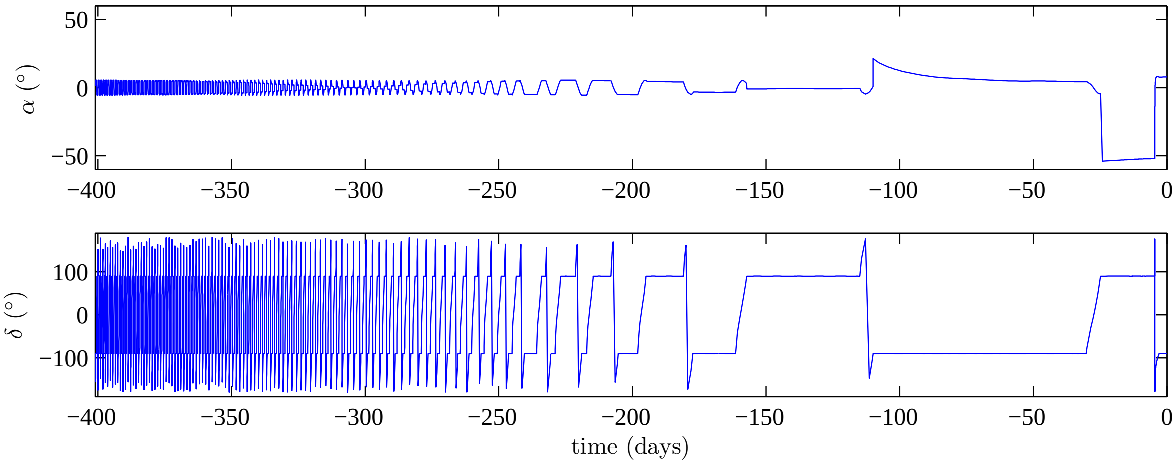

Figure 5.9. Control History for Transfer to the L_2, $\kappa = 0.58$ mm/s^2 Quasi-Periodic Pole-Sitter Orbit in the Higher-Fidelity Model.

5.3 Solar Electric Propulsion Transfers

After the feasible solution for a temporary coverage orbit using solar electric propulsion is computed, the focus shifts to assembling independent guesses for the remaining portions of the multi-phase optimization problem as outlined in Section 4.4. With the initial guess variables, $\boldsymbol{X}_2^0$, for the preliminary coverage orbit already established, initial guesses are required for the transfers in phases #1 and #3. Similar to the process for the solar sailing transfers, explicitly integrated initial guesses are determined first and, then, decomposed into collocation node points. In contrast to the solar sailing transfers, however, the transcription process is not immediately employed to generate converged transfer trajectories. Rather, the node points for phase #1 and phase #3 are assigned to the elements in the initial guess variable vectors $\boldsymbol{X}_1^0$ and $\boldsymbol{X}_3^0$, respectively. These initial guess vectors serve as input for a larger multi-phase transcription process. Each transfer phase is structured with a pre-determined thrust-coast-thrust sequence ($k = 2$), and a simple two-body inertial velocity-tangent steering law is employed to model thrusting. This control structure is a reasonable assumption due to the observed behavior of related solutions in the literature. [81]. The solar electric propulsion velocity-tangent law is less restrictive than the solar sailing version described in Section 5.2.1 because the thruster can always be aligned in the velocity direction if necessary (given that there is no shadowing). Since the solar electric propulsion pole-sitter mission is solved in both a lower- and higher-fidelity model, the specific details for generating each initial guess is appropriate.

5.3.1 Initial Guesses for the Lower-Fidelity Transfers

For preliminary design in the RTBP, the barycentric system model represented in equation (2.37) is employed and the ISS orbit is simulated as a circular orbit in the x-y plane, with an altitude equal to 325 km. Departing the ISS orbit in phase #1 involves hundreds of spirals around the Earth as the spacecraft builds up sufficient energy to escape. To avoid an unnecessary and possibly an intractable number of design variables in the transcription formulation, including possible problems with poorly scaled variables, an explicit integration process is used exclusively for the majority of the Earth escape. For practical application, a basic velocity-tangent steering law during Earth escape, one that maximizes the instantaneous two-body kinetic energy, is operationally simple and is observed to closely track the direction defined by Lawden's primer vector in similar optimal control formulations. [32] This phase #1 spiral sequence terminates once escape from Earth's gravity field is observed, after 202.16 days. (Note that, after this time, a velocity-pointing strategy no longer reflects the fully converged solution as the thrust-direction must support the boundary conditions in phase #2.) At this point, the boundary conditions are stored, and the entire sequence is not considered further as part of the eventual three-phase numerical procedure.

After spiral-out from the Earth, the remainder of phase #1 is the powered Earth-escape leg without spirals, the translunar coast, and the powered insertion into phase #2. These final stages of phase #1 are the only part that is decomposed into node point variables and stored for later use in the multi-phase solution. (Recall that the initial spiral out from Earth is fixed.) There are many ways to create an initial guess for input to the numerical procedure including a primer-vector law without the optimality constraints or, even more simply, the velocity-pointing law. A simultaneous forward and backward explicit integration process with the velocity-pointing law is sufficient. A large discontinuity is observed at the translunar coasting match point, but it is easily resolved in the multi-phase corrections process discussed in the next chapter.

Construction of the third phase (phase #3) of the trajectory follows a strategy similar to that used to develop phase #1, except that no preliminary spiraling is required; in phase #3 the entire initial guess is used to initiate the solution process. A variety of explicit integration and visual inspection procedures are available, with various of control law predictions. As in the initial guess process for phase #1, a discontinuity in the path is acceptable. In this case, for lunar orbit capture, the thrusting portion of the thrust-coast-thrust arc employs an anti-velocity pointing law. Also incorporated are the boundary conditions from phase #2 and the insertion conditions for a lunar frozen orbit. The frozen orbit state that serves as a boundary condition for this phase is the apoapse of an orbit from Ely. [47] (See Table 5.3 for the associated orbital elements.) Insertion occurs at apoapsis in a frozen lunar orbit with a 6,541.4 km semi-major axis and 0.6 eccentricity. The inclination with respect to the x-y plane is 56.2°. Once the integrated guesses for phase #1 and #3 are produced, the paths are decomposed into nodes, and used in conjunction with the coverage orbit solution as an initial guess to construct $\boldsymbol{X}^0$ consistent with equation (3.99). The assembly of this variable vector is detailed in Chapter 6.

5.3.2 Initial Guesses for the Higher-Fidelity Transfers

For phases #1 and #3, the same explicit integration process is employed with the higher-fidelity to model. However, the model and the associated boundary conditions are modified to produce a more accurate mission design trajectory. For phase #1, the full Earth-centered version of equation (2.62) is explicitly integrated, including shadowing conditions (Section 2.7.3), originating from an International Space Station ephemeris state in Table 5.3, and using velocity-tangent steering. The Julian date at epoch corresponds to July 17, 2009 at 16:00:00 UTC. Recall that the shadowing conditions imply that when the geometry between the sun-spacecraft, Earth-spacecraft, and Earth-sun vectors indicates eclipsing, the engine is turned off, i.e., $\boldsymbol{f}_T = \mathbf{0}$, because power is unavailable from the solar arrays. Additionally, the spacecraft experiences no SRP during the eclipse, and therefore $\boldsymbol{f}_S = \mathbf{0}$ in equation (2.69). As in the lower-fidelity case, the initial spiral-out from ISS terminates when the trajectory is observed to escape from the vicinity of the Earth and this sequence during phase #1 is fixed, i.e., it does not enter further numerical corrections in the direct transcription approach. This early part of the transfer is displayed in Figure 5.10, where it is noted that significant instances of shadowing are clearly evident that force the engine to switch off. (The time-of-flight penalty incurred due to this shadowing is discussed later.) The remaining portion of the phase #1 trajectory follows the prescribed thrust-coast-thrust pattern, and an initial guess is determined with explicit integration by varying the time associated with each arc until the final state approximately matches the initial state that defines the origin of phase #2. The initial guess for phase #3 is generated using the frozen orbit conditions in Table 5.3 and explicitly integrating the moon-centered version of equation (2.62), backward in time, using anti-velocity-tangent steering. A guess for the final time to initiate the backward integration is based on the results of the fully-converged lower-fidelity solution. The paths are decomposed into nodes as part of the guess for $\boldsymbol{X}^0$ consistent with equation (3.99), and the moon-centered version of equation (2.62) is used exclusively thereafter in the corrections processes. Given the geometry of the path-constrained coverage orbits, it is reasonable to assume that no shadowing occurs during instances when the moon-centered equations are employed.

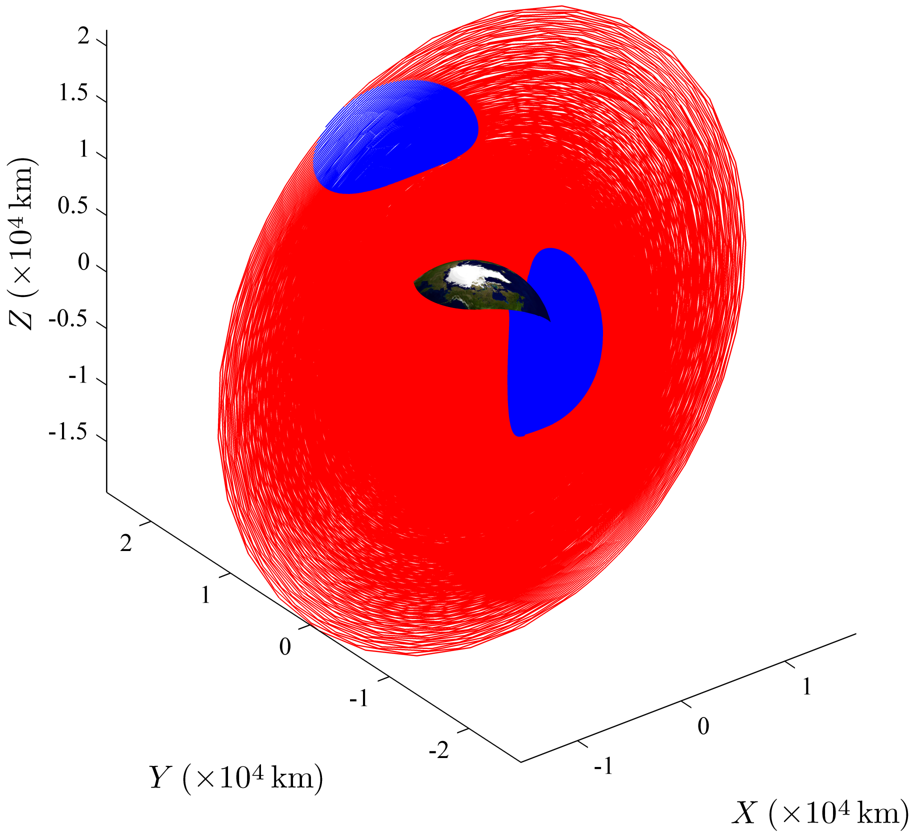

Figure 5.10. Higher-Fidelity, Fixed Earth Spiral-Out Trajectory in the ECI Frame, with CSI Engine Thrusting (Red) and Coasting due to Shadowing (Blue).

Table 5.3 Transfer Phase Boundary Conditions.

Parameter	Value	Units
Julian date at epoch	2455030.16666667	days
X_0	$-217,157.872523697$	km
Y_0	$-265,663.694939137$	km
Z_0	$-143,797.489787933$	km
V_{X_0}	7.14747905069707	km/s
V_{Y_0}	-0.072004027654518	km/s
V_{Z_0}	-4.64811621321917	km/s
$a_{\leftmoon f}$	$6,541.4$	km
$e_{\leftmoon f}$	0.6	°
$i_{\leftmoon f}$	56.2	°
$\omega_{\leftmoon f}$	-90	°

6. MULTI-PHASE DIRECT TRANSCRIPTION OF AN ELECTRIC PROPULSION POLE-SITTER MISSION

Producing an optimal, fully converged trajectory for a lunar pole-sitter mission, using solar electric propulsion, requires the full application of the direct transcription method, including parameter optimization with nonlinear programming. Recall that for temporary coverage of the lunar south pole, the end-to-end mission is ideally decomposed into three separate phases:

1. Earth-centered, spiral out from the International Space Station to the Moon.
2. Pole-sitting position maintained for as long as possible.
3. Moon-centered, spiral down to an elliptically inclined stable orbit.

For the temporary coverage mission, the optimization goal is maximization of the time-of-flight during phase #2 subject to the functional dependencies of phase #1 and phase #3. Recall that the problem is solved twice, using two different models as discussed previously. The first solution employs a lower-fidelity model and considerable simplifications to investigate whether or not a solution is possible. The second solution employs the higher-fidelity, moon-centered model and an implementation of the complete direct transcription procedure including the mesh refinement algorithm with NLP to validate the results. The full listing of differences in the two solutions is summarized in Table 6.1. Note that for the trajectory design in this mission scenario, all of the problem constants are found in Tables 2.1 and 5.3.

6.1 Combining the Phases for Direct Transcription

Sections 4.4 and 5.3 establish a framework for developing the initial guess for each of these three phases. First, Section 4.4 describes a means of generating a feasible

Table 6.1 Features of the Solar Electric Pole-Sitter Solutions.

	Lower-Fidelity Solution	Higher-Fidelity Solution
System Model	RTBP, Equation (2.37)	MCI Full Model, Equation (2.62)
Departure Orbit	Circular, Planar Orbit, 325 km Altitude	Ephemeris ISS State
End-of-Life Orbit	Lunar Frozen Orbit Conditions [47]	Lunar Frozen Orbit Conditions [47]
Ground Site	Lunar South Pole	Shackleton Crater
Gravitational Ephemerides	No	Yes
Lunar Librations	No	Yes
Shadowing	No	Yes*
SRP	No	Yes
Earth Oblateness	No	Yes
Mesh Refinement	No	Yes

---

*Shadowing is only assumed during the fixed ECI spiral-out computed in Section 5.3.

coverage orbit for phase #2 that continuously meets the path constraints representing the bounding cone using many thrusting and coasting arcs. Then, Section 5.3 outlines a method to produce a discretized initial guess for phases #1 and #3 that links the ISS orbit and end-of-life orbit, yet still possesses an arrival and departure discontinuity with phase #2. Now, the variables across all phases that comprise the complete, yet still discontinuous initial guess, enter the multi-phase direct transcription problem outlined in Section 3.5.4. Let the vector $\boldsymbol{X}_2$ represent the variables from a solution for phase #2, and $\boldsymbol{F}_2$ comprises the corresponding constraints. Similarly, let $\boldsymbol{X}_1$ and $\boldsymbol{X}_3$ be the variables for phases #1 and #3, with respective constraints $\boldsymbol{F}_1$ and $\boldsymbol{F}_3$. To solve the larger collocation problem, the total design variable vector is simply

$$\boldsymbol{X}^T = \left(\boldsymbol{X}_1^T, \boldsymbol{X}_2^T, \boldsymbol{X}_3^T\right) \tag{6.1}$$

and the entire constraint vector is

$$\boldsymbol{F}^T = \left(\boldsymbol{F}_1^T, \boldsymbol{F}_2^T, \boldsymbol{F}_3^T, \boldsymbol{F}_{\text{BC}}^T\right) \tag{6.2}$$

The resulting block-diagonal structure of the Jacobian matrix $D\boldsymbol{F}$ is depicted in Figure 6.1, where zero entries are shaded in gray. Recall, however, from Section 3.5.4

that each of the block elements of $\boldsymbol{DF}(\boldsymbol{X})$ in Figure 6.1 are actually sparse submatrices, leading to a very sparse matrix that can be economically exploited during numerical iterations.

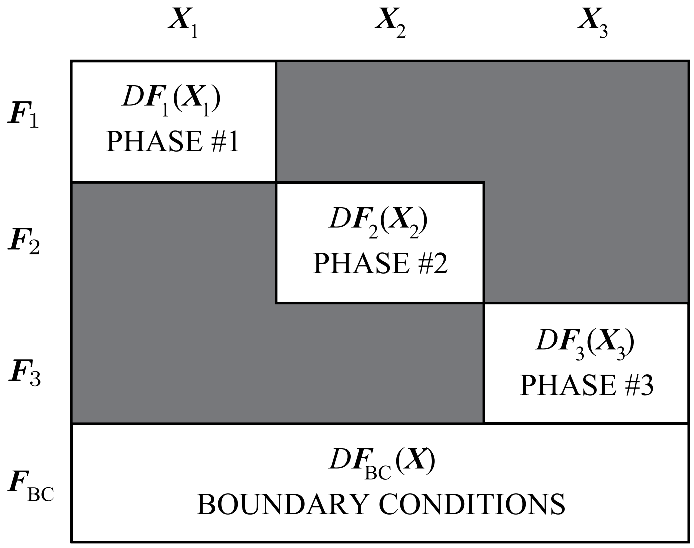

Figure 6.1. Complete Structure of Jacobian Matrix.

A feasible solution is first calculated with equation (3.2) and equation (3.11), where equation (6.1) and equation (6.2) specify the problem formulation. The elements of $\boldsymbol{DF}$ are computed analytically when possible, but the complex-step method is also used for cumbersome derivatives, as well as central differencing derivatives if perturbed ephemeris function evaluations are required. The feasible solution serves as an initial guess for the optimization with SNOPT where the time to complete phase #2 is maximized. That is, in equation (3.97), the objective is

$$F_0(\boldsymbol{X}_2) = -\sum_{j=1}^{k} T_{b,j} - \sum_{j=1}^{k-1} T_{c,j} \tag{6.3}$$

where $T_{b,j}$ and $T_{c,j}$ are the times along each arc in phase #2, or the coverage phase. The problem parameters for the thrust and coast arcs are initial mass, initial time, and arc duration. The variables that appear in equation (6.3) are, thus, the problem dependent variables corresponding to the last node segment along each arc, or $\boldsymbol{\mu}_{n_{b,j}-1}$

and $\boldsymbol{\mu}_{n_{c,j}-1}$. The problem parameters are assumed independent for each collocation segment and constraints are added to enforce equality in the parameters across the arc. (This assumption to maintain independent constraints aids in the numerical efficiency for large-dimensioned, sparse problems.) Additionally, there are constraints to ensure that arc duration is always positive and that initial mass and initial time for each arc is consistent with $T_{b,j}$ and $T_{c,j}$. The boundary conditions fix an initial state, control, time, and mass at the initiation of the variable portion of phase #1. Boundary conditions are also applied to ensure state, control, time, and mass continuity between the phases. Finally, a boundary condition forces the final state along the phase #3 trajectory arc to correspond to a semi-major axis, inclination, eccentricity, and argument of periapsis consistent with conditions of Table 5.3 for the final lunar frozen orbit. Constraints also force the insertion point into the lunar orbit to occur at apoapsis of the frozen orbit and in the x-z plane associated with the MCR frame.

6.2 Lower-Fidelity Solution without Mesh Refinement

After a thorough exploration of the coverage orbit design space, the direct transcription method, excluding mesh refinement, is applied simultaneously to all three phases to obtain the desired proof-of-concept lower-fidelity trajectory. Feasibility is obtained first with the minimum norm search direction and is then used as an initial guess for an optimal solution using NLP.

6.2.1 Feasible Solution

Even with a relatively large discontinuity in the phase #1 and phase #3 transfers that arrive and depart phase #2, the feasible three-phase solution is easily computed, yielding a coverage orbit of 447.04 days. (See Figure 6.2.) The spiraling portion denoted in purple, computed during the guess generation in Section 5.3.1, is not a part of the corrections process; only the red thrusting and blue coasting arcs are shifted during the collocation process. The plot also includes a propagation of the final stable lunar orbit (green) upon the completion of phase #3. The total time for the transfer to the moon, including the fixed transfer-out as well as the time for phase #1, is 244.97 days, corresponding to arrival at the coverage orbit with 315.90 kg of fuel. At this point, the spacecraft utilizes 264.19 kg of fuel to achieve a total duration of 447.04 days in the phase #2 coverage orbit. Although the coverage orbit uses 35 thrust arcs and 34 coast arcs, the minimum duration for any thrust or coast arc is still 8.85 days. This long arc length implies that the operationally difficult engine pulses are generally avoided. Since the thrust acceleration is high at the end of phase #2, and the moon is a smaller body than the Earth, only 2.36 days and 1.76 kg of propellant are necessary to complete phase #3.

The overall coverage time for the mission is limited by the amount of available propellant, and thus, the mass-time history plots in Fig. 6.3 offer additional insight into the performance. In the top plot in Figure 6.3, the overall spacecraft mass for all three phases appears (with vertical dashed lines separating the phases). Recall that the initial guess for the coverage orbit assumes equal time spacing along all of the thrusting and coasting arcs, thus, the relatively piecewise linear decrease in mass over time is not surprising during phase #2. Although the coast times gradually increase to maintain continuity, the thrust times maintain a similar interval. In the middle plot in Figure 6.3, the mass performance for phase #1 is clear and, as expected, a significant translunar coast period is apparent during the transit between the two primaries. Finally, the bottom plot in Fig. 6.3 reveals that only a very short coast time is necessary to achieve insertion into a stable lunar frozen orbit. Since the feasible three-phase solution is used as an initial guess for optimization, Figure 6.3 also serves as a basis for comparison with the direct transcription procedure that manipulates the design variables to adjust the relative phase of the thrusting intervals.

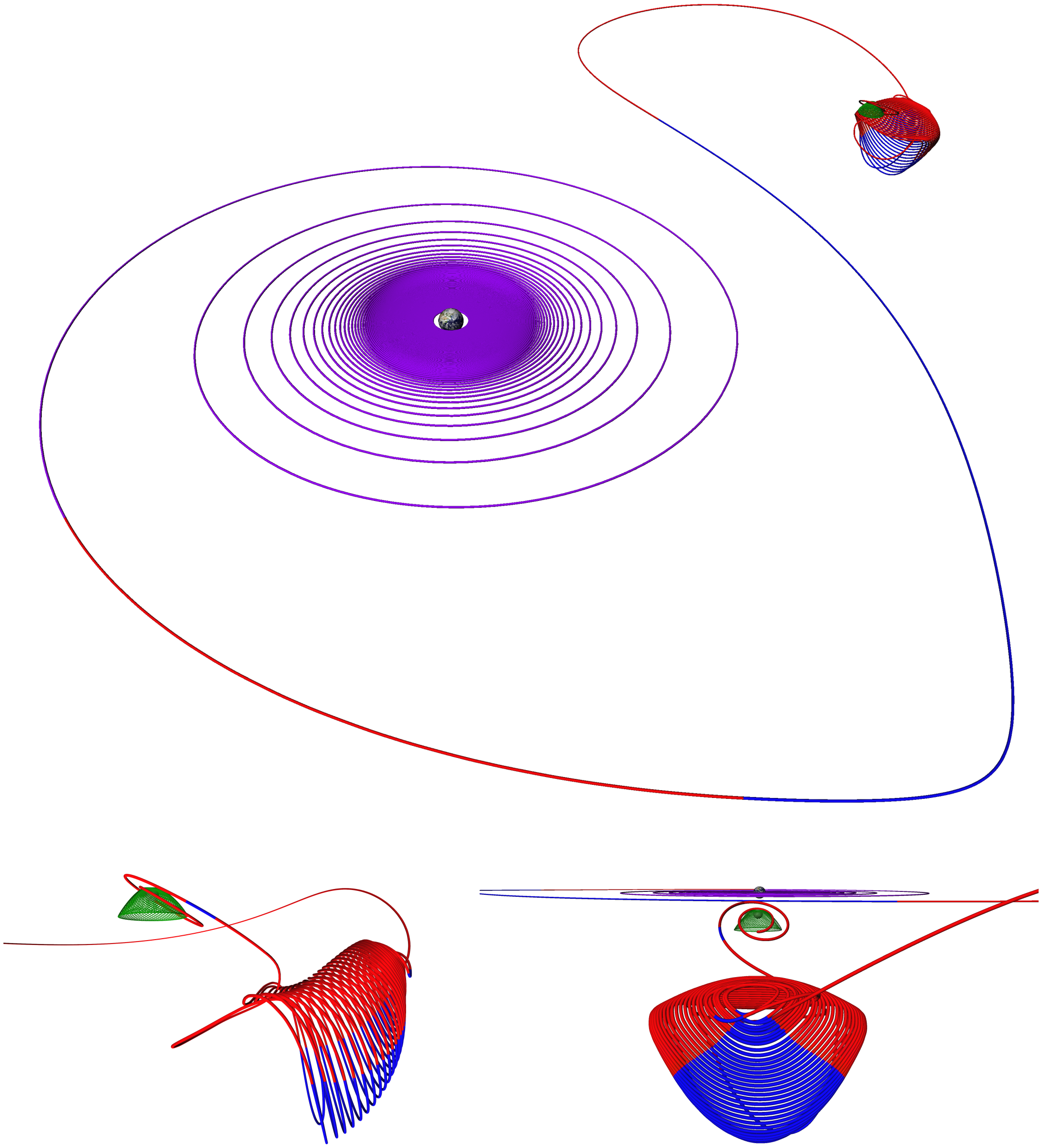

Figure 6.2. Feasible, Lower-Fidelity Three-Phase Trajectory, Earth-Moon Rotating Frame.

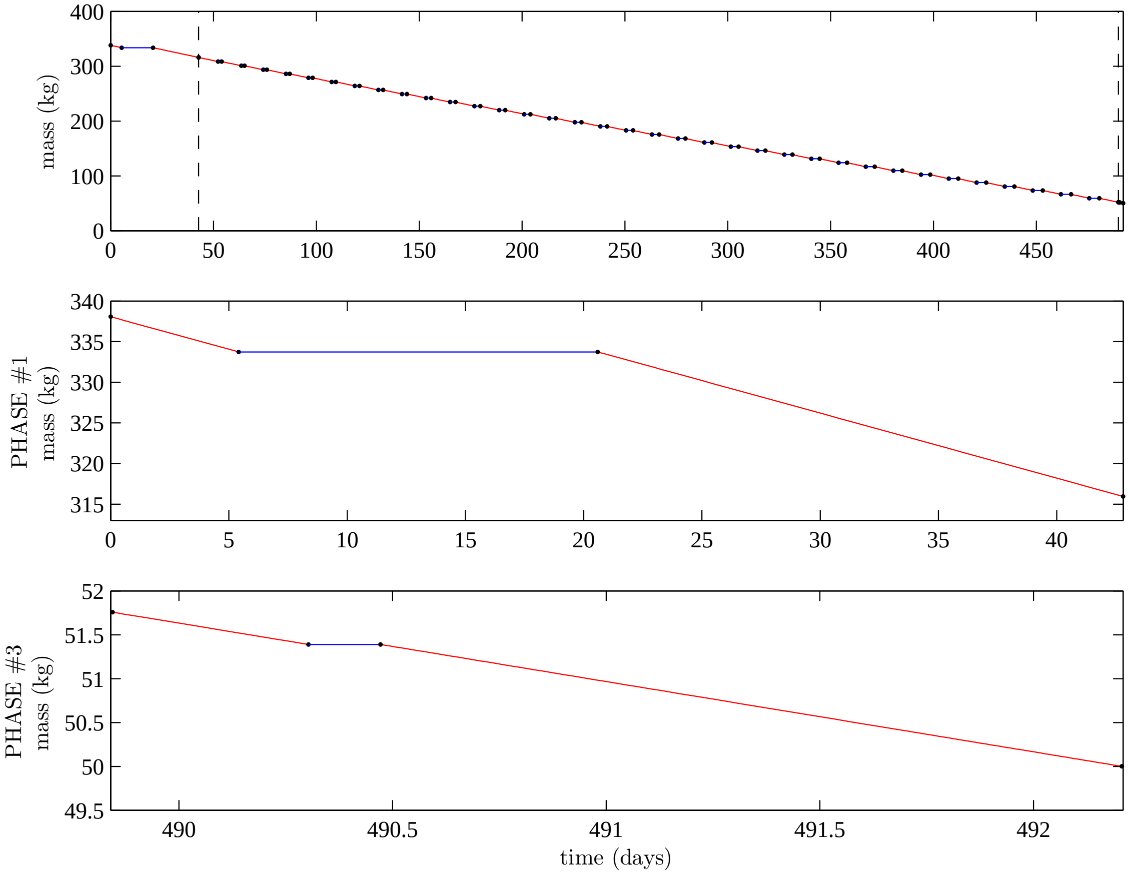

Figure 6.3. Spacecraft Mass for the Feasible, Lower-Fidelity, Three-Phase Solution, Including Phase #1 and #3.

6.2.2 Optimal Solution

The direct transcription procedure is successfully implemented using the converged feasible three-phase solution as an initial condition for $\boldsymbol{X}^0$. While the feasible solution is based on an existing trajectory that is near the initial guess, the direct transcription method with NLP iterates to produce a trajectory that minimizes the objective function in equation (6.3), or, in other words, maximizes the coverage time during phase #2. In total, an additional 107.14 days are added to the coverage orbit with this thrusting and coasting structure. The optimization procedure produces a significant variation from the initial guess. (Compare Figure 6.2 with Figure 6.4.) The new trajectory, in comparison to the feasible solution, appears to lie closer to the minimum elevation angle boundary constraint. Such a result is not surprising considering, from Figure 2.4, that this region corresponds to lower required thrust acceleration magnitudes to maintain the pole-sitter position. This observation compares with the same behavior that is observed with the solar sail pole-sitter orbits computed in Section 4.3. Thus, when the thrust acceleration magnitude is small early in the trajectory, the most effective arcs are located in the regions closer to L_2. Although this behavior is somewhat intuitive in hindsight, it is remarkable that an initial guess that is relatively far from the optimal solution is automatically discovered by the method. The optimal solution inserts into the coverage orbit after a 236.30 day transfer, and achieves a total coverage orbit time of 554.18 days. Surprisingly, only an additional 8.90 kg of mass are required to achieve this orbit in comparison to the feasible solution. Considering that a mere 3% increase in fuel mass consumption yields a 24% longer coverage phase suggests that the optimal trajectory is primarily exploiting natural (uncontrolled) dynamics. In fact, optimization adds only a 3% increase in the total thrust time for phase #2, whereas there is an 82% increase in coast time.

Further insight into the behavior of the optimal solution is available in Figure 6.5. Most obvious is that, compared to Figure 6.3, the thrust times for both phase #1 and phase #3 are shortened to maximize the total time in phase #2. In fact, the optimizer reduces the first thrust arc in phase #3 to zero days, which is the equivalent of shifting it into phase #2. In phase #2, the global trend is less linear compared to the feasible solution. For this phase, it is more effective to thrust over longer duration arcs early in the coverage orbit when the thrust acceleration magnitude is lower. Then, when the thrust acceleration magnitude is higher, near the end of the trajectory, less fuel is expended since it is only necessary to thrust in short bursts and coast during longer intervals. A useful comparison of the thrusting and coasting intervals between the feasible and optimal solutions appears in Figure 6.6. The time for each optimal

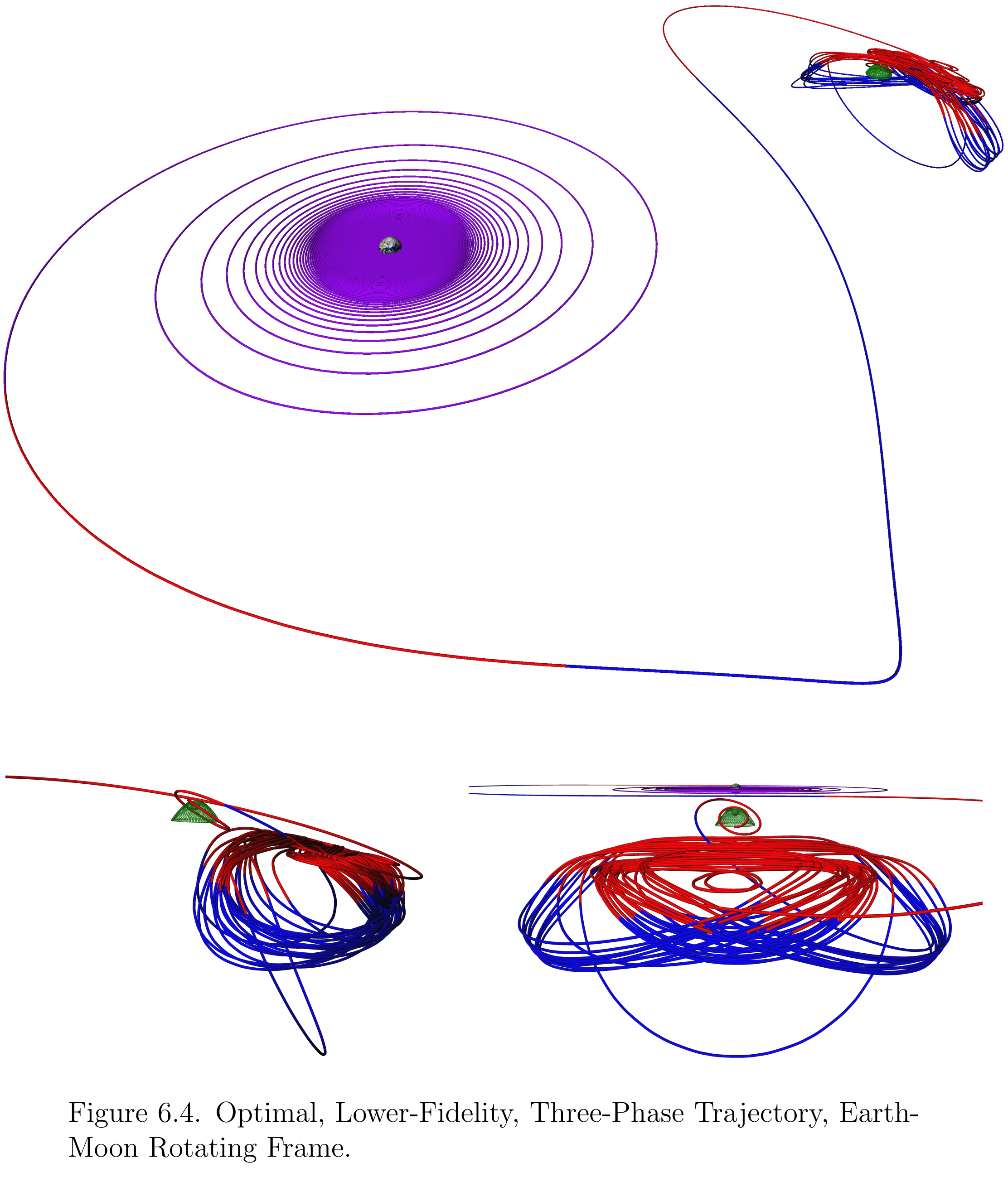

Figure 6.4. Optimal, Lower-Fidelity, Three-Phase Trajectory, Earth-Moon Rotating Frame.

coast arc always lasts 2-5 days longer than the corresponding feasible coast arc. This amounts to a total increase in coverage time of 96.03 days, just due to coasting. (Compare this to the total increase in thrusting time of 11.11 days.) From Figure 6.6 it is clear that the optimal solution emphasizes the early long-thrusting arcs, and then, later, thrusting arcs are actually shorter than coasting intervals. In contrast, this exchange in thrust and coast time never occurs in the feasible solution. Clearly, this solution supports the hypothesis deduced by visualizing the approximate gravity field in Figure 2.4. Although the time increase along the optimal solution is highly desirable, the well-behaved thrusting and coasting time intervals associated with the feasible solution may offer advantages operationally for implementation. However, the optimal solution may possesses operational advantages as well, for example, even though the final thrust arc is only 0.34 days, most thrust arcs last longer than 9 days. In fact, the duration of the first thrust arc is over 30 days.

6.3 High-Fidelity Solution with Mesh Refinement

With the initial proof-of-concept solution successfully computed and optimized, the next step is to validate and assess the trajectory performance when it is computed in a higher-fidelity model including the mesh refinement algorithm for accuracy. The problem is thus re-solved with the enhancements detailed in Table 6.1, and compared to the results in the lower-fidelity solution. The constraints and variables are still constructed in the same manner as in the procedure for the lower-fidelity solution, but the departure orbit boundary conditions are adjusted, and the system model is upgraded. Before the optimization and mesh refinement steps, the process is seeded by locating a feasible solution in SNOPT. Then, the complete multi-phase direct transcription algorithm using the mesh refinement algorithm detailed in Section 3.5.5 ensues using step 2b. In total, the process amounts to a nodal equidistributing and refining process that continually resolves the optimal control problem until the desired

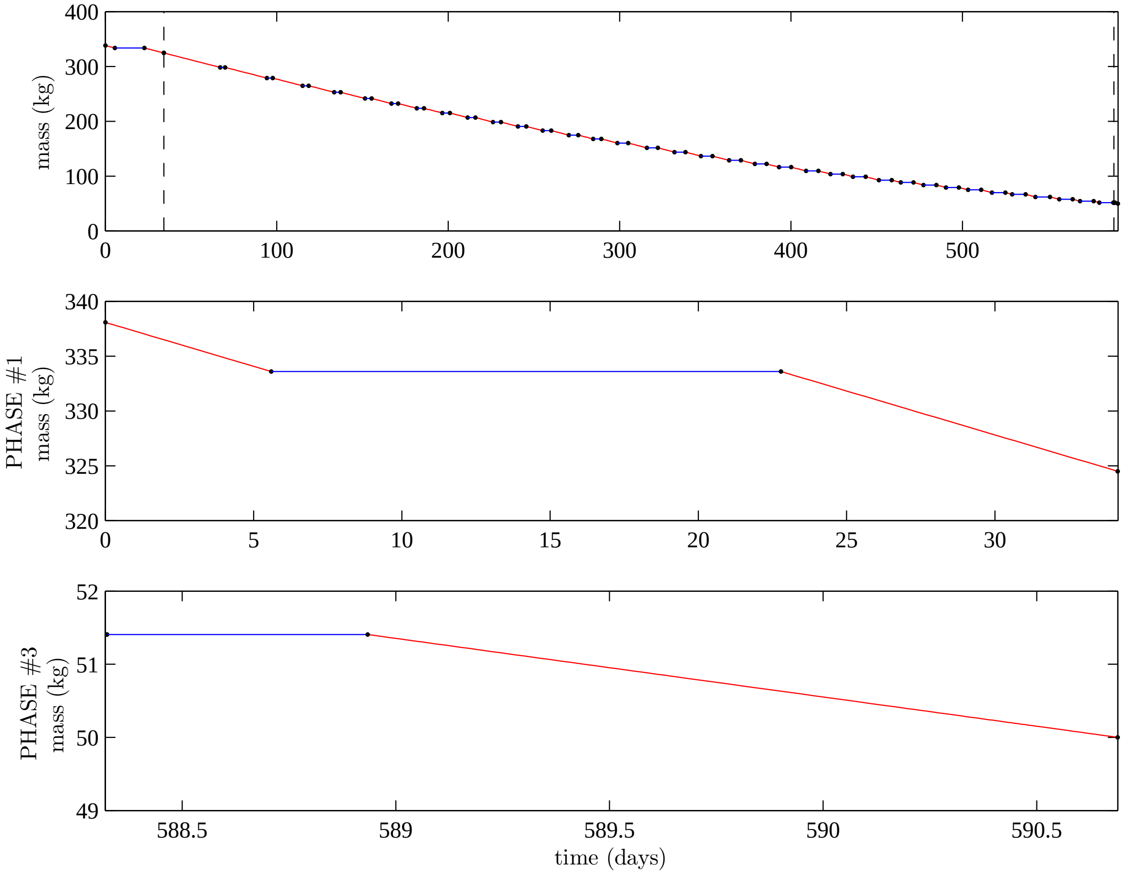

Figure 6.5. Spacecraft Mass for the Optimal, Lower-Fidelity, Three-Phase Solution, Including Phase #1 and #3.

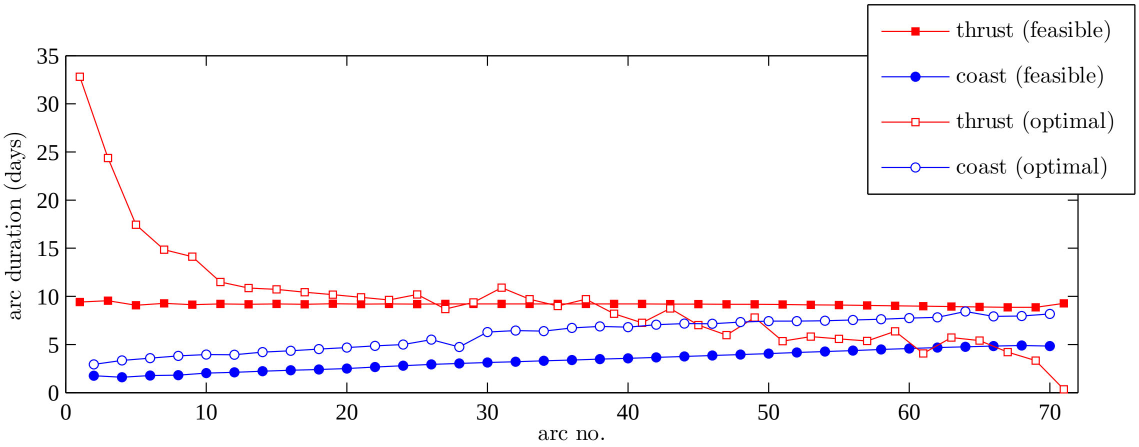

Figure 6.6. Arc Duration Comparison Between Feasible and Optimal Lower-Fidelity, Three-Phase Solutions.

accuracy is reached. All constraint tolerances are set to the SNOPT defaults (10^{-6}), and the mesh refinement tolerances are input as 10^{-8}.

6.3.1 Numerical Results

The solution procedure is successfully simulated to compute feasible and optimal solutions to the three-phase pole-sitter scenario in a higher-fidelity model. Given that the engine efficiency is 0.527, the engine power P is approximately 2.3 kW, corresponding to the thrust T and I_{sp} in Table 2.1.

To illustrate the results from phase #1, a complete ECI view of both the feasible and optimal solutions appears in Figure 6.7. Note that the black point labeled “1” near the center of the figure corresponds to the interface between the fixed portion of phase #1 that remains constant in both the feasible and optimal solution, and the portion that enters as part of the collocation and optimizing procedure, combined with the other phases. An initial observation of the fixed transfer portion that precedes the “1” label is that there are notable regions of coasting during the long-duration Earth spiral-out (plotted in blue). These engine-off durations result from shadowing, and ultimately cause 21.86 days of additional coasting, which is a 9.09% increase in total transfer time as compared to the phase #1 feasible solution and a 9.46% increase for the optimal solution. Compared to the lower-fidelity solution, the feasible transfer in the higher-fidelity model requres an extension of 17.35 days, or an additional 7.08%, and the optimal trajectory requires an interval that is longer by 16.59 days, or an increase of 7.02%. More extensive durations of shadowing are avoided because of the relatively high 51.6° inclination of the ISS departure orbit, as opposed to a departure within the ecliptic plane. In Fig. 6.7, it is also noted that beyond the point labeled "1," the optimal solution retains a much larger out-of-plane thrusting arc that reduces the time and the fuel consumed to be expended later in phase #2. This remarkable behavior highlights the importance of optimizing the time-of-flight in phase #2, subject to the design variables within the other phases. From the thrust-coast-thrust structure in phase #1 that is apparent in the feasible solution, the transfer corresponding to the optimal solution also relocates the large coast arc such that it is more efficiently incorporated near the moon for the start of phase #2. For further data regarding phase #1, see Table 6.2.

Since the remaining phases are difficult to interpret as viewed in Figure 6.7, phase #2 and phase #3 appear in the IAU frame (Figure 6.8), and the MCR frame. (See Figure 6.9.) Recall from Section 2.8.2 that the IAU frame is a moon-centered inertial frame with a $\hat{Z}$-axis directed towards the lunar north pole. For reference, the points along the trajectory as it enters phase #2 and phase #3 are noted in both the feasible and optimal solutions, and are identified with the corresponding "2" and "3" labels in Figure 6.9. The IAU plots in Figure 6.8 best reflect the continuous surveillance of both solutions in inertial space, as the coverage orbits maintain a crown-like shape that constantly hovers within a direct line-of-sight to the Shackleton crater. The rotating, pulsating plots in Figure 6.9 are useful for examining the similarity to the initial guess from the RTBP. (Compare with Figure 4.14 b). In both of the views in Figure 6.8 and Figure 6.9, it is apparent that the optimizing objective to maximize the time-of-flight during phase #2 is partly achieved by determining an orbit configuration that extends the allowable coast arc durations. (This same behavior is also noted in the lower-fidelity solution.) As a result, the optimal orbit utilizes coast arcs that "touch" the boundary of the prescribed altitude upper limit, whereas the feasible solution does not. Surprisingly, the optimal coverage orbit reaches altitudes as low as 7,941 km, as the final revolutions of the trajectory appears to pass closely by the moon and into the L_1 region before dropping into the lunar stable orbit. Even though the total fuel mass is fixed at 450 kg, the optimal orbit manages to utilize an additional 8.6 kg of fuel (from phases #1 and #3) due to the multi-phase direct transcription formulation. In the case of the optimal solution, only 0.89 kg are necessary to transfer into the lunar frozen orbit. Note that the lunar frozen orbit is propagated for several months to demonstrate its stable behavior without the use of any fuel.

In both the feasible and the optimal trajectories, the minimum elevation angle is equal to the minimum allowable value of $\phi_{lb} = 6^\circ$. This result is 7° smaller than the lower-fidelity solution due to the inclusion of lunar librations and the requirement to maintain line-of-sight with the ephemeris coordinates of the Shackleton site, rather than a static south pole reference. A time history of elevation angle performance is detailed in Figure 6.10. Here, some additional insight is also available between the two solutions. In the feasible solution, coast arcs are short or non-existent during the beginning segments of the trajectory. The coast arcs gradually elongate as the trajectory evolves. The minimum elevation angle also *increases* as time progresses. This initially unforeseen natural behavior evolves from the simple initial guess strategy, and may correspond to another desirable performance characteristic for a pole-sitter that is available at the expense of additional fuel mass. In contrast, the optimal solution employs more coast arcs at the beginning of the trajectory, and arcs along the trajectory continue to occasionally extend to the 6° minimum elevation boundary. Another noted feature of the collocation process is that a thrust or a coast arc can be automatically eliminated by shrinking its time to zero if it is unnecessary for the final solution.

In total, optimization results in 451.26 days of coverage time, an increase of 64.58 days, or 16.70% with only the 8.6 kg of additional fuel used in phase #2. (See Table 6.2.) As previously noted, the large increase in time-of-flight with only a small amount of additional fuel indicates that the optimizer locates an entirely new dynamical solution primarily through the use of coast arc placement. This optimal solution in the higher-fidelity model is still 102.92 days shorter than the result in the lower-fidelity model, but both solutions are *locally* optimal and may not be indicative of a true globally optimal comparison. Some of the time difference is also attributable to the behavior in the out-of-plane departure orbit. Compared to the study in the lower-fidelity model, the higher-fidelity departure spiral is a more complicated transfer trajectory with many higher-fidelity perturbations, and ultimately requires more fuel mass.

Table 6.2 Performance Comparison of Feasible and Optimal Three-Phase Solutions.

		Lower-Fidelity		Higher-Fidelity	
		Feasible	Optimal	Feasible	Optimal
PHASE #1	Fuel Mass Consumed (kg)	184.10	175.55	188.61	185.04
	Total Time (days)	244.97	236.30	262.32	252.89
PHASE #2	Fuel Mass Consumed (kg)	264.19	273.09	255.01	263.61
	Total Time (days)	447.04	554.18	386.68	451.26
	Min. Altitude (km)	32,400	24,750	29,916	7,941
	Max. Altitude (km)	80,000	100,000	97,364	100,000
	Min. Elevation Angle (°)	13.0	13.0	6.0	6.0
	Max. Elevation Angle (°)	79.5	60.5	67.5	70.0
PHASE #3	Fuel Mass Consumed (kg)	1.76	1.41	1.90	0.89
	Total Time (days)	2.36	2.37	2.37	1.11

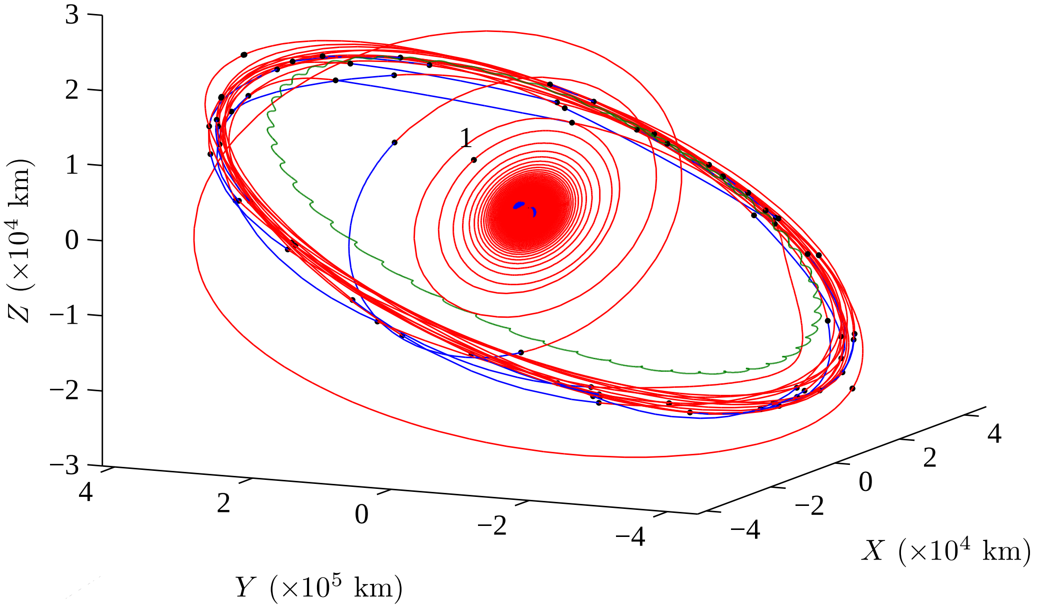

(a) Feasible

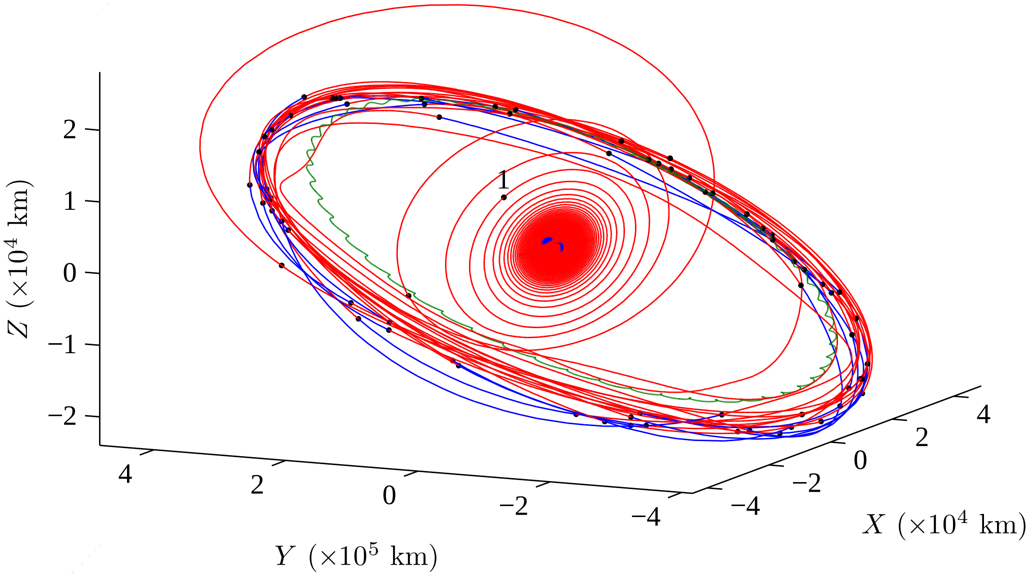

(b) Optimal

Figure 6.7. Higher-Fidelity, Three-Phase Solution in the ECI, EMEJ2000 Frame.

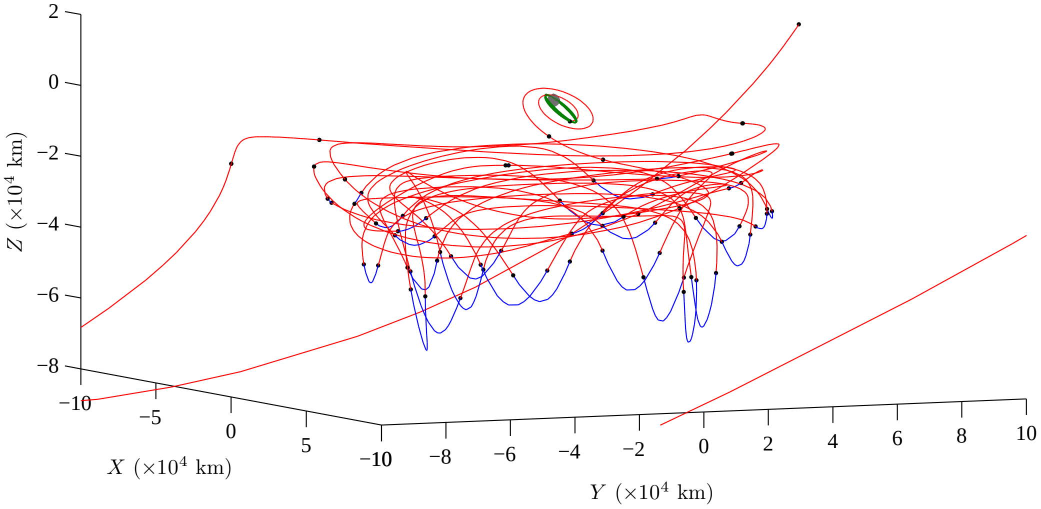

(a) Feasible

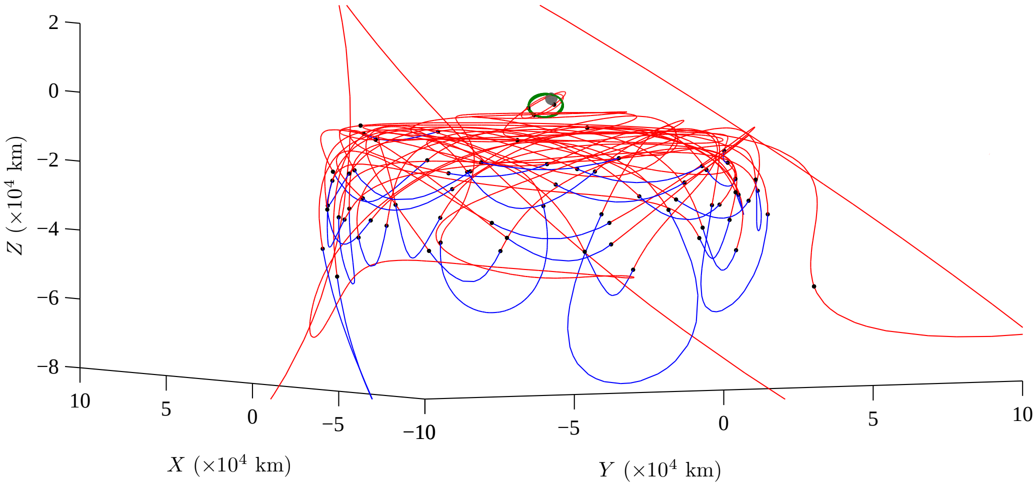

(b) Optimal

Figure 6.8. Higher-Fidelity Coverage Orbit (Phase #2) and End-of-Life (Phase #3) in the IAU Frame.

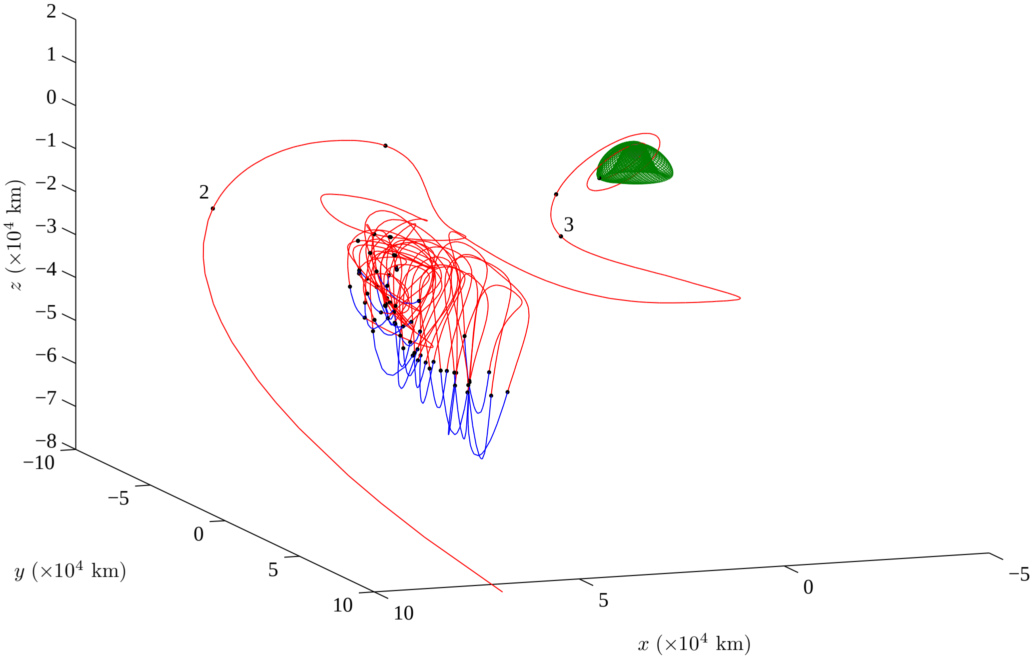

(a) Feasible

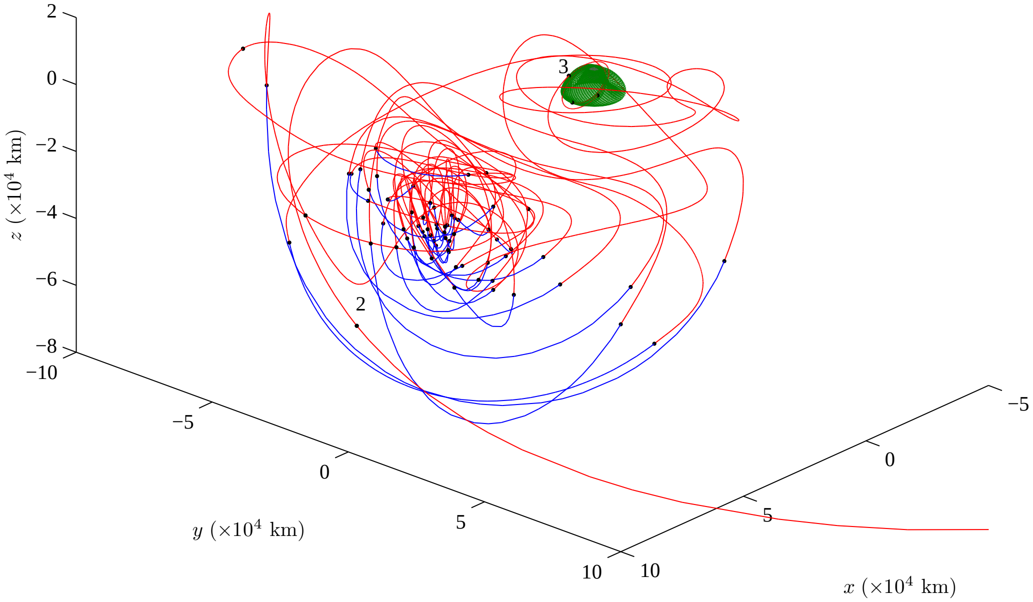

(b) Optimal

Figure 6.9. Higher-Fidelity Coverage Orbit (Phase #2) and End-of-Life (Phase #3) in the MCR Frame.

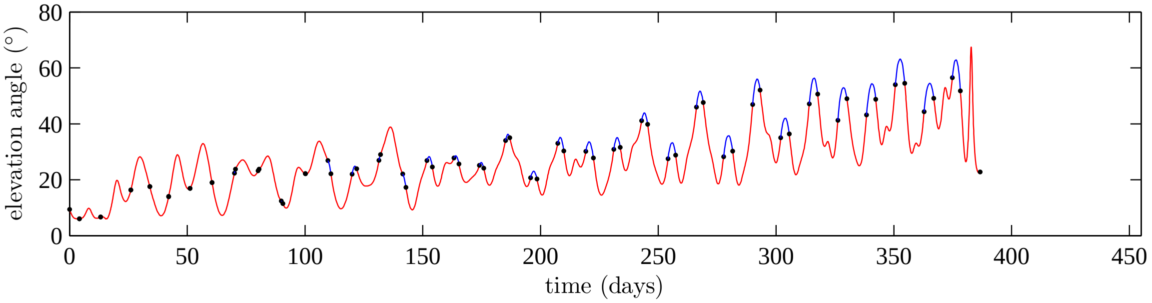

(a) Feasible

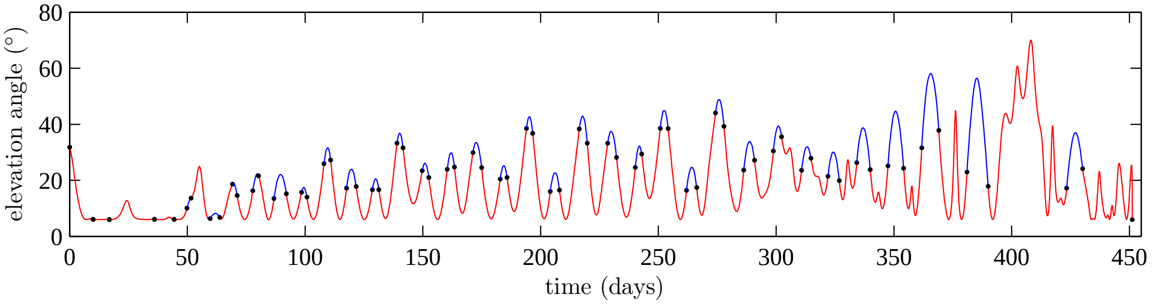

(b) Optimal

Figure 6.10. Elevation Angle Time History.

7. CONCLUSIONS

A thorough investigation of the design of lunar relay satellite missions with the exclusive use of low-thrust propulsion is completed. To accomplish this objective, a key focus of the investigation is the development of a systematic mathematical process and computational approach to design and optimize various phases trajectory. With this framework established, the trajectory design procedure centers on the selection of a coverage orbit or orbits that ensure that continuous communications links between the lunar south pole and the Earth are maintained. Low-thrust propulsion, while often envisioned as a means of achieving orbital transfer and performing stationkeeping, is also well-suited to the design of novel pole-sitter orbits that maintain continuous surveillance of the lunar south pole using only one spacecraft. The technology is also useful as a means of easily shifting between different libration point orbits of interest, or servicing cargo missions. The following sections summarize the accomplishments as a result of this work and recommend future efforts.

7.1 Discovery and Analysis of Pole-Sitter Orbits

Among the previously examined lunar frozen orbits and libration point orbits, a primary trajectory design focus in this analysis is the possibility of a pole-sitter orbit when an efficient source of low-thrust propulsion is available. The pole-sitter orbits supply two completely new trajectory options for developing a lunar south pole relay architecture. The first possibility is to deploy a solar sail to achieve the pole-sitter orbit. The current higher-fidelity designs indicates that a large solar sail can maintain ongoing, continuous line-of-sight of the lunar south pole for long durations. Assuming that a relatively small amount of control effort is required to continuously reorient the sail, then the orbits remain a long-term option for south pole coverage.

The second possibility for a pole-sitter mission is to implement more contemporary low-thrust technology, such as solar electric propulsion. Here, the pole-sitter orbit is selected as a temporary satellite that achieves a continuous communications link, before being transferred into a multiple satellite constellation, presumably composed of lunar frozen orbits. Such an option is desirable if there is a delay in launching all of the satellites into the frozen orbit constellation. Rigorous analysis indicates that even with advanced modeling effects considered, a small 500 kg satellite with a thruster comparable to the NSTAR engine can achieve a temporary pole-sitter trajectory that maintains single spacecraft coverage in excess of a year.

In total, the complete computation of a pole-sitter orbit, given the lack of a priori information when beginning the process, represents the discovery of a new type of controlled, path-constrained orbit. Prior literature indicates only that the pole-sitter orbit exists in concept with certain thruster capabilities, but offers no specifics concerning the shape of the orbits, the corresponding control history, or the precise locations that they must occupy. This analysis demonstrates that by exploiting the properties of the restricted three-body problem in the vicinity of the L_1 and L_2 collinear points, new regions requiring a small thrust acceleration input become available to maintain the pole-sitter orbit. Simple analysis of the associated pseudo-potential gradient associated with the Earth-moon system quickly reveals the available orbit regions for a given a thrust level, and then as previously noted, the direct transcription process is capable of automatically generating the controlled, path-constrained orbit. Regardless of the thruster, rigorous analysis in higher-fidelity models confirms that the best region to place an orbit in terms of minimum elevation angle performance is in the vicinity of the L_2 point.

7.2 Direct Transcription Methodology

The primary computational approach is the higher-order Gauss-Lobatto direct transcription method. In general, the direct collocation approaches represent a significant shift in the way spacecraft trajectories are designed and optimized that began during the 1980's. There are few other applications that highlight the computational benefits of the direct transcription and collocation method more than the design of lunar pole-sitter orbits. These orbits, a central design focus in the study, are computed given an almost complete lack of intuition of the shape of the final trajectory or the corresponding control history, yet the higher-order collocation method easily iterates to determine the orbit that satisfies all of the constraints. Such design difficulties are beyond the scope of the classical shooting method, and also exceed the capabilities of an exhaustive, semi-analytical process to generate a nearly convergent initial guess. Even in instances where the total number of variables exceeds 100,000, the ability to exploit the sparse matrix problem structure results in relatively efficient computation that often quickly generates a solution. The transcription methodology is also useful for adding an arbitrary number of thrusting and coasting arcs, and removing those that are unnecessary. Another advantage of the transcription process is the capability to link together multiple phases that comprise a trajectory, thus offering the potential for improved optimization results. Linking the phases allows variables that belong to potentially dissimilar system models to share functional dependencies and change to optimize a performance index. Finally, an accurate solution using the transcription process is obtained by updating the discrete mesh of data points until the result matches a user-specified accuracy. Thus, the completely discretized solution to the trajectory design and optimization problem is re-solved until it is as accurate as a solution obtained with an explicit propagator.

7.3 Transfer Trajectories and Intuitive Steering Law Guess Schemes

While highly sensitive, low-thrust transfers originating from Earth parking orbits (or lowering into lunar orbits) do not share the same robust convergence behavior as the preceding pole-sitter orbits, there are several schemes to generate an intuitive guess that can be implemented within the collocation structure to achieve convergence. Most of the rules are based on either orienting the thrust vector tangent to the velocity or anti-velocity vector when the system geometry permits. Once a few trajectories are explicitly propagated with these schemes, the transcription method corrects the trajectory, locating a nearby or optimal solution. Typically, convergence occurs even in the presence of large discontinuities in the boundary conditions.

7.4 Validation with Advanced Models

Since lunar pole-sitters are a largely unexplored concept, extra care is necessary to validate the solutions given a number of higher-fidelity modeling effects. After preliminary proof-of-concept analysis in the three-body problem, the solutions are demonstrated to exist even after incorporating effects such as planetary ephemerides, Earth oblateness, solar radiation pressure, and shadowing. In particular, shadowing adds a significant time-of-flight penalty to the Earth spiral-out trajectories given the many eclipsing incidents. However, the pole-sitter trajectories are still executed within the prescribed mission requirements, including the minimum time-of-flight duration of one year, as defined for the solar electric propulsion mission.

7.5 Transfers Between Libration Point Orbits

In situations when libration point orbit architectures are selected, the classical optimal control-based formulation is implemented instead of the transcription approach for the rapid generation of many solutions. The shorter times-of-flight and the reduced sensitivities, compared to long-duration spiral transfers or pole-sitter orbit designs, imply that the optimal control approach is well-suited for the computation of solutions with indirect or direct shooting. A sample implementation of this approach demonstrates that the multi-objective trade space involving fuel consumption and time-of-flight can be generated to select a transfer of interest. The entire process can then, if desired, be continuously repeated for many libration point orbit combinations of interest.

7.6 Recommended Future Efforts

There are several potential areas for additional investigation into low-thrust trajectories applied to lunar south pole coverage missions. There are also several tangent research topics that have arisen as a result of this investigation. These recommended future efforts include:

- A detailed investigation of transfer trajectories between libration point orbits should be continued. The current efforts primarily involve the development of a methodology to compute the orbits, and then only a single illustrative example scenario is included. However, an exhaustive exploration of the design space, the benefits of including invariant manifolds in the design formulation, and validation in the higher-fidelity model are all important steps to be considered in the future. A globally optimizing algorithm, such as a genetic algorithm, evolutionary algorithm, or particle swarm algorithm, are particularly well-suited to performing a thorough examination of the multi-objective time-of-flight and fuel consumption trade space.

- Many of the trajectory design problems explored herein offer a representative example of a highly challenging optimal control problem. There are high numerical sensitivities, continuous path constraints, a series of control parameters, and little intuition for many of the solutions. Re-solving some of the optimization problems presented in this investigation would provide a unique testbed for assessing the performance of some of the latest trajectory optimization software packages, such as the various pseudospectral approaches and other transcription methodologies for solving an optimal control problem. In particular, the pole-sitter problem requires a large amount of mesh points to generate a discretized solution, and therefore, re-solving the problem with other software packages would accentuate the computational efficiency or deficiencies inherent in these existing algorithms.

- Further development of complex-step, numerical derivatives is an important step towards completely automating the differentiation process when using a gradient-based corrections or optimization algorithm. The simplicity of completely automatic differentiation is especially enticing given that increasing computational capabilities reduce the time-penalty of obtaining numerical derivatives. Since the complex-step derivatives yield machine-precision accuracy, then only the variables, constraints, cost function, and system model are necessary to deliver to a trajectory optimization problem, and the formulation and solution of any problem are easily automated. By eliminating the cumbersome steps and propensity for human errors that are often associated with evaluating analytical derivatives, the optimization of new trajectory concepts would result in a much smoother process. Furthermore, the computation of Jacobian matrix derivatives may be distributed as a parallel process for increased computational speed.

- The trajectory designs produced in this analysis are "open-loop" solutions that obtain a baseline feasible or optimal control history that satisfies all of the constraints. Given a perturbation from this nominal, open-loop path, no detailed efforts are included to explore the ability to control to the reference orbit, or to assess the total stationkeeping costs. Such closed-loop control analysis clearly must be understood before these trajectories are implemented in an actual mission.

- Many other modeling effects can still be included into the system model. For example, an accurate solar array power degradation model, solar sail billowing effects, and implementation of a more accurate shadowing and SRP model might all create a significant impact on the dynamical behavior. In a mission scenario with a large solar sail, a full six degree-of-freedom simulation that incorporates the attitude dynamics would also more accurately reflect the repercussions of the maneuver sequence on the spacecraft performance. Other constraints may also become important to design a feasible mission trajectory, including thruster turning rate constraints, and pointing requirements to ensure power to the solar arrays.

- The general framework for the trajectory computation method allows for adaptation to many low-thrust and trajectory design problems of interest. In addition to re-solving the same problem involving other planetary moons of interest, the higher-order direct collocation approach is easily applicable to many other path-constrained design problems, including quasi-periodic orbit sizing, proximity operations missions, formation flight, and optimal satellite reorientation.

LIST OF REFERENCES

LIST OF REFERENCES

[1] *Lunar Reconnaissance Orbiter (LRO): Leading NASA's Way Back to the Moon, Lunar Crater Observation and Sensing Satellite (LCROSS): NASA's Mission to Search for Water on the Moon*, 2009 [accessed September 30, 2009]. `http://www.nasa.gov/pdf/360020main\_LRO\_LCROSS\_presskit2.pdf`.

[2] C. Pieters, J. Goswami, R. Clark, *et al.*, *Character and Spatial Distribution of OH/H_2O on the Surface of the Moon*, 2009 [accessed September 30, 2009]. `http://www.nasa.gov/pdf/360020main\_LRO\_LCROSS\_presskit2.pdf`.

[3] *SELENE: SELenological ENgineering Explorer "KAGUYA"*, 2009 [accessed September 15, 2009]. `http://www.jaxa.jp/pr/brochure/pdf/04/sat16.pdf`.

[4] J. Sovey, V. Rawlin, and M. Patterson, "Ion Propulsion Development Projects in U.S.: Space Electric Rocket Test I to Deep Space I," *Journal of Propulsion and Power*, vol. 17, pp. 517–526, May–June, 2001.

[5] R. Goddard, *Report Concerning Further Developments.* Smithsonian Institution Archives, Washington, D.C., 2009 [accessed October 26, 2009]. `http://siarchives.si.edu/history/exhibits/documents/goddardmarch1920.htm`.

[6] H. Oberth, "Ways to Spaceflight," tech. rep., NASA, NASA Technical Translation F-622, Washington, D.C., 1972.

[7] T. Masek and E. Pawlik, "Thrust System Technology for Solar Electric Propulsion," Paper AIAA-1968-541, *AIAA 4th Propulsion Joint Specialist Conference*, Cleveland, Ohio, June 10–14, 1968.

[8] D. Lawden, *Optimal Trajectories for Space Navigation.* London: Butterworths, 1963.

[9] W. Melbourne and C. Sauer, "Optimum Interplanetary Rendezvous with Power-Limited Vehicles," *AIAA Journal*, vol. 1, pp. 54–60, January, 1963.

[10] T. Edelbaum, "Optimum Power-Limited Orbit Transfer in Strong Gravity Fields," *AIAA Journal*, vol. 3, pp. 921–925, May, 1965.

[11] M. Rayman, P. Varghese, D. Lehman, and L. Livesay, "Design of the First Interplanetary Solar Electric Propulsion Mission," *Journal of Spacecraft and Rockets*, vol. 39, pp. 589–595, August, 2002.

[12] J. Polk, R. Kakuda, J. Anderson, J. Brophy, V. Rawlin, M. Patterson, J. Sovey, and J. Hamley, "Displaced Periodic Orbits With Low-Thrust Propulsion in the Earth-Moon System," Paper AAIA-99-2274, *35th AIAA/ASME/SAE/ASEE Joint Propulsion Conference and Exhibit*, Los Angeles, California, June 20–24, 1999.

[13] J. Schoenmaekers, D. Horas, and J. Pulido, "SMART-1: With Solar Electric Propulsion to the Moon," *Proceedings of the 16th International Symposium on Space Flight Dynamics*, 2001.

[14] M. Rayman, T. Fraschetti, C. Raymond, and C. Russell, "Dawn: A Mission in Development for Exploration of Main Belt Asteroids Vesta and Ceres," *Acta Astronautica*, vol. 58, pp. 605–616, June, 2006.

[15] E. Choueiri, "A Critical History of Electric Propulsion: The First 50 Years (1906-1956)," *Journal of Propulsion and Power*, vol. 20, March–April, 2004.

[16] The Boeing Company, *Hughes' Ion Engine Serving as Primary Propulsion to NASA's Deep Space 1*, 2010 [accessed March 20, 2010]. `http://www.boeing.com/defense-space/space/bss/factsheets/xips/nstar/ionengine.html`.

[17] Ad Astra Rocket Company, *VASIMR VX-200 Reaches 200 kW Power Milestone*, 2009 [accessed Ocotober 27, 2009]. `http://www.adastrarocket.com/Release_200kW_01Oct2009Final.pdf`.

[18] T. Glover, F. Diaz, A. Ilin, and R. Vondra, "Projected Lunar Cargo Capabilities of High-Power VASIMR Propulsion," Paper IEPC-2007-244, *30^{th} International Electric Propulsion Conference*, Florence, Italy, September 17–20, 2007.

[19] Ad Astra Rocket Company, *VASIMR Technology*, 2010 [accessed March 20, 2010]. `http://www.adastrarocket.com/aarc/Technology`.

[20] C. McInnes, *Solar Sailing: Technology, Dynamics and Mission Applications.* Berlin: Springer-Verlag, 1999.

[21] A. Clarke, *The Wind from the Sun.* New York, New York: Harcourt Brace Jovanovich, Inc., 1972.

[22] F. Vonbun, "A "Hummingbird" for the l_2 Lunar Libration Point," tech. rep., NASA Goddard Space Flight Center, NASA-TM-X-55778, Greenbelt, Maryland, April, 1968.

[23] R. Forward, "Statite: A Spacecraft That Does Not Orbit," *Journal of Spacecraft and Rockets*, vol. 28, pp. 606–611, September–October, 1991.

[24] D. Lichodzeijewski and B. Derbes, "Vacuum Deployment and Testing of a 20M Solar Sail System," Paper AIAA-2006-1705, *47^{th} AIAA/ASME/ASCE/AHS/ASC Structures, Structural Dynamics, and Materials Conference*, Newport, Rhode Island, May 1–4, 2006.

[25] J. West, "The Lunar Polesitter," Paper AIAA-2008-7073, *2008 AIAA/AAS Astrodynamics Specialist Conference*, Honolulu, Hawaii, August 18–21, 2008.

[26] B. Sauser, *Solar Sailing in Space*, 2010 [accessed March 20, 2010]. `http://www.technologyreview.com/energy/21122/`.

[27] H. Keller, *Numerical Methods for Two-Point Boundary Value Problems.* London: Blaisdell, 1968.

[28] J. Stoer and R. Bulirsch, *Introduction to Numerical Analysis.* New York, New York: Springer-Verlag, 1980.

[29] L. Dixon and M. Biggs, "The Advantages of Adjoint-Control Transformations When Determining Optimal Trajectories by Pontryagin's Maximum Principle," *Aeronautical Journal*, vol. 76, no. 735, pp. 169–174, 1972.

[30] S. Vadali and R. Nah, "Fuel-Optimal Planar Earth-Mars Trajectories Using Low-Thrust Exhaust-Modulated Propulsion," *Journal of Guidance, Control, and Dynamics*, vol. 23, pp. 476–482, May–June, 2000.

[31] Y. Gao and C. Kluever, "Low-Thrust Interplanetary Orbit Transfers Using Hybrid Trajectory Optimization Method with Multiple Shooting," Paper AIAA-2004-4088, *2004 AIAA/AAS Astrodynamics Specialist Conference and Exhibit*, Providence, Rhode Island, August 16–19, 2004.

[32] C. Ranieri and C. Ocampo, "Indirect Optimization of Spiral Trajectories," *Journal of Guidance, Control, and Dynamics*, vol. 29, pp. 1360–1366, November–December, 2006.

[33] R. Russell, "Primer Vector Theory Applied to Global Low-Thrust Trade Studies," *Journal of Guidance, Control, and Dynamics*, vol. 30, pp. 460–472, March–April, 2007.

[34] R. Russell and L. Shampine, "A Collocation Method for Boundary Value Problems," *Numerical Mathematics*, vol. 19, pp. 1–28, 1972.

[35] C. Hargraves and S. Paris, "Direct Trajectory Optimization Using Nonlinear Programming and Collocation," *Journal of Guidance, Control, and Dynamics*, vol. 10, no. 4, pp. 338–342, 1987.

[36] P. Enright and B. Conway, "Discrete Approximations to Optimal Trajectories Using Direct Transcription and Nonlinear Programming," *Journal of Guidance, Control, and Dynamics*, vol. 15, pp. 994–1002, July–August, 1992.

[37] D. Benson, *A Gauss Pseudospectral Transcription for Optimal Control.* PhD thesis, Department of Aeronautics and Astronautics, Massachusetts Institute of Technology, Cambridge, Massachusetts, November, 2004.

[38] G. Huntington, *Advancement and Analysis of a Gauss Pseudospectral Transcription for Optimal Control.* PhD thesis, Department of Aeronautics and Astronautics, Massachusetts Institute of Technology, Cambridge, Massachusetts, May, 2007.

[39] P. Enright, *Optimal Finite-Thrust Spacecraft Trajectories Using Direct Transcription and Nonlinear Programming.* PhD thesis, Department of Aerospace Engineering, University of Illinois at Urbana-Champaign, Urbana, Illinois, August, 1991.

[40] P. Gill, W. Murray, and M. Saunders, "SNOPT: An SQP Algorithm for Large-Scale Constrained Optimization," *SIAM Review*, vol. 47, no. 1, pp. 99–131, 2005.

[41] U. Ascher, J. Christiansen, and R. Russell, *COLSYS-A Collocation Code for Boundary-Value Problems.* Codes for Boundary Value Problems in Ordinary Differential Equations, Berlin, Germany: Springer-Verlag, 1979.

[42] E. Doedel, R. Paffenroth, A. Champneys, T. Fairgrieve, Y. Kuznetsov, , B. Oldeman, B. Sandstede, and X. Wang, *AUTO 2000: Continuation and Bifurcation Software for Ordinary Differential Equations (with HomCont).* California Institude of Technology, Pasadena, California, 2001. Technical Report.

[43] J. Betts and W. Huffman, "Sparse Optimal Control Software SOCS," tech. rep., Boeing Information and Support Service, The Boeing Company, Mathematics and Engineering Analysis Technical Document MEA-LR-085, Seattle, Washington, July, 1997.

[44] J. Hartmann, V. Coverstone-Carroll, and S. Williams, "Optimal Interplanetary Spacecraft Trajectories via a Pareto Genetic Algorithm," *Journal of the Astronautical Sciences*, vol. 46, no. 3, pp. 267–282, 1998.

[45] M. Vavrina and K. Howell, "Multiobjective Optimization of Low-Thrust Trajectories Using a Genetic Algorithm," Paper AAS 09-151, *19th AAS/AIAA Space Flight Mechanics Meeting*, Savannah, Georgia, February 8–12, 2009.

[46] "The Vision for Space Exploration," tech. rep., NASA, NP-2004-01-334-HQ, February, 2004.

[47] T. Ely, "Stable Constellations of Frozen Elliptical Inclined Orbits," *Journal of the Astronautical Sciences*, vol. 53, no. 3, pp. 301–316, 2005.

[48] T. Ely and E. Lieb, "Constellations of Elliptical Inclined Lunar Orbits Providing Polar and Global Coverage," *Journal of the Astronautical Sciences*, vol. 54, no. 1, pp. 53–67, 2006.

[49] D. Folta and D. Quinn, "Lunar Frozen Orbits," Paper AIAA-06-6749, *2006 AIAA/AAS Astrodynamics Specialist Conference*, Keystone, Colorado, August 21–24, 2006.

[50] K. Howell, D. Grebow, and Z. Olikara, "Design Using Gauss' Perturbing Equations with Applications to Lunar South Pole Coverage," Paper AIAA-2008-7073, *17th AAS/AIAA Spaceflight Mechanics Meeting*, Sedona, Arizona, January 28–February 1, 2007.

[51] D. Grebow, M. Ozimek, K. Howell, and D. Folta, "Multi-Body Orbit Architectures for Lunar South Pole Coverage," *Journal of Spacecraft and Rockets*, vol. 45, pp. 344–358, March–April, 2008.

[52] K. Hamera, T. Mosher, M. Gefreh, R. Paul, L. Savkin, and J. Trojan, "An Evolvable Lunar Communication and Navigation Constellation Architecture," Paper AIAA-2008-5480, *26th International Communications Satellite Systems Conference*, San Diego, California, June 10–12, 2008.

[53] M. Ozimek, D. Grebow, and K. Howell, "A Collocation Approach for Computing Solar Sail Lunar Pole-Sitter Orbits," Paper AAS 09-378, *2009 AAS/AIAA Astrodynamics Specialist Conference*, Pittsburgh, Pennsylvania, August 9–13, 2009.

[54] R. Chase, "Potential Military Space Systems Applications for Advanced Electric Propulsion Systems," Paper AIAA-1981-1536, *17th SAE and ASME, Joint Propulsion Conference*, Colorado Springs, Colorado, July 27–29, 1981.

[55] W. Deininger, “A Review of Nuclear Electric Propulsion Spacecraft System Concepts,” Paper AIAA-1990-2553, *21st DGLR and JSASS, International Electric Propulsion Conference*, Orlando, Florida, July 18–20, 1990.

[56] S. Wiggins, *Introduction to Applied Nonlinear Dynamical Systems and Chaos.* New York, New York: Springer-Verlag, 1990.

[57] T. Starchville and R. Melton, “Optimal Low-Thrust Trajectories to Earth-Moon L_2 Halo Orbits (Circular Problem),” Paper AAS 97-714, *1997 AAS/AIAA Astrodynamics Specialist Conference*, Sun Valley, Idaho, August 4–7, 1997.

[58] J. Senent, C. Ocampo, and A. Capella, “Low-Thrust Variable Specific Impulse Transfers and Guidance to Unstable Periodic Orbits,” *Journal of Guidance, Control, and Dynamics*, vol. 28, pp. 280–290, March–April, 2005.

[59] M. Ozimek, “A Low-Thrust Transfer Strategy to Earth-Moon Collinear Libration Point Orbits,” Master’s thesis, School of Aerosnautics and Astronautics, Purdue University, West Lafayette, Indiana, December, 2006.

[60] G. Mingotti, F. Topputo, and F. Bernelli-Zazzera, “Combined Optimal Low-Thrust and Stable-Manifold Trajectories to the Earth-Moon Halo Orbits,” *New Trends in Astrodynamics and Applications III*, vol. 886, pp. 100–112, February, 2007.

[61] M. Standish, “JPL Planetary and Lunar Ephemerides,” tech. rep., Jet Propulsion Laboratory, JPL IOM 312.F-98-048, Pasadena, California, August, 1998.

[62] C. Walker, *Solar-System Ephemeris Toolbox*, 2005 [accessed January 25, 2010]. NASA Tech Brief, `http://findarticles.com/p/articles/mi_qa3957/is_200510/ai_n15705616/`.

[63] R. Bate, D. Mueller, and J. White, *Fundamentals of Astrodynamics.* New York, New York: Dover Publications, Inc., 1971.

[64] J. Prussing and B. Conway, *Orbital Mechanics.* New York, New York: Oxford University Press, 1993.

[65] R. Farquhar, “The Control and Use of Libration-Point Satellites,” tech. rep., NASA Goddard Space Flight Center, NASA TR R-346, Greenbelt, Maryland, September, 1970.

[66] J. Bell, “The Impact of Solar Radiation Pressure on Sun-Earth L_1 Libration Point Orbits,” Master’s thesis, School of Aerosnautics and Astronautics, Purdue University, West Lafayette, Indiana, July, 1991.

[67] C. Kluever and S. Oleson, “Direct Approach for Computing Near-Optimal Low-Thrust Earth-Orbit Transfers,” *Journal of Spacecraft and Rockets*, vol. 35, pp. 509–515, July–August, 1998.

[68] J. Kechichian, “Orbit Raising with Low-Thrust Tangential Acceleration in Presence of Earth Shadow,” *Journal of Spacecraft and Rockets*, vol. 35, pp. 516–525, July–August, 1998.

[69] G. Flandro, “Asymptotic Solution for Solar Electric Low Thrust Orbit Raising with Eclipse Penalty,” Paper AIAA-74-802, *AIAA Mechanics and Control of Flight Conference*, Anaheim, California, August 5–9, 1974.

[70] J. Chapront and G. Francou, “The Lunar Libration: Comparisons Between Various Models - A Model Fitted to LLR Observations,” *Journes 2004. Fundamental Astronomy: New Concepts and Models for High Accuracy Observations*, Paris, France, September 20–24, 2004.

[71] J. Anderson, “Earth-to-Lissajous Transfers and Recovery Trajectories Using an Ephemeris Model,” Master’s thesis, School of Aerosnautics and Astronautics, Purdue University, West Lafayette, Indiana, December, 2001.

[72] The Orbital and Celestial Mechanics Website, *A Moon-Centered, Inertial Coordinate System for Spice*, 2010 [accessed March 27, 2010]. `http://www.cdeagle.com/pdf/moon_j2000_spice.pdf`.

[73] P. Gill, W. Murray, and M. Saunders, “User’s Guide for SNOPT Version 7: Software for Large-Scale Nonlinear Programming,” Tech. Rep. Report NA 05-2, Department of Mathematics, University of California, San Diego, San Diego, California, June, 2008. `http://www.cam.ucsd.edu/~peg/papers/sndoc7.pdf`.

[74] *HSL Archive: A Library of Subroutines*, 2007 [accessed February 3, 2010]. `ftp://ftp.numerical.rl.ac.uk/pub/hsl_catalogs/archive/catalog.pdf`.

[75] D. Grebow, *Trajectory Design For Lunar South Pole Coverage.* PhD thesis, School of Aerosnautics and Astronautics, Purdue University, West Lafayette, Indiana, May, 2010.

[76] P. Gill, W. Murray, M. Saunders, and M. Wright, *Practical Optimization.* London, England: Academic Press, 1991.

[77] J. Martins, I. Kroo, and J. Alonso, “An Automated Method for Sensitivity Analysis using Complex Variables,” Paper AIAA-2000-0689, *38th Aerospace Sciences Meeting and Exhibit*, Reno, Nevada, January 10–13, 2000.

[78] G. Lantoine, R. Russell, and T. Dargent, “Using Multicomplex Variables for Automatic Computation of High-Order Derivatives,” Paper AAS 10-4468, *20th AAS/AIAA Space Flight Mechanics Meeting*, San Diego, California, February 14–17, 2010.

[79] J. Betts, *Practical Methods for Optimal Control Using Nonlinear Programming.* Philadelphia, Pennsylvania: SIAM, 2001.

[80] A. Bryson and Y.-C. Ho, *Applied Optimal Control: Optimization, Estimation, and Control.* Washington, District of Columbia: Hemisphere Publishing Corporation, 1975.

[81] C. Kluever and B. Pierson, “Optimal Low-Thrust Three-Dimensional Earth-Moon Trajectories,” *Journal of Guidance, Control, and Dynamics*, vol. 18, pp. 830–837, July–August, 1995.

[82] M. Ozimek and K. Howell, “Low-Thrust Transfers in the Earth-Moon System Including Applications to Libration Point Orbits,” *Journal of Guidance, Control, and Dynamics*, vol. 33, pp. 533–549, March–April, 2010.

[83] G. Reddien, “Collocation at Gauss Points as a Discretization in Optimal Control,” *SIAM Journal of Control and Optimization*, vol. 17, pp. 298–306, March, 1979.

[84] J. Betts and W. Huffman, "Mesh Refinement in Direct Transcription Methods for Optimal Control," *Optimal Control Applications & Methods*, vol. 19, no. 1, pp. 1–21, 1998.

[85] R. Russell and J. Christiansen, "Adaptive Mesh Selection Strategies for Solving Boundary Value Problems," *SIAM Journal on Numerical Analysis*, vol. 15, no. 1, pp. 59–80, 1978.

[86] C. D. Boor, *Conference on the Numerical Solution of Differential Equations*, vol. 363 of *Lecture Notes in Mathematics*, ch. Good Approximation by Splines with Variable Knots. II. New York, New York: Springer, 1973.

[87] A. Elipe and M. Lara, "Frozen Orbits about the Moon," *Journal of Guidance, Control, and Dynamics*, vol. 26, pp. 238–243, March–April, 2003.

[88] A. Prado, "Third-Body Perturbation in Orbits Around Natural Satellites," *Journal of Guidance, Control, and Dynamics*, vol. 26, pp. 33–40, January–February, 2003.

[89] D. Grebow, "Generating Periodic Orbits in the Circular Restricted Three-Body Problem with Applications to Lunar South Pole Coverage," Master's thesis, School of Aerosnautics and Astronautics, Purdue University, West Lafayette, Indiana, May, 2006.

[90] R. Farquhar, "The Utilization of Halo Orbits in Advanced Lunar Operations," tech. rep., NASA Goddard Space Flight Center, NASA TM X-65409, Greenbelt, Maryland, December, 1970.

[91] J. Breakwell and J. Brown, "The 'Halo' Family of 3-Dimensional Periodic Orbits in the Earth-Moon Restricted 3-Body Problem," *Celestial Mechanics*, vol. 20, pp. 389–404, November, 1979.

[92] K. Howell, "Three-Dimensional, Periodic, 'Halo' Orbits," *Celestial Mechanics*, vol. 32, pp. 29–52, January, 1984.

[93] G. Gómez, A. Jorba, and J. Masdemont, "Study of the Transfer from the Earth to a Halo Orbit Around the Equilibrium Point L_1," *Celestial Mechanics and Dynamical Astronomy*, vol. 56, pp. 541–562, August, 1993.

[94] F. Moulton (in collaboration with D. Buchanan, T. Buck, F. Griffin, W. Longley, and W. MacMillan), *Perioic Orbits*. Carnegie Institution of Washington, Washington, 1929.

[95] D. Dichmann, E. Doedel, and R. Paffenroth, "The Computation of Periodic Solutions of the 3-Body Problem Using the Numerical Continuation Software AUTO," *Libration Point Orbits and Applications*, Hong Kong, China, World Scientific, 2003.

[96] I. Robin and V. Markellos, "Numerical Determinations of Three-Dimensional Orbits Generated From Vertical Self-Resonant Satellite Orbits," *Celestial Mechanics*, vol. 21, no. 1, pp. 1–28, 1980.

[97] Y. Chen, T. Davis, W. Hager, and S. Rajamanickam, "Algorithm 887: CHOLMOD, Supernodal Sparse Cholesky Factorization and Update/Downdate," *ACM Transactions on Mathematical Software*, vol. 35, October, 2008.

[98] C. McInnes, “Solar Sail Trajectories at the Lunar L_2 Lagrange Point,” *Journal of Spacecraft and Rockets*, vol. 30, no. 6, pp. 782–784, 1993.

APPENDICES

A. The Adjoint Control Transformation for Power-Limited, Finite-Burn Engines

To obtain an initial guess of the costate variables with some physical meaning, consider a reference frame centered at the spacecraft, defined by the unit vectors $\hat{v}$-$\hat{w}$-$\hat{h}$, i.e., the *vwh*-frame. The $\hat{v}$-axis is aligned with the velocity vector, $\boldsymbol{v}$. The $\hat{h}$-axis is parallel to the instantaneous angular momentum vector, $\boldsymbol{\mathcal{H}} = \boldsymbol{r} \times \boldsymbol{v}$. Finally, the $\hat{w}$-axis is defined to complete a right-handed system. These unit vectors, and the associated time derivatives, are defined as

$$\hat{v} = \frac{\boldsymbol{v}}{\|\boldsymbol{v}\|},\ \hat{h} = \frac{\boldsymbol{r} \times \boldsymbol{v}}{\|\boldsymbol{r} \times \boldsymbol{v}\|},\ \hat{w} = \hat{h} \times \hat{v} \tag{A.1}$$

$$\dot{\hat{v}} = \dot{\boldsymbol{v}} / \|\boldsymbol{v}\| - \boldsymbol{v} \|\dot{\boldsymbol{v}}\| / \|\boldsymbol{v}\|^2 \tag{A.2}$$

$$\dot{\hat{h}} = \dot{\boldsymbol{\mathcal{H}}} / \|\boldsymbol{\mathcal{H}}\| - \boldsymbol{\mathcal{H}}||\dot{\boldsymbol{\mathcal{H}}}||/||\boldsymbol{\mathcal{H}}||^2 \tag{A.3}$$

$$\dot{\hat{w}} = \dot{\hat{h}} \times \hat{v} + \hat{h} \times \dot{\hat{v}} \tag{A.4}$$

Given a vector and its time derivative, the following relationships are also exploited to fully determine equations (A.2)-(A.4),

$$\|\dot{\boldsymbol{v}}\| = \boldsymbol{v} \cdot \dot{\boldsymbol{v}} / \|\boldsymbol{v}\| \tag{A.5}$$

$$||\dot{\boldsymbol{\mathcal{H}}}|| = \boldsymbol{\mathcal{H}} \cdot \dot{\boldsymbol{\mathcal{H}}}/||\boldsymbol{\mathcal{H}}|| \tag{A.6}$$

Two spherical angles, $\alpha_{\boldsymbol{u}}$ and $\beta_{\boldsymbol{u}}$, as well as their time derivatives, $\dot{\alpha}_{\boldsymbol{u}}$ and $\dot{\beta}_{\boldsymbol{u}}$, specify the orientation of the thrust direction relative to this frame, $\hat{\boldsymbol{u}}_{vwh}$, and also the time derivative of the thrust direction, $\dot{\hat{\boldsymbol{u}}}_{vwh}$, that is,

$$\hat{\boldsymbol{u}}_{vwh} = \begin{bmatrix} \cos\alpha_{\boldsymbol{u}} \cos\beta_{\boldsymbol{u}} & \sin\alpha_{\boldsymbol{u}} \cos\beta_{\boldsymbol{u}} & \sin\beta_{\boldsymbol{u}} \end{bmatrix}^T \tag{A.7}$$

$$\dot{\hat{\boldsymbol{u}}}_{vwh} = \begin{bmatrix} -\dot{\alpha}_{\boldsymbol{u}} \sin\alpha_{\boldsymbol{u}} \cos\beta_{\boldsymbol{u}} - \dot{\beta}_{\boldsymbol{u}} \cos\alpha_{\boldsymbol{u}} \sin\beta_{\boldsymbol{u}} \\ \dot{\alpha}_{\boldsymbol{u}} \cos\alpha_{\boldsymbol{u}} \cos\beta_{\boldsymbol{u}} - \dot{\beta}_{\boldsymbol{u}} \sin\alpha_{\boldsymbol{u}} \sin\beta_{\boldsymbol{u}} \\ \dot{\beta}_{\boldsymbol{u}} \cos\beta_{\boldsymbol{u}} \end{bmatrix} \tag{A.8}$$

Since the equations of motion are integrated in the Cartesian, barycentric rotating frame (with unit vectors $\hat{x}$-$\hat{y}$-$\hat{z}$), a direction cosine matrix, $\mathbf{C}$, is required to transform the thrust direction, $\hat{\boldsymbol{u}}_{vwh}$ (and $\dot{\hat{\boldsymbol{u}}}_{vwh}$),

$$\mathbf{C} = \begin{bmatrix} \hat{x}\cdot\hat{v} & \hat{x}\cdot\hat{w} & \hat{x}\cdot\hat{h} \\ \hat{y}\cdot\hat{v} & \hat{y}\cdot\hat{w} & \hat{y}\cdot\hat{h} \\ \hat{z}\cdot\hat{v} & \hat{z}\cdot\hat{w} & \hat{z}\cdot\hat{h} \end{bmatrix}, \ \dot{\mathbf{C}} = \begin{bmatrix} \hat{x}\cdot\dot{\hat{v}} & \hat{x}\cdot\dot{\hat{w}} & \hat{x}\cdot\dot{\hat{h}} \\ \hat{y}\cdot\dot{\hat{v}} & \hat{y}\cdot\dot{\hat{w}} & \hat{y}\cdot\dot{\hat{h}} \\ \hat{z}\cdot\dot{\hat{v}} & \hat{z}\cdot\dot{\hat{w}} & \hat{z}\cdot\dot{\hat{h}} \end{bmatrix} \tag{A.9}$$

$$\hat{\boldsymbol{u}}_{ijk} = \mathbf{C}\hat{\boldsymbol{u}}_{vwh} \tag{A.10}$$

$$\dot{\hat{\boldsymbol{u}}}_{xyz} = \dot{\mathbf{C}}\hat{\boldsymbol{u}}_{vwh} + \mathbf{C}\dot{\hat{\boldsymbol{u}}}_{vwh} \tag{A.11}$$

The subscript "xyz" denotes that the thrust direction is expressed in terms of unit vectors in the original cartesian frame of the system model state variables. The definition of the thrust direction from equation (3.52), is employed to parameterize the primer vector,

$$\boldsymbol{\lambda}_{\boldsymbol{v}} = \|\boldsymbol{\lambda}_{\boldsymbol{v}}\| \, \hat{\boldsymbol{u}}_{xyz} \tag{A.12}$$

Then, the equation of motion for the primer vector, equation (3.44), is directly involved in parameterizing the position costate vector,

$$\boldsymbol{\lambda}_{\boldsymbol{r}} = -\dot{\boldsymbol{\lambda}}_{\boldsymbol{v}} - \boldsymbol{\lambda}_{\boldsymbol{v}}^T \frac{\partial \boldsymbol{g}}{\partial \boldsymbol{v}} \tag{A.13}$$

The derivative of the primer vector, $\dot{\boldsymbol{\lambda}}_{\boldsymbol{v}}$, is also available by differentiating equation (A.12), and substituting the result into equation (A.13),

$$\dot{\boldsymbol{\lambda}}_{\boldsymbol{v}} = -||\dot{\boldsymbol{\lambda}}_{\boldsymbol{v}}||\hat{\boldsymbol{u}}_{xyz} - \|\boldsymbol{\lambda}_{\boldsymbol{v}}\| \, \dot{\hat{\boldsymbol{u}}}_{xyz} \tag{A.14}$$

Additionally, equation (3.56) is used to parameterize $\|\boldsymbol{\lambda}_{\boldsymbol{v}}\|$ in terms of the thrust, T. Thus, the mapping sequence allows $\boldsymbol{\lambda}_{\boldsymbol{r}}$, $\boldsymbol{\lambda}_{\boldsymbol{v}}$ to be calculated from $\alpha_{\boldsymbol{u}}$, $\dot{\alpha}_{\boldsymbol{u}}$, $\beta_{\boldsymbol{u}}$, $\dot{\beta}_{\boldsymbol{u}}$, T, and $||\dot{\boldsymbol{\lambda}}_{\boldsymbol{v}}||$.

B. Jacobian Matrix for a Solar Sail Trajectory

$$\left[\begin{array}{ccccccccccccccccc|cccccccccccc}
\begin{matrix}\frac{\partial\boldsymbol{\Delta}_{1,1}}{\partial\boldsymbol{x}_1}\\\frac{\partial\boldsymbol{\Delta}_{1,c}}{\partial\boldsymbol{x}_1}\\\frac{\partial\boldsymbol{\Delta}_{1,4}}{\partial\boldsymbol{x}_1}\end{matrix} & \begin{matrix}\frac{\partial\boldsymbol{\Delta}_{1,1}}{\partial\boldsymbol{u}_1}\\\frac{\partial\boldsymbol{\Delta}_{1,c}}{\partial\boldsymbol{u}_1}\\\frac{\partial\boldsymbol{\Delta}_{1,4}}{\partial\boldsymbol{u}_1}\end{matrix} & \begin{matrix}\frac{\partial\boldsymbol{\Delta}_{1,1}}{\partial\boldsymbol{x}_{1,2}}\\\frac{\partial\boldsymbol{\Delta}_{1,c}}{\partial\boldsymbol{x}_{1,2}}\\\frac{\partial\boldsymbol{\Delta}_{1,4}}{\partial\boldsymbol{x}_{1,2}}\end{matrix} & \begin{matrix}\frac{\partial\boldsymbol{\Delta}_{1,1}}{\partial\boldsymbol{x}_{1,3}}\\\frac{\partial\boldsymbol{\Delta}_{1,c}}{\partial\boldsymbol{x}_{1,3}}\\\frac{\partial\boldsymbol{\Delta}_{1,4}}{\partial\boldsymbol{x}_{1,3}}\end{matrix} & \begin{matrix}\frac{\partial\boldsymbol{\Delta}_{1,1}}{\partial\boldsymbol{x}_2}\\\frac{\partial\boldsymbol{\Delta}_{1,c}}{\partial\boldsymbol{x}_2}\\\frac{\partial\boldsymbol{\Delta}_{1,4}}{\partial\boldsymbol{x}_2}\end{matrix} & \begin{matrix}\frac{\partial\boldsymbol{\Delta}_{1,1}}{\partial\boldsymbol{u}_2}\\\frac{\partial\boldsymbol{\Delta}_{1,c}}{\partial\boldsymbol{u}_2}\\\frac{\partial\boldsymbol{\Delta}_{1,4}}{\partial\boldsymbol{u}_2}\end{matrix} \\
& & & & \begin{matrix}\frac{\partial\boldsymbol{\Delta}_{2,1}}{\partial\boldsymbol{x}_2}\\\frac{\partial\boldsymbol{\Delta}_{2,c}}{\partial\boldsymbol{x}_2}\\\frac{\partial\boldsymbol{\Delta}_{2,4}}{\partial\boldsymbol{x}_2}\end{matrix} & \begin{matrix}\frac{\partial\boldsymbol{\Delta}_{2,1}}{\partial\boldsymbol{u}_2}\\\frac{\partial\boldsymbol{\Delta}_{2,c}}{\partial\boldsymbol{u}_2}\\\frac{\partial\boldsymbol{\Delta}_{2,4}}{\partial\boldsymbol{u}_2}\end{matrix} & \begin{matrix}\frac{\partial\boldsymbol{\Delta}_{2,1}}{\partial\boldsymbol{x}_{2,2}}\\\frac{\partial\boldsymbol{\Delta}_{2,c}}{\partial\boldsymbol{x}_{2,2}}\\\frac{\partial\boldsymbol{\Delta}_{2,4}}{\partial\boldsymbol{x}_{2,2}}\end{matrix} & \begin{matrix}\frac{\partial\boldsymbol{\Delta}_{2,1}}{\partial\boldsymbol{x}_{2,3}}\\\frac{\partial\boldsymbol{\Delta}_{2,c}}{\partial\boldsymbol{x}_{2,3}}\\\frac{\partial\boldsymbol{\Delta}_{2,4}}{\partial\boldsymbol{x}_{2,3}}\end{matrix} & \begin{matrix}\frac{\partial\boldsymbol{\Delta}_{2,1}}{\partial\boldsymbol{x}_3}\\\frac{\partial\boldsymbol{\Delta}_{2,c}}{\partial\boldsymbol{x}_3}\\\frac{\partial\boldsymbol{\Delta}_{2,4}}{\partial\boldsymbol{x}_3}\end{matrix} & \begin{matrix}\frac{\partial\boldsymbol{\Delta}_{2,1}}{\partial\boldsymbol{u}_3}\\\frac{\partial\boldsymbol{\Delta}_{2,c}}{\partial\boldsymbol{u}_3}\\\frac{\partial\boldsymbol{\Delta}_{2,4}}{\partial\boldsymbol{u}_3}\end{matrix} \\
& & & & & & & & & & \ddots \\
& & & & & & & & & & & \begin{matrix}\frac{\partial\boldsymbol{\Delta}_{n-1,1}}{\partial\boldsymbol{x}_{n-1}}\\\frac{\partial\boldsymbol{\Delta}_{n-1,c}}{\partial\boldsymbol{x}_{n-1}}\\\frac{\partial\boldsymbol{\Delta}_{n-1,4}}{\partial\boldsymbol{x}_{n-1}}\end{matrix} & \begin{matrix}\frac{\partial\boldsymbol{\Delta}_{n-1,1}}{\partial\boldsymbol{u}_{n-1}}\\\frac{\partial\boldsymbol{\Delta}_{n-1,c}}{\partial\boldsymbol{u}_{n-1}}\\\frac{\partial\boldsymbol{\Delta}_{n-1,4}}{\partial\boldsymbol{u}_{n-1}}\end{matrix} & \begin{matrix}\frac{\partial\boldsymbol{\Delta}_{n-1,1}}{\partial\boldsymbol{x}_{n-1,2}}\\\frac{\partial\boldsymbol{\Delta}_{n-1,c}}{\partial\boldsymbol{x}_{n-1,2}}\\\frac{\partial\boldsymbol{\Delta}_{n-1,4}}{\partial\boldsymbol{x}_{n-1,2}}\end{matrix} & \begin{matrix}\frac{\partial\boldsymbol{\Delta}_{n-1,1}}{\partial\boldsymbol{x}_{n-1,3}}\\\frac{\partial\boldsymbol{\Delta}_{n-1,c}}{\partial\boldsymbol{x}_{n-1,3}}\\\frac{\partial\boldsymbol{\Delta}_{n-1,4}}{\partial\boldsymbol{x}_{n-1,3}}\end{matrix} & \begin{matrix}\frac{\partial\boldsymbol{\Delta}_{n-1,1}}{\partial\boldsymbol{x}_n}\\\frac{\partial\boldsymbol{\Delta}_{n-1,c}}{\partial\boldsymbol{x}_n}\\\frac{\partial\boldsymbol{\Delta}_{n-1,4}}{\partial\boldsymbol{x}_n}\end{matrix} & \begin{matrix}\frac{\partial\boldsymbol{\Delta}_{n-1,1}}{\partial\boldsymbol{u}_n}\\\frac{\partial\boldsymbol{\Delta}_{n-1,c}}{\partial\boldsymbol{u}_n}\\\frac{\partial\boldsymbol{\Delta}_{n-1,4}}{\partial\boldsymbol{u}_n}\end{matrix} \\
\hline
& 2\boldsymbol{u}_1^T \\
& & & & & 2\boldsymbol{u}_2^T \\
& & & & & & & & & 2\boldsymbol{u}_3^T \\
& & & & & & & & & & \ddots \\
& & & & & & & & & & & & 2\boldsymbol{u}_{n-1}^T \\
& & & & & & & & & & & & & & & & 2\boldsymbol{u}_n^T \\
\hline
\frac{\partial\boldsymbol{g}_1}{\partial\boldsymbol{x}_1} & \frac{\partial\boldsymbol{g}_1}{\partial\boldsymbol{u}_1} & & & & & & & & & & & & & & & & 2\boldsymbol{\eta}_1^D \\
& & \frac{\partial\boldsymbol{g}_{1,2}}{\partial\boldsymbol{x}_{1,2}} & & & & & & & & & & & & & & & & 2\boldsymbol{\eta}_{1,2}^D \\
& & & \frac{\partial\boldsymbol{g}_{1,3}}{\partial\boldsymbol{x}_{1,3}} & & & & & & & & & & & & & & & & 2\boldsymbol{\eta}_{1,3}^D \\
& & & & \frac{\partial\boldsymbol{g}_2}{\partial\boldsymbol{x}_2} & \frac{\partial\boldsymbol{g}_2}{\partial\boldsymbol{u}_2} & & & & & & & & & & & & & & & 2\boldsymbol{\eta}_2^D \\
& & & & & & \frac{\partial\boldsymbol{g}_{2,2}}{\partial\boldsymbol{x}_{2,2}} & & & & & & & & & & & & & & & 2\boldsymbol{\eta}_{2,2}^D \\
& & & & & & & \frac{\partial\boldsymbol{g}_{2,3}}{\partial\boldsymbol{x}_{2,3}} & & & & & & & & & & & & & & & 2\boldsymbol{\eta}_{2,3}^D \\
& & & & & & & & \frac{\partial\boldsymbol{g}_3}{\partial\boldsymbol{x}_3} & \frac{\partial\boldsymbol{g}_3}{\partial\boldsymbol{u}_3} & & & & & & & & & & & & & & 2\boldsymbol{\eta}_3^D \\
& & & & & & & & & & \ddots & & & & & & & & & & & & & & \ddots \\
& & & & & & & & & & & \frac{\partial\boldsymbol{g}_{n-1}}{\partial\boldsymbol{x}_{n-1}} & \frac{\partial\boldsymbol{g}_{n-1}}{\partial\boldsymbol{u}_{n-1}} & & & & & & & & & & & & & 2\boldsymbol{\eta}_{n-1}^D \\
& & & & & & & & & & & & & \frac{\partial\boldsymbol{g}_{n-1,2}}{\partial\boldsymbol{x}_{n-1,2}} & & & & & & & & & & & & & 2\boldsymbol{\eta}_{n-1,2}^D \\
& & & & & & & & & & & & & & \frac{\partial\boldsymbol{g}_{n-1,3}}{\partial\boldsymbol{x}_{n-1,3}} & & & & & & & & & & & & & 2\boldsymbol{\eta}_{n-1,3}^D \\
& & & & & & & & & & & & & & & \frac{\partial\boldsymbol{g}_n}{\partial\boldsymbol{x}_n} & \frac{\partial\boldsymbol{g}_n}{\partial\boldsymbol{u}_n} & & & & & & & & & & & & 2\boldsymbol{\eta}_n^D
\end{array}\right]$$

Figure B.1. General Form of the Gauss-Lobatto Jacobian Matrix $D\boldsymbol{F}$ for $l = 0$, where $(\cdot)^D = \operatorname{diag}(\cdot)$.

VITA

VITA

Martin Thomas Ozimek was born on December 16, 1980 to Joseph Patrick Ozimek and Pamela Jean Ozimek in Buffalo, New York. He received his Bachelor of Science degree in Aerospace Engineering from The Pennsylvania State University in December of 2003, graduating with Highest Honors from the Schreyer Honors College. During his undergraduate education, Martin spent 4 semesters of cooperative education at the NASA Johnson Space Center, working with the Pyrotechnics group (2002), the International Space Station Trajectory Operations Group (2002), and the Descent Analysis Group (2003-2004). While at NASA, he was recognized with a Flag Award (2002) and a Special Achievement Award (2004).

Martin earned his Master of Science degree in Aeronautics and Astronautics at Purdue University in December of 2006. He was awarded the Andrews Doctoral Fellowship for the duration of his Masters studies. Martin spent the summers of 2005-2006 performing research at NASA Goddard Spaceflight Center, under the supervision of Mr. David Folta, including the summer of 2005 as a member of NASA Academy.

Martin earned his Ph.D. in Aeronautics and Astronautics at Purdue University in May of 2010. In 2007, he was awarded the NASA Graduate Student Research Program (GSRP) Fellowship for his Ph.D. research. Martin spent the summers of 2007-2009 continuing his fellowship research at NASA Goddard Spaceflight Center. In 2008 and 2010, he served as a judge for the Purdue AAE Research Symposium Series. In 2007, he won the AIAA Orville and Wilbur Wright Graduate Award. He was awarded the Best Paper of the Conference Award for his work on “Solar Sails and Lunar South Pole Coverage” that was presented at the 2008 Astrodynamics Specialist Conference. He was also named the 2010 Purdue AAE Outstanding Graduate Student. Martin has accepted an engineering staff position at the Johns Hopkins University Applied Physics Laboratory, where he will work on spacecraft mission design.